Radiocarbon Source Apportionment of Carbonaceous Aerosols using Water-Soluble Organic Carbon and Oxalate Fractions

Inauguraldissertation

der Philosophisch-naturwissenschaftlichen Fakultät

der Universität Bern

vorgelegt von

Martin Rauber

von Kandergrund BE

Leiter der Arbeit:

Prof. Dr. Sönke Szidat

Departement für Chemie, Biochemie und Pharmazie

Universität Bern

Radiocarbon Source Apportionment of Carbonaceous Aerosols using Water-Soluble Organic Carbon and Oxalate Fractions

Inauguraldissertation

der Philosophisch-naturwissenschaftlichen Fakultät

der Universität Bern

vorgelegt von

Martin Rauber

von Kandergrund BE

Leiter der Arbeit:

Prof. Dr. Sönke Szidat

Departement für Chemie, Biochemie und Pharmazie

Universität Bern

Von der Philosophisch-naturwissenschaftlichen Fakultät angenommen

Bern, 17.08.2022   Der Dekan

Prof. Dr. Zoltan Balogh

Table of Contents

1 Summary

Atmospheric aerosols are known for their effects on the cardiopulmonary system with an increase of human morbidity and mortality following acute and chronic exposure. Air pollution from atmospheric aerosols affects human well-being, fosters social inequality, and creates an economic burden. Understanding the sources and formation processes of atmospheric aerosols is crucial for targeted pollution mitigation. Beyond the effects on human health, society, and economic development, atmospheric aerosols affect the radiative forcing and are therefore relevant for the Earth's climate. Unlike the gases carbon dioxide and methane strongly contributing to a warming effect, atmospheric aerosols have an overall negative radiative forcing. Despite this overall negative radiative forcing, some atmospheric aerosol compounds or fractions exhibit a positive radiative forcing while others' forcing is negative.

Atmospheric aerosols can be classified, e.g., by their mode of formation, size, sampling environment, origin, or chemical composition. In terms of their chemical composition, atmospheric aerosols consist of inorganic compounds such as sodium, calcium, potassium, and magnesium as well as sulphate, nitrate, and chloride, however, a substantial fraction (20 to 90%) of atmospheric aerosols consists of carbonaceous compounds. Carbonaceous compounds (total carbon, TC) in atmospheric aerosols can be classified into organic carbon (OC) and black elemental carbon (EC) fractions. OC refers to the non-refractory carbonaceous aerosol fraction whereas EC is the refractory fraction. The OC fraction is frequently further separated into the water-soluble OC (WSOC) and water-insoluble OC (WINSOC) fraction. Beyond these large fractions, also single components and major compound classes may be analysed, including humic-like substances, carboxylic and dicarboxylic compounds, anhydrides, sugars, and sugar-alcohols. When analysing atmospheric aerosol samples from a receptor site, the sources and the fractions in which these sources contribute to the aerosols may be of interest. Of interest might also be secondary organic aerosols, i.e., organic aerosols that were formed by gaseous precursors in a gas-to-particle conversion.

Identifying air pollution sources and quantifying their contribution to air pollution is known as source apportionment. Exploratory factor analysis models like positive matrix factorisation are frequently used for source apportionment. Furthermore, tracer compounds such as levoglucosan for biomass burning are also frequently used. Source apportionment of fossil-fuel and biogenic sources of aerosol are difficult to achieve by traditional means as there may be no chemical difference in the compounds emitted by these sources. Instead of just analysing the chemical composition, the isotopic signature of a sample is analysed. For carbonaceous aerosols, radiocarbon (^{14}C, $t_{1/2} = 5730 \pm 40$) is a highly valuable tool for the source apportionment of fossil-fuel and biogenic fractions. Constantly formed in the upper atmosphere by cosmic ray bombardment of ^{14}N, radiocarbon is oxidised first to carbon monoxide (^{14}CO) and later to carbon dioxide ($^{14}CO_2$), from where it enters the global carbon cycle. Carbonaceous aerosols formed by biogenic emissions and biomass burning contain radiocarbon at a contemporary level while emissions formed by fossil-fuel are completely devoid of radiocarbon. This highly valuable tool for source apportionment was used in this work. Radiocarbon source apportionment was applied on the TC fraction as well as the

subfractions EC, WSOC, and WINSOC. Furthermore, radiocarbon source apportionment was also applied to single compounds, known as compound-specific radiocarbon analysis (CSRA) as demonstrated in this work with CSRA of oxalic acid.

In the first project, low-loaded aerosol filters from the Norwegian archipelago Svalbard were analysed with an optimised OC/EC separation method and direct WSOC measurement. The filter material subjected to OC/EC separation was water extracted for charring reduction, i.e., a reduction of OC pyrolysis. The eluate from the water extraction was used for direct WSOC measurement by chemical wet oxidation. Therefore, without an increase in filter material usage, EC and WSOC were analysed. Although not feasible with the Svalbard filters, radiocarbon measurements of the WINSOC fraction are also possible with higher loaded filters. Additional to EC and WSOC, TC was measured with residual filter material not utilised for water extraction.

Radiocarbon analysis requires physical OC/EC separation. This separation is affected by thermal desorption of EC (EC-loss) as well as the conversion of OC to EC by pyrolysis (charring). Both EC-loss and charring must be corrected for. For EC-loss, the currently accepted approach was based on a simple linear extrapolation made with multiple radiocarbon measurements of filters with deliberately lowered EC yields. In this work, a novel thermal-desorption model for the correction of ^{14}C-EC after thermal-optical separation was introduced. This thermal-desorption approach should supersede the current linear extrapolation approach. Additional to the ^{14}C-EC correction, a web application for analysing output files from the OC/EC analyser was made. Both tools were written in the R programming language and published as a free open-source software in a repository.

Although atmospheric aerosols are a highly heterogenic mixture of countless number of compounds, they contain a relatively high fractions of certain compound classes. A comparably large fraction in atmospheric aerosols consists of dicarboxylic acids, and, due to their abundance as well as their ability to act as cloud condensation nuclei, dicarboxylic acids have become of great interest. Nevertheless, their sources and formation process are not fully understood. Furthermore, previous studies indicate that dicarboxylic acids may be formed as secondary organic aerosols. The separation of dicarboxylic acids and subsequent radiocarbon measurement for a compound-specific radiocarbon analysis is therefore highly desirable. Oxalic acid is frequently the most prevalent dicarboxylic acid in atmospheric aerosols, and therefore the obvious choice for CSRA. Two previous studies reported CSRA of oxalate in atmospheric aerosols, however, only with a very limited number of measurements. In this work, a simpler method is presented and applied on filters from urban and rural sites. Here, extracted aerosol filters were separated by a single ion chromatography step followed by a chemical wet oxidation for radiocarbon measurement. Although CSRA is much more elaborate than WSOC analysis, this approach is much simpler than previous attempts of CSRA for oxalate while providing low processing blanks. Results indicate a predominant biogenic formation of oxalate as a secondary organic aerosol. The most significant difference was found for rural Råö (Sweden) with a higher nonfossil fraction for oxalate compared to WSOC. In filters from Delhi (India),

a significant difference for oxalate and WSOC was found for night-time filters, but not during daytime. Oxalate and WSOC were predominately formed from biogenic sources in Mexico City (Mexico), despite low nonfossil fractions for TC and EC. A high fossil contribution primarily from coal combustion was observed in all fractions (TC, EC, WSOC, WINSOC) from Kraków (Poland), however, oxalate concentrations were much lower than in other sites and insufficient for a radiocarbon measurement. Primary or secondary organic aerosols from coal combustion are therefore not a relevant contributor for oxalate formation.

With no permanent human population and very rough conditions, Antarctica is a challenging but highly interesting site for a wide range of research. In a collaboration with NILU, the Norwegian Institute for Air Research, aerosol filters from the Norwegian Troll station in Antarctica were analysed. The filters were each sampled for several weeks in austral winter and summer from February 2016 to September 2018. The sampling site is located between the Antarctic coastal zone and inland ice plateau, roughly 200 km inland on dry bedrock. Despite the very low loadings, radiocarbon analysis of the TC, WSOC and WINSOC fractions were successfully performed. Here, the findings of the austral summer filters are discussed. Radiocarbon measurements revealed a depleted levels of radiocarbon compared to contemporary sources. Our analysis indicate that ^{14}C-depleted primary marine aerosol (PMA) sources dominate in all measured carbonaceous fractions in austral summer. Secondary marine aerosols and biomass burning are only minor sources. PMA originates in the Southern Ocean surrounding Antarctica. Upwellings in the Southern Ocean bring aged dissolved organic carbon (DOC) to the surface while sea spray from breaking waves brings the ^{14}C-depleted DOC as PMA into the atmosphere.

1. Introduction

1.1 Fundamentals of carbon

1.1.1 Discovery, history, and relevance of carbon

Before the depths of carbonaceous atmospheric aerosols and the uses of radiocarbon can be explored, one needs to have a look at the big picture: what is carbon, why is it so relevant for humans and life in general and inconspicuous at the same time?

Carbon is the sixth element in the periodic table, and its name originates from the Latin *carbo* for coal and charcoal. Carbon is known as *Kohlenstoff* in German, which literally means coal-substance, and very similar in French and Dutch with *charbon* and *koolstof*, respectively. Carbon was known to man for millennia as charcoal and was used for the reduction of copper, zinc, and tin ores for bronze manufacturing by the Sumerians and Egyptians as far back as 3750 BCE[1]. Although carbon is not a particular abundant element in the Earth's crust, the unique property of carbon to form complex molecules such as proteins, nucleic acids, carbohydrates, and lipids makes life as we know it possible. Carbon fixation by plants (photosynthesis) converts inorganic carbon as CO_2 to organic compounds such as glucose. The human body consists of 18.5% of carbon, making it the second most prevalent element in the human body after oxygen[2]. The total amount of carbon in flora and fauna is roughly 10^{18} kg and 10^{12} kg, respectively, 10^{15} kg in the atmosphere, 10^{18} kg in sea water, and 10^{19} kg in the lithosphere. The sixth element in the periodic table is non-metallic and tetravalent, thus has four electrons available to form covalent chemical bonds[3]. Due to its valency, carbon can form many structurally different forms of the same element (allotropes), some of which have fundamentally divergent properties. The material with the highest hardness and thermal conductivity is best known as a gemstone: diamonds (see Figure 1a). Diamonds have been known as gemstones in India at least since 900 BCE[1]. Even before they have been used as gemstones, they have been utilised for making tools in China, however, people have been oblivious that this hard material is made of carbon[1,4]. Only Lavoisier[5] showed that diamonds are a form of carbon by the combustion of diamonds to carbon dioxide. Most diamonds are not of gemstones grade (bort) and are used for industrial applications. In fact, most mined diamonds are used in industrial tools for cutting, drilling, and grinding. Additional to mined diamonds, also synthetic diamonds have been made. Techniques to produce synthetic diamonds have been developed in the 1950s by General Electric and later refined to produce gemstones–like diamonds[6,7]. Nanocarbons such as fullerenes and carbon nanotubes are other carbon allotropes, which have been of great interest to researchers in recent decades with limited industrial use. Potential applications for fullerenes include their use for biomedical imaging as well as drug and gene delivery[8,9]. Carbon nanotubes (see Figure 1b) have been used as a composite in polymers and for Gecko–like nano tape[10,11]. The last carbon allotrope worth mentioning is graphite for its extensive used and wide range of applications. Best known as an ingredient in pencils (see Figure 1c), graphite is extensively used e.g., to rise the carbon content

of steel during steelmaking, for electrodes in batteries, its use as a heat-resistant material (refractory), in brake linings, and for lubricants. Graphite is crystalline and has carbon arranged in a hexagonal structure, whereas a single layer of graphite is called graphene (see Figure 1d) and the atoms are arranged in a two-dimensional honeycomb lattice[1].

Carbon played an important role in industrialisation through the transition to hydrocarbon-based fuels, which still provide most of the primary energy (see Figure 1e). Beginning with the 18th century, wind and water powered technologies were replaced with coal. As the industrialisation progressed, oil and natural gas was exploited as an additional energy source[12]. Although population grew by less than a factor of four from 1900 to 2000, the world total primary energy consumption multiplied from 22 to 355 exajoules (EJ), an increase of more than 16 times, with most of the energy provided by fossil fuels[13].
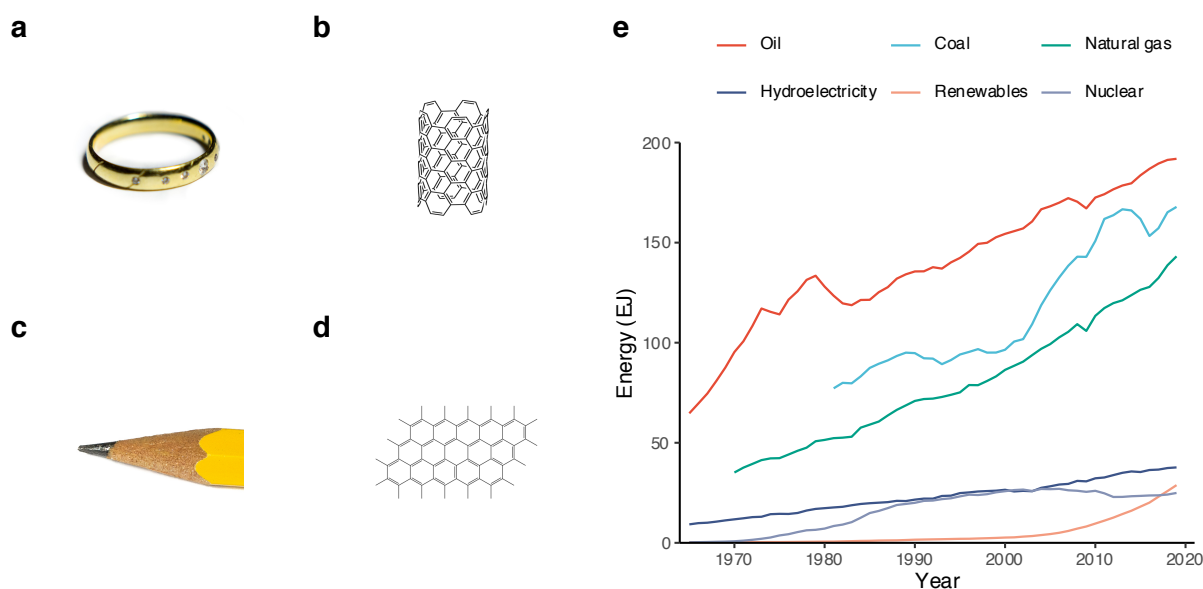
Figure 1: Allotropes of carbon are shown in a to d: diamonds on a gold ring (a), the structure of a carbon nanotube (b), a pencil containing graphite (c), and the structure of graphene (d). Graph e shows the amount of energy in exajoules (EJ) provided by hydrocarbon-based fuels (oil, natural gas, coal) in comparison to hydroelectricity, renewables (solar, wind, geothermal, biofuels), and nuclear in the last decades. Overall, fossil hydrocarbons provided most of the world's primary energy, contributing to 84.3% of the primary energy in 2019. Images a) and c) by Martin Rauber, structures in b) and d) generated with ChemDraw Professional 17.1. Data in e) from BP Statistical Review of World Energy 2021[14].

As of 2019, fossil hydrocarbons provided 492.4 exajoules or 84.3% of the world's primary energy with a 33.1% share of primary energy for oil, 24.2% for natural gas, and 27.0% for coal[15]. Economies of scale in hydrocarbon production provide energy at affordable prices. For the average consumer in the United States (USA), a litre of petrol at the service station is cheaper than a litre of milk or orange juice in a supermarket[16]. Additional to power generation, transport, and heating, a fraction of the fossil hydrocarbon is not combusted and used to produce petrochemicals, bitumen, and fertilisers. Petrochemicals are ubiquitous in

our daily life from anything like painkillers, polymers such as polyester in sportswear to plastics and high-performance composites[3,17]. Although petrochemicals can be substituted with biomass sourced building blocks, their fraction is currently exceedingly small. While there is great potential in biomass for chemical feedstock, many processes need to be developed[18].

1.1.2   Carbon isotopes and their applications

General

Carbon has 15 known isotopes, of which only ^{12}C, ^{13}C, and ^{14}C are found in nature with an occurrence of 98.93%, 1.07%, and ~10^{-10}%, respectively[19,20]. ^{12}C and ^{13}C are the only stable carbon isotopes, all others including the very low abundant ^{14}C are radioactive. Although there exists more than one radioactive carbon isotope, the term radiocarbon is used synonymously only with ^{14}C. Radiocarbon has a wide range of applications and was used for source apportionment in this work. Therefore, the fundamentals of radiocarbon are discussed in more detail in Chapter 1.2, while radiocarbon applications and measurement techniques are discussed in Chapter 1.3 and 1.4, respectively. Apart from ^{14}C, all radioactive isotopes are artificial and have very short half-lives, mostly in the range of seconds or less. ^{11}C is the only artificial isotope with a slightly longer half-life of 20.4 minutes and decays to the stable ^{11}B isotope, primarily by positron emission (β^+). This carbon isotope has a limited use in biomedical imaging applications. There, ^{11}C is incorporated in radiotracers and used for positron emission tomography[21,22]. The ^{12}C isotope is of little interest for analytical purposes due to its abundance, however, it is used to define fractions of ^{13}C to ^{12}C and ^{14}C to ^{12}C, respectively. ^{13}C is a useful nonradioactive isotopic marker for various applications and is elaborated in detail in the sections below.

Stable carbon isotope fractionation

Fractionation due to physical processes (e.g., precipitation) or different metabolic pathways in carbon fixation create small differences in the ^{13}C content of organic and inorganic carbonaceous compounds (see Figure 2). These small differences can be exploited for stable carbon isotope analysis, examples thereof are shown in the next section[20]. Different pathways have been found for photosynthetic carbon fixation in plants. Organisms generally show a preference for the lighter ^{12}C isotope, thus organic matter is ^{13}C-depleted compared to atmospheric CO_2. The amount of depletion is dependent on the carbon fixation pathway. There are three distinct types of higher plants distinguishable by their carbon fixation pathway: C_3 plants, C_4 plants, and crassulacean acid metabolism (CAM) plants. Although the minority of terrestrial plant biomass but important for agriculture, C_4 plants (e.g., sugarcane, corn) evolved multiple times independently and appeared at least 20–30 million years ago but were not frequent until 8–5 million years ago[23]. C_4 plants have only a slight ^{13}C depletion. C_3 plants (e.g., wheat, rice) have been around for much longer and strongly discriminate against the uptake of ^{13}C. There are multiple types of CAM pathways, however, in general the depletion in CAM plants (e.g., pineapple) is between C_3 and C_4 plants. In some plants, the CAM pathway is an adaptation to arid environments. With good water availability ^{13}C depletion

values of CAM plants are close to C_3 plants and in times of drought closer to the values of C_4 plants[24,25]. Organisms which later formed fossil fuels fed on C_3 plants as C_4 plants had not evolved yet, hence the significantly different $^{13}C/^{12}C$ ratio of CO_2 from fossil-fuel combustion to atmospheric CO_2[20].

$$\delta^{13}C = \left(\frac{\left(\frac{^{13}C}{^{12}C}\right)_{sample}}{\left(\frac{^{13}C}{^{12}C}\right)_{standard}} - 1 \right) \cdot 1000‰ \qquad \text{Equation 1}$$

The ^{13}C depletion in a sample is usually reported as $\delta^{13}C$ instead of stating the $^{13}C/^{12}C$ ratio directly (Equation 1). $\delta^{13}C$ is defined as the $^{13}C/^{12}C$ ratio of sample compared to the $^{13}C/^{12}C$ ratio of the Vienna Pee Dee Belemnite (VPDB) standard in parts per thousand (per mil, ‰). Strictly speaking, the 1000‰ factor should be omitted for the definition of $\delta^{13}C$, however, most literature reports the definition of $\delta^{13}C$ as shown in Equation 1. VPDB is a limestone replacement standard after the original standard Pee Dee Belemnite (PDB) was exhausted. PDB was based on a squid-like marine fossil with an anomalously high $^{13}C/^{12}C$ ratio. As shown in Figure 2, the reported $\delta^{13}C$ (‰) values are usually negative for that reason[20].
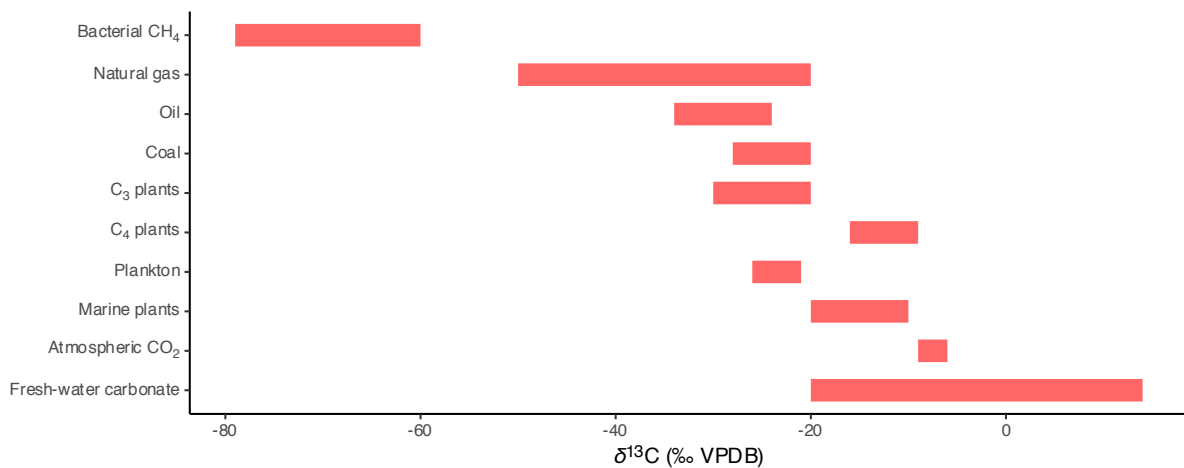
Figure 2: Variation of $^{13}C/^{12}C$ in natural compounds. Fossil-fuel sources are sources which are depleted in ^{13}C and the degree of depletion depends on the metabolic pathway for plants[26]. VPDB refers to Vienna Pee Dee Belemnite reference.

Stable carbon isotope applications

The use of ^{13}C is highly diverse and this section will highlight only a few applications, first and foremost for carbonaceous aerosols. This section is by no means conclusive and should just emphasize how broad

the use of ^{13}C for carbonaceous aerosols and beyond is, and, despite not utilised in this work, worth mentioning as complementary technique.

The ^{13}C signature observed in various combustible sources (see Figure 2) differ and can be used for source apportionment (see Chapter 1.5.4). For example, Masalaite et al.[27] utilised the ^{13}C signature to differentiate wintertime organic aerosols released by biomass burning from those released by fossil-fuel combustion in samples from Lithuania. Cao et al.[28] used stable carbon isotope analysis for the analysis of organic carbon and elemental carbon fractions (see Chapter 1.5.2) in summer and winter filters from China. They concluded that the carbonaceous aerosols were mainly formed from fossil-fuel sources such as coal combustion and motor vehicles, especially in wintertime. One might assume that the ^{13}C signature observed in the aerosols are identical to the source material signature, however, it has been shown that formation of aerosols is linked with isotopic fractionation[29].

Stable carbon isotope analysis can be applied beyond carbonaceous aerosols – for environmental research and more. This should also underline how ^{13}C can be used supplementary to radiocarbon analysis or completely replace ^{14}C as a tracer for certain applications. The intend of presenting ^{13}C analysis and their application here is to highlight its existence as a complementary technique in carbon isotope analysis, especially when radiocarbon analysis is not possible or not feasible. Four vastly different use cases are presented in this section below.

Due to fractionation, different food sources have different isotopic signatures, e.g., C_3 versus C_4 plants or marine versus freshwater food sources. Stable isotope analysis has frequently been used to trace wildlife. The isotopic signature is incorporated in the tissue of the organisms, which can be used to track animals moving between isotopically distinct food sources. A wide range of migrating species have been investigated including bats, birds, whales, and fish[30].

Owing to its nonradioactive nature, ^{13}C is a preferred isotopic tracer for *in vivo* metabolic research and diagnostics. ^{13}C-glucose has been used as a tracer to investigate glucose kinetics, ^{13}C-palmitate and ^{13}C-leucine have been used to trace fat and amino acid oxidation, respectively[31]. Ulcers and gastric cancer are diseases associated with the infection of *Helicobacter pylori*. Invasive tests require biopsies by gastrointestinal endoscopy, for which a non-invasive substitute would be preferred. The gram-negative bacteria produce large amounts of the enzyme urease to live in the acidic stomach environment. In presence of *Helicobacter pylori,* orally administered ^{13}C labelled urea is hydrolysed in ammonia and $^{13}CO_2$. The gas diffuses into the blood and is eliminated from the lungs by exhaled breath, where in presence of *Helicobacter pylori* [13]C levels above background are detected[32].

Compliance with labels and food standards requires analytical methods to detect misdescribed foodstuffs. Foods can be altered by substitution with cheaper ingredients, adding undeclared ingredients, or false claims regarding geographical or production origin. Stable isotope analysis can be a valuable tool in solving an investigation as the isotopic ratio can be used for authentication. Foods mostly consists of the elements hydrogen, carbon, nitrogen, and oxygen, all of which have two stable isotopic forms ($^2H/^1H$, $^{13}C/^{12}C$,

$^{15}N/^{14}N$, and $^{18}O/^{16}O$) useful for food forensics. As an example, Rhodes et al.[33] used stable carbon isotope analysis to authenticate the claims that poultry have been fed with maize. Maize is a C_4 plant and therefore not as ^{13}C depleted than alternative feed sources from C_3 plants. Chickens fed a higher proportion of maize in the diet showed higher $\delta^{13}C$ values, therefore maize-fed poultry can be differentiated from regular poultry. Customers may want to choose the geographical origin of the food they purchase, and the food safety authorities need to verify the origin claims made by the vendors. Heaton et al.[34] presented a method not only using ^{13}C but also ^2H and ^{18}O as well as trace elements to verify the geographical origin of beef. Depending on the countries under investigation, the method can provide information on the meat's origin.

Unconventional natural gas resources in shale gas deposits require advanced production methods and are exploited by directional drilling and hydraulic fracturing. Osborn et al.[35] analysed ground water wells in Pennsylvania and upstate New York as concerns about the drilling operations regarding groundwater contamination have frequently been raised. Not only did they find elevated methane concentrations close to active drilling sites but were also able to confirm by ^{13}C analysis that elevated methane levels were indeed caused by drilling operations.

Stable carbon isotope measurement

The much higher prevalence of ^{13}C compared to radiocarbon in samples simplifies the analysis of the stable isotope. Precise stable isotope analysis is usually performed with an isotope-ratio mass spectrometer (IRMS). Different techniques exist to convert the solid or liquid sample into a gas, which is fed into the analyser. There, the gaseous sample is positively charged in an ionisation chamber and accelerated with an electromagnet. The ions take a different flight path depending on their mass-to-charge ratio. A major difference of an IRMS system to a regular mass spectrometer is the presence of multiple faraday cup detectors at the end of the flight tube, which simultaneously detect the differently charged ions[36].

Alternative spectroscopic measurement techniques for stable carbon isotope have been developed. These techniques offer a greater mobility for field applications and aim to be more affordable. In general, these laser-based techniques are less sensitive than their mass spectrometry counterpart[37].

Furthermore, ^{13}C is used in nuclear magnetic resonance (NMR) spectroscopy for the identification of carbon atoms in organic molecules. ^{13}C has a nonzero nuclear spin and is therefore suitable for NMR spectroscopy. In NMR spectroscopy, ^{13}C is only used as a tool to analyse organic molecules[38]. This contrasts with other ^{13}C applications where the small differences in the ^{13}C content are relevant and of interest. Nevertheless, the use of NMR for ^{13}C discrimination is possible for isotopic fingerprinting e.g., for food forensics. Site-specific natural isotopic fractionation by nuclear magnetic resonance (SNIF-NMR) has been used to authenticate vanillin[39] and the botanical origin sugars in fruit juices[40].

1.2 Fundamentals of radiocarbon

Although stable carbon analysis can answer many scientific questions, radiocarbon analysis can go far beyond what is feasible with ^{13}C analysis. This Chapter discusses the historical background of radiocarbon measurements, the formation and distribution in the environment from natural and anthropogenic causes, radiocarbon notation, and the decay of ^{14}C. Radiocarbon applications are discussed in Chapter 1.3, while radiocarbon measurement techniques are discussed in Chapter 1.4.

1.2.1 Discovery and history of radiocarbon

Various physicists in the 1930s found evidence for the existence of ^{14}C in cloud chamber experiments[41–43]. In 1940, Martin Kamen and Sam Ruben bombarded graphite targets with deuterons. As the cyclotron at Berkeley utilised for this endeavour was also used to produce the established isotopes ^{32}P and ^{59}Fe during daytime for cancer therapies, the quest for ^{14}C was a night-time operation. Night after night, Kamen coated a copper plate with graphite before bombardment overnight in the cyclotron. During daytime, Ruben analysed last night's graphite sample. First, the graphite was combusted to CO_2 with cupric oxide, then reacted with calcium hydroxide to yield calcium carbonate as a precipitation. The carbonate was acidified with sulphuric acid to generate carbon dioxide again, which was transferred into the gas counter. The scientists could have analysed the CO_2 generated after graphite combustion directly, however, the acidification and precipitation made sure that the radioactivity measured originates from a carbon isotope. The observed radioactivity remained stable even after repeated precipitation and acidification cycles, supporting the hypothesis of the existence of a long-lived carbon isotope[44].

1.2.2 Formation and distribution of radiocarbon

Radiocarbon is formed by cosmic ray bombardment of ^{14}N in the upper atmosphere near the boundary between the stratosphere and troposphere at an altitude of 9–15 km. Cosmic rays collide with atoms in the atmosphere, creating a secondary cosmic ray in the form of a thermal neutron. The neutron enters the nucleus of an atmospheric ^{14}N to produce a ^{14}C atom and a proton in a (n-p) reaction as shown in Equation 2:

$$^{14}_{7}N + n \rightarrow {}^{14}_{6}C + p \qquad \qquad \text{Equation 2}$$

Radiocarbon production is also possible at lower altitudes including ground level; however, the production rates are two orders of magnitude lower[45]. The radiocarbon production varies slightly over time and is affected by the Earth's magnetic field, the carbon cycle, and the solar cycles. The differences in ^{14}C production by the magnetic field is >10%, however on a timescale of millennia to tens of millennia. In contrary, much shorter solar cycles are known, although with minor differences in ^{14}C production. A

difference in radiocarbon production of 5‰ is caused by Schwabe cycles with a periodicity of ~11 years as well as Gleissberg and DeVries cycles (periodicity: 90–200 years) with a difference in the ^{14}C production of 25‰, respectively. These cycles are caused by changes in the Sun's magnetic activity[20,46,47]. Additional to the production of radiocarbon in the atmosphere, anthropogenic activities affect the production and distribution of radiocarbon.

$$^{14}C + \frac{1}{2}O_2 \rightarrow {}^{14}CO \qquad\qquad \text{Equation 3}$$

$$^{14}CO + \cdot OH \rightarrow {}^{14}CO_2 + \cdot H \qquad\qquad \text{Equation 4}$$
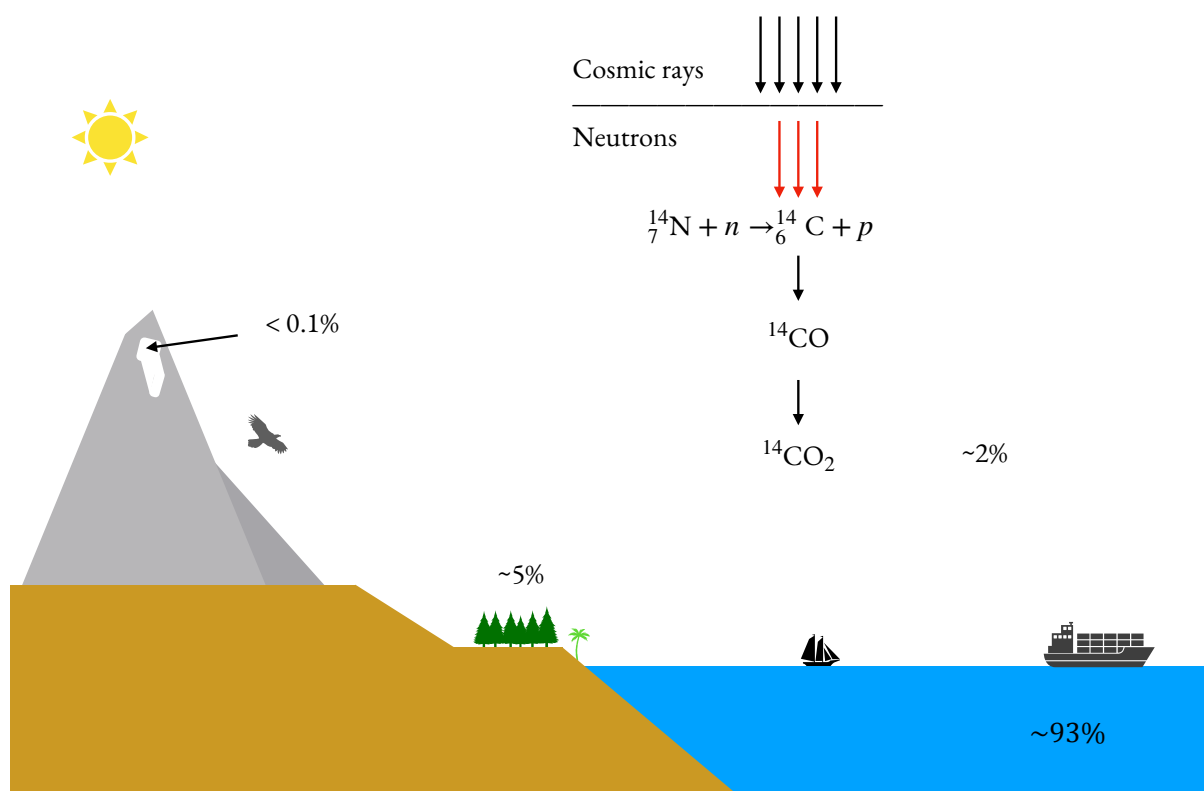
Figure 3: Formation of radiocarbon and the distribution of the global ^{14}C inventory. Cosmic rays collide with atoms in the upper atmosphere producing neutrons. The neutrons produce ^{14}C atoms in a (n-p) reaction. Below the major ^{14}C reservoirs: ~93% is stored in the oceans, ~5% in the biosphere, ~2% in the atmosphere and less than 0.1% in the ice caps and glaciers. Illustration made with data from Kutschera[48].

Nuclear weapon tests artificially increased the amount of ^{14}C in the atmosphere and the combustion of fossil hydrocarbons devoid of radiocarbon has diluting effect on the ^{14}C concentration in the atmosphere. These two anthropogenic influences are discussed separately in the sections Bomb peak and Suess effect

below. The majority (>90%) of the freshly formed ^{14}C is quickly oxidised to ^{14}CO as shown in Equation 3, the remaining is oxidised directly to ^{14}CO$_2$[49]. The oxidation of ^{14}CO to ^{14}CO$_2$ is much slower than the oxidation of ^{14}C to the monoxide, the global average atmospheric lifetime of carbon monoxide is about two months, however, the lifetime is shorter in the tropics (~1 months) and much longer in winter and high latitudes[50]. The oxidation reaction is induced by hydroxyl ($\cdot$OH) radicals (Equation 4). The hydroxyl radical is formed in the atmosphere either as a recycling product from previous $\cdot$OH reactions or to a minor extend when ultraviolet light (UV) strikes ozone (O$_3$) in the presence of water vapour. In the initial photolysis reaction with O$_3$ and UV light, an excited atomic oxygen is created, which further reacts with water vapour to the hydroxyl radical. The radical has a short atmospheric lifetime (<1 s) and there is a low abundance (<1 ppmv) present in the atmosphere. Nevertheless, $\cdot$OH is the most important oxidant in the tropo- and stratosphere and oxidises not only CO but also methane, volatile organic compounds (VOCs), and NO$_x$ (NO + NO$_2$) and is frequently described as the *detergent of the atmosphere*[51,52].

The formed ^{14}CO$_2$ remains in the atmosphere for 6–8 years and then enters the global carbon cycle[53]. The majority is taken up by the world's oceans, as oceans are not only the largest carbon reservoir but also the biggest carbon sink (see Figure 3). On land, plants incorporate ^{14}CO$_2$ by photosynthesis. From there, various organisms depend on plants as a source of food, which distributes radiocarbon to all living organisms. Radiocarbon is incorporated in all organisms continuously during their lifetime, the exchange only stops when an organism dies. The following decrease in the level of ^{14}C is due to radioactive decay (see Chapter 1.2.3). This can be used for radiocarbon dating applications (see Chapter 1.3.1).

Suess effect

Anaerobic decomposition processes of organisms dying millions of years ago formed fossil fuels. Radiocarbon present in the decomposing material has since been completely decayed. The combustion of this material known as fossil fuels since the beginning of the industrial age brought large quantities of CO$_2$ devoid of ^{14}C into the atmosphere. This dilution effect on the atmospheric radiocarbon level is the direct evidence of the effect fossil-fuel combustion has on the atmosphere. It is also evidence that the CO$_2$ level increase in the atmosphere is caused by anthropogenic activities[20]. The dilution effect was first observed by the Austrian chemist Hans Suess in the 1950s while studying wood samples, hence the name Suess effect[54]. The exchange process in the atmosphere to the oceans and terrestrial biosphere is complex. Furthermore, there is a significant natural fluctuation in the cosmogenic production of ^{14}C. Carbon reservoir models by Stuiver and Quay[55] considering the natural variation of ^{14}C production and addition of ^{14}C-free CO$_2$ from fossil-fuel combustion found good agreement with tree ring radiocarbon dating. They concluded that in 1950 at least 85% of the radiocarbon decline is attributed to human activity and natural variability accounts for the remaining 15%. This dilution effect is not limited to ^{14}C, ^{13}C is also affected (see Figure 4) as fossil fuels are not only devoid of ^{14}C but also depleted in ^{13}C and the dilution processes are similar (see Chapter 1.1.2).
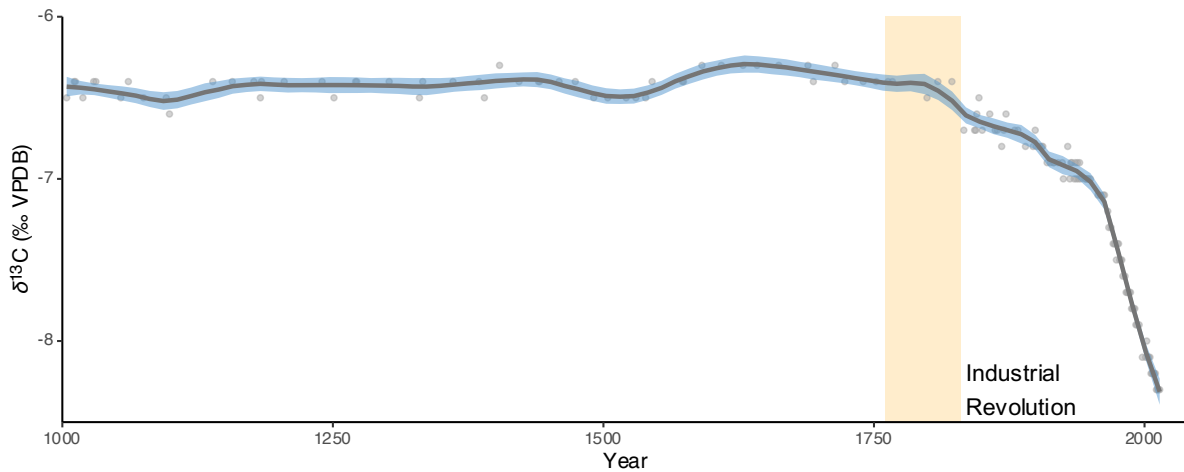
Figure 4: Atmospheric [13]C (per mil) for the last 1000 years with the historical time period of the Industrial Revolution (1760–1830) highlighted. The burning of fossil-fuels added significant amounts of ^{13}C-depleted carbon into the atmosphere and is direct evidence for anthropogenic activities. Plot adapted from Dombrosky[56].

Bomb peak

Nuclear weapon tests in the 20th century were a considerable source of additional radiocarbon as well as countless other artificial radionuclides in the atmosphere (see Figure 5). Code name *Trinity* was used for the first detonation of a nuclear device as part of the Manhattan Project. On July 16th, 1945, the first nuclear device informally nicknamed *The Gadget* exploded in New Mexico, USA with a yield of 21 kt. This was followed shortly by the deployment of nuclear weapons for warfare by dropping *Little Boy* and *Fat Man* on Hiroshima and Nagasaki on August 5th and August 9th, 1945[57,58]. In the following years, over 2000 nuclear devices were tested globally. The USA conducted over 1000 and the Soviet Union (USSR) over 700 nuclear explosions. At least five more nations conducted nuclear bomb tests, including France and the United Kingdom (UK)[59]. Above ground nuclear tests were banned in 1963 with the Partial Test Ban Treaty, which was signed and ratified among others by the UK, the USA, and the USSR. Underground nuclear tests continued until the Comprehensive Nuclear-Test-Ban Treaty in 1996, which banned all nuclear weapon tests altogether[60], however failed to enter into force as eight nations have not ratified the treaty. In the last two decades, North Korea was the only country to conduct a limited series of underground nuclear tests[61]. The explosion of a nuclear device releases large quantities of thermal neutrons, which react with atmospheric nitrogen to produce radiocarbon in a (n-p) reaction. Nuclear tests almost doubled the amount of radiocarbon in the atmosphere. After no further atmospheric tests were carried out, the radiocarbon concentration in the atmosphere steadily decreased. Owing to exchange with other carbon reservoirs in the Earth's carbon cycle, the ^{14}C levels are approaching pre-test levels again. Most nuclear weapon tests were conducted in the northern hemisphere, however, ^{14}C values rose globally. The time to mix the air masses around the globe caused a slight delay on the radiocarbon levels in the southern hemisphere. The interhemispheric exchange time for radiocarbon has been estimated at 1.4 years[62], which is consistent with

10

other gases such as sulphur hexafluoride[63]. The amount of radiocarbon measured in the southern hemisphere was initially lower due to reservoir uptake of the oceans while mixing the air masses. As no further tests were conducted, this effect diminished over time. Today, the amount of ^{14}C is roughly equal between the northern and southern hemisphere[20,64].
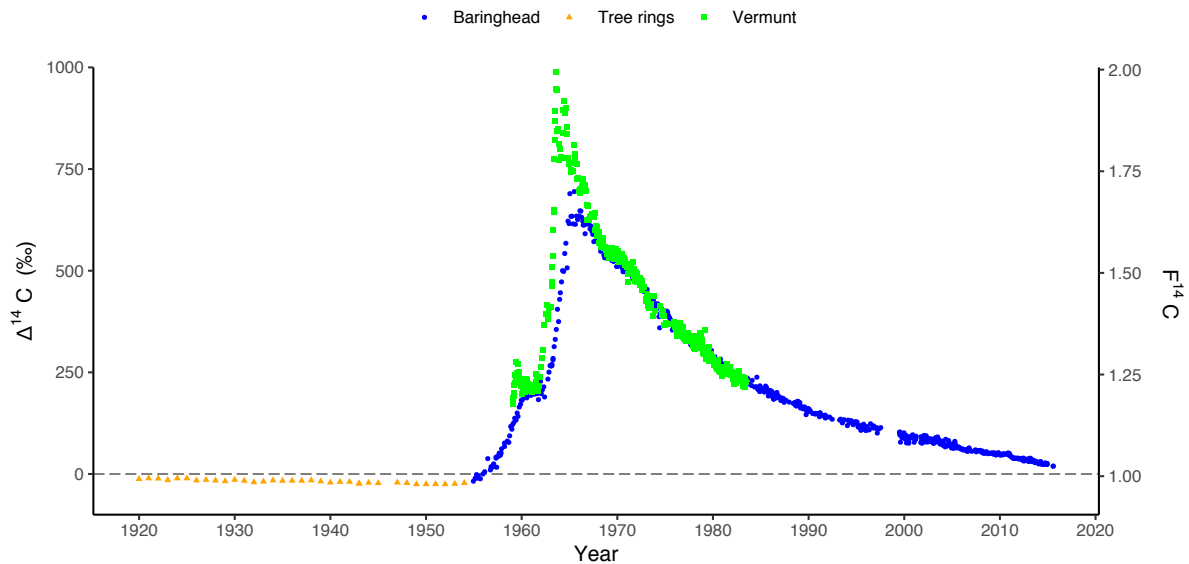
Figure 5: Atmospheric $\Delta^{14}CO_2$ measurements for the northern (Vermunt, Austria) and southern (Baringhead, New Zealand) hemisphere show the bomb peak[62,65]. Data from 1920 to 1954 has been derived from tree rings[55]. The Suess effect is apparent in the tree ring data. The dashed grey line (natural reference level) indicates the pre-industrial radiocarbon level without the influence of fossil-fuel combustion or nuclear bomb tests. The secondary axis is labelled F[14]C, which is a frequently used unit for radiocarbon measurements. Due to visually negligible differences, no differentiation for each data point regarding unit was made.

1.2.3 Decay of radiocarbon

For a single radioactive atom, no predictions can be made when this single atom will decay. However, when large number of nuclei are observed for some time, predictions can be made about the fraction of nuclei decayed as the decay is constant for a given radionuclide. Therefore, the process can be expressed as a first order reaction. The constant decay rate is frequently expressed with the term half-life ($t_{1/2}$). One half-life is the time it takes for radionuclides to lose half of their activity or the time it takes for half of the initial radionuclides to decay to their daughter products. As shown in Equation 5, radiocarbon decays by electron emission (β^- decay) to stable nitrogen:

$$^{14}_{6}C \rightarrow {}^{14}_{7}N + e^- + \bar{v}_e \qquad\qquad \text{Equation 5}$$

The half-life of different radionuclides ranges widely from $<10^{-6}$ s to $>10^{10}$ years. After the generation of radiocarbon by deuteron bombardment of graphite, it was clear that the newly discovered isotope was not very short lived, especially compared to the other radioactive carbon isotopes[19,20]. Ruben and Kamen[66] correctly constrained the half-life of the newly discovered isotope to be in the range of $10^3–10^5$ years. Only five years later, Reid et al.[67] measured 4700 ± 470 years and Norris and Ingram[68] measured 5300 ± 800 years. Various half-life measurements were then published in rapid succession in the following years. Engelkemeir et al.[69] reported 5720 ± 47 years and later corrected to 5580 ± 45 years[70], Jones[71] 5589 ± 75 years, and Miller et al.[72] 5513 ± 165 years. In 1952, Libby proposed to take the weighted means of three measurements with a half-life value of 5568 ± 30 years, which became later known as the "Libby half-life" for radiocarbon[73,74]. A decade later, Godwin[75] proposed a new value of 5730 ± 40 years based on the weighted mean of three new measurements. This radiocarbon half-life is still very commonly cited and known as the Cambridge half-life. A new calculation of weighted mean measurements concluded a half-life of 5700 ± 30 years[76], which is also in accordance with the value reported by the National Nuclear Data Centre of Brookhaven National Laboratory (https://www.nndc.bnl.gov).

1.2.4   Radiocarbon notation

Before the introduction of accelerator mass spectrometry (AMS), radiocarbon measurements were performed by measuring the radioactive decay of ^{14}C (see Chapter 1.4). On the other hand, AMS determines the abundance of ^{14}C directly in terms of isotope ratios. Various terms and symbols have been used in radiocarbon measurements, sometimes with more than one definition. Since its introduction by Reimer et al.[77], the isotopic ratio of ^{14}C is frequently given in Fraction Modern ($F^{14}C$), which indicates the fraction of radiocarbon found in a sample compared to the contemporary radiocarbon level. $F^{14}C$ was intended to reduce misunderstandings. As shown in Equation 6, $F^{14}C$ is defined as:

$$F^{14}C \ = \ \frac{\left(\frac{^{14}C}{^{12}C}\right)_{sample}}{\left(\frac{^{14}C}{^{12}C}\right)_{modern}} \qquad \qquad \text{Equation 6}$$

Fraction Modern is frequently also expressed as a percentage in percent modern carbon (pMC) and is simply calculated as:

$$pMC \ = \ F^{14}C \ \cdot 100 \qquad \qquad \text{Equation 7}$$

Fraction Modern and consequently also pMC include multiple conventions. The term *modern* or *present* in radiocarbon notation is defined with 1950 as the reference year. This notation is relevant for dating samples, where the age of a sample is referred to as before present (BP): before present for radiocarbon notations means before the year 1950, thus *present* is not now or today but a specific year from the past. Furthermore, the modern $^{14}C/^{12}C$ ratio is defined from NIST (National Institute of Standards and Technology) reference material. Moreover, F^{14}C is generally normalised to $-25‰$ with respect to VPDB to correct for isotopic fractionation[47,77].

$$\Delta^{14}C = \left(F^{14}C \, e^{\left(\frac{1950-t_0}{8267}\right)} - 1 \right) \cdot 1000‰ \qquad\qquad \text{Equation 8}$$

Publications for geochemical applications frequently report radiocarbon measurements in Δ^{14}C instead of Fraction Modern. As shown in Equation 8, Δ^{14}C is calculated from Fraction Modern with 1950 representing the reference year, t_0 the year of origin of the sample and 8267 the mean lifetime of ^{14}C based on the half-life proposed by Godwin known as the Cambridge half-life ($t_{1/2}$ = 5730)[47].

1.3 Radiocarbon applications

First example on how radiocarbon can be made useful was shown by Arnold and Libby[78]. They compared samples of a known age with their radiocarbon measurement and found satisfactory agreement. With this radiocarbon dating was born. In 1960, Libby was awarded the Nobel prize *for his method to use carbon-14 for age determination in archaeology, geology, geophysics, and other branches of science*. Others employed radiocarbon as an isotope tracer instead. Melvin Calvin and others investigated the route carbon takes during photosynthesis that forms glucose from CO_2[79]. For his work, Calvin was awarded the Nobel prize (1961) and the chemical pathway is widely known as the Calvin cycle[2]. The work of Arnold and Libby as well as Calvin was only the beginning. Atmospheric aerosol source apportionment with radiocarbon was used for the work presented in the following chapters and is discussed in detail in Chapter 1.5.4. In the sections below, various ^{14}C applications are discussed to emphasise the broad field of use, but with no ranking or claim of completeness.

1.3.1 Dating

Radiocarbon dating was the first application for ^{14}C measurements already proposed by Libby. Radiocarbon is suited for dating approximately the last 50 000 years, covering the latest period of human development for archaeologists and anthropologists[76]. Applications for dating are extremely diverse as virtually all organic compounds can be dated after physical and chemical pre-treatments. This is highlighted here with two examples: dating of a mummy and determining the life expectancy of a certain species of sharks.

In 1991, a very well-preserved iceman later named Ötzi was found in the Ötztal Alps at the Austrian-Italian border. Radiocarbon dating of the bone and tissue itself as well as various wood, charcoal, and leather parts the mummy was carrying was used to determine the age. The iceman died somewhere between 5300 and 5100 years ago, placing it in the Neolithic period[53]. Completely different to date mummies is the age determination of long-lived species. The eye lens nucleus in vertebrates is formed during prenatal development and some proteins remain metabolically inert throughout the life. The Greenland shark (*Somniosus microcephalus*) is a very slow growing and poorly understood vertebrate in the Arctic Ocean. Radiocarbon dating of the shark's eye lenses revealed a life span of at least 272 years with the largest specimen 392 ± 120 years old, making the Greenland shark the longest-lived vertebrate known[80].

1.3.2 Atmospheric gas source apportionment

Although a vital trace gas for the carbon cycle, land-use change and the combustion of large quantities of fossil fuels increased the CO_2 concentration in the atmosphere from the pre-industrial levels of 280 ppm to over 400 ppm[20,81] (see Figure 6a). Stable carbon isotope analysis and radiocarbon measurements of atmospheric CO_2 were key tools to find and evaluate anthropological influences on the atmosphere, including fossil-fuel combustion and nuclear weapon tests (see the subchapters Suess effect as well as bomb peak in Chapter 1.2.2). Furthermore, regional fossil-fuel surplus of CO_2 combustion can be calculated with comparisons to ^{14}C background sites[82]. Other carbonaceous atmospheric gases such as methane (CH_4) are

also of interest for radiocarbon analysis either directly or by analysing air trapped in ice[83–85]. Atmospheric methane concentration has been increasing since the beginning of the industrialisation; however, it has risen by nearly 10% over the last two decades (see Figure 6b).
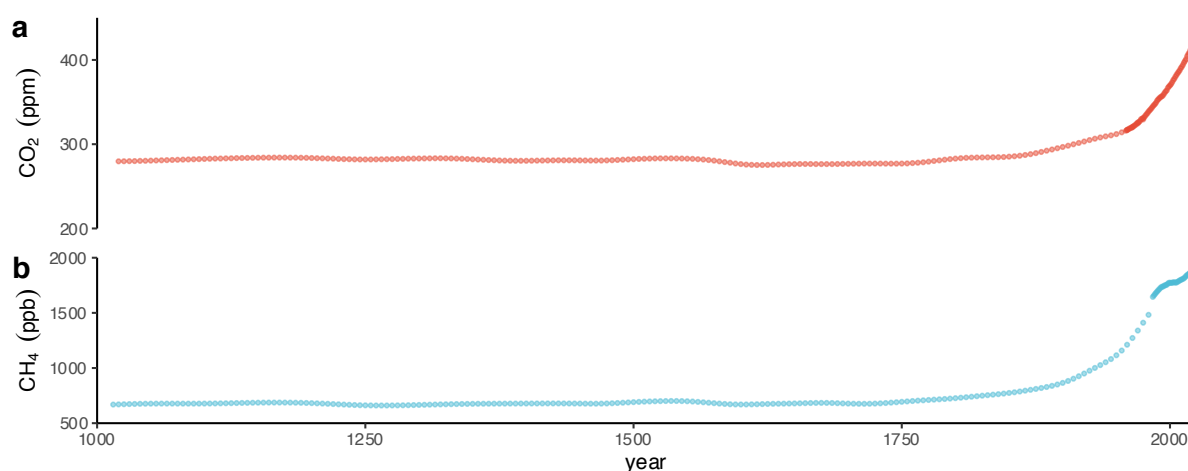
Figure 6: a) Concentration of CO_2 in the atmosphere since ~1000 CE obtained from Law Dome (Antarctica) ice cores by Etheridge et al.[86] and atmospheric CO_2 concentrations (since 1959) from the National Oceanic and Atmospheric Administration (NOAA)[87] derived from air measurements at Mauna Loa Observatory, Hawaii, USA. b) Methane concentrations in the atmosphere since ~1000 CE obtained from Law Dome (Antarctica) ice cores by Ethenridge et al.[88] and atmospheric CH_4 concentrations (since 1984) from NOAA[89].

After CO_2, methane is the second most relevant greenhouse gas, and despite its much lower concentration in the atmosphere it is very potent. The atmospheric lifetime of methane is around 12 years and much shorter than that of carbon dioxide (>100 years), but methane is 34 times as potent as a greenhouse gas on a century timescale and 86 times as potent on a 20-year timescale compared to CO_2[90,91]. Although the global budget is well constrained, the contribution of individual sources is difficult to assess and top-down and bottom-up inventory calculations deviate from each other[92,93]. Anthropogenic emissions of methane can be completely devoid of radiocarbon in the case of fossil-fuel derived emissions from production, distribution, and incomplete combustion of hydrocarbon fuels (coal, oil, natural gas; conventional and unconventional). Anthropogenic methane emissions from biogenic sources are primarily agriculture (e.g., livestock, rice cultivation), organic waste, and biomass burning. Additionally, depending on their reactor design, nuclear power plants emit intermittent little but highly ^{14}C-enriched amounts of CO_2 or CH_4, which further complicates source apportionment[94]. Natural fluxes include wetlands as a major contributor and other natural sources (e.g., volcanic gases, wildfires). Future methane emission projections are dependent on future emissions pathways and on the evolution of natural fluxes. Anthropogenic emissions rely on the mitigation technologies deployed for both fossil and biogenic methane[95]. In addition, natural fluxes might increase in a warming climate with positive feedback, e.g., the permafrost in the Arctic[96].

1.3.3 Biomedical applications

Approval for a pharmaceutical compound requires a detailed quantitative description of their metabolism and excretion in the body. The elimination pathway of a new drug is investigated in absorption, distribution, metabolism, and excretion (ADME) studies. To understand pharmacokinetics and excretion, tracer studies in rodents are performed prior to human trials for the detection of unknown metabolites, on which traditional LC-MS methods might fail. Radiolabelled ADME studies using ^{14}C provide the most comprehensive data set to understand how the human body interacts with a drug and are often essential in drug registration applications[97]. The potential of ^{14}C for biomedical use was rapidly recognised after its discovery. Liquid Scintillation Counting (LSC) and Accelerator Mass Spectrometry (AMS) are well established methods for radiocarbon measurements and are both used for ^{14}C tracer studies. LSC is still frequently used due to lower cost, high sample throughput and automatisation. Cost, availability, and space requirements for AMS systems have significantly improved over the last decades, making them suitable not only for carbon dating but also for testing radiolabelled compounds. AMS is used when limits of detection required are lower than those achievable by LSC. The increased sensitivity in AMS by a factor of 100–1000 vastly reduces radiative and chemical exposures by microtracing and microdosing, respectively, a crucial requirement for in-human studies[98].

1.3.4 Forensic applications

Nuclear weapon tests in the 20th century added numerous artificial radionuclides to the environment, including large quantities of radiocarbon. These artificial radionuclides as well as the radiocarbon bomb peak (see Chapter 1.2.2) can be used for dating and help to convict even very well-made fraud. A diverse range of very specific forensic questions can be answered by radiocarbon analysis, as any object made of organic material can be examined. Radiocarbon analysis is a destructive technique, therefore often not the method of first choice for very precious samples. Owing to recent advances in AMS measurement techniques, very little material is required and can be extracted with insignificant changes to the artefact. For instance, the authentication of wines can be made non-destructively with ^{137}Cs dating or destructively by ^{14}C dating[99,100]. Although destructive in nature, Fahrni et al.[101] presented a ^{14}C dating method for wine by alcohol diffusion through the cork, leaving the wine bottle otherwise untouched. Similarly, rising prices for rare Whisky attracts fraudsters and collectors alike. Like wine, bomb-pulse dating has been applied to Whisky as well[102]. Beyond alcoholic beverages, food additives such as sweeteners and flavourings can be made from plant extracts or artificially from petroleum derived precursors. Radiocarbon analysis can identify the origin of the ingredients and attest for fraudulent labelling on food packaging[103,104].

Artworks are another potential field of application for forensic radiocarbon dating. Sought after paintings achieve extraordinarily high prices at auctions. This makes paintings a target for forgers. Among a range of other tools, artwork authentication by radiocarbon measurement can be a key method by analysing canvas and organic binder. Radiocarbon measurement allows for a temporal classification of an artwork and detect forgeries[105,106].

Although again completely different from paintings, radiocarbon forensic applications using the bomb-curve can be used to date elephant tusks[107]. Illegally ivory trade by poaching is a significant threat to elephant populations. Measurements from Cerling et al.[108] show that ivory seizures contain predominately modern tusks with most ivory poached less than three years before confiscation.

1.3.5 Safety assessment of deep geological repositories

Radioactive waste generated by nuclear power plants, medicine, and research must be stored in isolation to protect life and avoid contamination of air and water. Deep geological repositories (DGR) within a stable geologic environment have been suggested as a viable method for long term storage[109]. In Switzerland, the Swiss National Cooperative for the Disposal of Radioactive Waste (Nagra) is the technical competence centre for deep geological disposal of radioactive waste and envisages the storage of radioactive waste in Opalinus Clay formation at depth[110]. Radiocarbon has been considered a key radionuclide for the safety analysis of DGRs because irradiated metallic wastes are a source of ^{14}C after disposal in a DGR[111]. Here it should be noted that compared to other applications, the safety analysis of DGRs is an almost irrelevant small part of radiocarbon analysis, but it emphasises the broad field of applications for ^{14}C analysis. For example, Guillemot et al.[112] report a study where two irradiated steel specimens were placed in a reactor with artificial cement pore water to simulate radioactive waste disposal conditions, and liquid and gas phase samples containing ^{14}C were collected over a period of more than four years. Among other techniques, the chemical wet oxidation method used in the following chapters of this work for the analysis of aerosols was adapted for total organic carbon (TOC) analysis. To have enough carbon for analysis, the samples were spiked with 50 μg ^{14}C-free acetate carrier material[112,113].

1.4 Radiocarbon measurement techniques

1.4.1 Beta counting

Libby counter

Geiger and Müller[114] reported in 1929 a device for detecting and measuring ionising radiation: the Geiger–Müller counter. Greatly simplified, a Geiger–Müller counter is a type of gaseous ionisation detector based on the Townsend discharge: an ionisation event in a gas liberates an electron, and subsequent collisions liberates further electrons, which can be measured[115]. Libby[116] modified the Geiger–Müller design by using a wire grid instead of solid metal as the cathode and published his findings in 1934. The Libby counter[117] contained a screen wall between the sample and the counter instead of a solid window, and the sample was placed directly inside the measurement apparatus and filled with counting gas[118]. The modified counter was used to study the soft beta-emitters ^{35}S, ^{198}Au, and ^{87}Rb. Measurement of ^{14}C with the Libby counter came more than a decade later and required further improvements to the design to reduce background and increase sensitivity. In 1949, Arnold and Libby[78] published results from dating wood of known age. They used one ounce (28.35 g) of wood sample combusted to CO_2 and reduced to graphite. Eight grams of graphite were used for the actual measurement.

Gas proportional counter

Gas counters consists of a central sample counter with the sample gas (e.g., CO_2, CH_4) filled at a pressure between 1×10^5 to 5×10^5 Pa. The gas eliminates the use of a window or screen wall inside the sample counter. The sample counter is surrounded by an inner lead shield and a guard counting system to eliminate the muons from cosmic rays. The setup is shielded from thermal neutrons by borated paraffin and more lead on the outside[119,120]. Gas counters were first reported by de Vries and Barendsen[121] and are still in use for some radiocarbon measurements[122].

Liquid scintillation counting

Liquid scintillation counting (LSC) is a detection method for alpha and beta emitters. The technique was first proposed by Arnold[123]. Although still a decay counting technique, sample throughput is faster than in Libby and gas counters. Samples for LSC can be prepared with or without separation and mixed with liquid scintillation solution and the method allows for automation. As a beta emitter, radiocarbon is well suited for analysis in an LSC. When a beta particle from a decaying ^{14}C hits the liquid scintillator, a flash of light is emitted and detected with a photomultiplier[124].

1.4.2 Accelerator mass spectrometry

Unlike the disintegration counting techniques, accelerator mass spectrometry (AMS) separates and counts atoms directly. Decoupling the detection from the decay of radioactive nuclides allows for measurements of isotopic ratios in samples with very low concentrations. This can be expressed as an efficiency, with efficiency defined as "the number of atoms detected compared to the number of atoms contained in the sample" according to Hellborg and Skog[125]. AMS systems are far more efficient than the decay counting techniques and their sensitivity does not depend on the half-life of the isotopes measured (see Figure 7). Measurements otherwise taking years in decay counters are performed in minutes with little sample material needed[126].
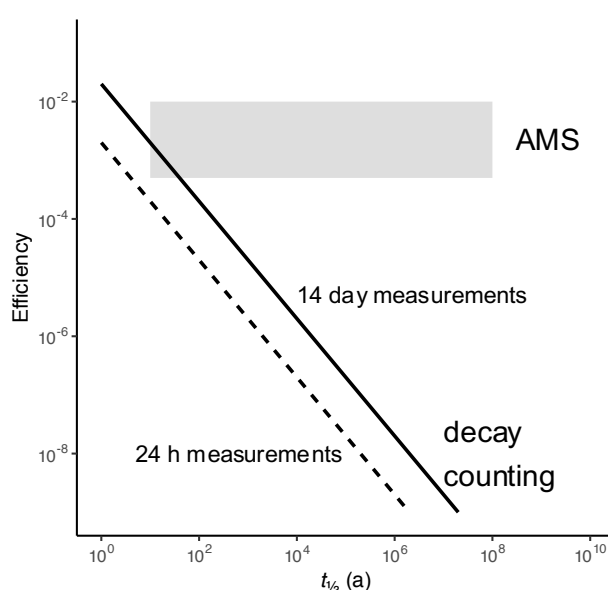
Figure 7: Efficiency of decay counting and AMS shown as a function of half-life ($t_{1/2}$). AMS is a mass spectrometry method, therefore, the efficiency is independent of the isotopes half-life. Decay counting is inefficient, especially for long-lived nuclides as only a small fraction of the nuclides decay in a reasonable (i.e., hours to days) measurement time. The visualisation was adapted from Hellborg and Skog[125].

AMS had its origin in nuclear physics research. A cyclotron was used by Alvarez and Cornog[127] for the separation and detection of ^{3}H. Almost four decades later, the combination of mass spectrometry and accelerator was used again by Mueller[128], who conducted radiocarbon measurements with a cyclotron mass spectrometer. Mueller's measurement was conducted with positive ^{14}C ions and suffered from the flood of the isobar ^{14}N present. The issue was addressed with the deployment of a range-separation technique to supress ^{14}N, however, the background of the measurements was still high, which Mueller attributed to highly radioactive carbon in the cyclotron[129]. Around the same time in the 1970s, a team of nuclear physicists at the University of Rochester (NY, USA) measured carbon with a tandem Van de Graaff electrostatic accelerator[130,131]. They were able to show that negative nitrogen ions are instable and nitrogen

contaminations in radiocarbon measurements are "effectively eliminated by the use of negative ions". The team successfully measured contemporary charcoal and fossil graphite samples. Almost simultaneously and not aware of the endeavours in Rochester, Nelson et al.[132] used a tandem accelerator at McMaster University in Canada on a sample of wood.

The potential to extend the AMS technique to other environmental radioisotopes was realised early, e.g., for groundwater dating with ^{36}Cl. The two stable chlorine isotopes (^{35}Cl, ^{37}Cl) are accompanied by trace amounts of ^{36}Cl, a long lived ($t_{1/2}= 3.01 \times 10^5$ a) cosmogenic radionuclide produced by spallation[19,133] of ^{40}Ar. The ^{36}Cl mixes with ordinary chloride mostly from the ocean and deposited on land by rain, snow, or aerosols. The radioactive clock is set when the ^{36}Cl containing water moves downward from surface water to ground water. The use of ^{36}Cl for groundwater dating was proposed by Bentley[134] and measurements followed soon thereafter[135,136]. Since then, AMS was adapted to a wide range of nuclides. Beside ^{14}C and ^{36}Cl, dating of groundwater now also includes the isotopes ^{81}Kr and ^{129}I. Ocean currents have been investigated with a wide range of radionuclides (^{14}C, ^{39}Ar, ^{99}Tc, ^{129}I, ^{231}Pa, ^{236}U). In the lithosphere, geologists use exposure dating of rocks with the isotopes ^{14}C, ^{10}Be, ^{26}Al, ^{36}Cl, and ^{53}Mn to track deglaciation and erosion. Measurements in the atmosphere beside source apportionment (^{14}C) investigate the production of radionuclides by cosmic rays (^{14}C, ^{10}Be, ^{26}Al, ^{32}Si, ^{36}Cl, ^{39}Ar, ^{81}Kr, ^{129}I) and the chemistry and dynamics of carbonaceous atmospheric gases (CO, CO_2, CH_4). Only a handful of domains and radionuclides investigated by AMS measurements have been mentioned here to highlight the versatility of the technique and broad range of applications. A comprehensive list of radionuclides measured with AMS is shown by Kutschera[76] and an overview of research areas where AMS measurements are used is summarised in a later publication of Kutschera[137]. Despite the large number of nuclides (>50) measurable by AMS, most measurements (>90%) are conducted with radiocarbon[137]. Furthermore, many AMS devices are dedicated to measure only radiocarbon and no other isotope. In this work, only radiocarbon was measured, thus any reference to AMS implies a radiocarbon measurement.

Nuclear physics tandem accelerators were initially used for AMS, however with the demand for radiocarbon measurements, dedicated AMS devices based on tandem accelerators were built[138]. Tandem accelerators are very large devices. Beside the capital cost of acquiring an AMS, a large laboratory room is required for such a device. Significant size reduction has been achieved. The standard size tandem accelerator VERA in Vienna with a terminal voltage of 3 MV uses a floor space of almost 200 m² (16 × 12 m). Developments such as compact AMS systems (500 kV) and mini AMS systems (200 kV) require only 30 m² (6 × 5 m) and less than 10 m², respectively[137]. In this work, an AMS system with very small dimensions (3.2 × 2.6 m) called MICADAS (MIni CArbon DAting System) was used. MICADAS was developed at ETH Zürich and is now available as a commercial product for ^{14}C analysis (Ionplus AG, Switzerland)[139,140]. Even smaller AMS systems are under development[141,142]. A MICADAS AMS consists of an ion source, a low energy (LE) magnet as the first mass filter, an accelerator unit with a stripper, a high energy (HE) magnet as the second mass filter, and a detector (see Figure 8). The AMS is constantly kept under high vacuum (range: $\sim 1 \times 10^{-7}$ hPa) with staged scroll- and turbopumps. In the ion source, a caesium vapour is thermally

generated. A spherical ioniser then produces the sputtering Cs^+ beam directed to the sample target. Two lenses are used to focus the beam onto the target and negative ions are extracted with energies of up to 40 keV. MICADAS consist of a hybrid ion source, which accepts both graphite (solid) and CO_2 (gas) samples. Therefore, the sample cathode consists either of pressed graphite or gaseous CO_2 directly fed into the ion source. At the low energy side, a first mass analysis is performed. The magnet on the low energy side deflects the beam by 90° to the accelerator. A fast beam pulsing system injects the different isotopes into the acceleration chamber in very fast succession. Furthermore, an offset Faraday cup measures the ^{12}C current on the low energy side. This enables transmission monitoring through the accelerator. To remove molecular interference (isobars: ^{13}CH, $^{12}CH_2$), a stripper gas is introduced into the accelerator unit. Originally equipped with N_2 as a stripper gas, new and upgraded MICADAS AMS systems are equipped with a He stripper for improved performance[140,143]. The charge of the extracted negative ions is exchanged in the stripper. Repulsion accelerates the positive ions further.
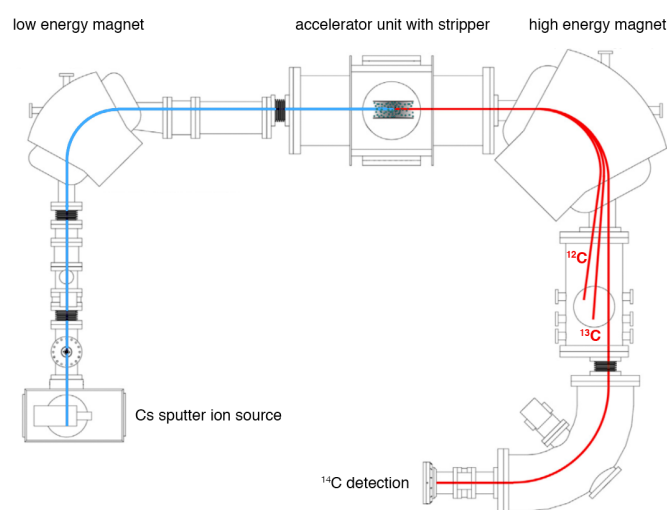
Figure 8: Layout of a MICADAS AMS with the ion source, the low energy magnet on the left, the accelerator and stripper unit in the middle, and the high energy beam line on the right. The blue line represents the negative charged ion beam, the red line the positive charged ions after the stripper. The lighter isotopes (^{12}C, ^{13}C) are detected prior in Faraday cups. At the end, ^{14}C is detected in an ionisation chamber detector. The layout of the MICADAS was adapted from Synal[144].

Positive ions leaving the accelerator are bend by 90° and analysed by the magnet on the high energy (HE) side. Faraday cups analyse the stable isotopes (^{12}C, ^{13}C) after separation by the HE magnet. An electrostatic deflector bends the remaining ^{14}C beam by another 90° before it reaches the gas ionisation chamber for ^{14}C detection. The detector is separated by a 50 nm thick silicon nitride ($Si_3N_{3.1}$) window and filled with isobutane (C_4H_{10}, 2-methylpropane) at a pressure of ~20 hPa[139].

1.4.3   Future measurement techniques

In an AMS, ions are negatively charged on the ion source side and positively charged after the stripping process. Freeman et al.[145] proposed a charge reversal in a new radiocarbon measurement device. In a positive-ion mass spectrometer (PIMS), electron cyclotron resonance is used as an ion source instead of a caesium sputter. Furthermore, the use of an accelerator is optional. In AMS either solid graphite or in a hybrid ion source both graphite and gaseous CO_2 is used. PIMS systems aim to achieve the same precision and accuracy as graphite AMS devices while only accepting CO_2, making the graphitisation step obsolete even for carbon dating. PIMS is currently under development in the prototype phase[146].

Laser absorption spectrometry techniques got much attention for their relative simplicity and high sample throughput with a lower limit of detection compared to LSC. In biomedical applications, sample throughput is more important than accuracy and the very low limit of detection required for carbon dating and source apportionment in environmental science applications. Cavity ring-down spectroscopy (CRDS) consists of a tunable laser, a gas accepting optical cavity with high reflectivity mirrors, and a photodetector. The laser pulse is reflected back and forth inside the cavity, and a small fraction of the light is transmitted through the mirror. This results in an exponentially decaying intensity called the cavity ring-down time[147]. Highly sensitive CRDS systems for radiocarbon measurement have been developed with detection limits well below modern ^{14}C levels[148]. More robust but less sensitive CRDS systems have been developed, however, with significant measurement uncertainties[149,150]. Nevertheless, several research groups made attempts to use CRDS systems for ADME studies and may fill the gap between AMS and LSC. For example, Sonnenschein et al.[151] used CRDS in a small rat study with ^{14}C-labelled tolbutamide, a potassium channel blocker. Kim et al.[152] used a radiolabelled serotonin receptor agonist in four human volunteers and analysed blood and urine with a CRDS system. CRDS may also be suited for automated ^{14}C monitoring. Lehmuskoski et al.[153] utilised a CRDS system for *in situ* monitoring of gaseous ^{14}C emitted by a nuclear power plant and therefore significantly improved the resolution of the ^{14}C monitoring.

Intracavity optogalvanic spectroscopy (ICOGS) was reported by Murnick et al.[154] for ^{14}C detection. ICOGS was developed from a laser assisted ratio analyser, which was successfully used for stable (^{13}C) isotope analysis[155]. ICOGS was intended to be a highly sensitive laser-based analytical technique for ^{14}C detection, however, other research groups were unable to replicate Murnick's results[156–158].

1.5 Atmospheric aerosols

1.5.1 Definitions

An aerosol is a suspension of small liquid and or solid particles in a gas such as air in the atmosphere. Frequently, the term aerosol is also used to describe just the particle instead of the suspension. Aerosol particles range in size from a few nanometres (nm) to more than 100 micrometres (μm)[159]. To put that into perspective, spherical influenza viruses are roughly 120 nm in diameter and completely invisible to the naked eye whereas the diameter of a human hair is just below 100 μm[160,161]. Figure 9 gives an overview of common small objects compared to the common aerosol size cuts:
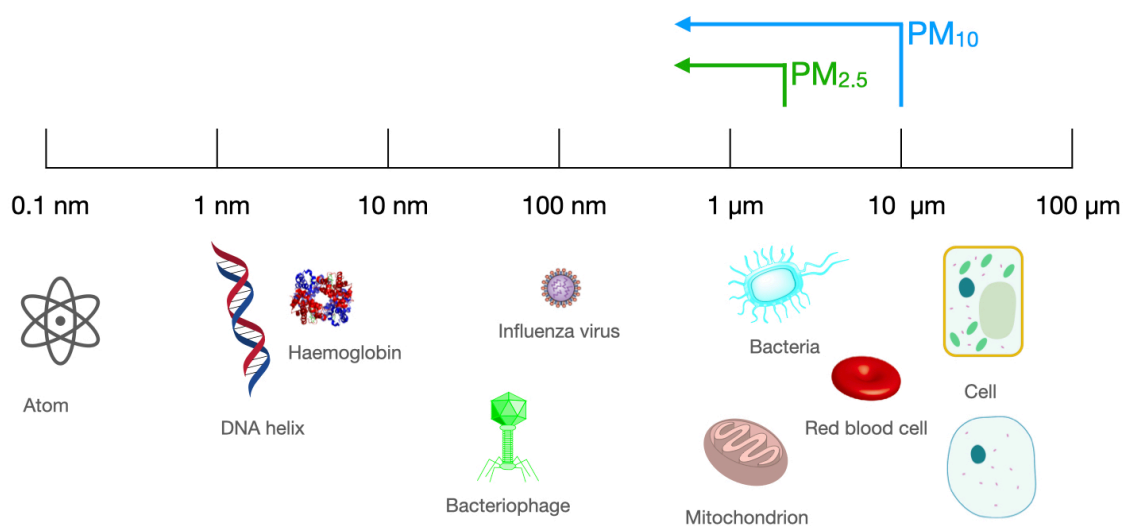
Figure 9: Size of the atmospheric aerosol size fractions (PM$_{10}$ and PM$_{2.5}$) compared to other well-known small objects. Note the logarithmic scale. Visualisation made with ChemDraw Professional 17.1 template objects; size data retrieved from Campbell et al.[2], Harris et al.[160], and Erickson[162].

Atmospheric aerosols are highly variable in concentration and vary in chemical composition with both organic and inorganic compounds. The simplest classification of aerosols is by size of the suspended particulate matter (PM). Total suspended particles (TSP) consist of all suspended particles with a size range <50–100 μm. For health, smaller inhalable particles are more relevant, thus particles with smaller size cuts are frequently collected, including PM$_{10}$, PM$_{2.5}$, PM$_1$ with the number in subscript indicating the size cut in micrometres[163].

1.5.2   Composition and sources

Atmospheric aerosols are a highly heterogenic mixture from different sources with a high spatial and temporal variability. Aerosols consist of soil and desert dust, sea spray, particles of biogenic origin (plant fragments, pollen, microorganisms) and particles from biomass and fossil-fuel combustion processes. Beside carbonaceous compounds, aerosols consist of inorganic species such as sulphate, nitrate, and ammonia[159]. In general, inorganic primary aerosols are rather large (>1 µm) whereas carbonaceous aerosols are generally smaller. For example, soot particles are usually smaller than 100 nm[164]. The composition of an aerosol reflects its sources and formation processes. Coastal sites are influenced by the sea, large cities by local pollution, and rural sites from biogenic emissions, however, the effects of long-range mass transport should not be underestimated. Nevertheless, compared to atmospheric trace gases where the lifetime can range from <1s to centuries, the residence time of aerosols in the atmosphere is typically in the order of hours to weeks[159,165,166].

One is usually interested in characterising a population of aerosols instead of individual particles. Interesting characteristics of aerosols in the broadest sense are origin, size distribution and the chemical composition. Nevertheless, there are several ways on how to classify aerosols. This frequently depends on the question to answer. The following non-finite list shows possible classification types for aerosols[159,164]:

- Mode of formation
- Size
- Sampling environment
- Origin
- Chemical composition

There are two main different formation processes for atmospheric aerosols. Aerosols emitted into the atmosphere as particles are referred to as primary aerosols. Processes forming primary aerosols include combustion processes e.g., forest fires or fossil-fuel combustion. Secondary aerosols, however, are formed from gaseous or semi-volatile precursors emitted into the atmosphere. There, these compounds can deposit on existing particles or form new particles. Precursors can be carbonaceous (e.g., volatile organic compounds (VOC)) or inorganic such as SO_2 and NO_2. These precursors can originate from biogenic sources (e.g., isoprene and other terpenes released from forests) and anthropogenic sources (e.g., incomplete fossil-fuel combustion) and can add to a substantial amount of aerosol[159,164]. Carbonaceous material containing secondary aerosols are referred to secondary organic aerosols (SOA). First hypothesised in 1960 by Went that VOC emissions could form SOA, they are of major interest in atmospheric aerosol research today[167,168]. SOA consist of organic species with a variety of chemical and physical properties including chemical composition, functional groups, hygroscopicity, and volatility. They are formed from

the atmospheric oxidation of VOC emitted by both natural and anthropogenic sources as low volatile oxidation products from VOC nucleate or condense on existing particles. It is estimated that SOA contribute up to 90% of the total organic aerosol mass[169].

The classification of aerosols by size is fundamental as the formation processes for fine and coarse particles vary significantly, they are transformed by different processes and are removed by different mechanisms from the atmosphere. They typically also have different chemical compositions and different optical properties. Additionally, substantial spatial differences in the composition of aerosols have been observed. Therefore, atmospheric aerosols can also be described by the environment in which they were sampled, e.g., *urban*, *rural*, *continental*, *polar* and *marine* aerosols. The spatial difference also applies to the location in the atmosphere and aerosols can be described as *tropospheric* or *stratospheric*. Although local emissions on the sampling site are dominating, long range transport as well as physical and chemical transformation can strongly affect the composition of the aerosols. Therefore, the sampling environment is only an incomplete description of aerosols[159,165].
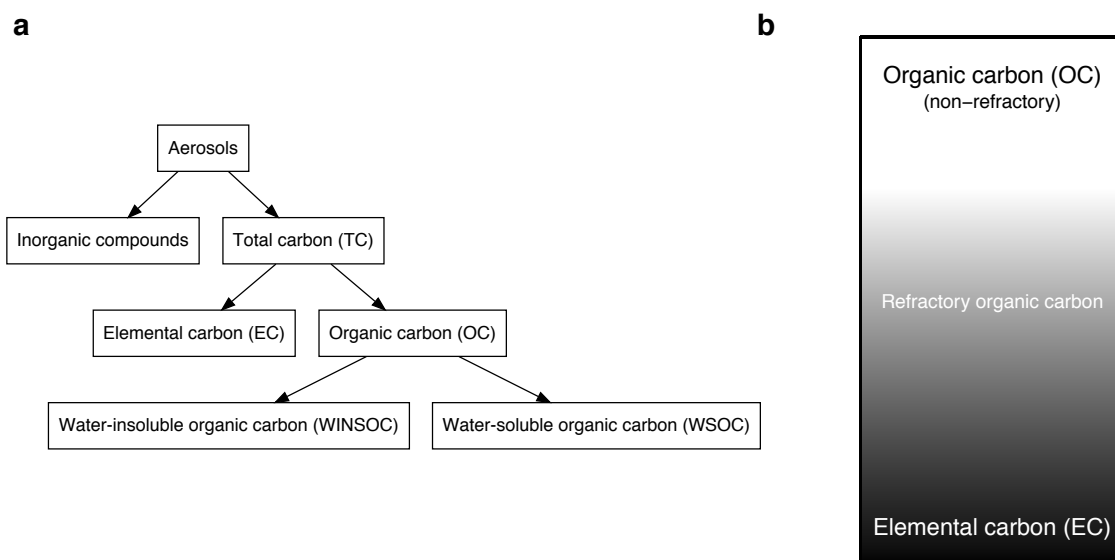
Figure 10: a) Composition of aerosols and the major carbonaceous aerosol fractions. b) Thermochemical classification of EC and OC with an increasing refractiveness from top to bottom. Representation adapted from Pöschl[170].

The origin of an aerosol can also be used for classification. Aerosols can be classified as natural (i.e., from the environment) or of anthropogenic origin. Natural sources include emissions from vegetation, soil, the oceans, fires, and geological activities (volcanoes). Anthropogenic sources consist of emissions from biomass burning (wood, peat, agricultural waste, dung, animal waste, vegetable oils) and the combustion of fossil fuels (natural gas, oil, coal)[159]. The classification of aerosols by origin can also be applied for the distinction of fossil from modern (in terms of radiocarbon dating: contemporary) carbon sources. For this,

radiocarbon source apportionment is the method of choice (see Chapter 1.5.4). The attentive reader might spot that the classification of natural and anthropogenic sources is not equivalent to modern and fossil carbon sources. Natural emissions contain solely modern carbon sources (excluding special cases such as pre-aged dissolved organic carbon in the oceans) whereas anthropogenic emissions include both fossil and modern carbon sources[20].

Finally on this list is the classification of aerosols by their chemical composition. The simplest dual classification of aerosols regarding their chemical composition is by the separation to inorganic and organic aerosols, the latter of particular interest for this work (see Figure 10). Carbonaceous aerosols can be further separated to organic carbon (OC) and black carbon (BC). BC is formed by incomplete combustion processes and describes light-absorbing graphite-like carbon with aggregate morphology. Furthermore, BC describes a wavelength-independent light absorption with a mass absorption coefficient (MAC) of at least 5 m^2g^{-1} at a wavelength of 550 nm, a vaporisation temperature near 4000 K, and insoluble in water as well as organic solvents[159,171,172]. Elemental carbon (EC) is defined as the fraction of the carbonaceous particles that is thermally stable in an inert (i.e., oxygen-free) atmosphere up to 4000 K and can only be oxidised at temperatures above 340°C[172]. Although sometimes used interchangeably, EC and BC are similar but not the same and the details on how the measurement was conducted should be given to avoid confusion. The term EC is used when aerosols are analysed with thermal or thermal-optical devices (e.g., Sunset OC/EC analyser, see Chapter 1.6.1), whereas BC is used for optical methods (e.g., aethalometer). Here, it should be noted that several other terms have been introduced for various measurement techniques including equivalent black carbon (eBC), refractory black carbon (rBC), and light absorbing carbon (LAC), however, they are not relevant for this work and would go beyond the scope of this introduction[173]. Nevertheless, more than OC/EC determination by thermal or thermal-optical methods, the fractions can be analysed for their isotopic signatures. Thus, stable isotope (^{13}C) analysis as well as radiocarbon analysis are valuable tools to analyse individual carbonaceous aerosol fractions (e.g., TC, EC) in atmospheric aerosols[174,175].
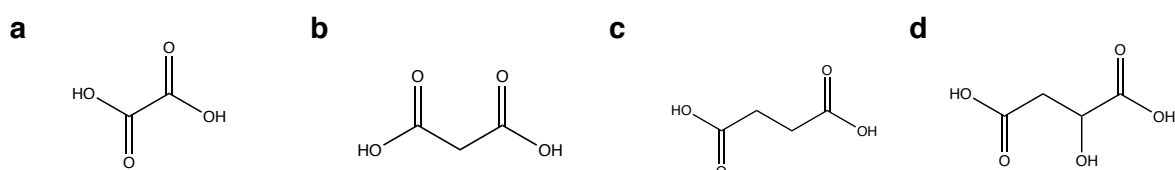
Figure 11: Structures of the most prevalent C_2–C_4 dicarboxylic acids (DCAs) with a) oxalic acid b) malonic acid c) succinic acid and d) malic acid. The structures were drawn with ChemDraw Professional 17.1.

OC consists of non-refractory hydrocarbons and carbon linked with other atoms (O, S, N etc.). The OC fraction can be further separated to water-soluble organic carbon (WSOC) and water-insoluble organic

carbon (WINSOC), referring to the fraction of OC that is soluble and insoluble when subjected to a water extraction step, respectively[173,176].

Additional to these major carbonaceous fractions, smaller compound classes and even individual compounds can be investigated when analysing atmospheric aerosols. Humic-like substances (HULIS) are compounds present in atmospheric aerosols that share many functional groups such as polycarboxylates, carbonyls, phenols, quinones, aliphatics, and aromatics[170,177]. Another frequently investigated class of compounds are organic acids including monocarboxylic acid (e.g., formic, acetic, and glycolic acid), dicarboxylic acids (DCA, e.g., oxalic acid, malonic acid, and succinic acid), and tricarboxylic acids (e.g., citric acid)[178]. Although many of these compound classes and compounds may be of interest, DCAs were analysed in this work and are therefore explained in detail here. DCAs can make up ~1% of the total aerosol and have received much attention due to their potential role in affecting the climate and as cloud condensation nuclei (CCN). A better understanding of their sources and formation processes is therefore of high relevance[179,180]. DCAs are part of the WSOC fraction, of which the majority is formed by SOA and some from primary organic aerosols (POA)[181–183]. Organics in aerosols undergo photochemical reactions in the atmosphere in a process generally referred to as aging. This adds polar groups (e.g., hydroxyl or carboxyl groups) to the OA, therefore increasing the water solubility of the OA fraction[184,185]. Low-molecular-weight dicarboxylic acids (C_2–C_4) such as oxalic acid constitutes a substantial fraction of the WSOC, with oxalic-, succinic-, malonic-, and malic acid among the most prevalent DCA (see Figure 11), and their low vapour pressure favours their adsorption onto airborne particles[186–188]. DCAs have been found in a wide range of environments from urban and rural to remote Arctic and Antarctic sites[186,187,189–193]. Despite decades of atmospheric aerosol analysis and concentration determinations of DCAs, the sources and formation processes of DCAs still remain poorly understood and are an opportunity for ongoing research.
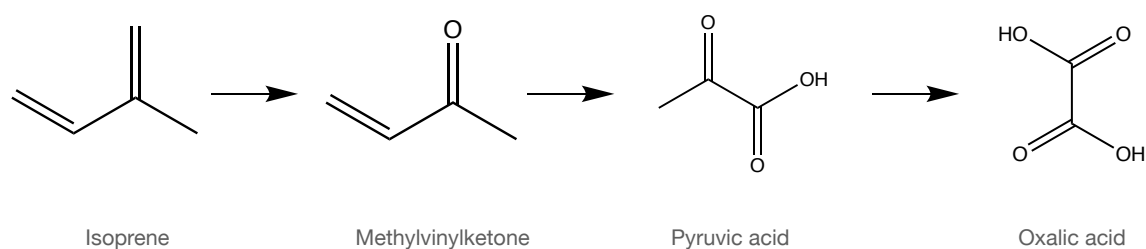
Figure 12: Proposed ozone oxidation pathway of isoprene to oxalic acid by Bikkina et al.[194]. Oxalic acid is formed via the intermediates methylvinyketone and pyruvic acid from isoprene. The structures were drawn with ChemDraw Professional 17.1.

Recent work on SOA formation showed that biogenic volatile organic compounds (BVOCs) are a major source[195–198]. Isoprene is the largest BVOC source with a total terrestrial emission of roughly 600 Tg yr^{-1} mainly emitted from tree canopies[199,200]. Studies have demonstrated that isoprene is oxidised to water-

soluble semi-volatile aldehydes and then further to carboxylic and dicarboxylic acids[201–203]. Bikkina et al.[194] further showed that oxalic, succinic, and glyoxylic acids can be formed through isoprene-ozonolysis in dry conditions (see Figure 12). Potentially fossil-fuel derived C_2 compounds such as acetylene and ethylene have also been proposed as precursors for oxalic acid formation[204]. Furthermore, various low molecular weight dicarboxylic acids have been found in combustion engine emissions[205,206].

To understand the sources better, the isotopic signature of DCAs may provide the answers needed. This requires isotopically pure separation techniques and sufficient sample material for analysis. So far, Aggarwal et al.[207] reported a stable (^{13}C) isotope analysis of DCAs sampled in Sapporo, Japan. Compound-specific stable isotope analysis (CISA) may therefore provide further insight in the sources of DCAs. Although more challenging, stable isotope analysis can be extended to radiocarbon analysis for a compound-specific radiocarbon analysis (CSRA), to apportion the DCAs in atmospheric aerosols to their fossil and non-fossil sources. Oxalic acid as the most prevalent DCA is the most important target compound. So far, there have been only two reports from CSRA of oxalate from atmospheric aerosols with a focus on method development and very few measurements, therefore offering an interesting research opportunity[180,208].

1.5.3 Impact of aerosols

Human health

Outdoor air pollution is responsible for a substantial number of premature deaths globally. In a 2015 study, Lelieveld et al.[209] estimated the worldwide number of premature deaths per year to at least three million, predominately in Southern and Eastern Asia where the outdoor air pollution is high, and a large fraction of the human population lives. In Figure 13, the mean annual $PM_{2.5}$ concentration in each country is shown:
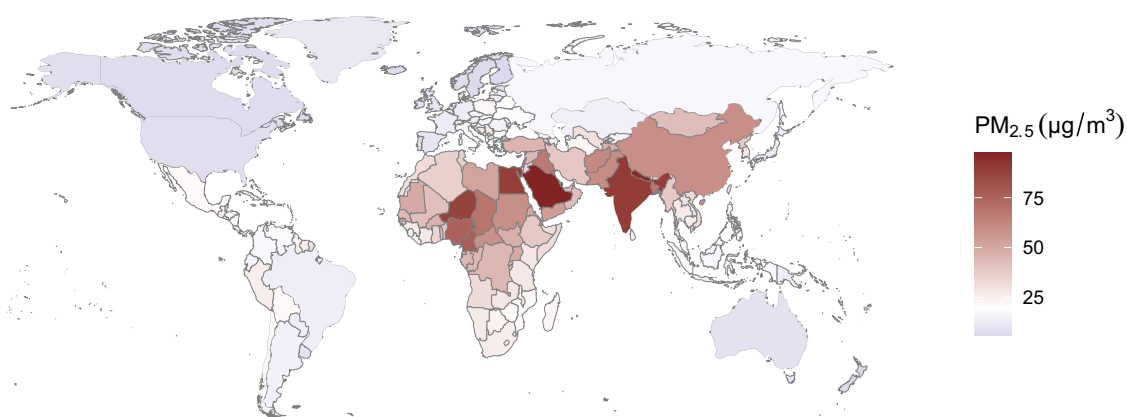
Figure 13: Mean annual $PM_{2.5}$ concentrations (µg/m³) by country for the year 2015 with Southern and Eastern Asia, Middle East, and large parts of Africa most affected by PM air pollution. Data was retrieved from the World Bank[210].

This is an increase to previous estimates a decade earlier with fewer than one million premature deaths[211]. In 2016, the findings of the Global Burden of Disease (GBD) study were published by Forouzanfar et al.[212]. The findings of this very comprehensive global research programme attributed 4.2 million (3.7–4.8 million) premature deaths in 2015 to outdoor air pollution[212]. For 2005, Forouzanfar et al.[212] estimated the number of premature deaths globally at 3.9 million (3.4–4.4 million), thus the number of premature deaths by outdoor air pollution increased by 300'000 for 2015 compared to 2005. Additional to outdoor air pollution, indoor (household) air pollution causes an additional number of premature deaths, globally estimated at 3.3 million (2.5–4.1 million) and 2.9 million (2.2–3.6 million) for 2005 and 2015, respectively. Added up, air pollution (indoor and outdoor) was estimated to be responsible for 6.5 million (5.7–7.3 million) premature deaths for 2015. The GBD study used disease-specific hazard ratio models requiring several assumptions regarding toxicity and exposure, however, more recent work by Burnett et al.[213] used only cohort studies of outdoor air pollution. They estimated solely for outdoor air pollution 8.9 million (7.5–10.3 million) deaths for 2015. These estimations are very difficult to perform, but disregarding of the exact number of premature deaths, there is strong evidence for millions of deaths. A summary of a selection of air pollution studies and the number of premature deaths is shown in Figure 14. To put these numbers into context: for 2015, alcohol and drug abuse caused 2.8 million (2.4–3.1 million) premature deaths. The number of premature deaths from air pollution is in a similar range to tobacco smoke, which caused an estimated 7.2 million (6.5–7.8 million) premature deaths in 2015[212]. Nevertheless, unlike breathing air and consequently the pollution present in the air, smoking is behavioural and therefore a lifestyle choice that is optional.
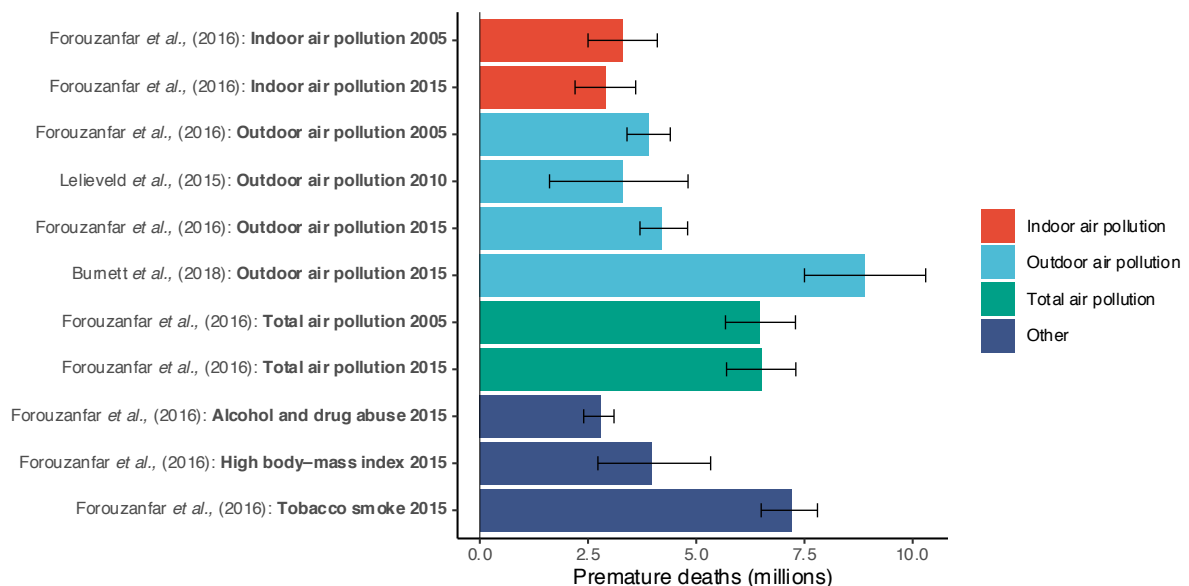
Figure 14: The number of premature deaths worldwide from indoor and outdoor air pollution compared to other causes of premature deaths from Burnett et al.[213], Forouzanfar et al.[212], and Lelieveld et al.[209].

Although the total number of premature deaths from air pollution (indoor and outdoor) did not change substantially from 2005 to 2015, indoor air pollution decreased while outdoor air pollution increased. The decrease in household air pollution has mostly been attributed in a change of fuel source primarily for cooking and to a lesser degree from heating. Solid fuels (coal, wood, charcoal, agricultural residues, and dung) are still a popular choice for cooking and heating in low-income countries, however, natural gas and liquified petroleum gas are increasingly used, thus leading to a reduction in indoor air pollution[212,214,215]. Indoor air pollution is not an issue limited to low-income countries. Humans spend approximately 80% of their time indoors. Additional to particulate matter from combustion sources (cooking and heating), also polycyclic aromatic hydrocarbons (PAH), nitrogen dioxide, VOCs, formaldehyde (e.g., composite wood products, paints, cleaning agents), biological contaminants (e.g., mould, pests, pets), and radon contribute to indoor air pollution[214]. Although some indoor pollution is caused by a certain lifestyle choice (tobacco, pets), others such as radon gas exposure and the fuel for cooking and heating are constrained by various factors, including building code and cost considerations with limited choice for residents. Gas stoves are still a popular choice in many high-income countries, however, cooking appliance electrification could further reduce indoor air pollution[216].
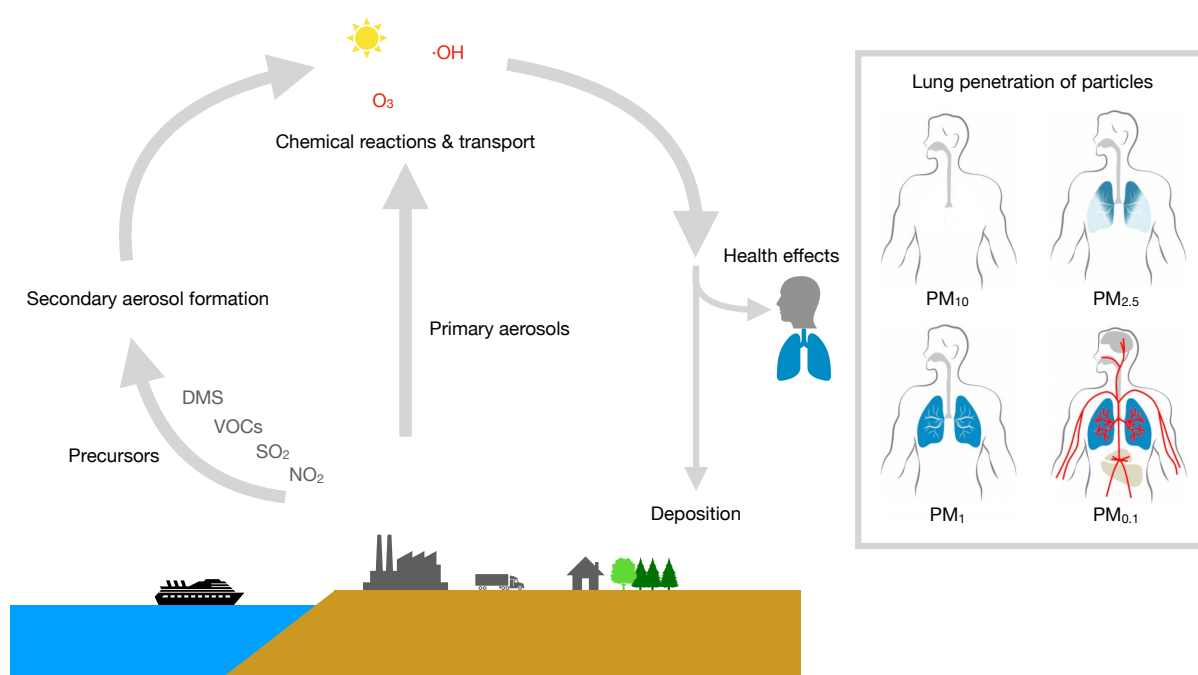
Figure 15: Atmospheric-aerosol-lifecycle with aerosol effects on health. Aerosols are generated and released into the atmosphere by a variety of natural and anthropogenic sources and additionally, gaseous precursors form SOA. Photochemical reactions and wind in the upper atmosphere modify and transport the aerosols from their source. Most of the PM is deposited by precipitation while some is inhaled and may cause adverse health effects. The penetration depth in the respiratory tract depends on the PM size cut with smaller particles penetrating further. Here, the size cut refers to the penetration depth of a given particle size, obviously larger size cuts generally also include smaller particles (see Chapter 1.5.1). Visualisation adapted from Berkemeier[217] and Vincent[218].

Aerosol effects on health are investigated either with epidemiological or with toxicological studies[219]. Epidemiological studies track the relationships between diseases and health factors. As an example, time series try to establish a link over a relatively short time e.g., an increase in death or cardiopulmonary diseases to the PM concentration. Cohort studies on the other hand monitor many people long term and take their habits and environments into account. Finally, statistical tests are required to establish causal and significant relationships in epidemiological studies[219,220]. Toxicological studies investigate the effects of aerosols at the cellular level and help understand the underlying mechanisms of action in the body[220].

The main mechanisms of action of aerosol particles are oxidative stress caused by reactive oxygen species (ROS) and the resulting inflammatory response. Upon respiration, aerosols are deposited in the epithelial lining fluid of the respiratory tract, where they induce and sustain chemical reactions to produce ROS. Well known ROS are the superoxide anion (O^{2-}), hydrogen peroxide (H_2O_2) and the hydroxyl radical ($\cdot OH$)[221,222]. The body is equipped with defence mechanisms, but when these are exhausted, inflammation occurs, which can even lead to cell death. Several studies have shown that ROS are increasingly produced when metals are present in PM, in particular iron and copper[222,223]. Further SOA[224] and carbonaceous soot[225] have been proposed to induce ROS production. Thus, the ROS potential of PM is dependent on the chemical composition and the PM oxidative potential has therefore been suggested as an additional indicator in addition to PM mass concentrations[226,227]. Several *in vivo* and *in vitro* acellular assays have been developed to estimate the oxidative potential of PM[228,229].

Particles with diameters smaller than 10 μm have the most impact on human health as smaller particles penetrate deeper into the respiratory tract (see Figure 15). Particles the size of PM_{10} and larger penetrate only the upper respiratory tract while fine particles (range $PM_{2.5}$ to PM_{10}) also penetrate the lower respiratory tract. Inhalable particles smaller than 1 μm (PM_1) reach the alveoli, the cavities in the lungs where oxygen is exchanged for carbon dioxide. Even smaller aerosols ($PM_{0.1}$, 0.1 μm and smaller) are known as ultrafine particles and penetrate beyond the respiratory tract into the bloodstream[230,231].

Society

Earliest reports of aerosol emission pollution as a nuisance go back to the 13th century to Eleanor of Provence (c. 1223 – 1291), the wife of King Henry III (1207 – 1272). She complained about the increasing use of coal instead of firewood as the significant higher sulphur content of the new fuel source contributed to the unpleasant sulphur smell[232]. Nevertheless, facing increasing energy demands, a growing population and diminishing wood resources, coal became increasingly a necessity. With James VI and I (1566 – 1625), the use of coal was further popularised despite the high sulphur content in the bituminous English coal, while the King used cleaner but more expensive anthracite from Scotland. Coal overtook wood as the major energy provider in England and Wales around 1619 and continued to become the predominant energy source by the beginning of the 20th century[233,234]. The heavy coal use caused considerable air pollution. In large cities such as London, smoke pollution decreased visibility substantially and especially in winter temperature inversions tapped the pollutants in the city[235]. Among the worst air pollution events ever

recorded was a five-day event in December 1952 in London, UK, generally known as the *Great Smog of London*. Cinemas were shut and busses had to cease operation due to bad visibility. Looting was widespread as no one was able to see more than a few metres[16]. At least 4000 people died in the smoke, however, more recent estimates put the number of excess deaths at 12 000[236,237]. Nevertheless, this heavy air pollution event prompted the UK to enact the 1956 Clean Air Act, a major turning point in air pollution regulation[238]. Although air pollution has significantly decreased over the last decades in high-income countries, emerging and developing nations in Asia suffer from air pollution, with China and India most affected[209].
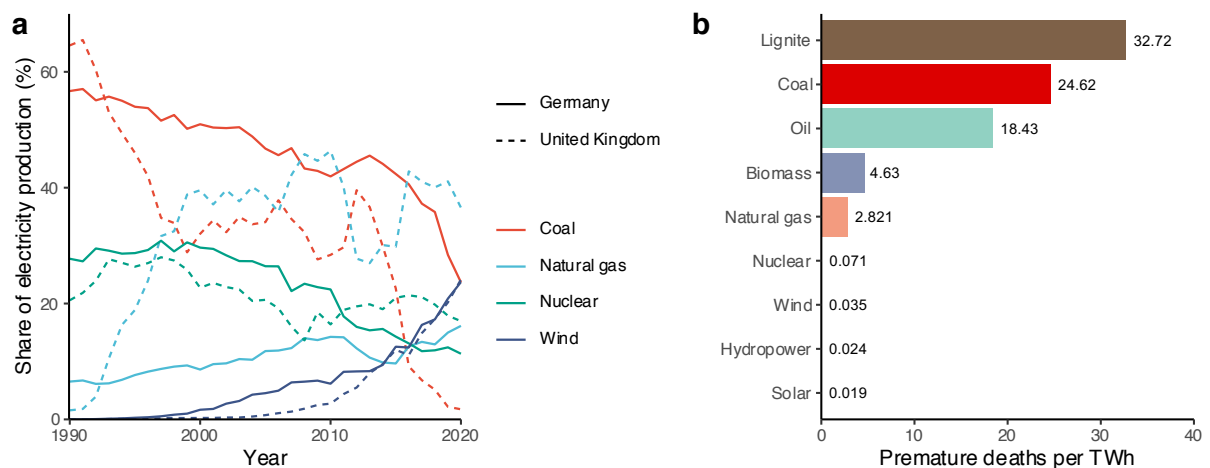
Figure 16: a) Share of electricity production of Germany and the United Kingdom for coal (all types), natural gas, nuclear, and wind for 1990 to 2020 with data from the BP Statistical Review of World Energy 2021[14]. b) The number of premature deaths per terawatt hour (TWh) from energy production. Values from Ritchie and Roser[239] based on data from Sovacool et al.[240] for nuclear and renewables and Markandya et al.[241] for fossil fuels, nuclear, and biomass.

Electricity production worldwide is still dominated by fossil fuels, however, wind, solar, hydropower, and nuclear are possible alternatives. Beside location, topography and economic feasibility, safety should be a factor to consider. In terms of safety, power sources have negative consequences in terms of the number of premature deaths per unit of power generated, mostly due to premature deaths from air pollution and accidents during operation (mining, transport, construction, power plant operation). Both the United Kingdom (UK) and Germany have historically relied heavily on coal for electrical power generation, with both using coal for roughly 60% of their energy production in 1990 (see Figure 16a). In the UK, coal has been replaced mostly by natural gas and since 2000, the share of wind power has grown from almost none to around 20% while nuclear fluctuated around 20%[14]. Furthermore, with an increasing share of renewables, natural gas power plants are well suited for fast changes in supply and demand (peaking power plant)[242].

Although with a decreasing share, Germany continues to rely on coal and lignite for a substantial fraction of their energy production[14]. As shown in Figure 16b, lignite and coal lead to the highest number of premature deaths per terawatt hour (TWh), far exceeding alternatives, including nuclear. Additionally,

Germany's detrimental political decision to prematurely shut down all their remaining nuclear reactors in 2022 due to safety concerns has achieved the opposite. Beside the higher CO_2 emissions per unit of power generated, the nuclear phase-out causes an estimated more than 1,100 additional deaths each year because of air pollution[243]. It has been estimated that the social cost of the shift from nuclear to coal power for Germany are approximately US$ 12 billions per year[243].

Climate

Aerosols affect the global radiation budget in two major ways: by changing the amount of heat that gets reflected in or out of the atmosphere, or by affecting the way clouds are formed. This is referred to as aerosol-radiation interaction and aerosol-cloud interactions, respectively (see Figure 17).

Figure 17: A highly simplified schematic of the direct aerosol-radiation interactions and indirect aerosol-cloud interactions by atmospheric aerosols; schematic adapted from Boucher et al.[244].

The effect of aerosols on the global radiation budget is expressed as radiative forcing and given as Watts per square metre (W m^{-2}). Radiative forcing is the change in energy flux in the atmosphere when the factors that affect the climate are altered. A positive radiative forcing would imply a warming effect while a negative radiative forcing a cooling effect. Greenhouse gases such as CO_2 and CH_4 are well known contributors to a positive radiative forcing, however, also tropospheric ozone, halogenated species, and nitrous oxide (N_2O) have a positive radiative forcing[245]. Atmospheric aerosols have a net negative effect (see Figure 18) on radiative forcing; however, the individual carbonaceous fractions have an opposite effect on radiative forcing. EC leads to a decrease in the surface albedo and an increased absorption of the incoming solar radiation, thus causing a positive radiative forcing. EC emission reductions therefore help to reduce the anthropogenic effects of climate change. Non-refractory carbonaceous aerosols (OC) and sulphate have a negative radiative forcing as they induce a cooling effect by reflecting the incoming radiation[244,246].

The negative radiative forcing of sulphate has far-reaching consequences. Stricter air pollution regulations in industrialised countries have lowered sulphur emissions substantially by using low sulphur fuels and flue-

gas desulphurisation in power plants[247,248]. Also, the global shipping industry has very recently drastically reduced their sulphur emissions with new regulations (IMO 2020) to cap the sulphur content in fuel to 0.5%. Although beneficial in several other ways, the sulphur emission reduction will further accelerate climate change as the negative radiative forcing effect of the sulphate emissions is lowered[249]. Proposals to utilise the negative radiative forcing properties of sulphate aerosols have been made to mitigate anthropogenic climate change[250]. Large scale artificial stratospheric sulphur injections would be necessary and sustained as those measures only last for the time they are applied. Beyond the lock-in effect, geoengineering techniques cannot offset the effects of greenhouse gases completely and the issue regarding ocean acidification with higher atmospheric CO_2 concentrations has not been addressed[159].
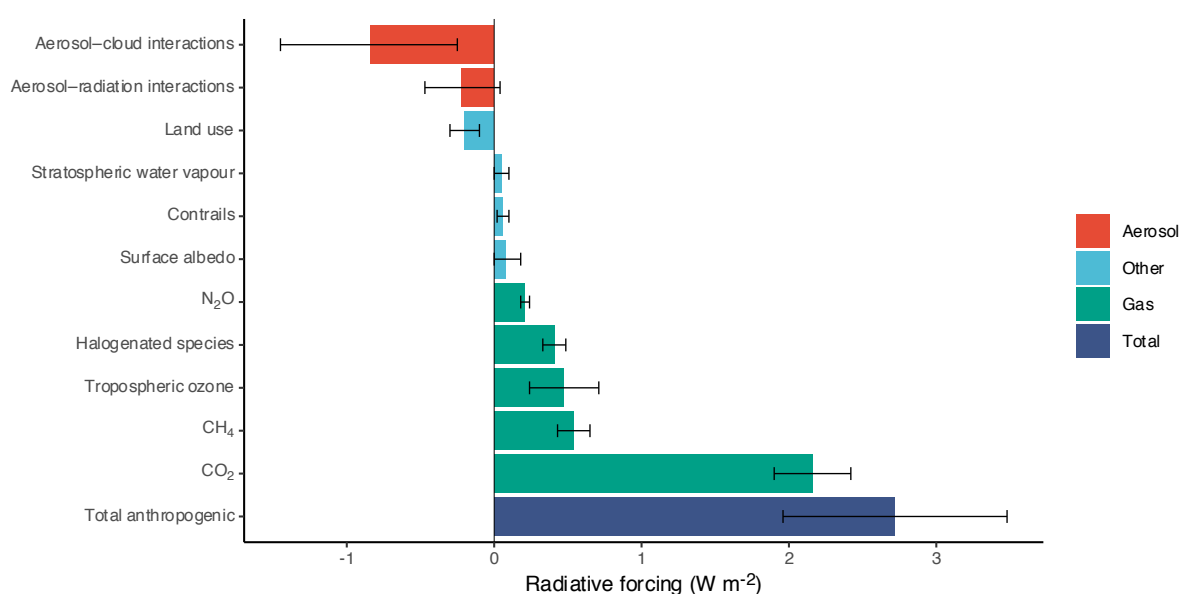
Figure 18: Radiative forcing estimates in 2015 relative to 1750 and the aggregated uncertainties. Greenhouse gases contribute to positive radiative forcing while the overall effect of aerosols leads to a negative contribution. Data retrieved from the IPCC 2021 report[245].

Particle emissions and their effect on the climate are of particular interest for Arctic research. Global temperature rise has a greater impact on the Arctic than at mid-latitudes due to the Arctic amplification phenomenon, i.e., the phenomenon that any change in the global net radiation balance produces larger temperature changes in the Arctic[251]. In the last 100 years, the atmospheric temperatures in the Arctic have risen twice the global average[252]. As shown in Figure 19a as a temperature anomaly relative to the 1961–1990 period, the global temperature has increased substantially in the last decades. The sea ice thickness and extent has decreased over the past decades and the Arctic may seasonally become ice-free in the 2030s[253,254]. Figure 19b shows the sea ice extent recordings (1979–2021) and the minimum sea ice extent projections to 2100 depending on the greenhouse gas concentration model. Disregarding on the model, parts of the Arctic will very likely seasonally be ice free. This may lead to an increase in Arctic shipping due

to shorter distances from Asia to Europe: instead of using the Suez Canal route, some ships may use the Northern Sea route through the Arctic instead[255,256]. An increase in Arctic shipping will certainly lead to more aerosols emissions in the Arctic. Understanding the sources and mechanisms of aerosols also in polar regions is therefore crucial for future projections and the implementation of mitigation strategies[257].

Measurements are needed to understand these changes in the polar regions, which remains challenging in many aspects including difficult logistics, low temperatures, and strong winds. For atmospheric aerosols, numerous studies analysed EC sampled at various sites. Early Arctic atmospheric aerosols measurements go back to the 1960s and 1970s with measurements of inorganic compounds as well as BC and OC concentrations[258].
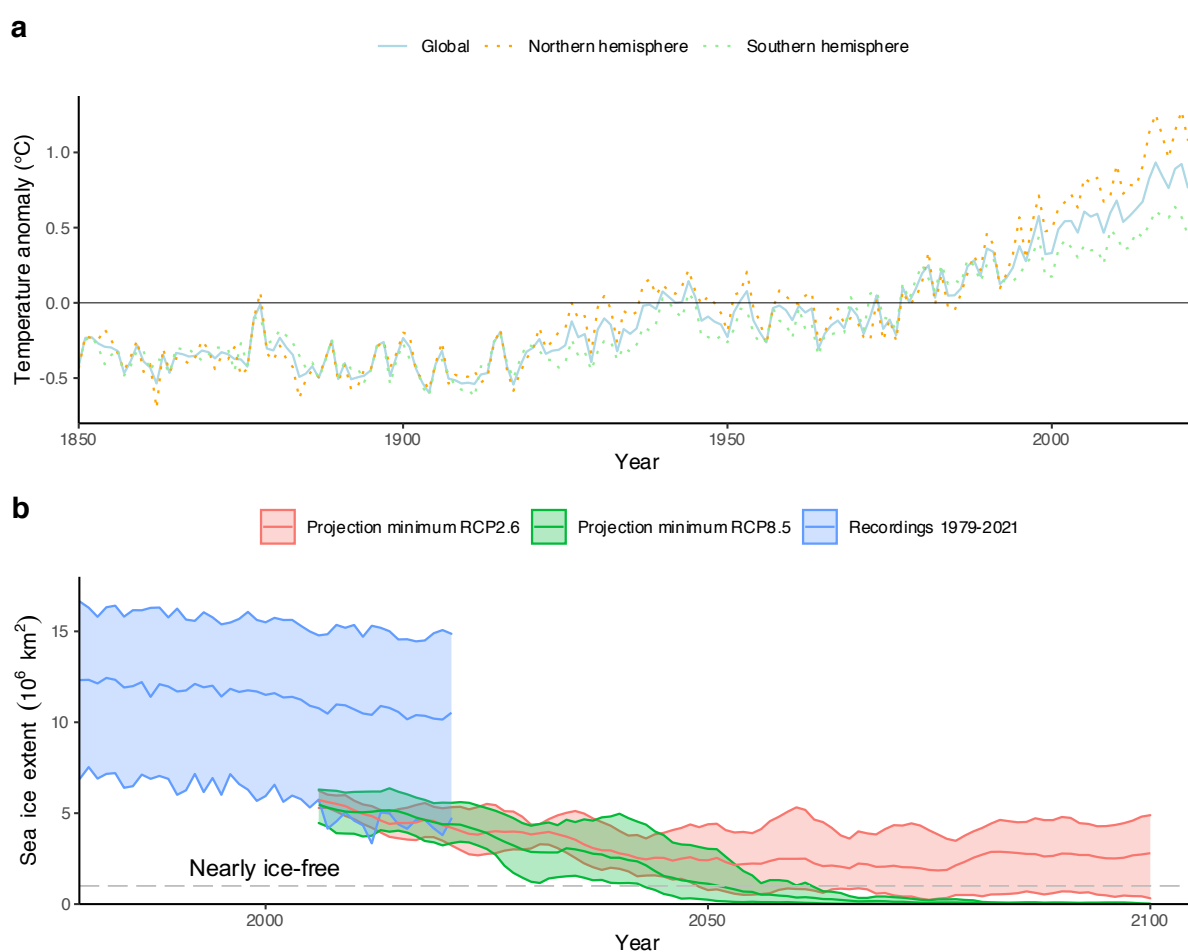
Figure 19: a) Hemispheric and global average temperature anomaly shown from 1850 to 2021, relative to the 1961–1990 period. The HadCRUT5 data set was retrieved from Morice et al.[259] and the Met Office Hadley Centre/Climatic Research Unit (HadCRUT). b) Arctic sea ice extent from 1979 to 2021 and projections of minimum sea ice extent with uncertainties according to the Representative Concentration Pathway (RCP) 2.6 and 8.5 from the Coupled Model Intercomparison Project Phase 5 (CMIP5). The dashed line corresponds to a sea ice extent of 1 million square kilometres, which is considered a nearly ice-free Arctic. Sea ice extent data was retrieved from Fetterer et al.[260], minimum sea ice projections from the European Environmental Agency[261].

To investigate the Arctic haze phenomenon as well as fossil-fuel combustion, several have studied atmospheric aerosols in the Arctic (north of 66°N latitude). As an example, Kahl and Hansen[262] analysed BC sampled at Point Barrow, Alaska with an aethalometer and made back trajectory analysis. Since these early measurements, many more have analysed Arctic aerosols. So far, BC (or EC) was the focus and frequently also included $\delta^{13}C$ and ^{14}C measurements for source apportionment[263–266]. More recently, also OC and its subfractions were investigated and remain an important topic and an opportunity for future research[267,268]. Therefore, the radiocarbon measurements of EC and WSOC on low-loaded aerosol filter samples from Svalbard, Norway discussed in Chapter 2 are of high relevance in current research.

Antarctica is even more remote than the Arctic and truly a continent of the extremes. The polar desert is covered on average with 2 km of ice. Despite no permanent human population, several nations have research stations in Antarctica and on nearby islands. The remoteness of the continent coupled with little human presence makes Antarctica a true remote site. Nevertheless, Antarctica is already experiencing a rapid climate change and understanding these processes is of high importance[269]. The remote location and harsh conditions make research difficult, and publications investigating atmospheric aerosols are scarce compared to the Arctic. Concentrations of carbonaceous aerosols are generally low and decrease from the Antarctic coast to the interior of the continent[270–275]. SOAs contribute to a substantial fraction of the total OA in Antarctica and are driven by phytoplankton blooms[276,277]. Furthermore, it is known that the oceans are a source of primary and secondary OA in Antarctica[278–280]. Although radiocarbon measurements in samples from Antarctica have been performed, they are rare. For example, Clarke et al.[281] investigated $\delta^{13}C$ and ^{14}C in Antarctic moss, Emslie et al.[282] dated penguin remains (bone, feather, and egg membranes), and several[283–286] measured dissolved organic carbon (DOC) sampled in the Southern Ocean. Nevertheless, no publication discussing ^{14}C analysis of atmospheric aerosols from Antarctica was found. This underlines the difficulty of such an endeavour from aerosol sampling to the radiocarbon analysis. The lack of radiocarbon measurements in atmospheric aerosols from Antarctica thus provides an opportunity for our research. In Chapter 4, the radiocarbon measurement results of PM_{10} filters sampled at the Trollhaugen Observatory from 2016–2018 are discussed.

Economy

The industrial revolution fuelled by coal and later also by oil and natural gas completely changed on how mankind lives on Earth. The revolution fuelled by cheap and readily accessible energy enabled innovations in the agricultural sector with mechanisation and nitrogen fixation (Haber-Bosch process) developed in the early 20th century[248]. The industrial revolution also enabled innovations directly benefiting human health such as anaesthetics[287], the development of vaccines as the most effective method of preventing infectious diseases[288,289], and the discovery of antibiotics to fight off bacterial infections[290]. Never in the human history before was the human population so large and the life expectancy so high. On the other hand, never did fewer children die of infectious diseases, and fewer people suffer from malnutrition and famine[291].

The industrial revolution brought economic prosperity and provided the basis of all amenities we enjoy and cherish today, however at a substantial cost for the environment (e.g., greenhouse gas emissions, biodiversity and habitat loss), which again affects the human life on Earth[292]. As an example, the release of various compounds into the atmosphere creates air pollution, which adversely affects human health following acute and chronic exposure[212]. Air pollution is not only a threat to the individual affected but has consequences for society. An increase in air pollution-induced health issues leads to increased health care costs, reduced abilities to work, and lower work force participation rates, therefore, creating a significant economic burden (see Figure 20).

Health care expenditures, labour productivity, and agricultural yields are considered market costs and therefore measurable by economic activity and the gross domestic product (GDP). Non-market costs are monetised welfare costs from disutility of illness and mortality, which means putting a price tag on pain and suffering and premature deaths, respectively[293]. Dechezleprêtre et al.[294] estimated for the European Union (2000–2015 period) that an increase of 1 µg/m³ in $PM_{2.5}$ causes a 0.8% reduction in real GDP with 95% of the reduction attributed to a reduced labour force output. The World Health Organisation (WHO) estimated for Europe (53 countries, WHO European Region) in a study for the year 2010 an overall annual economic cost of health impacts and mortality from air pollution at US$ 1.6 trillion[295]. The estimated cost from air pollution as a percentage of GDP ranged from 0.3% (Norway) to double digit percentages for poor nations, with the major Western European countries generally below 5% (e.g., Germany 4.5%, France 2.3%, Switzerland 2.5%)[295].

Emissions PM, NH_3, NO_X, SO_2, VOCs	→	Chemical reactions & transport primary and secondary particle generation	→	Exposure people, crops	→	Impact mortality, morbidity, crop loss	→	Economic value
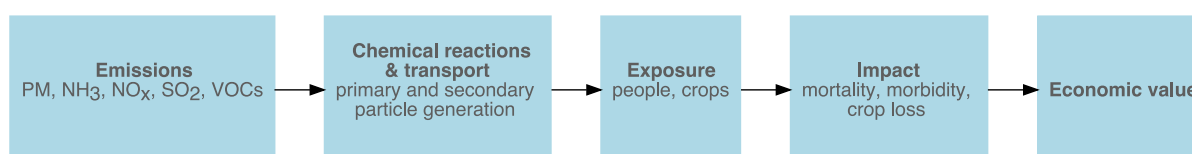
Figure 20: The emission of pollutants generates external costs. Emissions released into the atmosphere are transported and undergo chemical reactions and expose crops and people. This exposure has an impact: for people, a higher mortality and morbidity are the outcome, and for crops the yields decrease, thus these effects have an economic value. Scheme adapted from Amann et al.[296].

A study published by the Organisation for Economic Cooperation and Development (OECD) compared the economic costs of ambient particulate matter pollution in the BRIICS (Brazil, Russia, India, Indonesia, China, South Africa) countries to the 35 OECD countries. For 2015, ambient PM pollution (see Figure 21a) was calculated to cost 7.9%, 10.6%, and 12.5% of the GDP for China, India, and Russia. The mean value over all OECD countries was 3.5% of the GDP, with the costs estimated at 4.6%, 2.9%, and 2.2% of the GDP for Germany, France, and Switzerland, respectively[297]. These costs for PM pollution for 2015 are very similar to the air pollution costs calculated by the WHO for 2010, which also includes other types of air pollution (e.g., ozone). The Centre for Research on Energy and Clean Air more recently estimated

for 2018 the worldwide economic cost of air pollution at US$ 2.9 trillion or 3.3% of the global GDP, with the highest cost for China at over US$ 900 billions or 6.6% of the GDP[298,299]. In terms of air pollution costs per capita, the highest values were reported for Luxembourg at US$ 2,600, while the second and third highest costs were reported for the USA and Switzerland with both valued at US$ 1,900[298].

Effective air pollution mitigation policies should be implemented with cost-effective measurements to have the greatest impact on society with the benefits exceeding the implementing costs by a large factor. Like effective climate policy, air pollution mitigation policies should be efficient, cost-transparent, maintain technological neutrality, and lead to an actual reduction of air pollution[300,301]. The United States Clean Air Act enacted in 1970 has been seen as one of the most effective public health policies with estimated benefits valued at US$ 2 billion for 2020 and exceeding the implementation costs by a factor of 32:1[302]. As shown in Figure 21b, most air pollutants in the USA decreased substantially despite a growing population, doubling of the GDP per capita (constant 2015 US$), and tripling the vehicle miles travelled.
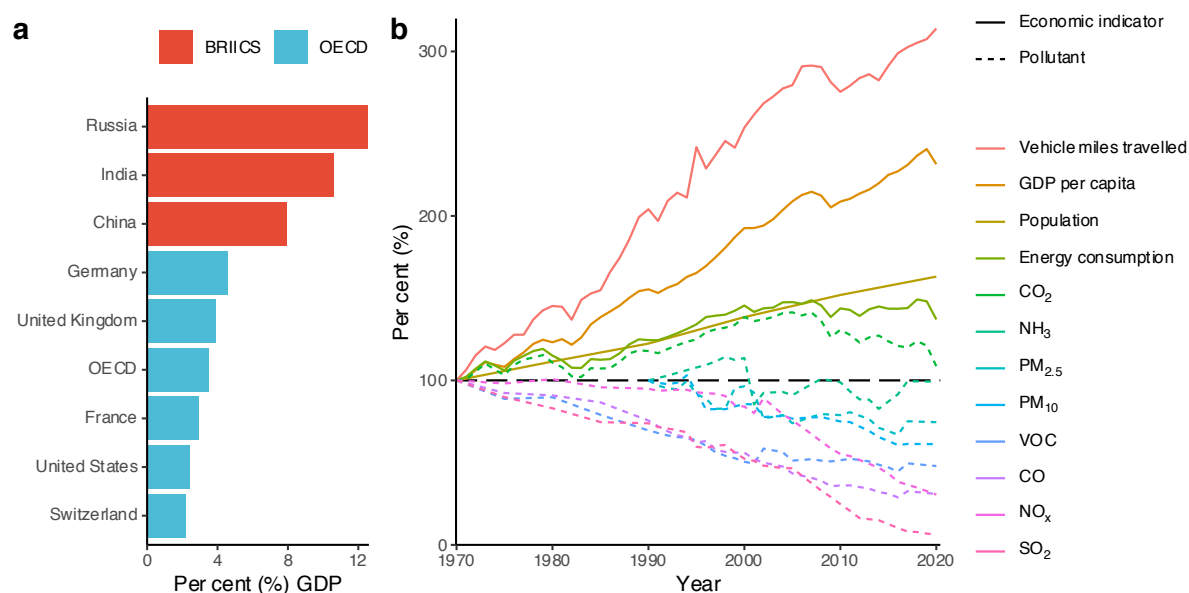
Figure 21: a) Cost of ambient PM pollution for the year 2015 as a percentage of the GDP for a selection of BRIICS and OECD countries, data retrieved from OECD[297]. b) Economic indicators (vehicle miles travelled, GDP per capita, population, energy consumption) compared to environmental pollutants in the USA. Data shown from 1970–2020 for all data except for PM_{10}, $PM_{2.5}$, and NH_3, which are shown from 1990–2020. Data was normalised to 100% for 1970 and 1990, respectively. Data for the vehicle miles travelled were retrieved from the U.S. Federal Highway Administration[303], GDP per capita (constant 2015 US$) from the world bank[210], U.S. population data from the U.S. Census Bureau[304], the energy consumption data from the U.S. Energy Information Administration[305], and the data for environmental pollutants trends was retrieved from the U.S. Environmental Protection Agency[306]. Although CO_2 does not pose a risk to human health at atmospheric concentration, CO_2 is shown as a pollutant as it contributes to climate change, which has adverse effects to human health[245]. CO_2 data was retrieved from Friedlingstein et al.[307].

1.5.4 Aerosol source apportionment

Source apportionment is the idea to identify air pollution sources and quantify their contribution to the pollution. This can be accomplished with different approaches such as emission inventories, source-oriented models, and receptor-oriented models. Emission inventories attempt to quantify in detail all sources of air pollutants within a defined time span and geographical area. Source-oriented models estimate the contribution of sources to PM, and receptor-oriented models attempt to identify and quantify the sources of air pollutants at the receptor location (i.e., air pollution sampling site)[308–310]. For receptor modelling, various approaches are in use depending on the knowledge of the pollution sources. When little is known, exploratory factor analysis models such as principal component analysis (PCA) and positive matrix factorisation (PMF) are used and apportions to the sources are made based on observations[309,310]. Since its inception in 1993 based on factor analysis by Paatero et al.[311], PMF has been widely used for source apportionment[312,313]. Chemical mass balance (CMB) models on the other hand assume to know the composition of the emissions for all sources[314]. Furthermore, hybrid expanded models (e.g., COPREM) are between PMF and CMB and provide the opportunity to introduce constrains or combine different types of data including meteorological, physical, and chemical parameters[315,316]. Frequently, multiple source apportionment receptor models are used in a study[317,318].

Models require input data, usually from measurements. A large variety of chemical tracers have been used as a valuable tool for aerosol source apportionment including PM mass of a certain size fraction (e.g., PM_{10}, $PM_{2.5}$), carbonaceous fractions (EC, OC), metals (e.g., Fe, Pb, Hg, Ni), ions (e.g., SO_4^{2-}, NH_4^+), stable isotope (e.g., $\delta^{13}C$, $\delta^{15}N$, $\delta^{18}O$), VOCs, PAHs, and polychlorinated biphenyls (PCBs)[175,319–321]. Some of the chemical tracers are very specific to a source. For example, biomass burning tracers include levoglucosan originating from cellulose or methoxyphenols originating from lignin[322].

Various analytical techniques are used for the analysis of chemical tracers in aerosols. For OC and EC analysis, thermo-optical carbon (TOA) analysis (see Chapter 1.6.1) is a widely used technique[323–325]. Many also employ some form of Liquid Chromatography (LC), frequently coupled with Mass Spectrometry (MS). For example, Yittri et al.[323] used High Performance Liquid Chromatography (HPLC) in combination with High Resolution Mass Spectrometry Time-of-Flight (HRMS-ToF) to separate and detect the monosaccharide anhydrides levoglucosan, mannosan, and galactosan. The analysis of monosaccharide anhydrides, sugars, and sugar–alcohols are also performed by Gas Chromatography (GC) in combination with MS[326]. Ions such as sulphate, ammonium, and nitrate are commonly analysed by Ion Chromatography (IC)[327,328]. For the analysis of cellulose, an enzymatic assay developed by Knut and Puxbaum[329] is frequently used[326,330]. Furthermore, Time-of-Flight aerosol mass spectrometry (HR-ToF-AMS) has become a frequently used measurement technique for atmospheric aerosols. The device provides quantitative size and chemical mass loading information and can be used in the lab with previously sampled filters (offline) or deployed into the field (online), including aircraft[331,332]. HR-ToF-AMS is often used in combination with PMF for source apportionment[333,334].

Chemical tracers have the disadvantage that they frequently do not originate from a single source, they degrade (age) over time and undergo chemical reactions in the atmosphere[335]. Source apportionment with radiocarbon on the other hand has the advantage that it allows for a clear apportionment of fossil and modern sources (see Figure 22); masking by degradation and chemical reactions (aging) in the atmosphere is not of concern[174,336]. Radiocarbon is constantly formed in the upper atmosphere (see Chapter 1.2.2) and biogenic sources contain a modern level of radiocarbon with a $^{14}C/^{12}C$ ratio of 1.2×10^{-12}, whereas fossil sources are completely devoid of radiocarbon[337]. The radiocarbon formed in the atmosphere is in exchange with the biogenic sources and remains relatively stable over time besides small differences (relevant for dating) and anthropogenic influences (see Chapter 1.2.2)[47,338].
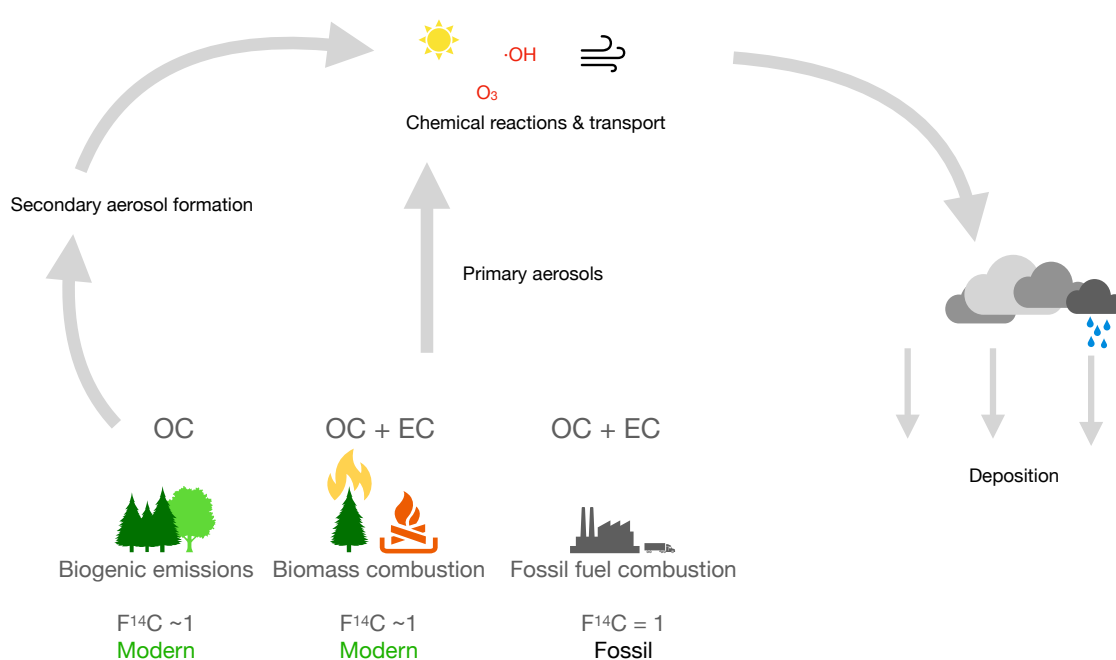
Figure 22: Simplified scheme of the formation of carbonaceous aerosols from biogenic and fossil precursors. Biogenic emissions (e.g., isoprene) consist of only OC, whereas biomass combustion and fossil-fuel combustion are a mixture of OC and EC. Biogenic emissions and biomass combustion release carbonaceous compounds with a modern $F^{14}C$ value of around 1, whereas carbon from fossil-fuel combustion processes is completely devoid ($F^{14}C = 0$) of radiocarbon. Carbonaceous aerosols are either formed from gaseous precursors (SOA formation) or directly released as primary aerosols (OC, EC) from their sources. The aerosols undergo reactions and are transported before deposition.

Fossil fuels were formed under anaerobic conditions over millions of years from phytoplankton and terrestrial plants. These materials were completely cut off from atmospheric exchange during this process and all radiocarbon has completely decayed[339]. Radiocarbon for source apportionment was first applied by Clayton et al.[340] in 1955, who collected air samples on filters in Detroit and Los Angeles (USA) and measured the radiocarbon content using LSC. For his measurements, Clayton et al.[340] used 3–8 g C for each sample with a cumbersome chemical process until measurement. Nevertheless, measurements from

Clayton et al.[340] showed that a substantial fraction of carbonaceous aerosols stem from fossil-fuel combustion processes. Radiocarbon source apportionment with smaller amounts of sample would be highly desirable. In 1981, Cooper et al.[341] used radiocarbon source apportionment on particulate matter (TSP <100 μm and fine <2 μm) collected in Portland (USA) using low-level gas proportional counters with only 5–10 mg C of sample. Cooper et al.[341] predicted that AMS could be a valuable tool for fast sample analysis. In fact, AMS (see Chapter 1.4.2) was a major leap forward, which enabled radiocarbon source apportionment with a higher sample throughput and even smaller amounts. Today, AMS allows for the measurement of a wide range of aerosol fractions including TC, EC, and OC; and even CSRA is feasible now[174,180,208].

1.6 Other methods

Radiocarbon analysis was coupled with other methods for sample separation or combustion before direct gas measurement in the hybrid ion source of the MICADAS AMS. As summarised in Figure 23, this Chapter compiles these methods and discusses them in relation to radiocarbon measurements with AMS. TC combustion and OC/EC separation were performed with a Sunset OC/EC thermal-optical analyser before radiocarbon measurement on a MICADAS AMS, hence, thermal-optical analysis is discussed in-depth in Chapter 1.6.1. Prior to OC/EC separation, the aerosol filters were frequently water extracted (see Chapter 1.6.2) for better performance in OC/EC separation as well as direct WSOC measurement. For CSRA of oxalate extracted from filters, separation by ion chromatography was used as described in Chapter 1.6.3. Chemical wet oxidation was used for direct WSOC measurement of the water extracted aerosol filters as well as oxalate after separation by ion chromatography. Chemical wet oxidation is described below in Chapter 1.6.4.
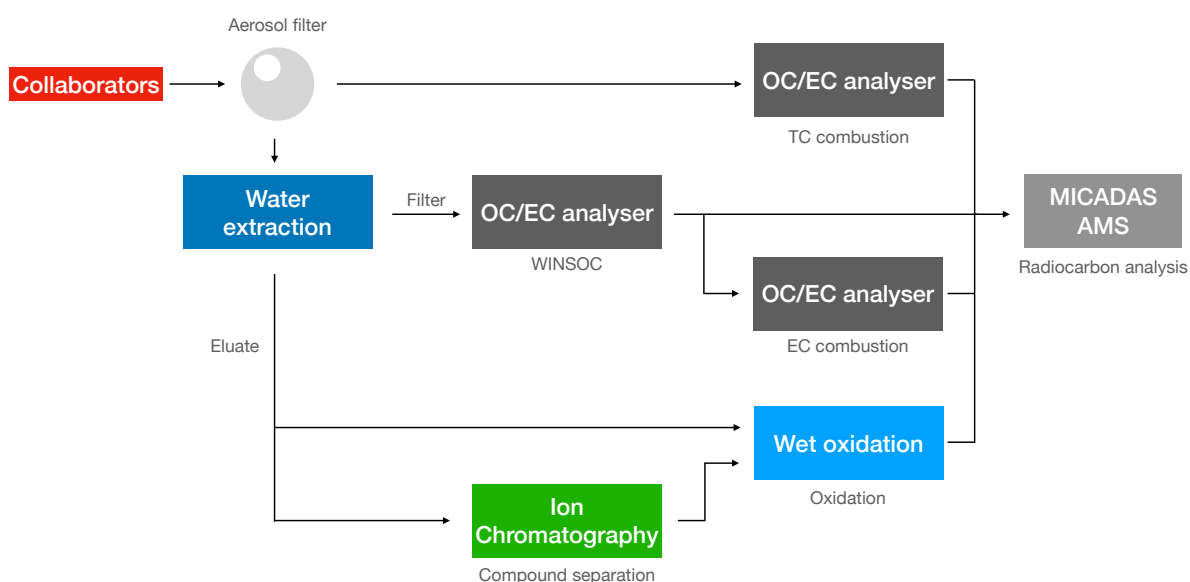
Figure 23: Summary of the separation techniques and hyphenation tools used in this work. The workflow summarises the TC analysis, water extraction, WINSOC removal or WINSOC radiocarbon measurement, and EC analysis for the filters. The WSOC eluate after the water extraction is either oxidised directly by chemical wet oxidation or separated by IC for CSRA before chemical wet oxidation. Note that here wet oxidation is shown for the oxidation of WSOC after filter extraction and oxalate after IC separation, however, any dissolved carbonaceous compound can be oxidised. Aerosol filter sampling was performed by collaborators and usually, untreated filters were received and treated according to this workflow.

1.6.1 Thermal-optical analysis

OC/EC analysers are small desktop devices for thermal-optical analysis (TOA) of OC and EC in atmospheric aerosols and are commercially available since the 1990s[342]. The Sunset OC/EC (alternative spelling: Sunset OCEC or Sunset OC-EC) devices are made by Sunset Laboratories (abbreviation: Sunlab), a company out of Tigard, OR, USA. The Sunlab Sunset Model 5L device was used for TOA in this work and will be presented here in more detail.
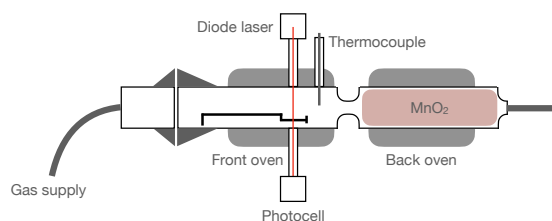
Figure 24: Simplified Sunlab Sunset Model 5L oven assembly scheme with gas supply and joint with O-ring seal and a clamp (not shown) on the left. The front oven assembly contains the sample spoon with the aerosol filter punch in the front of the spoon, the diode laser for sample monitoring, and the thermocouple to accurately monitor the temperature the sample is exposed to. The back oven is filled with MnO_2 beads to oxidise all carbonaceous compounds to CO_2.

The Sunset TOA consists of a quartz glass oven containing a sample side and a combustion oven (back oven) side with a heating zone on each side provided by heating coils wrapped around (see Figure 24). On the sample side, mounting points for the 658 nm (range: 655–660 nm) wavelength laser diode and photocell detector on the quartz are provided. The laser transmission signal monitors the charring process (i.e., the conversion of organic carbon to elemental carbon) and the loss of EC observed with a decrease and increase in light transmission, respectively[343,344].
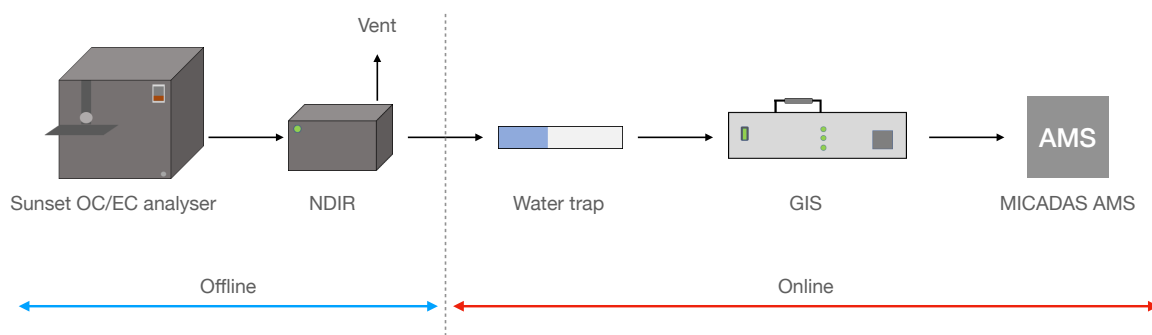
Figure 25: Sunset as a standalone device (offline) or coupled with radiocarbon measurement with the MICADAS AMS (online). The sample is combusted in the Sunset OC/EC analyser, CO_2 detected in the NDIR. In offline mode, the gas is vented, otherwise it is dried with a SICAPENT® (phosphorous pentoxide on inert carrier material with colour indicator), trapped in the gas ion source interface (GIS), and measured by AMS.

The aerosol sample on a quartz fibre filter is placed on the Sunset quartz spoon (sample area: 10 × 15 mm, 1.5 cm^2) and placed in the quartz oven sample area. The sample loading side is closed off with a connection providing carrier or combustion gas (He, O$_2$, or a O$_2$/He mixture). The carbonaceous compounds released from the aerosol filters are carried to the back oven and oxidised to CO$_2$, carried through a copper trap, and analysed in the NDIR. When operated as a standalone device (offline), the measured gas is vented (see Figure 25). In hyphenation with AMS (online), the gas is dried with SICAPENT® (drying agent, phosphorous pentoxide on an inert matrix) and transferred to the gas ion source interface (GIS), where the CO$_2$ is trapped on a X13–zeolite trap before radiocarbon measurement with AMS[345,346].
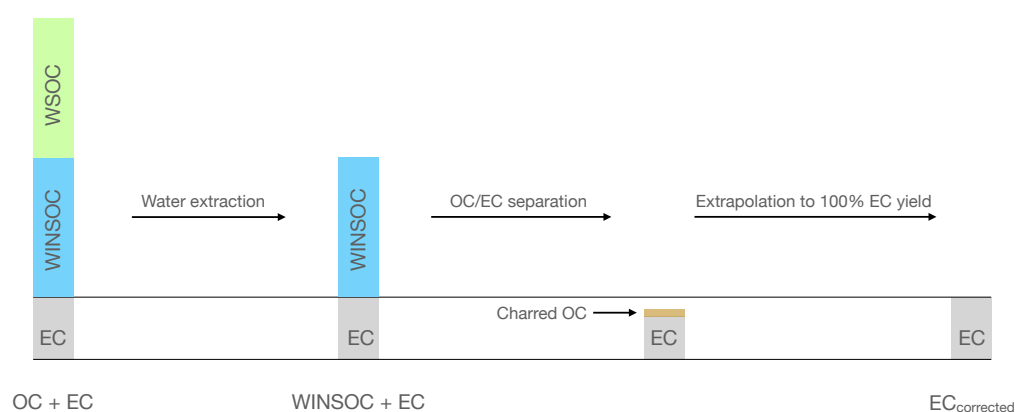
Figure 26: Schematic of a water extraction followed by an OC/EC separation step and extrapolation to 100% EC yield. The water extraction removes WSOC and leaves EC + WINSOC behind. The following OC/EC separation removes the WINSOC fraction. The resulting EC amount is smaller due to EC losses and contains some charred OC. Finally, the EC is extrapolated to 100% EC yield with 0% charring for both the amount of EC and Fraction Modern.

Using the laser signal information, this EC loss and charring can be corrected again to know the true EC amount and with some assumptions, also the Fraction Modern of the true EC can be calculated (see Figure 26). The combustion oven side contains MnO$_2$ beads to oxidise all carbonaceous compounds to CO$_2$. Thermocouples are used in the sample desorption/combustion area as well as in the back oven area. The sample thermocouple is calibrated with an extra thermocouple probe after each oven change; the probe is inserted instead of a sample spoon for temperature calibration to correct any offsets from the sample thermocouple to the temperature the sample experiences. The back oven coils do not need calibration: the temperature on the sample side needs to be precise for accurate sample desorption and combustion and undergoes many temperature cycles according to the analysis protocol, the back oven is constantly at 870°C during operation or at 500°C when the Sunset device is in standby. For CO$_2$ analysis, a non-dispersive infrared detector (NDIR) from LI-COR Biosciences (Lincoln, NE, USA) is used. The quartz oven gets opaque over time by usage, hence reducing the laser transmission signal. Therefore, the quartz oven, thermocouples and heating coils are all user replaceable. Furthermore, unlike earlier OC/EC analyser set ups, the Sunset OC/EC analyser uses a diode laser and a NDIR instead of a He-Ne laser and a flame

ionisation detector (FID), respectively. This simplifies the analysis for the user and likely reduces the cost per sample.

Various methods have been developed for the analysis of aerosols on quartz fibre filters. Chow et al.[347] developed the Interagency Monitoring of Protected Visual Environments (IMPROVE) thermal evolution protocol and has been applied to a wide range of filter samples. The IMPROVE method consists of four OC temperature steps in pure He followed by three EC steps in a 2% oxygen and 98% helium atmosphere. The analysis was monitored by a He-Ne laser (632.8 nm) in reflectance mode and the evolving CO_2 was analysed by FID after methanation[347].

Table 1: Summary of frequently used protocols for thermo-optical carbonaceous aerosols analysis with type of gas, T (°C), t (s). He and O_2 describes the pure gas, He/O_2 a mixture of 2% oxygen in helium.

IMPROVE[a]	NIOSH 5040[b]	NIOSH[c]	EUSAAR_2[d]	Swiss_4S[e]
He, 120, 150-580	He, 250, 60	He, 310, 60	He, 200, 120	O_2, 180, 50
He, 250, 150-580	He, 500, 60	He, 475, 60	He, 300, 150	O_2, 375, 150
He, 450, 150-580	He, 650, 60	He, 615, 60	He, 450, 180	O_2, 475, 120
He, 550, 150-580	He, 850, 90	He, 900, 90	He, 650, 180	He, 450, 180
He/O_2, 550, 150-580	He/O_2, 650, 30	He/O_2, 600, 45	He/O_2, 500, 120	He, 650, 180
He/O_2, 700, 150-580	He/O_2, 750, 30	He/O_2, 675, 45	He/O_2, 550, 120	O_2, 500, 120
He/O_2, 800, 150-580	He/O_2, 850, 30	He/O_2, 750, 45	He/O_2, 700, 70	O_2, 760, 150
	He/O_2, 940, 120	He/O_2, 825, 45	He/O_2, 850, 80	
		He/O_2, 920, 120		

[a]Chow et al.[347]
[b]Eller and Cassinelli[348]
[c]Peterson and Richards[349]
[d]Cavalli et al.[325]
[e]Zhang et al.[176]

Birch and Cary[350] developed a thermo-optical separation method for the analysis of diesel exhaust particulates. As diesel particulate emissions are predominantly consisting of EC, the goal of this method was to separate OC from EC. Charring was monitored by transmission with a He-Ne laser and the generated CO_2 analysed by an FID after methanation. The method was later published as Method 5040 by the National Institute for Occupational Safety and Health (NIOSH); therefore, the method is frequently known as NIOSH or NIOSH 5040[348]. An improved NIOSH method was later published by Peterson and Richards[351]. To demonstrate the differences between the protocols, a summary is shown in Table 1. Cavalli et al.[325] aimed to develop a standardised OC/EC separation protocol for Europe, as labs used different protocols and the reported values were considered not comparable. In the framework of the EU project EUSAAR (European Supersites for Atmospheric Aerosol Research), the EUSAAR_2 protocol for TOA was developed, with pure helium for OC and a 2% oxygen and 98% helium atmosphere used for EC.

The TOA protocols presented above may still contain unaltered or charred OC after the split point, however, radiocarbon analysis requires complete physical separation for source apportionment[176,268]. Gustafsson et al.[352] and Szidat et al.[353] developed and applied thermal separation techniques on aerosol filters[354–357]. Most recently, Zhang et al.[176] developed the revamp TOA separation protocol Swiss_4S, which was the first to correct for EC artefacts in ^{14}C analysis. To reduce charring, filters are water extracted (see Figure 26 and Chapter 1.6.2) prior to TOA with Swiss_4S and instead of He and O_2/He mixtures, pure He and O_2 were used. The Swiss_4S protocol consists of pure O_2 steps at low temperature already before the OC/EC split point to quantitatively desorb all OC from the filter with little charring and recover unaltered EC, an important prerequisite for radiocarbon analysis. An example of a Swiss_4S protocol applied on an aerosol filter sample from Svalbard is shown in Figure 27:
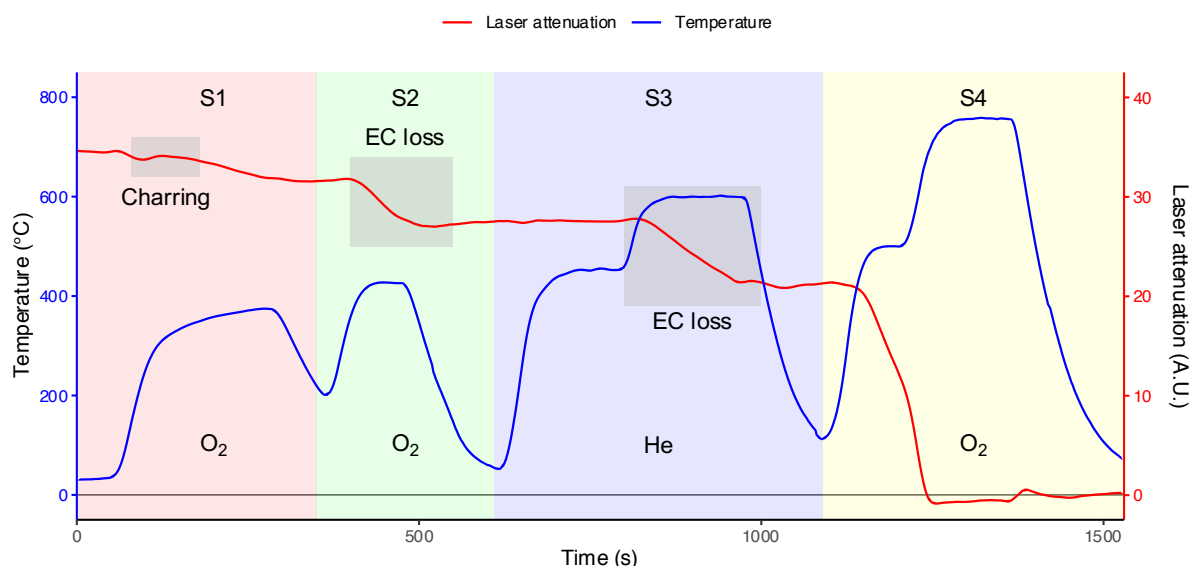
Figure 27: Example of a TOA with the Swiss_4S protocol applied on a water-extracted aerosol filter sampled 23/02/17–02/03/17 in Ny-Ålesund, Svalbard, Norway. The blue line shows the oven temperature (left axis) the filter sample was exposed to, the red line shows the laser attenuation signal on a secondary axis on the right. The type of gas for each step is shown with the labels O_2 (oxygen) and He (helium), respectively. In the first step (S1), a small increase of the attenuation is visible, thus indicating a small contribution of charring. As labelled in the second and third step (S2, S3), a decrease of the attenuation signal indicates a loss of EC. The decrease in S4 is intentional: the S4 step combusts all remaining carbonaceous material on the filter. Note that to further minimise charring and EC loss for this sample, the temperatures in S2 and S3 were lowered from 450°C and 650°C to 425°C and 600°C, respectively.

1.6.2 Water extraction

Water extraction of aerosol filters is the method to separate the WSOC from the remaining fractions (WINSOC and EC) on the filter material (see Figure 26), or to solubilise water-soluble compounds for further investigation. Hsieh et al.[187] analysed DCAs in atmospheric aerosols using ion chromatography and simply placed the aerosol filters in a polyethylene bottle with ultrapure water at 4°C for 90 min for extraction. No extraction yield was given with this method. Several[208,358,359] applied sonication additional to vortex mixing for organic acid extraction, with Fahrni et al.[208] reporting extraction yields of >97%. Studies investigating the oxidative potential of PM with dithiothreitol (DTT) assays frequently use ultrapure water or organic solvents such as methanol for filter extraction[360]. For samples subjected to AMS measurements, extractions with organic solvents should be avoided due to the risk of additional contamination. Nevertheless, vortex mixing and sonication with ultrapure water (see Figure 28a) are well known methods for water extracting aerosol filters when the eluate is of interest.
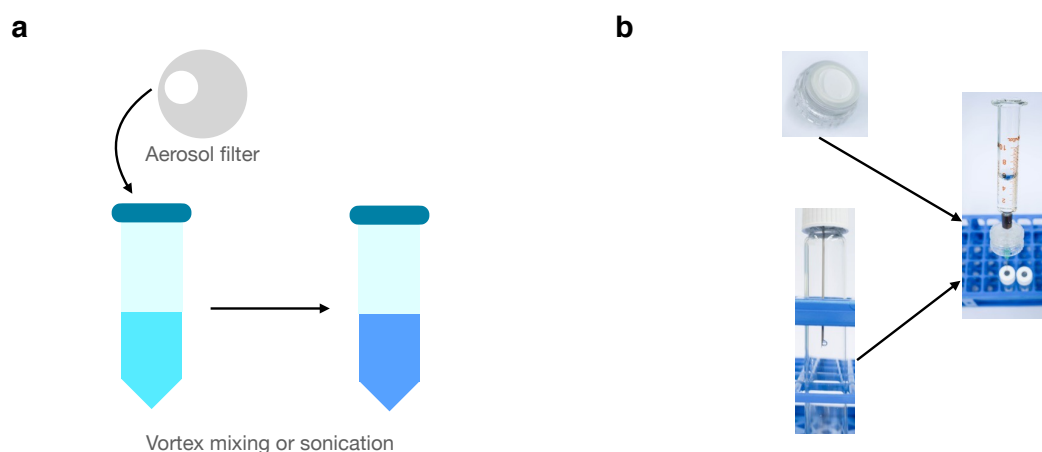
Figure 28: a) Aerosol filter water extraction visualisation with vortex mixing or sonication in a centrifuge tube. This process will render the filters unsuited for other applications (e.g., TOA), and will lead to EC dispersed in the solution, thus the extract must be filtrated before further use. b) Top image shows bottom part of the polycarbonate filter holder with a blank filter and a silicone O-ring on top. Image on the right shows assembled WSOC extraction setup and bottom image shows the needle in the Exetainer vial. Stacked and intercalated filters in the polycarbonate filter holders will leave EC on the filters unperturbed and usable for TOA after drying. The quartz filter will further retain EC from going into the WSOC extract, therefore, both the extract and the water-extracted filter can be utilised for further analysis. All images by Martin Rauber.

WSOC leads to additional pyrolysed carbon (charring) during TOA, therefore, water extraction has been identified as an effective method for a better OC/EC separation[344,361]. Consequently, water extraction has been used as a pre-treatment for TOA and for an optimal OC removal with reduced charring before radiocarbon analysis[176]. This requires that all insoluble material is preserved on the quartz fibre filter after with little additional inhomogeneity. Placing the filters in a vial with ultrapure water, vigorous vortex mixing, and sonication will not yield the desired outcome. Therefore, Zhang et al.[176] stacked and intercalated aerosol

filters with silicone O-rings in 25 mm polycarbonate filter holders topped by a plastic syringe (see Figure 28b). He reported little variation of the attenuation signal (up to 3%) from the Sunset OC/EC analyser comparing untreated and water extracted filters, indicating that there is little loss of EC and additional inhomogeneity induced during water extraction.

In this work, frequently both the eluate and the remaining filter material were used for further analysis; the water extracted aerosol filter for (online) OC/EC analysis and the eluate for WSOC analysis.

1.6.3 Chromatography

Liquid chromatography (LC) is a versatile tool for separating compounds, today usually performed with small packaging particles as a stationary phase and a liquid mobile phase under high pressure and therefore referred to as high pressure or high-performance liquid chromatography (HPLC). HPLC is one of the most widely used analytical techniques to separate, identify and qualify compounds, and can also be coupled with a large variety of detectors including mass spectrometry (MS)[362]. It is also frequently used in aerosol research; for example, Yittri et al.[323] used HPLC with HRMS-ToF for monosaccharide anhydrides analysis. Ion-exchange chromatography, often just referred to as ion chromatography (IC), is a related chromatographic technique based on the attraction between solute ions and charged sites on the stationary phase (see Figure 29). Ions with the opposite charge are retained on the column while ions with the same charge as the charged sites are excluded from binding. By changing the eluent conditions e.g., with an increase in concentration of the eluent, the retained ions are eluted again from the column[362].

a   **b**   **c**
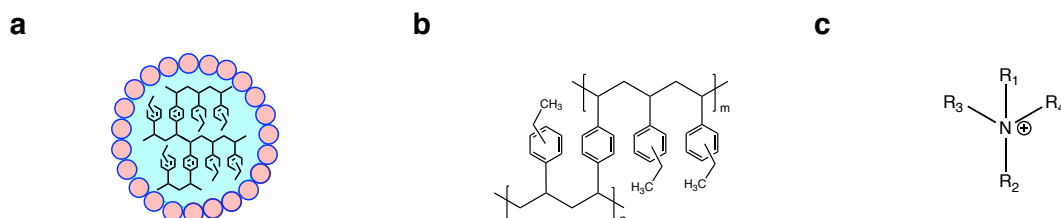
Figure 29: Schematic view of the column packing material of the Dionex IonPac AS11-HC column used in this work for DCA separation. a) the column consists of a divinylbenzene cross-linked ethyl vinylbenzene polymer core with latex beads on the outside containing the functional groups. b) core polymer structure. c) quaternary ammonium compounds are used as a functional group. Visualisation of a bead adapted from Rauber[363]; chemical structures drawn with ChemDraw Professional 17.1 according to Thermo Fisher Scientific product manual information[364].

Earliest reports of the predecessors of modern IC systems date back to the Manhattan Project, where lanthanides were separated using cation-exchange columns, and the separation of amino acids using ion-exchange chromatography in the 1950s[362]. A breakthrough came in the 1970s by Small et al.[365] while working for Down Chemical with solvent suppression. Previously, IC separation was followed by wet chemistry, which was a laborious and time-consuming process. The suppressor strips the eluent from the

high conducting effluent and only leaves the analyte and water behind. This allows for a simple detection of many analytes in an electrical conductivity detector with a very high sensitivity. Many IC systems in use today do not differ widely in the basics to what Small et al.[365] have used, however, with a large selection of high-performance columns and automatization, IC continues to be the analytical tool of choice for the analysis of organic and inorganic ions[362].

Characterisations of atmospheric aerosols frequently rely on IC measurements and numerous inorganic anions (e.g., F^-, Cl^-, NO_2^-, Br^-, NO_3^-, and SO_4^{2-}) and cations (e.g., NH_4^+, Na^+, K^+, Mg^{2+}) are analysed. Additionally, also DCAs and monosaccharide anhydrides from aerosol filters have been analysed with IC[186,187,328].

1.6.4   Chemical wet oxidation

The oxidation of carbonaceous compounds to CO_2 for further analysis is a frequently applied technique for stable isotope and radiocarbon analysis. For the measurement of carbonate samples such as speleothems, foraminifera, and corals, a simple acidification step using phosphoric acid is sufficient to dissolve the sample and generate CO_2. Carbonate samples mostly consist of $CaCO_3$, a compound labile to acid, which decomposes to CO_2. DOC cannot simply be acidified and decomposed to CO_2; an oxidation step is required. A previously employed method starts with the removal of the aqueous solution by lyophilisation and oxidation of the residue to CO_2. After lyophilisation, the residue is sealed in quartz tubes with cupric oxide and heated to 900°C in a muffle furnace[366]. Another possibility is provided with UV oxidation. This method provides the possibility to analyse saline samples, provides low blanks, and allows for sufficient CO_2 generation also from samples with a low carbon concentration[367–369]. The downside of UV oxidation is the reaction speed: it is rather slow and therefore results in a low sample throughput[370].
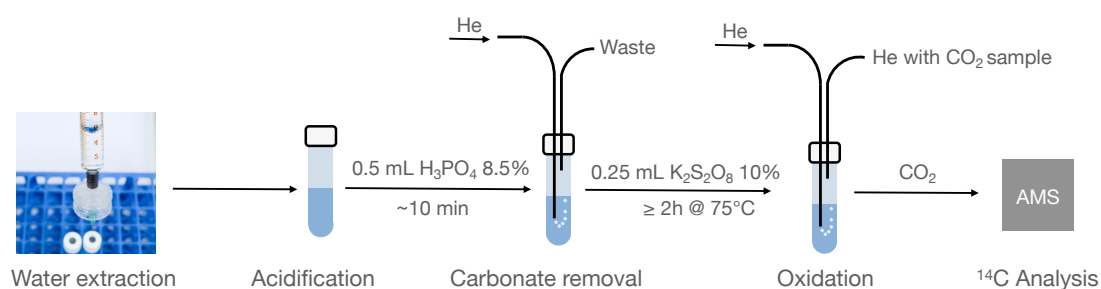
Figure 30: Schematic of a chemical wet oxidation coupled with water extraction of aerosol filters and radiocarbon measurement in an AMS. The aerosol filters are water extracted, the WSOC containing filtrate is acidified for carbonate removal, then oxidiser is added and reacted at elevated temperature. Finally, the generated CO_2 is transferred to the AMS for radiocarbon analysis. Water extraction image by Martin Rauber.

Chemical wet oxidation is the idea to oxidise organic compounds to CO_2 with the aid of a chemical oxidiser. Potassium and silver dichromate are strong oxidisers and have been used to oxidise DOC[371]. Sharp[372] reported the use of the less harmful potassium persulphate ($K_2S_2O_8$) as an oxidiser by several other researchers and utilised $K_2S_2O_8$ for TOC analysis in seawater. Generally, persulphates are used as oxidisers in organic chemistry (e.g., Elbs persulphate oxidation) or as an initiator for polymerisation reactions[373,374]. More recently, chemical wet oxidation was used to oxidise samples for stable carbon and radiocarbon analysis. Lang et al.[375] used chemical wet oxidation with $K_2S_2O_8$ for stable isotope (^{13}C) analysis for DOC in freshwater, which was later adapted for radiocarbon analysis[370]. Furthermore, any other aqueous liquid containing carbonaceous material can be oxidised; Lang et al.[376] also analysed organic acids in marine samples and Guillemot et al.[112] used wet oxidation for a nuclear waste study (see Chapter 1.3.5).

Here it should be noted that persulphate is not the only oxidiser in use for chemical wet oxidation together with AMS measurements: Leonard et al.[377] used potassium permanganate as an oxidiser instead for the DOC analysis of water samples. Most important is the complete oxidation of the sample material to CO_2 and little contribution from contamination during the oxidation step.

For this work, chemical wet oxidation was used for direct WSOC measurement: the WSOC containing filtrate after water extraction was collected in Exetainer® vials, later acidified, flushed with helium, and oxidised using $K_2S_2O_8$. The oxidation was performed using a carbonate handling system (CHS, Ionplus AG, Switzerland), which was used in conjunction with a PAL autosampler (CTC Analytics AG, Switzerland) for gas sampling. The procedure is summarised in Figure 30.

1.7 Motivation

Atmospheric particulate matter is a contributor to air pollution and harmful to human health after acute and chronic exposure. Particulate matter further affects the radiative forcing, thus influences the climate on Earth. Curiosity and the desire to understand nature have been deeply rooted in humanity for centuries, if not millennia. Curiosity and a sense of purpose is still a very good intrinsic motivation for a scientist; however, this alone is probably not a sufficient reason for society to fund research in environmental sciences.

Environment and climate protection may be seen by many for the sake of all flora and fauna, however, it is about ensuring the survival of humanity. Major and minor extinction events killing a large fraction of the species have happened several times throughout the last 500 million years. Although many will go extinct, it is very likely that some species would survive and adapt to a much warmer climate, far beyond on what humanity could survive. It should not be forgotten that the primary goal of environmental and climate protection is humankind.

Unlike greenhouse gases that persist decades and longer in the atmosphere, air pollution by atmospheric aerosols affects more local and regional areas on a relatively short time span. Air pollution reduction strategies therefore have visible positive effects. For example, in heavily polluted cities, the sky will be blue more often and when a city is close to mountains, the mountain ranges in the background will be more visible again. These are the directly noticeable positive effects of air pollution reduction. However, other benefits are better measurable than visible, for instance how air pollution affects human health or how crops are affected by air pollution. The reduction in morbidity and mortality may not be immediately noticeable, but long-term studies clearly show a link and causality with the reduction in air pollution. This also allows to put a price tag on pollution for mortality, morbidity, and reduced crop yields. Economic considerations are very important, and benefits of air pollution control measures must outweigh implementation costs several times over to be reasonable. Failure to take targeted and cost-effective action will lead to inefficiencies that will hinder economic growth and possibly the progress of society. Understanding the sources of air pollution is of utmost importance today for targeted and cost-effective air pollution reduction policies. Without sound knowledge of the formation, distribution, and deposition processes of atmospheric aerosols as well as their effect on human health, air pollution measures may be well intended but fail to address the issue appropriately and efficiently.

This work is part of fundamental research in the understanding of carbonaceous aerosols, especially the less understood water soluble and oxalate fractions, and a small puzzle piece among thousands of research articles contributing to this field. In the Chapters 2-4, new methods as well as aerosol filter measurements from various sites are presented and discussed while Chapter 5 summarises the results and provides an outlook for future measurement opportunities.

Chapter 2 discusses an OC/EC separation procedure coupled with chemical wet oxidation for the WSOC fraction. In this work, aerosol filter usage was optimised by utilising the water-extraction eluate for chemical wet oxidation while the water-extracted filter material was used for WINSOC removal and EC measurement. Material not utilised for water extraction was used for TC measurements. Furthermore, we developed a novel thermal-desorption model for the correction of ^{14}C-EC after thermal-optical separation, which should supersede the current linear extrapolation approach. We applied our novel method on selected low-loaded filters from Svalbard, Norway.

Chapter 3 presents a new method for CSRA of oxalate, the major dicarboxylic acid present in atmospheric aerosols. Dicarboxylic acids may be formed by both biogenic and fossil precursors; thus, they might be of interest for CSRA in order to highlight, which sources are actually relevant. Furthermore, dicarboxylic acids have been found in a wide range of sampling sites. We combined an ion chromatographic separation of oxalate with chemical wet oxidation. Our approach simplifies previous CSRA approaches for oxalate and provides low processing blanks. Our method was applied on a selection of aerosol filters from urban and rural sites, namely from rural Råö (Sweden), Mexico City (Mexico), and Delhi (India).

Chapter 4 presents ^{14}C results of an aerosol filter sampling campaign from Troll, Antarctica. Covered mostly by ice, the southernmost continent almost twice the size of Australia is the driest, coldest, and windiest continent with no permanent human population. The remoteness from other land masses and very few sources coupled with the harsh environment makes aerosol filter sampling and analysis very challenging. Nevertheless, we managed to perform ^{14}C analysis of TC, WSOC, and WINSOC on 13 filters each sampled for several weeks in austral winter and summer from February 2016 to September 2018. In this work, the results for austral summer measurements are reported and discussed.

Chapter 5 summarises the major results reported in this thesis and presents some ideas for the improvement of the wet oxidation procedure as well as proposals for the adaptation of the software tools. Further, aerosol filter measurements to continue and underline the results found in this work are proposed.

1.8 References

1. Gupta, T. *Carbon. Carbon* (Springer International Publishing, 2018). doi:10.1007/978-3-319-66405-7.

2. Campbell, N. A. *et al. Biology.* (Pearson, 2008).

3. Mortimer, C. E. & Müller, U. *Chemie: Das Basiswissen der Chemie.* (Georg Thieme Verlag, 2020).

4. Lu, P. J. *et al.* The earliest use of corundum and diamond, in prehistoric China. *Archaeometry* **47**, 1–12 (2005).

5. Lavoisier, A. Premier mémoire sur la destruction du diamant par le feu. *Histoire de l'Académie royale des sciences. Avec les Mémoires de Mathématique & de Physique* (1772).

6. Callister, W. D. *Materials Science and Engineering: An Introduction.* (Wiley, 2007).

7. Bundy, F. P., Hall, H. T., Strong, H. M. & Wentorf, R. H. Man-Made diamonds. *Nature* **176**, 51–55 (1955).

8. Lalwani, G. & Sitharaman, B. Multifunctional Fullerene- and Metallofullerene-Based Nanobiomaterials. *Nano Life* **03**, 1342003 (2013).

9. Li, T. & Dorn, H. C. Biomedical Applications of Metal-Encapsulated Fullerene Nanoparticles. *Small* **13**, 1–13 (2017).

10. Ge, L., Sethi, S., Ci, L., Ajayan, P. M. & Dhinojwala, A. Carbon nanotube-based synthetic gecko tapes. *Proceedings of the National Academy of Sciences* **104**, 10792–10795 (2007).

11. Liu, Y. & Kumar, S. Polymer/Carbon Nanotube Nano Composite Fibers–A Review. *ACS Applied Materials & Interfaces* **6**, 6069–6087 (2014).

12. Hall, C., Tharakan, P., Hallock, J., Cleveland, C. & Jefferson, M. Hydrocarbons and the evolution of human culture. *Nature* **426**, 318–322 (2003).

13. Smil, V. Energy in the Twentieth Century: Resources, Conversions, Costs, Uses, and Consequences. *Annual Review of Energy and the Environment* **25**, 21–51 (2000).

14. BP. *Statistical Review of World Energy 2021.* https://www.bp.com/en/global/corporate/energy-economics/statistical-review-of-world-energy.html (2021).

15. BP. *Statistical Review of World Energy 2020.* https://www.bp.com/content/dam/bp/business-sites/en/global/corporate/pdfs/energy-economics/statistical-review/bp-stats-review-2020-full-report.pdf (2020).

16. Gates, B. *How to Avoid a Climate Disaster: The Solutions We Have and the Breakthroughs We Need.* (2021).

17. Clayden, J., Greeves, N., Warren, S. & Wothers, P. *Organic Chemistry.* (Oxford University Press, 2001).

18. Keim, W. Petrochemicals: Raw material change from fossil to biomass? *Petroleum Chemistry* **50**, 298–304 (2010).

19. *CRC Handbook of Chemistry and Physics (Internet Version 2009).* (CRC Press/Taylor and Francis, 2009).

20. Schuur, E. A. G., Druffel, E. R. M. & Trumbore, S. E. *Radiocarbon and Climate Change - Mechanisms, Applications and Laboratory Techniques.* (Springer, 2016). doi:10.1007/978-3-319-25643-6.

21. Barrimi, M. *et al. Positron Emission Tomography. Encephale* (Springer Berlin Heidelberg, 2013). doi:10.1007/978-3-642-21120-1.

22. Qaim, S. M. *Medical Radionuclide Production. Medical Radionuclide Production* (De Gruyter, 2019). doi:10.1515/9783110604375.

23. Sage, R. F. Phylogenetic Analyses on the Evolution of C_4 Photosynthesis. *New Phytologist* **161**, 341–370 (2004).

24. O'Leary, M. H. Carbon Isotopes in Photosynthesis. *BioScience* **38**, 328–336 (1988).

25. Bathellier, C., Badeck, F.-W. & Ghashghaie, J. *Plant Respiration: Metabolic Fluxes and Carbon Balance.* (Springer International Publishing, 2017). doi:10.1007/978-3-319-68703-2_3.

26. Mook, W. G. Environmental isotopes in the hydrological cycle: Principles and applications, Volume I: Introduction: Theory, Methods, Review. *International Hydrological Programme IHP-V* **1**, 1–165 (2001).

27. Masalaite, A., Holzinger, R., Remeikis, V., Röckmann, T. & Dusek, U. Characteristics, sources and evolution of fine aerosol (PM_1) at urban, coastal and forest background sites in Lithuania. *Atmospheric Environment* **148**, 62–76 (2017).

28. Cao, J. *et al.* Stable carbon isotopes in aerosols from Chinese cities: Influence of fossil fuels. *Atmospheric Environment* **45**, 1359–1363 (2011).

29. Garbaras, A. *et al.* Stable carbon fractionation in size-segregated aerosol particles produced by controlled biomass burning. *Journal of Aerosol Science* **79**, 86–96 (2015).

30. Hobson, K. A. Tracing origins and migration. *Oecologia* **120**, 314–326 (1999).

31. Kim, I. Y., Suh, S. H., Lee, I. K. & Wolfe, R. R. Applications of stable, nonradioactive isotope tracers in in vivo human metabolic research. *Experimental and Molecular Medicine* **48**, (2016).

32. Leal, Y. A., Flores, L. L., Fuentes-Pananá, E. M., Cedillo-Rivera, R. & Torres, J. ^{13}C-Urea Breath Test for the Diagnosis of *Helicobacter pylori* Infection in Children: A Systematic Review and Meta-Analysis. *Helicobacter* **16**, 327–337 (2011).

33. Rhodes, C. N. *et al.* The use of stable carbon isotopes to authenticate claims that poultry have been corn-fed. *Food Chemistry* **118**, 927–932 (2010).

34. Heaton, K., Kelly, S. D., Hoogewerff, J. & Woolfe, M. Verifying the geographical origin of beef: The application of multi-element isotope and trace element analysis. *Food Chemistry* **107**, 506–515 (2008).

35. Osborn, S. G., Vengosh, A., Warner, N. R. & Jackson, R. B. Methane contamination of drinking water accompanying gas-well drilling and hydraulic fracturing. *Proceedings of the National Academy of Sciences* **108**, 8172–8176 (2011).

36. *Analytical Techniques in Forensic Science.* (Wiley, 2021). doi:10.1002/9781119373421.

37. Voglar, G. E., Zavadlav, S., Levanič, T. & Ferlan, M. Measuring techniques for concentration and stable isotopologues of CO_2 in a terrestrial ecosystem: A review. *Earth-Science Reviews* **199**, (2019).

38. Günzler, H. & Williams, A. *Handbook of Analytical Techniques.* (Wiley, 2001). doi:10.1002/9783527618323.

39. Guyader, S. *et al.* Combination of ^{13}C and ^2H SNIF - NMR isotopic fingerprints of vanillin to control its precursors. *Flavour and Fragrance Journal* **34**, 133–144 (2019).

40. Thomas, F. *et al.* Improved characterization of the botanical origin of sugar by carbon-13 SNIF-NMR applied to ethanol. *J Agric Food Chem* **58**, 11580–11585 (2010).

41. Kurie, F. N. D. A New Mode of Disintegration Induced by Neutrons. *Physical Review* **45**, 904–905 (1934).

42. Bonner, T. W. & Brubaker, W. M. The Disintegration of Nitrogen by Neutrons. *Physical Review* **49**, 223–229 (1936).

43. Burcham, W. E. & Goldhaber, M. The disintegration of nitrogen by slow neutrons. *Mathematical Proceedings of the Cambridge Philosophical Society* **32**, 632–636 (1936).

44. Marra, J. F. *Hot Carbon.* (Columbia University Press, 2019). doi:10.7312/marr18670.

45. Mak, J. E., Brenninkmeijer, C. A. M. & Southon, J. R. Direct measurement of the production rate of ^{14}C near Earth's surface. *Geophysical Research Letters* **26**, 3381–3384 (1999).

46. Grootes, P. M. Radiocarbon: Clock and Tracer. *Encyclopedia of Marine Geosciences* (2015) doi:10.1007/978-94-007-6644-0_89-2.

47. Gäggeler, H. & Szidat, S. 5. Nuclear dating: in (ed. Rösch, F.) 133–168 (De Gruyter, 2016). doi:10.1515/9783110221862-006.

48. Kutschera, W. Radiocarbon dating coming of age. *Proceedings of the 50th International Winter Meeting on Nuclear Physics* **160**, 1–21 (2012).

49. Pandow, M., Mackay, C. & Wolfgang, R. The reaction of atomic carbon with oxygen: significance for the natural radio-carbon cycle. *Journal of Inorganic and Nuclear Chemistry* **14**, 153–158 (1960).

50.   Khalil, M. A. K. & Rasmussen, R. A. The global cycle of carbon monoxide: Trends and mass balance. *Chemosphere* **20**, 227–242 (1990).

51.   Comes, F. J. Recycling in the Earth's Atmosphere: The OH Radical—Its Importance for the Chemistry of the Atmosphere and the Determination of Its Concentration. *Angewandte Chemie International Edition in English* **33**, 1816–1826 (1994).

52.   Li, M. *et al.* Tropospheric OH and stratospheric OH and Cl concentrations determined from CH_4, CH_3Cl, and SF_6 measurements. *npj Climate and Atmospheric Science* **1**, 1–7 (2018).

53.   Kutschera, W. & Rom, W. Ötzi, the prehistoric Iceman. *Nuclear Instruments and Methods in Physics Research, Section B: Beam Interactions with Materials and Atoms* **164**, 12–22 (2000).

54.   Suess, H. E. Radiocarbon Concentration in Modern Wood. *Science* **122**, 415–417 (1955).

55.   Stuiver, M. & Quay, P. D. Atmospheric ^{14}C changes resulting from fossil fuel CO_2 release and cosmic ray flux variability. *Earth and Planetary Science Letters* **53**, 349–362 (1981).

56.   Dombrosky, J. A ~1000-year ^{13}C Suess correction model for the study of past ecosystems. *Holocene* **30**, 474–478 (2020).

57.   Rhodes, R. *The Making of the Atomic Bomb.* (Simon and Schuster, 2012).

58.   US Department of Energy. *United States Nuclear Tests: July 1945 through September 1992. DOE/NV-209-Rev 15* (2015).

59.   Yang, X., North, R., Romney, C. & Richards, P. G. Worldwide Nuclear Explosions. *International Geophysics* **81**, 1595–1599 (2003).

60.   Richards, P. G. The history and outlook for seismic monitoring of nuclear explosions in the context of the comprehensive nuclear-test-ban treaty. *Nonproliferation Review* **23**, 287–300 (2016).

61.   Kim, W. Y. & Richards, P. G. North Korean nuclear test: Seismic discrimination at low yield. *Eos (Washington DC)* **88**, 158–161 (2007).

62.   Turnbull, J. C. *et al.* Sixty years of radiocarbon dioxide measurements at Wellington, New Zealand: 1954–2014. *Atmospheric Chemistry and Physics* **17**, 14771–14784 (2017).

63.   Patra, P. K. *et al.* TransCom model simulations of CH_4 and related species: linking transport, surface flux and chemical loss with CH_4 variability in the troposphere and lower stratosphere. *Atmospheric Chemistry and Physics* **11**, 12813–12837 (2011).

64.   Taylor, R. E. & Bar-Yosef, O. *Radiocarbon Dating: An Archaeological Perspective.* (Taylor&Francis, 2016). doi:10.4324/9781315421216.

65.   Levin, I. *et al. Delta $^{14}CO_2$ Record from Vermunt, Austria, February 1959 - June 1983.* (1994) doi:10.3334/CDIAC/ATG.028.

66. Ruben, S. & Kamen, M. D. Long-Lived Radioactive Carbon: C14. *Physical Review* **59**, 349–354 (1941).

67. Reid, A. F., Dunning, J. R., Weinhouse, S. & Grosse, A. v. Half-Life of C14. *Physical Review* **70**, 431–431 (1946).

68. Norris, L. D. & Inghram, M. G. Half-Life Determination of Carbon (14) with a Mass Spectrometer and Low Absorption Counter. *Physical Review* **70**, 772–773 (1946).

69. Engelkemeir, A. G., Hamill, W. H., Inghram, M. G. & Libby, W. F. The Half-Life of Radiocarbon (C14). *Physical Review* **75**, 1825–1833 (1949).

70. Engelkemeir, A. G. & Libby, W. F. End and wall corrections for absolute beta-counting in gas counters. *Review of Scientific Instruments* **21**, 550–554 (1950).

71. Jones, W. M. A Determination of the Half-Life of Carbon 14. *Physical Review* **76**, 885–889 (1949).

72. Miller, W. W. *et al.* The Half-Life of Carbon Fourteen and a Comparison of Gas Phase Counter Methods. *Physical Review* **77**, 714–715 (1950).

73. Libby, W. F. *Radiocarbon dating.* (University of Chicago Press, 1952).

74. Currie, L. A. The remarkable metrological history of radiocarbon dating [II]. *Journal of Research of the National Institute of Standards and Technology* **109**, 185 (2004).

75. Godwin, H. Half-life of Radiocarbon. *Nature* **195**, 984–984 (1962).

76. Kutschera, W. Applications of accelerator mass spectrometry. *International Journal of Mass Spectrometry* **349–350**, 203–218 (2013).

77. Reimer, P. J., Brown, T. A. & Reimer, R. W. Discussion: Reporting and Calibration of Post-Bomb 14C Data. *Radiocarbon* **46**, 1299–1304 (2004).

78. Arnold, J. R. & Libby, W. F. Age Determinations by Radiocarbon Content: Checks with Samples of Known Age. *Science* **110**, 678–680 (1949).

79. Bassham, J. A., Barker, S. A., Calvin, M. & Quarck, U. C. Intermediates in the photosynthetic cycle. *Biochimica et Biophysica Acta* **21**, 376–377 (1956).

80. Nielsen, J. *et al.* Eye lens radiocarbon reveals centuries of longevity in the Greenland shark (Somniosus microcephalus). *Science* **353**, 702–704 (2016).

81. Monastersky, R. Global carbon dioxide levels near worrisome milestone. *Nature* **497**, 13–14 (2013).

82. Levin, I., Hammer, S., Kromer, B. & Meinhardt, F. Radiocarbon observations in atmospheric CO_2: Determining fossil fuel CO_2 over Europe using Jungfraujoch observations as background. *Science of The Total Environment* **391**, 211–216 (2008).

83. Espic, C. *et al.* Compound-Specific Radiocarbon Analysis of Atmospheric Methane: A New Preconcentration and Purification Setup. *Radiocarbon* **61**, 1461–1476 (2019).

84.   Petrenko, V. *et al.* A New Method for Analyzing ^{14}C of Methane in Ancient Air Extracted from Glacial Ice. *Radiocarbon* **50**, 53–73 (2008).

85.   Hmiel, B. *et al.* Preindustrial $^{14}CH_4$ indicates greater anthropogenic fossil CH_4 emissions. *Nature* **578**, 409–412 (2020).

86.   Etheridge, D. M. *et al.* Historical CO_2 Records from the Law Dome DE08, DE08-2, and DSS Ice Cores (1006 A.D.-1978 A.D). Preprint at https://doi.org/10.3334/CDIAC/ATG.011 (1998).

87.   Tans, P. & Keeling, R. Trends in Atmospheric Carbon Dioxide. *NOAA/GML, Scripps Institution of Oceanography* gml.noaa.gov/ccgg/trends/ (2022).

88.   Etheridge, D. M., Steele, L. P., Francey, R. J. & Langenfelds, R. L. Atmospheric methane between 1000 A.D. and present: Evidence of anthropogenic emissions and climatic variability. *Journal of Geophysical Research: Atmospheres* **103**, 15979–15993 (1998).

89.   Dlugokencky, E. Global CH_4 Monthly Means. *NOAA/ESRL* www.esrl.noaa.gov/gmd/ccgg/trends_ch4/ (2022).

90.   Jackson, R. B. *et al.* Atmospheric methane removal: a research agenda. *Philosophical Transactions of the Royal Society A: Mathematical, Physical and Engineering Sciences* **379**, 20200454 (2021).

91.   Schiermeier, Q. Global methane levels soar to record high. *Nature* (2020) doi:10.1038/d41586-020-02116-8.

92.   Jacob, D. J. *et al.* Satellite observations of atmospheric methane and their value for quantifying methane emissions. *Atmospheric Chemistry and Physics* **16**, 14371–14396 (2016).

93.   Nisbet, E. & Weiss, R. Top-Down Versus Bottom-Up. *Science* **328**, 1241–1243 (2010).

94.   Zazzeri, G., Yeomans, E. A. & Graven, H. D. Global and regional emissions of radiocarbon from nuclear power plants from 1972 to 2016. *Radiocarbon* **60**, 1068–1081 (2018).

95.   Harmsen, M. *et al.* The role of methane in future climate strategies: mitigation potentials and climate impacts. *Climatic Change* **163**, 1409–1425 (2020).

96.   Schuur, E. A. G. *et al.* Climate change and the permafrost carbon feedback. *Nature* **520**, 171–179 (2015).

97.   Vuong, L. T. *et al.* Opportunities in low-level radiocarbon microtracing: applications and new technology. *Future Science OA* **2**, fso.15.74 (2016).

98.   Spracklin, D. K., Chen, D., Bergman, A. J., Callegari, E. & Obach, R. S. Mini-Review: Comprehensive Drug Disposition Knowledge Generated in the Modern Human Radiolabeled ADME Study. *CPT: Pharmacometrics and Systems Pharmacology* **9**, 428–434 (2020).

99.   Povinec, P. P. *et al.* Radiocarbon and ^{137}Cs dating of wines. *Journal of Environmental Radioactivity* **217**, 106205 (2020).

100. Asenstorfer, R. E., Jones, G. P., Laurence, G. & Zoppi, U. Authentication of Red Wine Vintage Using Bomb-Pulse [14]C. in *ACS Symposium Series* vol. 1081 89–99 (2011).

101. Fahrni, S. M., Fuller, B. T. & Southon, J. R. Angel's Share Combats Wine Fraud: [14]C Dating of Wine without Opening the Bottle. *Analytical Chemistry* **87**, 8646–8650 (2015).

102. Cook, G. T., Dunbar, E., Tripney, B. G. & Fabel, D. Using Carbon Isotopes to Fight the Rise in Fraudulent Whisky. *Radiocarbon* **62**, 51–62 (2020).

103. Buchholz, B. A., Sarachine, M. J. & Zermeño, P. Establishing natural product content with the natural radiocarbon signature. *ACS Symposium Series* **1081**, 27–37 (2011).

104. Gershon, H., Lykkeberg, A., Goren, F. & Mason, S. Identifying Fraudulent Natural Products: A Perspective on the Application of Carbon-14 Analysis. *Journal of Agricultural and Food Chemistry* **67**, 13393–13399 (2019).

105. Hajdas, I. *et al.* Bomb ^{14}C on paper and detection of the Forged Paintings of T'ang Haywen. *Radiocarbon* **61**, 1905–1912 (2019).

106. Hendriks, L. *et al.* Combined [14]C Analysis of Canvas and Organic Binder for Dating a Painting. *Radiocarbon* **60**, 207–218 (2018).

107. Uno, K. T. *et al.* Bomb-curve radiocarbon measurement of recent biologic tissues and applications to wildlife forensics and stable isotope (paleo)ecology. *Proceedings of the National Academy of Sciences* **110**, 11736–11741 (2013).

108. Cerling, T. E. *et al.* Radiocarbon dating of seized ivory confirms rapid decline in African elephant populations and provides insight into illegal trade. *Proceedings of the National Academy of Sciences* **113**, 13330–13335 (2016).

109. Alexander, W. R., Reijonen, H. M. & McKinley, I. G. Natural analogues: studies of geological processes relevant to radioactive waste disposal in deep geological repositories. *Swiss Journal of Geosciences* **108**, 75–100 (2015).

110. Nagra. *Waste Management Programme 2016 of the Waste Producers. Nagra Technical Report NTB 16-01E.* (2016).

111. Yim, M.-S. & Caron, F. Life cycle and management of carbon-14 from nuclear power generation. *Progress in Nuclear Energy* **48**, 2–36 (2006).

112. Guillemot, T. *et al.* Carbon-14 release and speciation during corrosion of irradiated steel under radioactive waste disposal conditions. *Science of The Total Environment* **817**, 152596 (2022).

113. Guillemot, T. *et al. Development of Analytical Methods for the Detection of ^{14}C-bearing Carbon Compounds at Ultra-low Concentrations. Nagra Working Report NAB 21-03.* (2021).

114. Geiger, H. & Müller, W. Technische Bemerkungen zum Elektronenzäherohr. *Zeitschrift für Physik* **30**, 489 (1929).

115. Loveland, W. D., Morrissey, D. J. & Seaborg, G. T. *Modern Nuclear Chemistry.* (John Wiley & Sons, Inc., 2017). doi:10.1002/9781119348450.

116. Libby, W. F. Radioactivity of neodymium and samarium. *Physical Review* **46**, 196–204 (1934).

117. Libby, W. F. & Lee, D. D. Energies of the soft beta-radiations of rubidium and other bodies. Method for their determination. *Physical Review* **55**, 245–251 (1939).

118. Povinec, P. P., Litherland, A. E. & von Reden, K. F. Developments in Radiocarbon Technologies: From the Libby Counter to Compound-Specific AMS Analyses. *Radiocarbon* **51**, 45–78 (2009).

119. Mook, W. G. International Comparison of Proportional Gas Counters for ^{14}C Activity Measurements. *Radiocarbon* **25**, 475–484 (1983).

120. Theodórsson, P. Quantifying Background Components of Low-Level Gas Proportional Counters. *Radiocarbon* **34**, 420–427 (1992).

121. de Vries, Hl. & Barendsen, G. W. Radio-carbon dating by a proportional counter filled with carbondioxide. *Physica* **19**, 987–1003 (1953).

122. Povinec, P. P. *et al.* Radiocarbon in the Atmosphere of the Žlkovce Monitoring Station of the Bohunice NPP: 25 Years of Continuous Monthly Measurements. *Radiocarbon* **57**, 355–362 (2015).

123. Arnold, J. R. Scintillation Counting of Natural Radiocarbon: I. The Counting Method. *Science* **119**, 155–157 (1954).

124. Passo, C. J. & Cook, G. T. *Handbook of Environmental Liquid Scintillation Spectrometry: A Compilation of Theory and Methods.* (Packard Instrument Company, 1994).

125. Hellborg, R. & Skog, G. Accelerator mass spectrometry. *Mass Spectrometry Reviews* **27**, 398–427 (2008).

126. Elmore, D. & Phillips, F. M. Accelerator Mass Spectrometry for Measurement of Long-Lived Radioisotopes. *Science* **236**, 543–550 (1987).

127. Alvarez, L. W. & Cornog, R. Helium and Hydrogen of Mass 3. *Physical Review* **56**, 613–613 (1939).

128. Mueller, R. A. Radioisotope Dating with a Cyclotron. *Science* **196**, 489–494 (1977).

129. Mueller, R. A., Stephenson, E. J. & Mast, T. S. Radioisotope Dating with an Accelerator: A Blind Measurement. *Science* **201**, 347–348 (1978).

130. Purser, K. H. Ultra-sensitive spectrometer for making mass and elemental analyses (United States Patent US4037100A). (1977).

131.   Bennett, C. L. *et al.* Radiocarbon Dating Using Electrostatic Accelerators: Negative Ions Provide the Key. *Science* **198**, 508–510 (1977).

132.   Nelson, D. E., Korteling R. G. & Stoot, W. R. Carbon-14: Direct Detection at Natural Concentrations. *Science* **198**, 507–508 (1977).

133.   INTERNATIONAL ATOMIC ENERGY AGENCY. *Isotope Methods for Dating Old Groundwater, Non-serial Publications.* (2013).

134.   Bentley, H. W. Some comments on the use of chlorine-36 for dating very old ground water. in *Workshop on Dating Old Ground Water. Dep. Hydrol. Water Resour., Univ. of Arizona, Tucson, Ariz., Rep. Y/OWI/SUB-78/55412* 102–111 (1978).

135.   Naylor, H. *et al.* Determination of ^{36}Cl isotopic ratios. in *Proc. 1st Conf. On Radiocarbon Dating with Accelerators, University of Rochester, April 20* 360 (1978).

136.   Elmore, D. *et al.* Analysis of ^{36}Cl in environmental water samples using an electrostatic accelerator. *Nature* **277**, 22–25 (1979).

137.   Kutschera, W. Accelerator mass spectrometry: state of the art and perspectives. *Advances in Physics: X* **1**, 570–595 (2016).

138.   Purser, K. H., Liebert, R. B. & Russo, C. J. Macs: An Accelerator-Based Radioisotope Measuring System. *Radiocarbon* **22**, 794–806 (1980).

139.   Synal, H. A., Stocker, M. & Suter, M. MICADAS: A new compact radiocarbon AMS system. *Nuclear Instruments and Methods in Physics Research, Section B: Beam Interactions with Materials and Atoms* **259**, 7–13 (2007).

140.   Ionplus AG. https://www.ionplus.ch (2021).

141.   Seiler, M., Maxeiner, S., Wacker, L. & Synal, H. A. Status of mass spectrometric radiocarbon detection at ETHZ. *Nuclear Instruments and Methods in Physics Research, Section B: Beam Interactions with Materials and Atoms* **361**, 245–249 (2015).

142.   de Maria, D. Towards a new horizon for biomedical applications of AMS. (2021). doi:10.3929/ethz-b-000497563.

143.   Schulze-König, T., Seiler, M., Suter, M., Wacker, L. & Synal, H. A. The dissociation of ^{13}CH and ^{12}CH$_2$ molecules in He and N$_2$ at beam energies of 80-250 keV and possible implications for radiocarbon mass spectrometry. *Nuclear Instruments and Methods in Physics Research, Section B: Beam Interactions with Materials and Atoms* **269**, 34–39 (2011).

144.   Synal, H. A. Developments in accelerator mass spectrometry. *International Journal of Mass Spectrometry* **349–350**, 192–202 (2013).

145. Freeman, S. P. H. T., Shanks, R. P., Donzel, X. & Gaubert, G. Radiocarbon positive-ion mass spectrometry. *Nuclear Instruments and Methods in Physics Research, Section B: Beam Interactions with Materials and Atoms* **361**, 229–232 (2015).

146. NEC. Positive Ion Mass Spectrometry (PIMS) Systems. https://www.pelletron.com/products/positive-ion-mass-spectrometry-pims-systems/ (2021).

147. *Cavity Ring-Down Spectroscopy: Techniques and Applications.* (John Wiley & Sons, Ltd, 2009). doi:10.1002/9781444308259.

148. Galli, I. *et al.* Molecular gas sensing below parts per trillion: Radiocarbon-dioxide optical detection. *Physical Review Letters* **107**, 1–4 (2011).

149. McCartt, A. D., Ognibene, T., Bench, G. & Turteltaub, K. Measurements of carbon-14 with cavity ring-down spectroscopy. *Nuclear Instruments and Methods in Physics Research, Section B: Beam Interactions with Materials and Atoms* **361**, 277–280 (2015).

150. McCartt, A. D., Ognibene, T. J., Bench, G. & Turteltaub, K. W. Quantifying Carbon-14 for Biology Using Cavity Ring-Down Spectroscopy. *Analytical Chemistry* **88**, 8714–8719 (2016).

151. Sonnenschein, V. *et al.* A cavity ring-down spectrometer for study of biomedical radiocarbon-labeled samples. *Journal of Applied Physics* **124**, 033101 (2018).

152. Kim, A. *et al.* Human ADME for YH12852 using wavelength scanning cavity ring-down spectroscopy (WS-CRDS) after a low radioactivity dose. *Bioanalysis* **12**, 87–98 (2020).

153. Lehmuskoski, J. *et al.* On-Line Monitoring of Radiocarbon Emissions in a Nuclear Facility with Cavity Ring-Down Spectroscopy. *Analytical Chemistry* **93**, 16096–16104 (2021).

154. Murnick, D. E., Dogru, O. & Ilkmen, E. Intracavity Optogalvanic Spectroscopy. An Analytical Technique for [14]C Analysis with Subattomole Sensitivity. *Analytical Chemistry* **80**, 4820–4824 (2008).

155. Murnick, D. E. & Peer, B. J. Laser-based analysis of carbon isotope ratios. *Science* **263**, 945–947 (1994).

156. Paul, D. & Meijer, H. A. J. Intracavity OptoGalvanic Spectroscopy Not Suitable for Ambient Level Radiocarbon Detection. *Analytical Chemistry* **87**, 9025–9032 (2015).

157. Persson, A. & Salehpour, M. Intracavity optogalvanic spectroscopy: Is there any evidence of a radiocarbon signal? *Nuclear Instruments and Methods in Physics Research, Section B: Beam Interactions with Materials and Atoms* **361**, 8–12 (2015).

158. Carson, C. G. *et al.* Invalidation of the intracavity optogalvanic method for radiocarbon detection. *Radiocarbon* **58**, 213–225 (2016).

159. Boucher, O. *Atmospheric Aerosols: Properties and Climate Impacts.* (Springer, 2015). doi:10.1007/978-94-017-9649-1.

160. Harris, A. *et al.* Influenza virus pleiomorphy characterized by cryoelectron tomography. *Proceedings of the National Academy of Sciences* **103**, 19123–19127 (2006).

161. Loussouarn, G. *et al.* Diversity in human hair growth, diameter, colour and shape. An in vivo study on young adults from 24 different ethnic groups observed in the five continents. *European Journal of Dermatology* **26**, 144–154 (2016).

162. Erickson, H. P. Size and Shape of Protein Molecules at the Nanometer Level Determined by Sedimentation, Gel Filtration, and Electron Microscopy. *Biological Procedures Online* **11**, 32–51 (2009).

163. World Health Organization. *WHO Air quality guidelines for particulate matter, ozone, nitrogen dioxide and sulfur dioxide: global update 2005: summary of risk assessment.* (WHO Press, 2006).

164. *Atmospheric Aerosols.* (Wiley-VCH Verlag GmbH & Co. KGaA, 2017). doi:10.1002/9783527336449.

165. Schlesinger, W. H. & Bernhardt, E. S. The Atmosphere. in *Biogeochemistry* 51–97 (Elsevier, 2020). doi:10.1016/B978-0-12-814608-8.00003-7.

166. Stevenson, D. S. *et al.* Trends in global tropospheric hydroxyl radical and methane lifetime since 1850 from AerChemMIP. *Atmospheric Chemistry and Physics* **20**, 12905–12920 (2020).

167. Glasius, M. & Goldstein, A. H. Recent Discoveries and Future Challenges in Atmospheric Organic Chemistry. *Environmental Science & Technology* **50**, 2754–2764 (2016).

168. Went, F. W. Blue Hazes in the Atmosphere. *Nature* **187**, 641–643 (1960).

169. Docherty, K. S. *et al.* Apportionment of Primary and Secondary Organic Aerosols in Southern California during the 2005 Study of Organic Aerosols in Riverside (SOAR-1). *Environmental Science & Technology* **42**, 7655–7662 (2008).

170. Pöschl, U. Atmospheric Aerosols: Composition, Transformation, Climate and Health Effects. *Angewandte Chemie International Edition* **44**, 7520–7540 (2005).

171. Bond, T. C. *et al.* Bounding the role of black carbon in the climate system: A scientific assessment. *Journal of Geophysical Research Atmospheres* **118**, 5380–5552 (2013).

172. Petzold, A. *et al.* Recommendations for reporting "black carbon" measurements. *Atmospheric Chemistry and Physics* **13**, 8365–8379 (2013).

173. Lack, D. A., Moosmüller, H., McMeeking, G. R., Chakrabarty, R. K. & Baumgardner, D. Characterizing elemental, equivalent black, and refractory black carbon aerosol particles: a review of techniques, their limitations and uncertainties. *Analytical and Bioanalytical Chemistry* **406**, 99–122 (2014).

174. Szidat, S. [14]C Research at the Laboratory for the Analysis of Radiocarbon with AMS (LARA), University of Bern. *CHIMIA* **74**, 1010 (2020).

175. Zenker, K. *et al.* δ¹³C signatures of organic aerosols: Measurement method evaluation and application in a source study. *Journal of Aerosol Science* **145**, 105534 (2020).

176. Zhang, Y. L. *et al.* On the isolation of OC and EC and the optimal strategy of radiocarbon-based source apportionment of carbonaceous aerosols. *Atmospheric Chemistry and Physics* **12**, 10841–10856 (2012).

177. Zheng, G., He, K., Duan, F., Cheng, Y. & Ma, Y. Measurement of humic-like substances in aerosols: A review. *Environmental Pollution* **181**, 301–314 (2013).

178. Falkovich, A. H. *et al.* Low molecular weight organic acids in aerosol particles from Rondônia, Brazil, during the biomass-burning, transition and wet periods. *Atmospheric Chemistry and Physics* **5**, 781–797 (2005).

179. Kawamura, K. & Bikkina, S. A review of dicarboxylic acids and related compounds in atmospheric aerosols: Molecular distributions, sources and transformation. *Atmospheric Research* **170**, 140–160 (2016).

180. Xu, B. *et al.* Compound-Specific Radiocarbon Analysis of Low Molecular Weight Dicarboxylic Acids in Ambient Aerosols Using Preparative Gas Chromatography: Method Development. *Environmental Science & Technology Letters* **8**, 135–141 (2021).

181. Lim, Y. B., Tan, Y., Perri, M. J., Seitzinger, S. P. & Turpin, B. J. Aqueous chemistry and its role in secondary organic aerosol (SOA) formation. *Atmospheric Chemistry and Physics* **10**, 10521–10539 (2010).

182. Na, K., Sawant, A. A., Song, C. & Cocker, D. R. Primary and secondary carbonaceous species in the atmosphere of Western Riverside County, California. *Atmospheric Environment* **38**, 1345–1355 (2004).

183. Jaffrezo, J. L., Aymoz, G., Delaval, C. & Cozic, J. Seasonal variations of the water soluble organic carbon mass fraction of aerosol in two valleys of the French Alps. *Atmospheric Chemistry and Physics* **5**, 2809–2821 (2005).

184. Kawamura, K., Kasukabe, H. & Barrie, L. A. Secondary formation of water-soluble organic acids and α-dicarbonyls and their contributions to total carbon and water-soluble organic carbon: Photochemical aging of organic aerosols in the Arctic spring. *Journal of Geophysical Research Atmospheres* **115**, (2010).

185. Jimenez, J. L. *et al.* Evolution of Organic Aerosols in the Atmosphere. *Science* **326**, 1525–1529 (2009).

186. Hsieh, L., Kuo, S., Chen, C. & Tsai, Y. I. Origin of low-molecular-weight dicarboxylic acids and their concentration and size distribution variation in suburban aerosol. *Atmospheric Environment* **41**, 6648–6661 (2007).

187.   Hsieh, L.-Y., Chen, C.-L., Wan, M.-W., Tsai, C.-H. & Tsai, Y. I. Speciation and temporal characterization of dicarboxylic acids in PM$_{2.5}$ during a PM episode and a period of non-episodic pollution. *Atmospheric Environment* **42**, 6836–6850 (2008).

188.   Yang, L., Ray, M. B. & Yu, L. E. Photooxidation of dicarboxylic acids—Part II: Kinetics, intermediates and field observations. *Atmospheric Environment* **42**, 868–880 (2008).

189.   Ho, K. F. *et al.* Dicarboxylic acids, ketocarboxylic acids, α-dicarbonyls, fatty acids, and benzoic acid in urban aerosols collected during the 2006 Campaign of Air Quality Research in Beijing (CAREBeijing-2006). *Journal of Geophysical Research Atmospheres* **115**, 1–14 (2010).

190.   Cao, F. *et al.* Chemical characteristics of dicarboxylic acids and related organic compounds in PM$_{2.5}$ during biomass-burning and non-biomass-burning seasons at a rural site of Northeast China. *Environmental Pollution* **231**, 654–662 (2017).

191.   Limbeck, A., Puxbaum, H., Otter, L. & Scholes, M. C. Semivolatile behavior of dicarboxylic acids and other polar organic species at a rural background site (Nylsvley, RSA). *Atmospheric Environment* **35**, 1853–1862 (2001).

192.   Narukawa, M., Kawamura, K., Li, S. M. & Bottenheim, J. W. Dicarboxylic acids in the Arctic aerosols and snowpacks collected during ALERT 2000. *Atmospheric Environment* **36**, 2491–2499 (2002).

193.   Kawamura, K., Seméré, R., Imai, Y., Fujii, Y. & Hayashi, M. Water soluble dicarboxylic acids and related compounds in Antarctic aerosols. *Journal of Geophysical Research Atmospheres* **101**, 18721–18728 (1996).

194.   Bikkina, S., Kawamura, K., Sakamoto, Y. & Hirokawa, J. Low molecular weight dicarboxylic acids, oxocarboxylic acids and α-dicarbonyls as ozonolysis products of isoprene: Implication for the gaseous-phase formation of secondary organic aerosols. *Science of The Total Environment* **769**, 144472 (2021).

195.   Kroll, J. H., Ng, N. L., Murphy, S. M., Flagan, R. C. & Seinfeld, J. H. Secondary organic aerosol formation from isoprene photooxidation under high-NO$_x$ conditions. *Geophysical Research Letters* **32**, 1–4 (2005).

196.   Kroll, J. H., Ng, N. L., Murphy, S. M., Flagan, R. C. & Seinfeld, J. H. Secondary Organic Aerosol Formation from Isoprene Photooxidation. *Environmental Science & Technology* **40**, 1869–1877 (2006).

197.   Kleindienst, T. E., Lewandowski, M., Offenberg, J. H., Jaoui, M. & Edney, E. O. Ozone-isoprene reaction: Re-examination of the formation of secondary organic aerosol. *Geophysical Research Letters* **34**, L01805 (2007).

198.   Edney, E. O. *et al.* Formation of 2-methyl tetrols and 2-methylglyceric acid in secondary organic aerosol from laboratory irradiated isoprene/NO_X/SO_2/air mixtures and their detection in ambient $PM_{2.5}$ samples collected in the eastern United States. *Atmospheric Environment* **39**, 5281–5289 (2005).

199.   Guenther, A. *et al.* Estimates of global terrestrial isoprene emissions using MEGAN (Model of Emissions of Gases and Aerosols from Nature). *Atmospheric Chemistry and Physics* **6**, 3181–3210 (2006).

200.   Sharkey, T. D. & Yeh, S. Isoprene emissions from plants. *Annual Review of Plant Physiology and Plant Molecular Biology* **52**, 407–436 (2001).

201.   Carlton, A. G., Wiedinmyer, C. & Kroll, J. H. A review of Secondary Organic Aerosol (SOA) formation from isoprene. *Atmospheric Chemistry and Physics* **9**, 4987–5005 (2009).

202.   Carlton, A. G. *et al.* Atmospheric oxalic acid and SOA production from glyoxal: Results of aqueous photooxidation experiments. *Atmospheric Environment* **41**, 7588–7602 (2007).

203.   Herrmann, H. *et al.* Tropospheric Aqueous-Phase Chemistry: Kinetics, Mechanisms, and Its Coupling to a Changing Gas Phase. *Chemical Reviews* **115**, 4259–4334 (2015).

204.   Warneck, P. In-cloud chemistry opens pathway to the formation of oxalic acid in the marine atmosphere. *Atmospheric Environment* **37**, 2423–2427 (2003).

205.   Kawamura, Kimitaka. & Kaplan, I. R. Motor exhaust emissions as a primary source for dicarboxylic acids in Los Angeles ambient air. *Environmental Science & Technology* **21**, 105–110 (1987).

206.   Bock, N., Baum, M. M., Anderson, M. B., Pesta, A. & Northrop, W. F. Dicarboxylic Acid Emissions from Aftertreatment Equipped Diesel Engines. *Environmental Science and Technology* **51**, 13036–13043 (2017).

207.   Aggarwal, S. G. & Kawamura, K. Molecular distributions and stable carbon isotopic compositions of dicarboxylic acids and related compounds in aerosols from Sapporo, Japan: Implications for photochemical aging during long-range atmospheric transport. *Journal of Geophysical Research* **113**, D14301 (2008).

208.   Fahrni, S. M. *et al.* A Preparative 2D-Chromatography Method for Compound-Specific Radiocarbon Analysis of Dicarboxylic Acids in Aerosols. *Radiocarbon* **52**, 752–760 (2010).

209.   Lelieveld, J., Evans, J. S., Fnais, M., Giannadaki, D. & Pozzer, A. The contribution of outdoor air pollution sources to premature mortality on a global scale. *Nature* **525**, 367–371 (2015).

210.   World Bank. DataBank – World Development Indicators. https://databank.worldbank.org/reports.aspx?source=world-development-indicators.

211.   Cohen, A. J. *et al.* The Global Burden of Disease Due to Outdoor Air Pollution. *Journal of Toxicology and Environmental Health, Part A* **68**, 1301–1307 (2005).

212. Forouzanfar *et al.* Global, regional, and national comparative risk assessment of 79 behavioural, environmental and occupational, and metabolic risks or clusters of risks, 1990–2015: a systematic analysis for the Global Burden of Disease Study 2015. *The Lancet* **388**, 1659–1724 (2016).

213. Burnett, R. *et al.* Global estimates of mortality associated with long-term exposure to outdoor fine particulate matter. *Proceedings of the National Academy of Sciences* **115**, 9592–9597 (2018).

214. Jeuland, M., Pattanayak, S. K. & Bluffstone, R. The Economics of Household Air Pollution. *Annual Review of Resource Economics* **7**, 81–108 (2015).

215. Landrigan, P. J. Air pollution and health. *The Lancet Public Health* **2**, e4–e5 (2017).

216. Logue, J. M., Klepeis, N. E., Lobscheid, A. B. & Singer, B. C. Pollutant Exposures from Natural Gas Cooking Burners: A Simulation-Based Assessment for Southern California. *Environmental Health Perspectives* **122**, 43–50 (2014).

217. Berkemeier, T. Kinetic modelling of secondary organic aerosol (SOA) formation: connecting the data points. *International Aerosol Modeling Algorithms Conference* Preprint at (2019).

218. Vincent, D. Particules en suspension dans l'air : leurs effets sur la santé. *Encyclopédie de l'Environnement* https://www.encyclopedie-environnement.org/sante/particules-air-effets-sante/ (2019).

219. Schlesinger, R. B., Kunzli, N., Hidy, G. M., Gotschi, T. & Jerrett, M. The Health Relevance of Ambient Particulate Matter Characteristics: Coherence of Toxicological and Epidemiological Inferences. *Inhalation Toxicology* **18**, 95–125 (2006).

220. Kelly, F. J. & Fussell, J. C. Toxicity of airborne particles—established evidence, knowledge gaps and emerging areas of importance. *Philosophical Transactions of the Royal Society A: Mathematical, Physical and Engineering Sciences* **378**, 20190322 (2020).

221. Bates, J. T. *et al.* Reactive Oxygen Species Generation Linked to Sources of Atmospheric Particulate Matter and Cardiorespiratory Effects. *Environmental Science and Technology* **49**, 13605–13612 (2015).

222. Lakey, P. S. J. *et al.* Chemical exposure-response relationship between air pollutants and reactive oxygen species in the human respiratory tract. *Scientific Reports* **6**, 32916 (2016).

223. Charrier, J. G. & Anastasio, C. Impacts of antioxidants on hydroxyl radical production from individual and mixed transition metals in a surrogate lung fluid. *Atmospheric Environment* **45**, 7555–7562 (2011).

224. Wei, J., Fang, T., Lakey, P. S. J. & Shiraiwa, M. Iron-Facilitated Organic Radical Formation from Secondary Organic Aerosols in Surrogate Lung Fluid. *Environmental Science & Technology* **56**, 7234–7243 (2022).

225. Jung, H., Guo, B., Anastasio, C. & Kennedy, I. M. Quantitative measurements of the generation of hydroxyl radicals by soot particles in a surrogate lung fluid. *Atmospheric Environment* **40**, 1043–1052 (2006).

226. Saffari, A., Daher, N., Shafer, M. M., Schauer, J. J. & Sioutas, C. Global Perspective on the Oxidative Potential of Airborne Particulate Matter: A Synthesis of Research Findings. *Environmental Science and Technology* **48**, 7576–7583 (2014).

227. Daellenbach, K. R. *et al.* Sources of particulate-matter air pollution and its oxidative potential in Europe. *Nature* **587**, 414–419 (2020).

228. Calas, A. *et al.* The importance of simulated lung fluid (SLF) extractions for a more relevant evaluation of the oxidative potential of particulate matter. *Scientific Reports* **7**, 11617 (2017).

229. Calas, A. *et al.* Comparison between five acellular oxidative potential measurement assays performed with detailed chemistry on PM_{10} samples from the city of Chamonix (France). *Atmospheric Chemistry and Physics* **18**, 7863–7875 (2018).

230. Brown, J. S., Gordon, T., Price, O. & Asgharian, B. Thoracic and respirable particle definitions for human health risk assessment. *Particle and Fibre Toxicology* **10**, (2013).

231. Schraufnagel, D. E. The health effects of ultrafine particles. *Experimental & Molecular Medicine* **52**, (2020).

232. Brimblecombe, P. Air Pollution and Health History. in *Air Pollution and Health* (Elsevier, 1999). doi:10.1016/B978-012352335-8/50077-6.

233. Warde, P. *Energy Consumption in England & Wales, 1560-2000.* (Consiglio Nazionale delle Ricerche Istituto di Studi sulle Società del Mediterraneo, 2007).

234. Rhodes, R. *Energy: A Human History.* (Simon & Schuster, 2018).

235. *The Basic Environmental History.* (Springer International Publishing, 2014). doi:10.1007/978-3-319-09180-8.

236. Wilkins, E. T. Air pollution aspects of the London fog of December 1952. *Quarterly Journal of the Royal Meteorological Society* **80**, 267–271 (1954).

237. Bell, M. L. & Davis, D. L. Reassessment of the Lethal London Fog of 1952: Novel Indicators of Acute and Chronic Consequences of Acute Exposure to Air Pollution. *Environmental Health Perspectives* **109**, (2001).

238. The Clean Air Act, 1956. *Nature* **182**, 226 (1958).

239. Ritchie, H. & Roser, M. Energy. *Our World in Data* (2020).

240. Sovacool, B. K. *et al.* Balancing safety with sustainability: assessing the risk of accidents for modern low-carbon energy systems. *Journal of Cleaner Production* **112**, 3952–3965 (2016).

241.   Markandya, A. & Wilkinson, P. Electricity generation and health. *The Lancet* **370**, 979–990 (2007).

242.   Safari, A., Das, N., Langhelle, O., Roy, J. & Assadi, M. Natural gas: A transition fuel for sustainable energy system transformation? *Energy Science & Engineering* **7**, 1075–1094 (2019).

243.   Jarvis, S., Deschenes, O. & Jha, A. *The Private and External Costs of Germany's Nuclear Phase-Out.* http://www.nber.org/papers/w26598.pdf (2019) doi:10.3386/w26598.

244.   Boucher, O. *et al. Clouds and Aerosols. Climate Change 2013: The Physical Science Basis. Contribution of Working Group I to the Fifth Assessment Report of the Intergovernmental Panel on Climate Change [Stocker, T.F., D. Qin, G.-K. Plattner, M. Tignor, S.K. Allen, J. Boschung, A. Nauels, Y. Xia,* (Cambridge University Press, 2013).

245.   IPCC. *Climate Change 2021: The Physical Science Basis. Contribution of Working Group I to the Sixth Assessment Report of the Intergovernmental Panel on Climate Change. Cambridge University Press* (2021).

246.   Hansen, J. & Nazarenko, L. Soot climate forcing via snow and ice albedos. *Proceedings of the National Academy of Sciences* **101**, 423–428 (2004).

247.   EPA. National Air Quality: Status and Trends of Key Air Pollutants. https://www.epa.gov/air-trends (2018).

248.   Smil, V. *Energy and Civilization: A History.* (MIT Press, 2017).

249.   Sofiev, M. *et al.* Cleaner fuels for ships provide public health benefits with climate tradeoffs. *Nature Communications* **9**, 406 (2018).

250.   Crutzen, P. J. Albedo Enhancement by Stratospheric Sulfur Injections: A Contribution to Resolve a Policy Dilemma? *Climatic Change* **77**, 211 (2006).

251.   Cohen, J. *et al.* Divergent consensuses on Arctic amplification influence on midlatitude severe winter weather. *Nature Climate Change* **10**, 20–29 (2020).

252.   IPCC. *Climate Change 2013 - The Physical Science Basis.* (2013) doi:10.1017/CBO9781107415324.

253.   Stroeve, J. C. *et al.* Trends in Arctic sea ice extent from CMIP5, CMIP3 and observations. *Geophysical Research Letters* **39**, 1–7 (2012).

254.   Wang, M. & Overland, J. E. A sea ice free summer Arctic within 30 years: An update from CMIP5 models. *Geophysical Research Letters* **39**, 6–11 (2012).

255.   Schröder, C., Reimer, N. & Jochmann, P. Environmental impact of exhaust emissions by Arctic shipping. *Ambio* **46**, 400–409 (2017).

256.   Yumashev, D., van Hussen, K., Gille, J. & Whiteman, G. Towards a balanced view of Arctic shipping: estimating economic impacts of emissions from increased traffic on the Northern Sea Route. *Climatic Change* **143**, 143–155 (2017).

257. Quinn, P. K. *et al.* Short-lived pollutants in the Arctic: Their climate impact and possible mitigation strategies. *Atmospheric Chemistry and Physics* **8**, 1723–1735 (2008).

258. Barrie, L. A. Arctic air pollution: An overview of current knowledge. *Atmospheric Environment* **20**, 643–663 (1986).

259. Morice, C. P. *et al.* An Updated Assessment of Near-Surface Temperature Change From 1850: The HadCRUT5 Data Set. *Journal of Geophysical Research: Atmospheres* **126**, e2019JD03236 (2021).

260. Fetterer, F., Knowles, K., Meier, W. N., Savoie, M. & Windnagel, A. K. Sea Ice Index, Version 3. *NSIDC: National Snow and Ice Data Center* Preprint at https://doi.org/10.7265/N5K072F8 (2017).

261. European Environmental Agency. Projected changes in sea ice extent in the northern hemisphere in September. https://www.eea.europa.eu/ds_resolveuid/8d37f0972fef4462bd4aa3e565a2eaec (2014).

262. Kahl, J. D. & Hansen, A. D. A. Determination of regional sources of aerosol black carbon in the Arctic. *Geophysical Research Letters* **16**, 327–330 (1989).

263. Winiger, P. *et al.* Source apportionment of circum-Arctic atmospheric black carbon from isotopes and modeling. *Science Advances* **5**, eaau8052 (2019).

264. Winiger, P., Andersson, A., Eckhardt, S., Stohl, A. & Gustafsson, Ö. The sources of atmospheric black carbon at a European gateway to the Arctic. *Nature Communications* **7**, 12776 (2016).

265. Winiger, P., Andersson, A., Yttri, K. E., Tunved, P. & Gustafsson, Ö. Isotope-Based Source Apportionment of EC Aerosol Particles during Winter High-Pollution Events at the Zeppelin Observatory, Svalbard. *Environmental Science and Technology* **49**, 11959–11966 (2015).

266. Winiger, P. *et al.* Siberian Arctic black carbon sources constrained by model and observation. *Proceedings of the National Academy of Sciences* **114**, E1054–E1061 (2017).

267. Moschos, V. *et al.* Equal abundance of summertime natural and wintertime anthropogenic Arctic organic aerosols. *Nature Geoscience* **15**, 196–202 (2022).

268. Barrett, T. E., Robinson, E. M., Usenko, S. & Sheesley, R. J. Source Contributions to Wintertime Elemental and Organic Carbon in the Western Arctic Based on Radiocarbon and Tracer Apportionment. *Environmental science and technology* **49**, 11631–11639 (2015).

269. Cook, D. & Zolnikov, T. R. Antarctica. in 31–49 (2019). doi:10.1007/978-3-030-01213-7_3.

270. Hansen, A. D. A., Bodhaine, B. A., Dutton, E. G. & Schnell, R. C. Aerosol black carbon measurements at the South Pole: Initial results, 1986-1987. *Geophysical Research Letters* **15**, 1193–1196 (1988).

271. Wolff, E. W. & Cachier, H. Concentrations and seasonal cycle of black carbon in aerosol at a coastal Antarctic station. *Journal of Geophysical Research: Atmospheres* **103**, 11033–11041 (1998).

272.   Weller, R., Minikin, A., Petzold, A., Wagenbach, D. & König-Langlo, G. Characterization of long-term and seasonal variations of black carbon (BC) concentrations at Neumayer, Antarctica. *Atmospheric Chemistry and Physics* **13**, 1579–1590 (2013).

273.   Pereira, E. B., Evangelista, H., Pereira, K. C. D., Cavalcanti, I. F. A. & Setzer, A. W. Apportionment of black carbon in the South Shetland Islands, Antarctic Peninsula. *Journal of Geophysical Research* **111**, D03303 (2006).

274.   Hansen, A. D. A., Lowenthal, D. H., Chow, J. C. & Watson, J. G. Black carbon aerosol at McMurdo Station, Antarctica. *Journal of the Air and Waste Management Association* **51**, 593–600 (2001).

275.   Bodhaine, B. A. Aerosol absorption measurements at Barrow, Mauna Loa and the south pole. *Journal of Geophysical Research* **100**, 8967 (1995).

276.   Hu, Q.-H. *et al.* Secondary organic aerosols over oceans via oxidation of isoprene and monoterpenes from Arctic to Antarctic. *Scientific Reports* **3**, 2280 (2013).

277.   Fiebig, M. *et al.* Annual cycle of Antarctic baseline aerosol: Controlled by photooxidation-limited aerosol formation. *Atmospheric Chemistry and Physics* **14**, 3083–3093 (2014).

278.   O'Dowd, C. D. *et al.* Biogenically driven organic contribution to marine aerosol. *Nature* **431**, 676–680 (2004).

279.   Spracklen, D. v., Arnold, S. R., Sciare, J., Carslaw, K. S. & Pio, C. Globally significant oceanic source of organic carbon aerosol. *Geophysical Research Letters* **35**, L12811 (2008).

280.   Beaupré, S. R. *et al.* Oceanic efflux of ancient marine dissolved organic carbon in primary marine aerosol. *Science Advances* **5**, (2019).

281.   Clarke, L. J., Robinson, S. A., Hua, Q., Ayre, D. J. & Fink, D. Radiocarbon bomb spike reveals biological effects of antarctic climate change. *Global Change Biology* **18**, 301–310 (2012).

282.   Emslie, S. D., McKenzie, A., Marti, L. J. & Santos, M. Recent occupation by Adélie Penguins (*Pygoscelis adeliae*) at Hope Bay and Seymour Island and the 'northern enigma' in the Antarctic Peninsula. *Polar Biology* **41**, 71–77 (2018).

283.   Lechtenfeld, O. J. *et al.* Molecular transformation and degradation of refractory dissolved organic matter in the Atlantic and Southern Ocean. *Geochimica et Cosmochimica Acta* **126**, 321–337 (2014).

284.   Fang, L. *et al.* Removal of Refractory Dissolved Organic Carbon in the Amundsen Sea, Antarctica. *Scientific Reports* **10**, 1–8 (2020).

285.   Bercovici, S. K., McNichol, A. P., Xu, L. & Hansell, D. A. Radiocarbon Content of Dissolved Organic Carbon in the South Indian Ocean. *Geophysical Research Letters* **45**, 872–879 (2018).

286.   Druffel, E. R. M. *et al.* Dissolved Organic Radiocarbon in the Eastern Pacific and Southern Oceans. *Geophysical Research Letters* **48**, 1–9 (2021).

287. Zimmermann, M. Geschichte der Schmerztherapie 1500 bis 1900. *Der Schmerz* **21**, 297–306 (2007).

288. Chang, K. Vaccination for Disease Prevention and Control: the Necessity of Renewed Emphasis and New Approaches. *Journal of Immunology and Immunotechniques* **1**, (2014).

289. Chevalier-Cottin, E.-P. *et al.* Communicating Benefits from Vaccines Beyond Preventing Infectious Diseases. *Infectious Diseases and Therapy* **9**, 467–480 (2020).

290. Aminov, R. I. A Brief History of the Antibiotic Era: Lessons Learned and Challenges for the Future. *Frontiers in Microbiology* **1**, (2010).

291. Pinker, S. *Enlightenment now: The case for reason, science, humanism, and progress.* (Penguin, 2018).

292. Brauman, K. A. *et al.* Global trends in nature's contributions to people. *Proceedings of the National Academy of Sciences* **117**, 32799–32805 (2020).

293. OECD. *The economic consequences of outdoor air pollution.* (OECD Publishing, 2016).

294. Dechezleprêtre, A., Rivers, N. & Stadler, B. The economic cost of air pollution: Evidence from Europe. *OECD Economics Department Working Papers* Preprint at https://doi.org/10.1787/56119490-en (2019).

295. WHO Regional Office for Europe & OECD. *Economic cost of the health impact of air pollution in Europe: Clean air, health and wealth.* https://apps.who.int/iris/handle/10665/350716 (2015).

296. Amann, M., Holland, M., Maas, R., Saveyn, B. & Vandyck, T. *Costs, benefits and economic impacts of the EU clean air strategies and their implications on innovation and competitiveness.* (2017).

297. Roy, R. & Braathen, N. A. The Rising Cost of Ambient Air Pollution thus far in the 21st Century: Results from the BRIICS and the OECD Countries. *OECD Environment Working Papers* Preprint at https://doi.org/10.1787/d1b2b844-en (2017).

298. Centre for Research on Energy and Clean Air. *Quantifying the Economic Costs of Air Pollution from Fossil Fuels.* (2020).

299. World Bank. DataBank Global Economic Monitor (GEM). https://databank.worldbank.org/source/global-economic-monitor-(gem) (2021).

300. Henneman, L. R. F., Liu, C., Mulholland, J. A. & Russell, A. G. Evaluating the effectiveness of air quality regulations: A review of accountability studies and frameworks. *Journal of the Air & Waste Management Association* **67**, 144–172 (2017).

301. Dümmler, P., Rühli, L., Hug Alonso, T. & Bonato, M. *Wirkungsvolle Klimapolitik: Der liberale Weg zu einer CO₂-neutralen Zukunft.* (2021).

302. Schraufnagel, D. E. *et al.* Health Benefits of Air Pollution Reduction. *Annals of the American Thoracic Society* **16**, 1478–1487 (2019).

303.   U.S. Federal Highway Administration. Vehicle Miles Traveled [TRFVOLUSM227NFWA], retrieved from FRED, Federal Reserve Bank of St. Louis. https://fred.stlouisfed.org/series/TRFVOLUSM227NFWA.

304.   U.S. Census Bureau. Historical Population Change Data (1910-2020). https://www.census.gov/data/tables/time-series/dec/popchange-data-text.html.

305.   U.S. Energy Information Administration. Total Energy. https://www.eia.gov/totalenergy/data/browser/?tbl=T02.01.

306.   U.S. Environmental Protection Agency. Air Pollutant Emissions Trends Data. https://www.epa.gov/air-emissions-inventories/air-pollutant-emissions-trends-data.

307.   Friedlingstein, P. *et al.* Global Carbon Budget 2021. *Earth System Science Data* **14**, 1917–2005 (2022).

308.   Belis, C. A. *et al.* *European Guide on Air Pollution Source Apportionment with Receptor Models.* (2019).

309.   Belis, C. A. *et al.* *European Guide on Air Pollution Source Apportionment with Receptor Models.* (2014).

310.   Hopke, P. K. Review of receptor modeling methods for source apportionment. *Journal of the Air & Waste Management Association* **66**, 237–259 (2016).

311.   Paatero, P. & Tapper, U. Analysis of different modes of factor analysis as least squares fit problems. *Chemometrics and Intelligent Laboratory Systems* **18**, 183–194 (1993).

312.   Chen, G. *et al.* Time-dependent source apportionment of submicron organic aerosol for a rural site in an alpine valley using a rolling positive matrix factorisation (PMF) window. *Atmospheric Chemistry and Physics* **21**, 15081–15101 (2021).

313.   Jain, S., Sharma, S. K., Vijayan, N. & Mandal, T. K. Seasonal characteristics of aerosols (PM$_{2.5}$ and PM$_{10}$) and their source apportionment using PMF: A four year study over Delhi, India. *Environmental Pollution* **262**, 114337 (2020).

314.   Xu, J. *et al.* Source apportionment of fine organic carbon at an urban site of Beijing using a chemical mass balance model. *Atmospheric Chemistry and Physics* **21**, 7321–7341 (2021).

315.   Wåhlin, P. COPREM—A multivariate receptor model with a physical approach. *Atmospheric Environment* **37**, 4861–4867 (2003).

316.   Nguyen, Q. T. *et al.* Source apportionment of particles at Station Nord, North East Greenland during 2008–2010 using COPREM and PMF analysis. *Atmospheric Chemistry and Physics* **13**, 35–49 (2013).

317.   Deng, J. *et al.* Source apportionment of PM$_{2.5}$ at the Lin'an regional background site in China with three receptor models. *Atmospheric Research* **202**, 23–32 (2018).

318.   Xu, J. *et al.* An evaluation of source apportionment of fine OC and PM$_{2.5}$ by multiple methods: APHH-Beijing campaigns as a case study. *Faraday Discussions* **226**, 290–313 (2021).

319. Wang, F. *et al.* Review of online source apportionment research based on observation for ambient particulate matter. *Science of The Total Environment* **762**, 144095 (2021).

320. Sun, X. *et al.* Positive matrix factorization on source apportionment for typical pollutants in different environmental media: a review. *Environmental Science: Processes & Impacts* **22**, 239–255 (2020).

321. Shang, X. *et al.* Riverine nitrate source apportionment using dual stable isotopes in a drinking water source watershed of southeast China. *Science of The Total Environment* **724**, 137975 (2020).

322. Simoneit, B. R. T. Biomass burning — a review of organic tracers for smoke from incomplete combustion. *Applied Geochemistry* **17**, 129–162 (2002).

323. Yttri, K. E. *et al.* Source apportionment of the summer time carbonaceous aerosol at Nordic rural background sites. *Atmospheric Chemistry and Physics* **11**, 13339–13357 (2011).

324. Yttri, K. E. *et al.* Trends, composition, and sources of carbonaceous aerosol at the Birkenes Observatory, northern Europe, 2001–2018. *Atmospheric Chemistry and Physics* **21**, 7149–7170 (2021).

325. Cavalli, F., Viana, M., Yttri, K. E., Genberg, J. & Putaud, J. P. Toward a standardised thermal-optical protocol for measuring atmospheric organic and elemental carbon: The EUSAAR protocol. *Atmospheric Measurement Techniques* **3**, 79–89 (2010).

326. Glasius, M. *et al.* Composition and sources of carbonaceous aerosols in Northern Europe during winter. *Atmospheric Environment* **173**, 127–141 (2018).

327. Xu, J. *et al.* An interlaboratory comparison of aerosol inorganic ion measurements by ion chromatography: implications for aerosol pH estimate. *Atmospheric Measurement Techniques* **13**, 6325–6341 (2020).

328. Yttri, K. E. *et al.* An intercomparison study of analytical methods used for quantification of levoglucosan in ambient aerosol filter samples. *Atmospheric Measurement Techniques* **8**, 125–147 (2015).

329. Kunit, M. & Puxbaum, H. Enzymatic determination of the cellulose content of atmospheric aerosols. *Atmospheric Environment* **30**, 1233–1236 (1996).

330. Yttri, K. E., Simpson, D., Stenström, K., Puxbaum, H. & Svendby, T. Source apportionment of the carbonaceous aerosol in Norway – quantitative estimates based on ^{14}C, thermal-optical and organic tracer analysis. *Atmospheric Chemistry and Physics* **11**, 9375–9394 (2011).

331. Bahreini, R. Aircraft-based aerosol size and composition measurements during ACE-Asia using an Aerodyne aerosol mass spectrometer. *Journal of Geophysical Research* **108**, 8645 (2003).

332. Canagaratna, M. R. *et al.* Chemical and microphysical characterization of ambient aerosols with the aerodyne aerosol mass spectrometer. *Mass Spectrometry Reviews* **26**, 185–222 (2007).

333. Daellenbach, K. R. *et al.* Characterization and source apportionment of organic aerosol using offline aerosol mass spectrometry. *Atmospheric Measurement Techniques* **9**, 23–39 (2016).

334. Vlachou, A. *et al.* Advanced source apportionment of carbonaceous aerosols by coupling offline AMS and radiocarbon size-segregated measurements over a nearly 2-year period. *Atmospheric Chemistry and Physics* **18**, 6187–6206 (2018).

335. Rudich, Y., Donahue, N. M. & Mentel, T. F. Aging of Organic Aerosol: Bridging the Gap Between Laboratory and Field Studies. *Annual Review of Physical Chemistry* **58**, 321–352 (2007).

336. Szidat, S. Sources of Asian Haze. *Science* **323**, 470–471 (2009).

337. Stuiver, M. Workshop [14]C Data Reporting. *Radiocarbon* **22**, 964–966 (1980).

338. Reimer, P. J. *et al.* The IntCal20 Northern Hemisphere Radiocarbon Age Calibration Curve (0–55 cal kBP). *Radiocarbon* **62**, 725–757 (2020).

339. Durand, B. *Petroleum, natural gas and coal.* (EDP Sciences, 2020). doi:10.1051/978-2-7598-2232-4.

340. Clayton, G. D., Arnold, J. R. & Patty, F. A. Determination of Sources of Particulate Atmospheric Carbon. *Science* **122**, 751–753 (1955).

341. Cooper, J. A., Currie, L. A. & Klouda, G. A. Assessment of contemporary carbon combustion source contributions to urban air particulate levels using carbon-14 measurements. *Environmental Science & Technology* **15**, 1045–1050 (1981).

342. Sunlab – About Us. https://www.sunlab.com/about-us/.

343. Cadle, S. H., Groblicki, P. J. & Stroup, D. P. Automated Carbon Analyzer For Particulate Samples. *Analytical Chemistry* **52**, 2201–2206 (1980).

344. Yu, J. Z., Xu, J. & Yang, H. Charring characteristics of atmospheric organic particulate matter in thermal analysis. *Environmental Science and Technology* **36**, 754–761 (2002).

345. Ruff, M. *et al.* A Gas Ion Source for Radiocarbon Measurements at 200 kV. *Radiocarbon* **49**, 307–314 (2007).

346. Wacker, L. *et al.* A versatile gas interface for routine radiocarbon analysis with a gas ion source. *Nuclear Instruments and Methods in Physics Research, Section B: Beam Interactions with Materials and Atoms* **294**, 315–319 (2013).

347. Chow, J. C. *et al.* The DRI thermal/optical reflectance carbon analysis system: description, evaluation and applications in U.S. Air quality studies. *Atmospheric Environment. Part A. General Topics* **27**, 1185–1201 (1993).

348. Eller, P. M. & Cassinelli, M. E. Niosh, Elemental Carbon (Diesel Particulate): Method 5040. NIOSH Manual of Analytical Methods. *National Institute for Occupational Safety and Health: Cincinatti, OH, USA* 2003–2154 (1996).

349. Peterson, M. R. & Richards, M. H. *Thermal-Optical-Transmittance Analysis for Organic, Elemental, Carbonate, Total Carbon, and OCX2 in PM₂.₅ by the EPA/NIOSH Method. Proceedings, Symposium on Air Quality Measurement Methods and Technology - 2002, Pittsburgh, PA* (2002).

350. Birch, M. E. & Cary, R. A. Elemental Carbon-Based Method for Monitoring Occupational Exposures to Particulate Diesel Exhaust. *Aerosol Science and Technology* **25**, 221–241 (1996).

351. Peterson, M. R. & Richards, M. H. Thermal-optical-transmittance analysis for organic, elemental, carbonate, total carbon, and OCX2 in PM₂.₅ by the EPA/NIOSH method. in *Proceedings of the Symposium on Air Quality Measurement Methods and Technology* (eds. Winegard, E. D. & Tropp, R. J.) 83–1–83–19 (Air & Waste Management Association, 2002).

352. Gustafsson, Ö. *et al.* Evaluation of a protocol for the quantification of black carbon in sediments. *Global Biogeochemical Cycles* **15**, 881–890 (2001).

353. Szidat, S. *et al.* THEODORE, a two-step heating system for the EC/OC determination of radiocarbon (^{14}C) in the environment. *Nuclear Instruments and Methods in Physics Research Section B: Beam Interactions with Materials and Atoms* **223–224**, 829–836 (2004).

354. Zencak, Z., Elmquist, M. & Gustafsson, Ö. Quantification and radiocarbon source apportionment of black carbon in atmospheric aerosols using the CTO-375 method. *Atmospheric Environment* **41**, 7895–7906 (2007).

355. Zhang, Y. L., Liu, D., Shen, C. D., Ding, P. & Zhang, G. Development of a preparation system for the radiocarbon analysis of organic carbon in carbonaceous aerosols in China. *Nuclear Instruments and Methods in Physics Research, Section B: Beam Interactions with Materials and Atoms* **268**, 2831–2834 (2010).

356. Szidat, S. *et al.* Radiocarbon (^{14}C)-deduced biogenic and anthropogenic contributions to organic carbon (OC) of urban aerosols from Zürich, Switzerland. *Atmospheric Environment* **38**, 4035–4044 (2004).

357. Jenk, T. M. *et al.* Microgram level radiocarbon (^{14}C) determination on carbonaceous particles in ice. *Nuclear Instruments and Methods in Physics Research Section B: Beam Interactions with Materials and Atoms* **259**, 518–525 (2007).

358. Huang, X., Hu, M., He, L. & Tang, X. Chemical characterization of water-soluble organic acids in PM₂.₅ in Beijing, China. *Atmospheric Environment* **39**, 2819–2827 (2005).

359. Kerminen, V. M., Teinilä, K., Hillamo, R. & Mäkelä, T. Size-segregated chemistry of particulate dicarboxylic acids in the Arctic atmosphere. *Atmospheric Environment* **33**, 2089–2100 (1999).

360. Fang, T. *et al.* A semi-automated system for quantifying the oxidative potential of ambient particles in aqueous extracts using the dithiothreitol (DTT) assay: results from the Southeastern Center for Air Pollution and Epidemiology (SCAPE). *Atmospheric Measurement Techniques* **8**, 471–482 (2015).

361. Novakov, T. & Corrigan, C. E. Mikrochimica Acta Thermal Characterization of Biomass Smoke Particles. *Mikrochimica Acta* **166**, 157–166 (1995).

362. Fanali, S., Haddad, P. R., Poole, C. & Riekkola, M.-L. *Liquid Chromatography: Fundamentals and Instrumentation*. (Elsevier, 2017).

363. Rauber, M. Compound-specific Radiocarbon Analysis of Aerosols: Master Thesis University of Bern. (2018).

364. Thermo Fisher Scientific. IonPac AS11-HC Manual. Preprint at (2012).

365. Small, Hamish., Stevens, T. S. & Bauman, W. C. Novel ion exchange chromatographic method using conductimetric detection. *Analytical Chemistry* **47**, 1801–1809 (1975).

366. Palmer, S. M., Hope, D., Billett, M. F., Dawson, J. J. C. & Bryant, C. L. Sources of organic and inorganic carbon in a headwater stream: Evidence from carbon isotope studies. *Biogeochemistry* **52**, 321–338 (2001).

367. Armstrong, F. a. J., Williams, P. M. & Strickland, J. D. H. Photo-oxidation of Organic Matter in Sea Water by Ultra-violet Radiation, Analytical and Other Applications. *Nature* **211**, 481–483 (1966).

368. Druffel, E. R. M. *et al.* Radiocarbon in Dissolved Organic and Inorganic. *Radiocarbon* **31**, 523–532 (1989).

369. Beaupré, S. R., Druffel, E. R. M. & Griffin, S. A low-blank photochemical extraction system for concentration and isotopic analyses of marine dissolved organic carbon. *Limnology and Oceanography: Methods* **5**, 174–184 (2007).

370. Lang, S. Q. *et al.* Rapid [14]C Analysis of Dissolved Organic Carbon in Non-Saline Waters. *Radiocarbon* **58**, 505–515 (2016).

371. Duursma, E. K. Dissolved organic carbon, nitrogen and phosphorus in the sea. *Netherlands Journal of Sea Research* **1**, 1–141 (1961).

372. Sharp, J. H. Total organic carbon in seawater - comparison of measurements using persulfate oxidation and high temperature combustion. *Marine Chemistry* **1**, 211–229 (1973).

373. Smith, M. B. & March, J. *March's Advanced Organic Chemistry: Reactions, Mechanisms, and Structure*. (John Wiley & Sons, 2007).

374. Cowie, J. M. G. & Arrighi, V. *Polymers: Chemistry and Physics of Modern Materials*. (CRC Press, 2007).

375. Lang, S. Q., Bernasconi, S. M. & Früh-Green, G. L. Stable isotope analysis of organic carbon in small (μg C) samples and dissolved organic matter using a GasBench preparation device. *Rapid Communications in Mass Spectrometry* **26**, 9–16 (2012).

376. Lang, S. Q., Früh-Green, G. L., Bernasconi, S. M. & Wacker, L. Isotopic ($\delta^{13}C$, $\Delta^{14}C$) analysis of organic acids in marine samples using wet chemical oxidation. *Limnology and Oceanography: Methods* **11**, 161–175 (2013).

377. Leonard, A. A Wet Oxidation Method for AMS Radiocarbon Analysis of Dissolved Organic Carbon in Water. *Radiocarbon* **55**, 545–552 (2013).

2 An Optimised OC/EC Fraction Separation Method for Radiocarbon Source Apportionment Applied to Low-Loaded Arctic Aerosol Filters

Martin Rauber[1,2], Gary Salazar[1,2], Karl Espen Yttri[3], Sönke Szidat[1,2]

[1]Department of Chemistry, Biochemistry and Pharmaceutical Sciences, University of Bern, Bern, Switzerland
[2]Oeschger Centre for Climate Change Research, University of Bern, Bern, Switzerland
[3]Department of Atmospheric and Climate Research, NILU – Norwegian Institute for Air Research, Kjeller, Norway

Correspondence to: Sönke Szidat (soenke.szidat@unibe.ch)

Abstract

Radiocarbon (^{14}C) analysis of carbonaceous aerosols is used for source apportionment, separating the carbon content into fossil vs. non-fossil origin, and is particularly useful when applied to subfractions of total carbon (TC), i.e., elemental carbon (EC), organic carbon (OC), water-soluble OC (WSOC), and water-insoluble OC (WINSOC). However, this requires an unbiased physical separation of these fractions, which is difficult to achieve. Separation of EC from OC using thermal-optical analysis (TOA) can cause EC loss during the OC removal step and form artificial EC from pyrolysis of OC (i.e., so-called charring), both distorting the ^{14}C analysis of EC. Previous work showed that water extraction reduces charring. Here, we apply a new combination of a WSOC extraction and ^{14}C analysis method with an optimised OC/EC separation that is coupled with a novel approach of thermal-desorption modelling for compensation of EC losses. As water-soluble components promote the formation of pyrolytic carbon, water extraction was used to minimise the charring artefact of EC, and the eluate subjected to chemical wet oxidation to CO_2 before direct ^{14}C analysis in a gas-accepting accelerator mass spectrometer (AMS). This approach was applied to 13 aerosol filter samples collected at the Arctic Zeppelin Observatory (Svalbard) in 2017 and 2018, covering all seasons, which bear challenges for a simplified ^{14}C source apportionment due to their low loading and the large portion of pyrolysable species. Our approach provided a mean EC yield of 0.87 ± 0.07 and reduced the charring to 6.5 % of the recovered EC amounts. The mean Fraction Modern (F^{14}C) over all seasons was 0.85 ± 0.17 for TC, 0.61 ± 0.17 and 0.66 ± 0.16 for EC before and after correction with the thermal-desorption model, respectively, and 0.81 ± 0.20 for WSOC.

2.1 Introduction

Considerable efforts have been made to investigate atmospheric aerosol due to its relevance on a wide range of environmental topics, including change of radiative forcing and adverse effect on human health (McNeill, 2017; Lelieveld et al., 2015; Landrigan, 2017; Pope et al., 2020). Exposure to ambient atmospheric particulate matter (PM) has been associated with damage to the cardiopulmonary system and causing at least 3 million premature deaths per year globally (Kim et al., 2015; Lelieveld et al., 2015; Forouzanfar et al., 2016). Understanding aerosols is therefore crucial for future projections and for the improvement of air quality especially for severely affected areas (Quinn et al., 2008; Bond et al., 2013; Schmale et al., 2021). Although the Arctic is considered a pristine part of the world, it is also affected by emissions from polluted regions in the northern hemisphere, causing the Arctic haze phenomenon (Barrie, 1986; Heidam et al., 2004; Quinn et al., 2002; Zhao and Garrett, 2015; Engelmann et al., 2021; Jouan et al., 2014), occurring in late winter and early spring and have been known for decades (Barrie et al., 1981). Arctic haze consists mainly of sulfate and carbonaceous aerosols trapped in the cold retracting polar dome in spring, coupled with reduced wet scavenging in winter and spring (Abbatt et al., 2019; Moschos et al., 2022).

Carbonaceous aerosols (here: total carbon, TC) consists of an organic fraction referred to as organic carbon (OC), and a refractory light-absorbing component named elemental carbon (EC) or equivalent black carbon (eBC) when quantified with thermal-optical analysis or optical methods, respectively (Contini et al., 2018; Bond et al., 2013; Petzold et al., 2013). TC constitutes 20 to 90 % of the aerosol mass (Kanakidou et al., 2005; Putaud et al., 2010; Gentner et al., 2017). As a main PM component, it thus contributes to adverse effects on public health and climate. On the one hand, carbonaceous aerosols may contain toxic or carcinogenic compounds such as polycyclic aromatic hydrocarbons (PAH) (Mauderly and Chow, 2008; Kim et al., 2013; Smichowski et al., 2005; Daellenbach et al., 2020). On the other hand, both EC and OC are climate relevant: The effective radiative forcing (ERF) for atmospheric aerosols is negative, and while the OC fraction has a negative ERF the EC fraction has a positive ERF (IPCC, 2021). Overall, the surface albedo for BC and OC on snow and ice is positive with a global mean ERF of 0.08 (0.00 to 0.18) (IPCC, 2021). Consequently, sources of OC, EC and subfractions must be understood to improve air quality and mitigate adverse effects of carbonaceous aerosols. Due to its complex composition and multitude of sources, however, carbonaceous aerosols are still inadequately understood.

Source apportionment is a widely used approach to gain understanding on emission, formation, and transformation of carbonaceous aerosols. It investigates the chemical and physical composition of aerosols at receptor sites to disentangle the contributions of individual emissions and the attribution to different source categories. Radiocarbon (^{14}C) measurements is an important source apportionment tool that can unambiguously separate between fossil and contemporary carbon present in carbonaceous aerosol, including in the OC and EC subfractions (Szidat et al., 2006; Winiger et al., 2015; Zotter et al., 2014). Sources of OC and EC are often very different, and such additional information is obtained by means of ^{14}C source apportionment of both EC and OC compared to a radiocarbon of TC analysis alone. The

analysis of the OC subfractions water-soluble OC (WSOC) and water-insoluble OC (WINSOC) can lead to further information of the fossil and non-fossil fractions of the emitting sources (Zhang et al., 2014b).

Separation of OC and EC are method dependent, but the classification is widely recognised (Pöschl, 2003). EC is a primary particle, i.e., emitted directly to the atmosphere, generated by incomplete combustion of fossil fuels and biomass, whereas OC is either primary or secondary, i.e., emitted directly or formed in the atmosphere by oxidation of both anthropogenic and biogenic precursor gases (Kanakidou et al., 2005). Thermal-optical analysis (TOA) is a well-established and commonly used technique for OC/EC determination (Chow et al., 2004; Cavalli et al., 2010; Chow et al., 1993; Schmid et al., 2001; Huntzicker et al., 1982). Typically, two or more heating steps in an inert (i.e., helium) and in an oxidative atmosphere (i.e., 2 % oxygen in helium) are used to desorb OC and EC, respectively. During analysis, the transmission or reflectance of the filter sample is continuously measured (Birch and Cary, 1996; Schmid et al., 2001). A change in the transmission or reflectance signal indicates charring and EC loss. Charring is known as the process when OC pyrolyses into EC, thus decreasing the transmission signal and creating a positive EC artefact (Cadle et al., 1980; Yu et al., 2002). Charring leads to an overestimation of EC and an underestimation of OC. Additional to charring, some EC is lost by desorption during thermal separation of OC, leading to a negative EC artefact. Both the positive EC artefact (i.e., charring) and the negative artefact (i.e., partial EC loss) may induce a bias to ^{14}C measurement of EC. Charring adds OC, which is typically more non-fossil than EC (Szidat et al., 2006, 2009; Zhang et al., 2012, 2014b; Zotter et al., 2014; Vlachou et al., 2018), so that the measured ^{14}C of EC may appear more non-fossil than it is. Partial EC loss usually affects non-fossil EC (e.g., from biomass burning) more than fossil EC (e.g., from traffic or coal combustion) so that the remaining EC may be altered and seem more fossil. A correction of both artefacts is therefore required for the accurate quantification of the fossil vs. non-fossil shares of EC. EC recovery after OC/EC separation is determined using the transmission or reflectance signal (Gundel et al., 1984; Zhang et al., 2012). Frequently used TOA protocols for OC/EC determination include EUSAAR_2 (Cavalli et al., 2010), IMPROVE (Chow et al., 1993), and NIOSH (Eller and Cassinelli, 1996). Radiocarbon measurement requires a clear physical separation of OC and EC, since OC and EC do not originate from the same processes and often show very different radiocarbon signatures (Szidat et al., 2006, 2007; Zhang et al., 2014b). Traditional TOA protocols may still contain some OC in charred or an unaltered form after the split point, thus fail to perform the physical separation adequately for radiocarbon source apportionment (Barrett et al., 2015; Zhang et al., 2012). Gustafsson et al. (2001) developed a separation technique (CTO-375) in soil sediments, which was later applied to radiocarbon source apportionment of atmospheric aerosols (Zencak et al., 2007). A two-step separation method developed by Szidat et al. (2004b) was utilised for radiocarbon source apportionment (Zhang et al., 2010; Jenk et al., 2007; Szidat et al., 2004b). As these simplified approaches still failed to provide an isolation of EC, our group (Zhang et al., 2012) established an improved four step method (Swiss_4S) using water extraction before TOA and pure O_2 for an optimised EC recovery and reduced charring. Later, Agrios et al. (2015) coupled the Sunset thermo-

optical OC/EC analyser with on-line measurement in an accelerator mass spectrometer (AMS) and implemented the previously developed Swiss_4S protocol.

Many have investigated EC in the Arctic including stable isotope (^{13}C) and radiocarbon analysis for source apportionment (Winiger et al., 2016, 2017, 2015; Moschos et al., 2021). The fossil contribution of OC and WSOC is often not measured directly but calculated by the isotope mass balance approach (Vlachou et al., 2018). Zhang et al. (2014a) lyophilised and re-solubilised the eluate from water extraction before combustion in an elemental analyser coupled with radiocarbon measurement. Menzel and Vaccaro (1964) as well as Sharp (1973) used potassium persulfate for the oxidation of dissolved organic carbon in seawater. Lang et al. (2012) employed such a chemical wet oxidation for stable isotope analysis of dissolved organic matter in freshwater samples. This method was later used for stable and radiocarbon analysis of marine samples as well as compound-specific analysis of pyrogenic carbon (Lang et al., 2013; Wiedemeier et al., 2016), but has not been adapted for ^{14}C analysis of WSOC from carbonaceous aerosols so far.

The present study provides a framework for an optimal OC/EC separation and radiocarbon analysis coupled with direct ^{14}C(WSOC) analysis (i.e., the ^{14}C analysis of WSOC) by chemical wet oxidation applied on low-loaded Arctic filters. We provide a novel method for the EC yield extrapolation and charring correction based on a chemical desorption model that represent the behaviour of EC from different sources more realistically. Arctic filters were utilised as they are challenging for radiocarbon analysis due to their low loading and the large portion of pyrolysable species. Using an optimised strategy, we can measure the F^{14}C value (i.e., the Fraction Modern) in all major aerosol filter fractions (TC, EC, WSOC, WINSOC) with the lowest possible amount of filter material.

2.2   Experimental

2.2.1   Overview of the analytical procedures

Aerosol filter samples were first water extracted to collect WSOC for subsequent radiocarbon measurement and to minimise formation of pyrolytic carbon (PC), caused primarily by WSOC, otherwise causing a dilution of the true EC signal. We then used the first three steps of the Swiss_4S protocol (Zhang et al., 2012) to remove WINSOC from the filter by thermal-optical analysis, isolating EC. The filter's EC content were evolved by total combustion in a TOA analyser and subjected to on-line radiocarbon measurements. The WSOC eluate was converted to CO_2 by chemical wet oxidation before radiocarbon measurement. The following chapters explain the different procedures in brief, whereas the SI provides information that is more detailed.

2.2.2 Sampling and filter selection

Aerosol filter samples were collected between February 2017 and November 2018 at the Zeppelin Observatory (Svalbard) (78° 54' N, 11° 52' E) (475 m a.s.l.), which is part of the Global Atmospheric Watch (GAW) programme, the Arctic Monitoring and Assessment Programme (AMAP), and the European Evaluation and Monitoring Programme (EMEP) (Hung et al., 2010; Tørseth et al., 2012; Platt et al., 2022). Aerosol particles were collected on pre-fired (850 °C, 3 h) quartz fibre filters (PALLFLEX® Tissuquartz 2500QAT-UP; 150 mm in diameter) downstream of a PM_{10} inlet, using a Digitel high-volume sampler (DH-77, Hegenau, Switzerland). The sampler operated at a flow rate of 689 L min⁻¹, corresponding to an air volume of 6945 m³ for a sampling time of one week. Filter samples were collected according to the quartz behind quartz (QBQ) set up (McDow and Huntzicker, 1990), allowing for an estimate of the positive sampling artifact of OC.
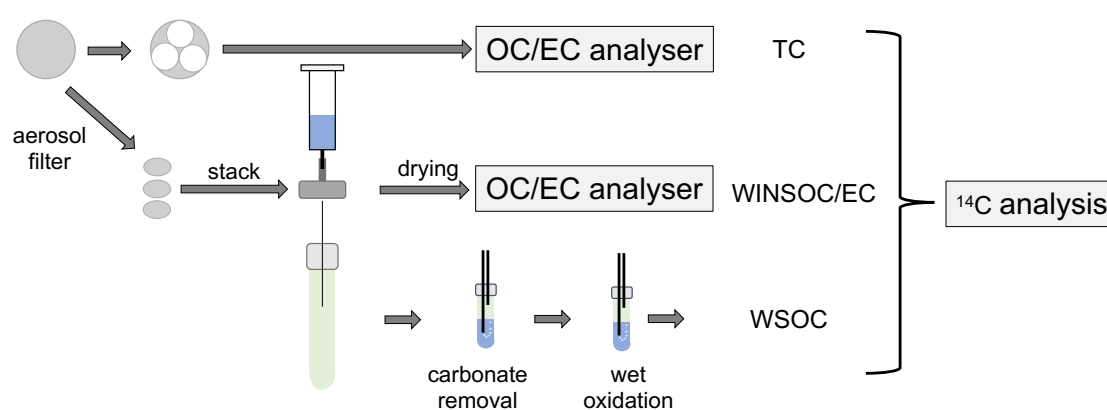
Figure 1: Separation of the different fractions for ¹⁴C analysis starting from the aerosol filters. One or multiple circular quartz fibre filter punches are stacked and intercalated in the water extraction set-up. The residual filter material used for WINSOC and EC analysis after drying, and the extract oxidised by chemical wet oxidation. The remaining filter material is used for TC analysis.

A fraction (46 mm diameter, corresponding to 16.6 cm²) of the total filter area (153.9 cm²) were cut for radiocarbon measurement of ¹⁴C(TC), ¹⁴C(WSOC) and ¹⁴C(EC) (Fig. 1). The filter's TC, EC, and OC content were quantified according the EUSAAR_2 temperature programme (Cavalli et al., 2010), using transmission for charring correction. 18 filter samples were received for radiocarbon measurement, but due to low EC loadings pooling of five subsequent filters was necessary (Fig. 1). Owing to the low filter loading, the water extraction for ¹⁴C(WSOC) and ¹⁴C(EC) was only performed on the front filters, whereas ¹⁴C(TC) analysis was performed on both front and back filters.

2.2.3   Water extraction

Three circular punches 22 mm (diameter) made from the 46 mm (diameter) aerosol filter were stacked and intercalated with silicone O-rings in 25 mm polycarbonate filter holders (Sartorius GmbH, Germany) with the exposed side facing upwards. A cleaned glass syringe (10 mL, ETERNA MATIC, Sanitex SA, Switzerland) was rinsed and filled with ultrapure water (18.2 MΩ·cm, Elga Purelab Flex 2, High Wycombe, UK) and attached to the filter holder with a 21G × 4 3⁄4 inch needle (Sterican, B. Braun, Germany) at the filter holder outlet (Fig. 1). The needle pierced through a 12 mL EXETAINER® vial septum (12 mL, screw cap, item 938 W, Labco Ltd., Lampeter, UK). 5.0 ± 0.2 mL of water passed through the filters by gravity and collected in the EXETAINER® vials. Excess air could exit the vial by opening the screw cap half a turn before needle insertion. After water extraction, the vials were closed and stored at 4 °C until WSOC measurement. Excess water in the filter holder was removed using low-lint tissues and the water-extracted filters were dried overnight. The water-extracted area (18 mm diameter) of the filter disc was punched out to remove the circumference that is not extracted, wrapped in aluminium foil, packed in air-tight plastic bags, and stored in a freezer at -20 °C for subsequent WINSOC removal.

2.2.4   WINSOC removal

WINSOC was removed from the water-extracted filters using a thermal-optical OC/EC analyser (Model 5L, Sunset Laboratories Inc., USA) for separation of EC. WINSOC removal was performed with the first three steps of the Swiss_4S protocol, thus denoted as Swiss_3S. This allows for individual WINSOC removal runs and pooling of several filters for ^{14}C(EC) analysis. The water-extracted filters were cut in quadrants (0.64 cm^2 each) to fit the OC/EC analyser sample holder (10 × 15 mm). Up to 12 WINSOC removal runs per single sample and 24 runs for pooled samples were performed. After WINSOC removal, the filters were stored in a freezer (-20 °C) until ^{14}C(EC) analysis. In the final step, EC was combusted in the thermal-optical OC/EC analyser subjected to online radiocarbon measurement (Agrios et al., 2015). The protocol was modified to compensate for EC losses (see section 2.2.10) observed with the standard protocol (Zhang et al., 2012). WINSOC removal was performed in these three steps: step 1 (pure O_2, 375 °C, 240 s), step 2 (pure O_2, 425 °C, 120 s), and step 3 (pure He, 600 °C, 120s). This procedure provided EC yields >0.7.

2.2.5   Direct ^{14}C(WSOC) measurement

Inorganic carbonaceous impurities were removed by acidification and helium flushing. For this, H_3PO_4 (0.5 mL 8.5 %) freshly prepared from H_3PO_4 (85 %, Suprapur grade, Merck KGaA, Germany) was added using a 1 mL Hamilton (Reno, NV, USA) glass syringe, and high-purity (99.999 %) helium was purged (50 mL min^{-1}) through the sample at room temperature for 3 min. The sample septum was pierced with a custom-made needle with a gas inlet and outlet hole, where the gas outlet was submerged (~1 cm) and the gas inlet was placed in the upper part of the headspace. These steps were robotically performed by a PAL

HTC–xt (CTC Analytics AG, Switzerland) mounted on top of a carbonate handling system (CHS, Ionplus AG, Switzerland).

The chemical wet oxidation procedure was used to oxidise WSOC to CO_2 for radiocarbon measurement (Lang et al., 2012; Wiedemeier et al., 2016). The oxidiser (10 % potassium persulfate (ACS grade, Sigma-Aldrich, USA)) was freshly prepared, dissolved in H_3PO_4 (5 %, m m^{-1}), pre-oxidised (90 °C, 30 min), and flushed with helium (50 mL min^{-1}, 3 min) to remove all carbonaceous contaminants. Oxidiser (0.25 mL) was added to each sample and the reaction progressed overnight at 75 °C on the hot plate of the CHS. For sampling the generated CO_2 (50 mL min^{-1}, 3 min), we used the custom-made needle and PAL autosampler described above. The CHS was connected to a custom-built water trap to retain liquid water in a wash bottle (25 mL), whereas the remaining water vapour was trapped using P_2O_5 (SICAPENT®, Merck KGaA, Germany). The dry gas was then carried to the gas interface system (GIS) and trapped on a X13–zeolite trap (Ruff et al., 2007; Wacker et al., 2013). After sampling, the trapped CO_2 was thermally released and mixed with helium for ^{14}C measurement. We applied a cross-contamination of 0.5 % and a constant contamination of 0.9 ± 0.2 µg C with $F^{14}C = 0.20 \pm 0.08$ on samples subjected to chemical wet oxidation (see Text S5).

2.2.6 Online [14]C(TC) and [14]C(EC) measurement

5.2 cm^2 of each filter (16.6 cm^2) was used for [14]C(TC) analysis and 10.4 cm^2 for pooled samples. [14]C(TC) was measured by complete combustion (240 s, 870 °C, pure O_2) in the Sunset OC/EC analyser before ^{14}C analysis (see section 2.2.7). Complete combustion was ensured by passing through the second furnace of the analyser containing MnO_2 at 870 °C. The evolved CO_2 was analysed by the non-dispersive infrared (NDIR) detector, resulting in 20.2–116.2 µg C and 27.0–99.3 µg C for single and pooled filters, respectively. An equivalent area was used for back filters, yielding 3.4–11.3 µg C and 6.2–11.8 µg C for single and pooled filters, respectively.

For [14]C(EC) analysis, the filters consisting of only EC after water extraction (see section 2.2.3) and WINSOC removal (see section 2.2.4) were combusted in the Sunset OC/EC analyser. Between 3.8 to 15.3 cm^2 of filter material was combusted for EC, yielding 3.9–16.8 µg C. After combustion, the released gas was dried (P_2O_5, SICAPENT®, Merck KGaA, Germany) and transferred to the GIS where CO_2 was trapped and thermally released for on-line measurement in the AMS (Agrios et al., 2015) (see section 2.2.7). We applied a cross-contamination correction of 0.2 % due to a CO_2 adsorption memory effect on the zeolite trap for TC and EC (Salazar et al., 2015). A constant contamination correction of 0.40 ± 0.20 µg with $F^{14}C = 0.80 \pm 0.36$ was applied. To account for EC loss and charring during TOA, $F^{14}C(EC)$ values were corrected using the "COMPYCALC" script (see section 2.2.10).

2.2.7 Radiocarbon measurement

Radiocarbon measurement was performed using a MICADAS (Mini radioCArbon DAting System) accelerator mass spectrometer (AMS) at the University of Bern (Synal et al., 2007; Szidat et al., 2014; Fahrni et al., 2013). On each AMS measurement day, multiple OxII (Oxalic Acid II, SRM 4990 C, National Institute of Standards and Technology, NIST, Gaithersburg, USA) and fossil NaAc (sodium acetate, Sigma-Aldrich, No. 71180) (Szidat et al., 2014) standards were analysed. BATS software version 3.6 (Wacker et al., 2010) was used for standard normalisation as well as data correction for background, blank, and mass-fractionation.

2.2.8 Contamination precautions

All filter handling and water extraction was performed in a laminar flow cabinet. All glassware was cleaned using H_3PO_4 (1M, ACS grade, Merck KGaA, Germany) and pre-fired (500 °C, 5 h), as described by Lang et al. (2012). The vials were leak tested overnight at 75 °C and ~4 bar of N_2. The glass syringe used for water extraction was rinsed before use using ultrapure water and then pre-fired (500 °C, 2 h). The filter holders and silicone O-rings were rinsed and sonicated with ultrapure water before use and dried in a laminar flow cabinet.

2.2.9 EC correction model

OC/EC separation leads to losses of EC during thermal desorption, which needs to be corrected by an $F^{14}C(EC)$ yield extrapolation. The correction supposes that the EC fraction consists of two subfractions, a subfraction with certain volatility at the temperature of steps S1, S2 and S3 and a refractory subfraction. The yield (Y) and $F^{14}C$ of EC (F_{EC}) of the mixture are empirically determined as explained in sections 2.2.9 and 2.2.5, respectively. For further information, Y and F_{EC} are modelled from the mass balance as follows:

$$Y = \frac{m_v + m_{nv}}{m_{v0} + m_{nv0}} = \frac{q_m * \alpha_v + \alpha_{nv}}{q_m + 1} \text{‰} \tag{1}$$

$$F_{EC} = \frac{m_v * F_v + m_{nv} * F_{nv}}{m_v + m_{nv}} = \frac{q_m * \alpha_v * F_v + \alpha_{nv} * F_{nv}}{q_m * \alpha_v + \alpha_{nv}} \tag{2}$$

$$q_m = \frac{m_{v0}}{m_{nv0}} \tag{3}$$

The parameter q_m is the quotient of the initial masses of the non-refractory (m_{v0}) to refractory (m_{nv0}) subfractions and it is calculated with Eq. 3. F_v and F_{nv} are the Fraction Modern of the non-refractory

($F^{14}C = 1$) and refractory ($F^{14}C = 0$) subfractions. α_v is the mass fraction of the non-refractory EC subfraction that withstands the WINSOC removal procedure relative to the initial mass calculated as $a_v = m_v m_{v0}^{-1}$. a_{nv} is the analogue of α_v for the refractory subfraction. Each step of the WINSOC removal has a value of a, which is calculated with Eq. 4 by a first-order kinetic equation

$$\alpha = e^{-t*K(T)} = e^{-t*K(T_{ref})}e^{\left(\frac{E_a}{RT_{ref}} - \frac{b*E_a}{RT}\right)} \tag{4}$$

where t is the step desorption time (s) and the desorption rate K (s^{-1}) is calculated with the temperature-dependent Arrhenius equation. The global a is the joint yield of all the steps $a = a_1*a_2*a_3$. Bedjanian et al. (2010) also used a first-order kinetic coupled to Arrhenius for investigating the thermal desorption of polyaromatic hydrocarbons (PAH) from soot surfaces. The main composition of EC fraction is soot with compounds molecularly similar to PAHs of diverse sizes. Bedjanian et al. (2010) found that the activation energy (E_a) for PAH is in the range of 85 kJ mol^{-1} to 134 kJ mol^{-1} linearly depending on the molecular weight for the range of 178-302 g mol^{-1}. The desorption rate K was ranging from 3×10^{-3} s^{-1} to 5×10^{-5} s^{-1} for a temperature range of 370–350 K. The Arrhenius pre-exponential factor was solved by using the concept of the reference temperature (Peleg et al., 2012; Schwaab and Pinto, 2007). The scale of the desorption rate K is logarithmic, meaning that a small increase or decrease in temperature leads to a substantial change in the desorption rate. Our optimised E_a is 100 kJ mol^{-1}, and our reference desorption rate K is 1.5×10^{-6} s^{-1} at 340 K (T_{ref}) which is in the range of the desorption rates from Ghosh et al. (2001) converted from room temperature to our reference temperature. The data can be found in Table 3 of Ghosh et al. (2001) with values between 1.2×10^{-9} to 3.6×10^{-9} s^{-1} at 293 K ($E_a = 116$ to 133 kJ mol^{-1}), which results in desorption rates at $T_{ref} = 340$ K of 9×10^{-7} to 7×10^{-6} s^{-1}. The activation energy for the refractory fraction is unknown, but we may assume that the molecular weights of the compounds of the refractory fraction are much heavier. Bedjanian et al. (2010) showed a linear relationship between molecular size and volatility with E_a; therefore, we introduce an empirical factor b, which represents how much bigger E_a is for the refractory relative to the non-refractory fraction as shown in Eq. 5. E_a and $K(T_{ref})$ values were kept within the references ranges and optimised with the data from our previous works (see section 2.3.1 and Fig. S2 in Zotter et al., 2014); E_a and $K(T_{ref})$ were taken from the references; t and T were fixed to the WINSOC removal conditions.

$$E_{a_{nv}} = b * E_{a_v} \tag{5}$$

The values for the parameters b and q_m are optimised for each individual sample as follows. The q_m and b parameters are selected, the mathematical model estimates α for both refractory and non-refractory

fractions with Eq. 4 and Eq. 5. Then the yield and F_{EC} are calculated with Eq. 1 and Eq. 2. The yield and F_{EC} from the model are compared with the empirical yield and F_{EC} using a cost function shown in Eq. 6. The cost function is minimised by a gradient descent method from the R script. q_m and b are not general parameters or general coefficients; usually their values are different between samples because their molecular compositions are different. The number of data values in the cost function is only two.

$$J(q_m, b) = \left[F_{EC,data} - F_{EC,model}(q_m, b)\right]^2 + \left[Y_{data} - Y_{model}(q_m, b)\right]^2 \tag{6}$$

Our model is a two-component model used to describe a multicomponent system. Two-component models are common: for example, the Keeling approach to describe the mixing of one component onto a background component in complex atmospheric air or dissolved organic carbon in ocean waters (Keeling, 1958; Walker et al., 2016). Each refractory and non-refractory subfraction are composed of a complex mixture of compounds with a continuum of volatilities and ^{14}C content. However, the mean desorption energy of the subfractions obeys Eq. 5. The ^{14}C content of both subfractions is not exactly 1.0 or 0.0 but a continuum where the mean $F^{14}C$ of the refractory subfraction trends to fossil values while the opposite occurs to the non-refractory subfraction.

2.2.10 EC and OC correction calculations

The $F^{14}C(EC)$ yield extrapolation and charring correction was performed with a script named COMPYCALC (COMprehensive Yield CALCulation) written in R (R Core Team, 2020), available on GitHub (github.com/martin-rauber/compycalc) and archived in Zenodo (Rauber and Salazar, 2022). Using Eq. 7, an initial value of $F^{14}C(OC)$ is calculated prior running the script using the uncorrected $F^{14}C(EC)$ value, as $F^{14}C(OC)$ is needed for the charring correction (see Table S1). F_{TC} and F_{EC} are the radiocarbon values (Fraction Modern, $F^{14}C$) for TC and EC before correction, respectively, whereas r is the EC/TC ratio.

$$F_{OC} = \frac{F_{TC} - F_{EC} * r}{1 - r} \tag{7}$$

The EC yield was calculated using the laser transmission signal (655–660 nm) of the OC/EC analyser. Each WINSOC raw data file from the Sunset OC/EC analyser is loaded by the COMPYCALC script. The laser transmission is dependent on the temperature (Peterson and Richards, 2002). By applying a correction on the complete laser signal of the thermogram, this temperature–induced change in transmission is accounted for. For COMPYCALC, a generic file corresponding to the S4 step in the Swiss_4S protocol is used for the calculation of the temperature dependence correction of the laser transmission signal. The EC yield (Y)

after the three WINSOC removal steps was calculated as the ratio of the attenuation (ATN) after S3 to the initial ATN after water extraction. ATN is a unitless parameter proportional to the light-absorbing EC mass calculated using the Beer-Lambert Law and the laser transmission signal (Gundel et al., 1984; Zhang et al., 2012). Here, the temperature-dependence correction of the laser transmission signal is applied. Formation of pyrolysed OC (i.e., charring, see below) is quantified by the ratio of the difference between the maximum ATN and the initial ATN of each step (Gundel et al., 1984; Zhang et al., 2012; Vlachou et al., 2018). When filter punches do not cover the sample holder spoon area completely, small filter movements from vibrations caused by the OC/EC analyser may occur. This may inflict faulty laser signals when filters are smaller than the sample holder area (10 × 15 mm). WINSOC removal is usually performed on multiple filter cuts and EC yield and charring is calculated for each filter cut. COMPYCALC filters by the interquartile range of < 1.5 individually for EC yield and charring in S1, S2, and S3, and removes the row(s) containing outliers in the data frame. The number of filters cuts used for calculation is summarised in Table S5. The COMPYCALC summary output (see Fig. S2 and Table S2) only includes the filtered data, however, the raw data (not filtered) is preserved and given as an output as well. The EC yield and charring before filtering is shown in Table S6.

The measured F^{14}C(EC) values (F_{EC}) were extrapolated to 100 % EC yield ($F_{EC(corr)}$) using Eq. 9 to account for the EC loss during WINSOC removal. For the empirical data, the yield Y and the F_{EC} are directly measured while α is calculated with Eq. 4 The reader must note that Eq. 8 is obtained when Eq. 1 is input in the denominator of Eq. 2 and solving for parameter q_m. If $Y = 1$, then Eq. 8 becomes the F_{EC} extrapolated at 100 % yield (Eq. 9).

$$F_{EC} = \frac{q_m * \alpha_v * F_v + \alpha_{nv} * F_{nv}}{Y(1 + q_m)} \tag{8}$$

$$F_{EC(corr)} = \frac{q_m * F_v + F_{nv}}{1 + q_m} \tag{9}$$

Beside extrapolation to 100 % EC yield, the Fraction Modern must be corrected for charring as some OC is pyrolysed into EC. The charring corrected Fraction Modern (F_{charrA}) is calculated in Eq. 10 using the Fraction Modern of EC ($F_{EC(corr)}$) extrapolated to 100 %. Fraction Modern of OC (F_{OC}) was previously calculated using Eq. 7, ε is the total charring. It is assumed that 50 % of the pyrolysed OC is lost in the subsequent temperature steps as EC loss again, thus a factor of 0.5 is used for correction of these losses of pyrolysed OC (Zotter et al., 2014). For Eq. 11, the Fraction Modern of EC without extrapolation to 100 % EC yield is used. In Eq. 12, the Fraction Modern with charring correction (F_{charrC}) is calculated with the charring correction slope β and EC yield (Y). β is the slope between the Fraction Modern and EC yield as

defined previously (Zotter et al., 2014; Zhang et al., 2012). The final Fraction Modern with charring correction in Eq. 13 is calculated as the mean of Eq. 10 and Eq. 12.

$$F_{charrA} = \frac{F_{EC(corr)} - F_{OC} * 0.5 * \varepsilon}{1 - 0.5 * \varepsilon} \tag{10}$$

$$F_{charrB} = \frac{F_{EC} - F_{OC} * 0.5 * \varepsilon}{1 - 0.5 * \varepsilon} \tag{11}$$

$$F_{charrC} = \beta * (1 - Y) + F_{charrB} \tag{12}$$

$$F_{EC(final)} = \frac{F_{charrA} + F_{charrC}}{2} \tag{13}$$

After all calculations, a data file with overall EC yield, the charring contribution for each OC removal step (S1, S2, S3), the total charring contribution as well as the F[14]C(EC) input value F_{EC}, F[14]C(EC) extrapolated to 100 % EC yield ($F_{EC(corr)}$), and F[14]C(EC) extrapolated to 100 % EC yield and corrected for charring ($F_{EC(final)}$) is generated as an output. The final F[14]C(OC) is calculated using Eq. 7 with $F_{EC(corr)}$ and reported as $F_{OC(corr)}$.

2.2.11 EC yield calculation and WINSOC amount calculation

EC yield calculation and amount calculation of each WINSOC step was performed with the R script "Sunset-calc", written as an R Shiny application (R Core Team, 2020; Chang et al., 2017). Sunset-calc provides amount calculation for each step in the Swiss_3S and Swiss_4S protocols (Zhang et al., 2012) as well as EC yield and charring calculation (see Table S7). Furthermore, EC yield and charring corrected OC (WINSOC) and EC amounts are calculated (see Table S4). The Sunset OC/EC analyser raw files are loaded in a web graphical user interface and the results are received as a downloadable file. EC yield and charring calculation is based on COMPYCALC as described in 2.9. The amount calculation is made with an integration of the NDIR signal. The application has been deployed on an R server (14c.unibe.ch/sunsetcalc). Sunset-calc is available on GitHub (github.com/martin-rauber/sunset-calc) and archived in Zenodo (Rauber, 2021).

2.3 Results and Discussion

2.3.1 Validation of the correction

Figure 2a shows the comparison of the modelled F_{EC} versus the empirical F_{EC}, and Fig. 2b shows the modelled EC yield versus the empirical EC yield. The empirical data is taken from Fig. S2 of our previous work (Zotter et al., 2014). Figures 2a and 2b indicate that our model provides good accuracy for predicting the FEC and the EC yields. We determined a relative accuracy of 109 ± 4 % as an agreement of the measured values compared to the modelled values using a linear model and its residual standard uncertainty. Therefore, the b and q_m values are reliable. Figure 2c indicates that the b parameter falls into two volatility groups. The group close to $b = 1.0$ and the group mainly within 2.0 to 2.5. These are interesting results as the initial value for b is 2.0 at the start of the gradient descend optimisation. We examined the optimisation again and the script does check values in the range of 1.0 to 2.0. Figure 2c is an indirect probing of the volatility of the sample compounds. Figure 2d shows the calculated parameters for each sample revealing that q_m increases with F_{EC}. This indicates that for higher F_{EC} values, closer to the atmospheric non-fossil levels, the initial mass of the non-refractory biogenic EC (section 2.2.9) subfraction must be higher than the initial mass of the more fossil refractory EC subfraction.
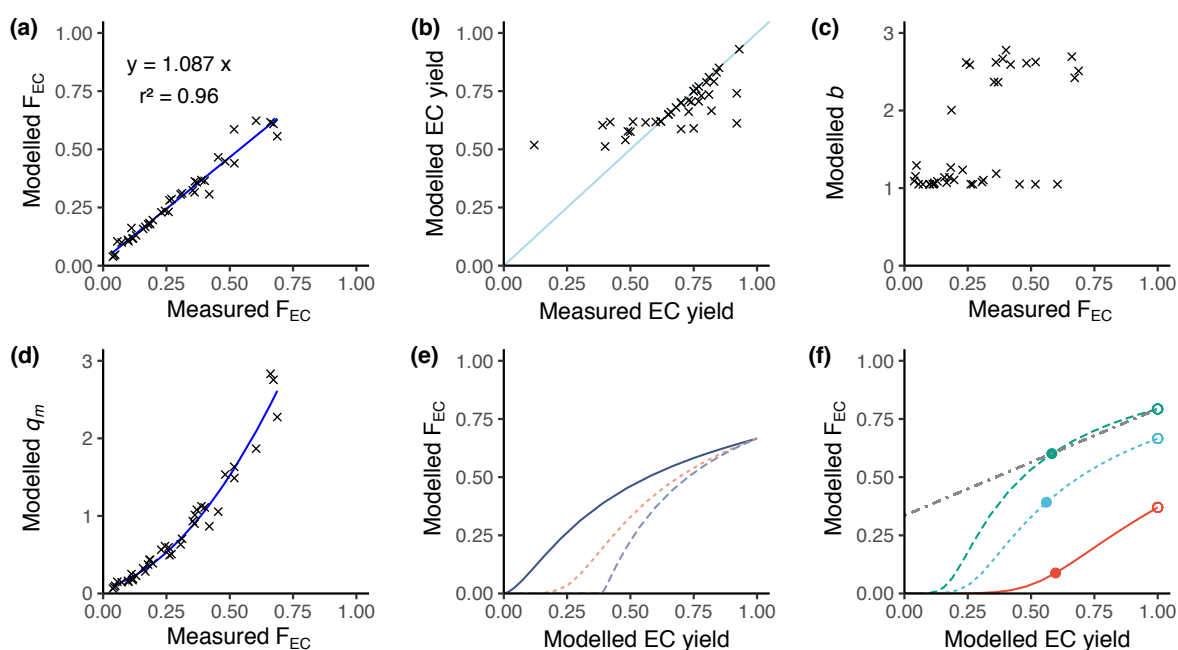
Figure 2: Summary of the modelled EC correction to an EC yield = 1. a) Model accuracy: modelled F_{EC} vs measured F_{EC}. b) Modelled EC yield vs measured EC yield according to Zotter et al. (2014) (see text). c) Model calculated parameters b. d) Model calculated parameters q_m. e) General behaviour of F_{EC} vs EC yield for different b values (solid line $b = 1.1$, dashed line $b = 1.2$, long-dashed line $b = 1.5$) with a fixed q_m of 1.5. f) General behaviour of F_{EC} vs EC yield for different q_m values (solid line $q_m = 0.5$, dashed line $q_m = 1.5$, long-dashed line $q_m = 2.5$) with a fixed b value of 1.2 and a linear model (dot-dashed line) for a sample with extrapolation at EC yield = 1. Filled dot shows the measured value and the open dots show the value after extrapolation.

Figure 2e provides examples of the modelling of the F_{EC} versus the modelled EC yields for different values of the parameter b. The EC yield is decreased by proportionally increasing the temperature of each of the three steps of the WINSOC removal. The model allows us to extrapolate the F_{EC} value of any sample with a yield lower than 100 % to the F_{EC} value corresponding to 100 % yield, which defines the correction for EC loss. According to the Arrhenius approach, the model has a non-linear shape which may be approximated by a linear model in the region of EC yields higher than 0.5. Before developing this non-linear model, we applied a simple linear model for the EC loss correction according to previous publications (Zotter et al., 2014). The measurement conditions usually keep the EC yield higher than 0.4, thus the linear model remains useful under certain conditions. Nevertheless, the non-linear model is superior and shall be used in future. Figure 2f is similar to Fig. 2e but for different q_m values. As shown in Zotter et al. (2014), different samples may show different slopes and intercepts for the linear model. Figure 2e and Fig. 2f show that different values of b and q_m explain the different slopes and intercepts observed previously in the data. Extrapolation and correction to $F_{EC(corr)}$ of the data from Zotter et al. (2014) is shown in Fig. S6. In Fig. S6, same-colour results belong to punches from the same filter, however the experimental conditions of their online TC/EC measurements were variated in order to obtain different yields and F_{EC} values. Therefore, the same-colour results in Fig. S6, ideally, should have the same F_{EC} value extrapolated to 100 % yield. As indicated in section 2.2.9, this data was useful to optimise the E_a and $K(T_{ref})$ values by minimising the differences between the yield-corrected F_{EC} of the same-colour results. This optimisation was performed prior to the application of the non-linear model to the results of this paper.

2.3.2   Concentrations of carbonaceous aerosols

Results from the 21-month sampling period (Table 1) showed a mean TC concentration of 137 ng C m^{-3} (range: 65–264 ng C m^{-3}) and a mean EC concentration of 14 ng C m^{-3} (range:3–40 ng C m^{-3}), resulting in a mean OC/EC ratio of 11.7 (range: 4.5–27). The filter sampled from 28 September to 06 October 2017, had elevated TC (601 ng m^{-3}) and EC (52 ng C m^{-3}) levels, and were excluded from the mean reported above as this would clearly distort the mean. The OC/EC ratio for this filter sample was 10.5 and thus comparable to the mean of the other samples. For 5 of the 13 samples, two consecutive filter samples were pooled to obtain a sufficient carbon amount for ^{14}C analysis (see Table 1).

Table 1: OC/EC ratios and filter loadings measured by NILU using the EUSAAR_2 protocol. Filters that were pooled for 14C analysis are marked with an asterisk.

Start date	End date	TC	EC	OC	OC/EC ratio
		ng C m^{-3}	ng C m^{-3}	ng C m^{-3}	
23 Feb 2017	02 Mar 2017	256	40	216	5.4
05 May 2017	15 May 2017	158	24	135	5.7
31 May 2017	26 Jun 2017	123	6	117	20.5
*08 Sep 2017	28 Sep 2017	114	6	108	16.7
28 Sep 2017	06 Oct 2017	601	52	549	10.5
*06 Oct 2017	24 Oct 2017	88	8	81	10.4
*05 Dec 2017	21 Dec 2017	73	12	61	7.7
23 Jan 2018	31 Jan 2018	174	16	157	9.6
21 Mar 2018	29 Mar 2018	127	18	109	6.1
06 Apr 2018	16 Apr 2018	129	17	111	6.4
*12 Jul 2018	30 Jul 2018	65	3	62	20.7
*30 Jul 2018	15 Aug 2018	264	9	254	27.0
23 Nov 2018	03 Dec 2018	72	13	59	4.5
*Pooled filters					

Table 2: WINSOC amounts for each step of the Swiss_3S protocol measured at the University of Bern and corresponding WSOC amounts. Fraction S1 is considered pure WINSOC, whereas S2 and S3 are mixed fractions of WINSOC and EC. WSOC was determined by subtraction of EC and total WINSOC from TC.

Start date	End date	WINSOC (ng C m^{-3})				WSOC	WSOC/WINSOC
		S1	S2	S3	total	ng C m^{-3}	ratio
23 Feb 2017	02 Mar 2017	43	10	16	70	92	1.6
05 May 2017	15 May 2017	20	3	8	31	70	2.5
31 May 2017	26 Jun 2017	71	9	12	93	4	<0.1
*08 Sep 2017	28 Sep 2017	13	1	2	16	15	1.6
28 Sep 2017	06 Oct 2017	111	26	27	164	284	1.9
*06 Oct 2017	24 Oct 2017	9	1	2	12	15	1.7
*05 Dec 2017	21 Dec 2017	13	1	4	18	0	1.3
23 Jan 2018	31 Jan 2018	33	5	15	54	59	1.1
21 Mar 2018	29 Mar 2018	29	3	5	38	57	1.6
06 Apr 2018	16 Apr 2018	26	4	8	37	54	1.5
*12 Jul 2018	30 Jul 2018	11	0	1	13	7	0.7
*30 Jul 2018	15 Aug 2018	23	2	3	28	65	2.7
23 Nov 2018	03 Dec 2018	22	5	4	32	26	0.9
*Pooled filters							

Lower TC values were seen in winter (November to March) compared to summer (April to October), whereas it was the other way around for EC. Consequently, the OC/EC ratio shows a seasonality with lower values in winter and higher in summer. TC on back filters had a mean concentration of 152 ng C m⁻³ (range: 63–254 ng C m⁻³) and showed no seasonality. The mean pure WINSOC concentration (Table 2), corresponding to Step 1 of the Swiss_3S protocol, was 26 ng C m⁻³ (range: 9–71 ng C m⁻³), whereas the mixed (WINSOC + EC) S2 and S3 fractions had mean concentrations of 4 ng C m⁻³ (range: 0.5–26 ng C m⁻³) and 7 ng C m⁻³ (range:1.5–16 ng C m⁻³). The aforementioned high loading filter sample from the transition September/October 2017 (111 ng C m⁻³ (S1), 26 ng C m⁻³ (S2), and 27 ng C m⁻³ (S3)) were excluded from the mean. The total amount of WINSOC including EC loss was 37 ng C m⁻³ (range:1.5– 16 ng C m⁻³, excluded filter: 164 ng C m⁻³). WSOC was calculated by subtracting EC and total WINSOC from TC, which gave a mean of 39 ng C m⁻³ (range: 0.5–92 ng C m⁻³). The September/October 2017 filter sample had a loading of 284 ng C m⁻³ and was excluded from the mean. The charring and EC loss corrected mean amount calculated with Sunset-calc (see section 2.2.11, Table S4) for WINSOC was 34 ng C m⁻³ (range: 11–90 ng C m⁻³, excluded filter: 151 ng C m⁻³) and the mean corrected amount for EC was 15 ng C m⁻³ (range: 3.7–39 ng C m⁻³, excluded filter: 67 ng C m⁻³). For these calculations and corrections, the R Shiny application Sunset-calc was necessary as this is not possible with the default software tools provided for the Sunset OC/EC analyser. ¹⁴C(TC) measurements on back filters (see Table 3) revealed a mean filter loading of 90 ng C m⁻³ (range: 26–189 ng C m⁻³) excluding the autumn 2017 filter, which had a back filter loading of 501 ng C m⁻³.

Table 3: Filter loadings and fractions for front and back filters for TC measured at the University of Bern. n.d. means not determined.

Start date	End date	TC front filter ng C m⁻³	TC back filter ng C m⁻³	TC$_P$ ng C m⁻³
23 Feb 2017	02 Mar 2017	189	n.d.	n.d.
05 May 2017	15 May 2017	121	28	93
31 May 2017	26 Jun 2017	113	26	87
*08 Sep 2017	28 Sep 2017	39	11	29
28 Sep 2017	06 Oct 2017	501	49	453
*06 Oct 2017	24 Oct 2017	35	10	25
*05 Dec 2017	21 Dec 2017	36	9	27
23 Jan 2018	31 Jan 2018	135	14	121
21 Mar 2018	29 Mar 2018	109	15	94
06 Apr 2018	16 Apr 2018	105	35	70
*12 Jul 2018	30 Jul 2018	26	n.d.	n.d.
*30 Jul 2018	15 Aug 2018	104	n.d.	n.d.
23 Nov 2018	03 Dec 2018	67	12	54

*Pooled filters

2.3.3 Development of preparation methods

Water extraction

For water extraction, three filter punches were stacked to maximise the amount of extractable WSOC. Prior to filter sample extraction, trials with empty filters and the screw type polycarbonate water extraction unit were made. Stacking more than three filters was not feasible, as it makes the water extraction housing prone to leakage. The sample water extraction was gravity-fed. Ultrapure water was filled in the pre-combusted glass syringe directly from the tap of the ultrapure water system and screwed onto the previously assembled water extraction unit to avoid unnecessary liquid transfer. The extraction of 5 mL took 2-3 min depending on the number of filters stacked.

The water-extracted filter material was subjected to WINSOC removal and EC measurement. Elimination of WSOC is beneficial as it is shown to pyrolyse into EC (charring) when subjected to thermal-optical analysis (Yu et al., 2002; Cadle et al., 1980). The $F^{14}C(OC)$ is generally higher than for $F^{14}C(EC)$ (Szidat et al., 2004b, 2009; Zhang et al., 2012), but often exceeded by $F^{14}C(WSOC)$ due to substantial contributions from biogenic sources and biomass-burning emissions (Zhang et al., 2014a; Kirillova et al., 2013; Weber et al., 2007). Therefore, a small contribution of charred OC significantly biases the measured $F^{14}C$ of the EC fraction, which is prevented by the WSOC removal.

Adaptations of the OC/EC analyser for WINSOC removal

The filter holders for water extraction are of screw type, thus round punches were required for water extraction. For WINSOC removal, a single layer of filter material cannot exceed the area (1.5 cm^2) of the sample holder spoon in the Sunset OC/EC analyser. Although it is not necessary to fully cover the sample holder area, the filter cut should cover most the area to utilise the laser transmission signal for calculations. Stacking of filters should be avoided, as lower filters may not encounter the same conditions as the topmost filter, especially in terms of oxygen supply, which may cause differences with respect to both charring and EC losses within the stack. Furthermore, calculating an EC yield is not feasible after stacking two or more filters. We observed spikes in the laser transmission signal for small filter punches (<0.5 cm^2), possibly due to filter movements caused by instrument vibrations. Due to the limitation of circular cuts for water extraction and a rectangular shaped sample holder in the OC/EC analyser, the water-extracted filter was cut in quadrants. This enables the complete use of filter material; however, at the expense of a more labour intensive WINSOC removal. The three water-extracted punches from each filter were cut into 12 quadrants and 24 for each pooled sample. WINSOC was then removed from each sector using the Swiss_3S protocol (Zhang et al., 2012), requiring 18.5 min per run. High EC losses were observed with the standard Swiss_3S protocol, hence the protocol was adapted. Decreasing the temperature from 450 to 425 °C in S2 and from 650 to 600 °C in S3 increased EC yields from < 0.4 to 0.6. Shortening the 600 °C pure He step in S3 from 180 s to 120 s, further reduced EC losses, leading to a mean EC yield of 0.87 (range: 0.72–0.95) (Figs. 3 and 4). As shown in Fig. 4, the average charring after WINSOC removal was 2.8 % (range of 1–6.8 %) for S1,

0.6 % (0–2.4 %) for S2, and 3 % (1.3–9.0 %) for S3, with a total charring of 6.5 % (2.5–12.9 %). The OC and EC concentrations must be corrected for charring and EC losses using Sunset-calc (see sections 2.2.11 and 3.2). This enables a simple WINSOC removal protocol optimisation and adaptation after each run. The outcome of Sunset-calc is also employed for the correction of biases of ^{14}C(EC) results caused by charring and EC losses.
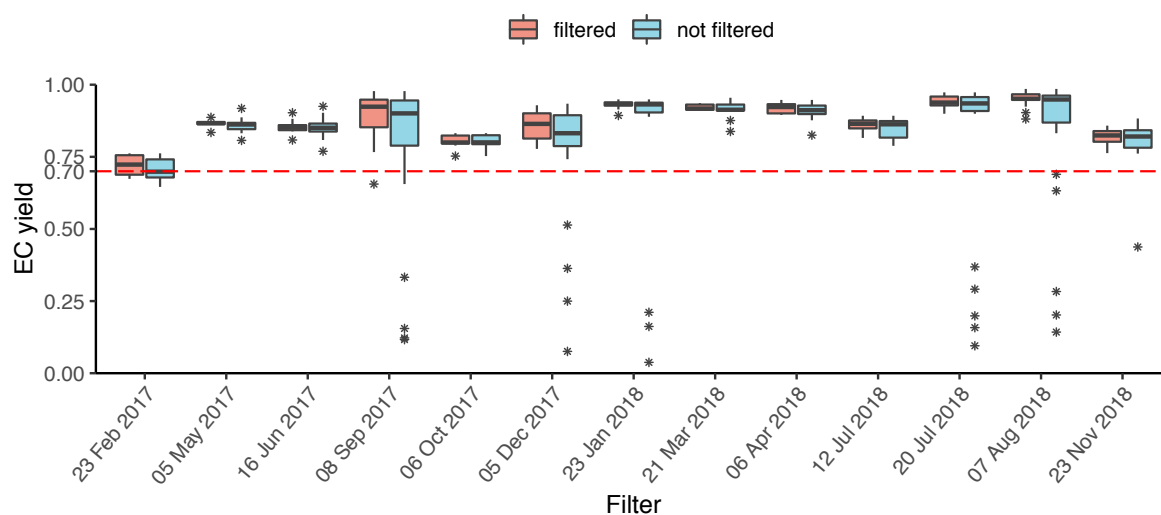
Figure 3: EC yield after WINSOC removal for each filter with the sampling start date. Filtered (WINSOC removal containing outliers in EC yield, fraction of charring S1, S2, or S3 removed) and unfiltered EC yields for each filter shown. The box plot box shows the first and third quartiles with the mean as a thick horizontal line for the individual groups (filtered and not filtered). The values outside the 3/2 interquartile range are shown with an asterisk. The horizontal line at 0.7 shows that at least 70 % of the initial EC has been recovered.

In the present work, WINSOC was removed, but not subjected to radiocarbon measurement due to the very low filter loading. In the Swiss_3S protocol, only the S1 fraction consists of pure WINSOC, as S2 and S3 are considered a mixture of WINSOC and EC. The average WINSOC loading in S1 was 1.8 μg C cm^{-2}, ranging from 0.9 to 3.7 μg C cm^{-2}, whereas radiocarbon measurements require at least 3 μg C. With higher loaded filters, ^{14}C(WINSOC) measurements can be implemented in the workflow presented.
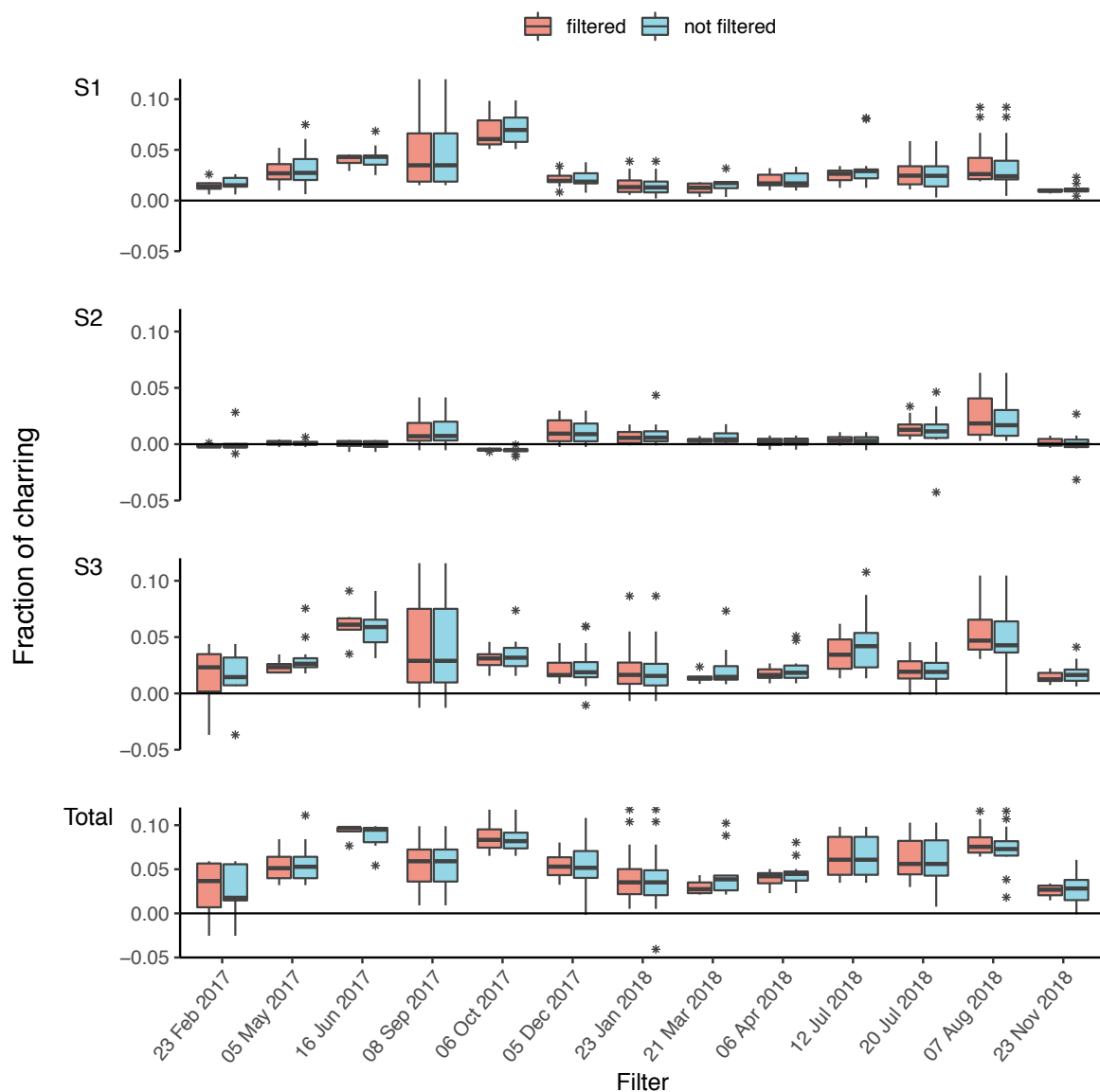
Figure 4: Fraction of charring observed for each filter at the individual steps (S1, S2, S3) and the total (sum of S1, S2, S3) with the sampling start date. Filtered (WINSOC removal containing outliers in EC yield, fraction of charring S1, S2, or S3 removed) and unfiltered fractions of charring for each filter shown. The fraction of charring describes the amount of artificially produced EC by charring OC related to the amount of EC on the filter based on the laser transmission signal, i.e., a total charring of 0.05 means a 5 % contamination of the total EC amount.

Wet oxidation and WSOC measurement

Filter extraction and chemical wet oxidation may add contaminants and stringent preparations (section 2.2.5) were needed to ensure low procedural blanks. This included the use of acid-cleaned (high purity grade H_3PO_4) and baked out glassware, and pre-oxidation of the oxidiser solution used to remove contaminants. The freshly prepared oxidiser solution was pre-oxidised at 90 °C for 30 min before helium flushing with helium to remove carbonaceous contaminants. This step removes contaminants in the oxidiser itself as well

as in the ultrapure water and equipment used. The oxidiser concentration was increased to 10 % from 4 %, whereas the amount of oxidiser added to the sample was reduced to 0.25 mL from 1 mL, compared to Lang et al. (2012). Oxidation was performed at 75 °C overnight, deviating from previous studies by Lang et al. (2012) (100 °C for 60 min) and Lang et al. (2013) (90 °C for 30 min). EXETAINER® vials store gas with little leakage even after multiple needle punctures (Glatzel and Well, 2008). Al vials used for samples, standards and blanks were leak tested before use (section 2.2.8) at the same temperature (75 °C) as the oxidation step takes place. Vials are more prone to leakage at higher temperatures; hence we lowered the reaction temperature to 75 °C. Both leak testing and a lower reaction temperature kept loss of precious sample material at a minimum. The sample acidification, helium flushing, and chemical wet oxidation was performed the day before measurement. The butyl rubber septum of the EXETAINER® may contaminate the sample over time when exposed to the strongly acidic and oxidative environment. As a cautionary principle, samples should be measured the day after preparation to minimise any losses, contaminations, and potential isotopic fractionation. In the present work, helium was purged at 75 °C with the gas needle through the oxidised sample, unlike Lang et al. (2012), where only the headspace was sampled at room temperature. Considerable amounts of liquid (~0.3 mL per sample) that were carried with the gas were trapped in a custom-build gas wash bottle (25 mL). Remaining water vapour was removed by a Sicapent® trap (P_2O_5 on inert carrier material) to protect the zeolite trap in the gas interface system (GIS). The CO_2 amount was determined by the GIS pressure gauge based on the ideal gas law before dilution with helium and feeding the gas mixture into the ion source of the AMS. This procedure provides an estimation of the amount of WSOC only.

Procedural blank

The WSOC procedural blank was determined by performing the water extraction and wet oxidation procedure, using pre-baked (2 h, 750 °C) quartz fibre filters (PALLFLEX® Tissuquartz 2500QAT-UP), as described in section 2.2.3. After extraction, different amounts of OxII (SRM 4990 C) or fossil NaAc solutions (~1000 ppm) were added to the vials and subjected to chemical wet oxidation (section 2.2.4). The mass and Fraction Modern of the contaminant was determined based on the constant contamination approach by a drift model (Hanke et al., 2017; Salazar et al., 2015) (see Supplementary Material, Fig. S7). In previous studies, the WSOC eluate was dehydrated by lyophilisation before re-dissolving and combustion in an elemental analyser coupled to an AMS (Zhang et al., 2014a). Compared to the lyophilisation method, the procedural blank was lower for chemical wet oxidation, with a mass of contamination of 0.9 ± 0.2 µg C and the corresponding $F^{14}C$ of 0.20 ± 0.08.

2.4 Radiocarbon results

2.4.1 Correction of the ^{14}C(EC) results

Early approaches of ^{14}C(EC) measurements focused on the separation of OC and EC (Zhang et al., 2012; Barrett et al., 2015; Zencak et al., 2007), however, some OC pyrolyses into EC creating a positive artefact, and some EC is lost by desorption, degradation or oxidation (Cadle et al., 1980; Yu et al., 2002; Gundel et al., 1984; Zhang et al., 2012), but efforts to correct ^{14}C(EC) were not considered then (Szidat et al., 2006, 2004b, a; Dusek et al., 2014; Andersson et al., 2011; Bernardoni et al., 2013). Zhang et al. (2012) implemented a linear correction for EC losses to account for the underestimation of biomass burning EC. The composition of OC and EC underlies spatial and temporal variability and thus the linear correction slope will differ. Zotter et al. (2014) addressed this issue by introducing different slopes for winter and summer, as the linear correction slope for EC differs considerably between these two seasons. Consequently, the linear correction slope must either be established for each site with multiple EC yield measurements or estimated based on previous measurements. For low-loaded filters and for sites with limited filter availability such as the Arctic, this can be a particular challenge. Here, we apply an optimised approach, using COMPYCALC that combines the determination of both EC losses and EC bias from charring of OC with the thermal desorption model (section 2.2.10). Furthermore, COMPYCALC uses the basis of Zhang et al. (2012) for the EC yield calculation and the charring calculation, where the attenuation (ATN, section 2.2.10) calculated from the laser transmission signal is used. Charring correction after EC yield extrapolation was performed in accordance with Zotter et al. (2014), assuming that half of the pyrolytic EC that forms during the analysis is lost by the last heating step during WINSOC removal. Table 4 summarises EC and OC before and after corrections for EC yield and charring. The initial F^{14}C(OC) value (F_{OC}) is calculated with the initial EC value (F_{EC}) for correction. As described in section 2.2.10, the COMPYCALC script is run for the extrapolation of EC yield and charring correction to yield the final corrected EC value ($F_{EC(final)}$). Then, using $F_{EC(final)}$, the final OC value ($F_{OC(final)}$) is calculated.

2.4.2 Quality aspects of the F^{14}C(OC) calculation

Thermal-optical OC/EC separation discussed in the present work focuses on EC and WSOC and the optimisation thereof. Early work on ^{14}C analysis did not include measures to reduce charring, which included substantial biases in the ^{14}C analysis particularly for EC but also for OC, as ^{14}C(OC) was determined directly by combustion of the filters in oxygen at 340 °C (Szidat et al., 2004b). Later work included water extraction for charring reduction of EC (Yu et al., 2002; Novakov and Corrigan, 1995). Zhang et al. (2012) combined water extraction with an optimised four-step protocol and, thus, further improved OC/EC separation. However, only S1 was considered as pure OC in this first TOA protocol and thus may include two possible biases of the ^{14}C(OC) result, as different OC fractions were not considered: first, the portion of OC that undergoes charring in S1 and, thus, is shifted to later steps, and second, more refractory OC that evolves during S2 and S3. This flaw was improved later by Zhang et al. (2015) by

omitting the direct ^{14}C measurement of OC, calculating F^{14}C(OC) as the difference between F^{14}C(TC) and F^{14}C(EC), as it is in the present study (Eq. 7). Hence, a better OC/EC separation improves both the quality of the measured F^{14}C(EC) value and the calculated F^{14}C(OC) value.

2.4.3 Measurement limitations

Radiocarbon measurement requires a minimum of 2-3 μg C per sample disregarding of the hyphenation method (Wacker et al., 2013). With the setup used in the present work, the water extraction method is limited by extraction setup diameter and the number of punches to be stacked. Accordingly, for WSOC a minimum filter loading of 0.3 μg C cm^{-2} is required. Within reason, there is no known limit for the chemical wet oxidation. Radiocarbon measurements coupled with the Sunset OC/EC analyser are limited by the sample holder, allowing for stacking up to six rectangular 1.5 cm^2 filters punches (9 cm^2 in total). In the present work, the remains after punching out the circular filters for WSOC were used for TC, which makes it difficult to fit the material on the regular sample holder. For pooled samples, the filter area used for TC was 10.4 cm^2, slightly exceeding the 9 cm^2 limit. Therefore, for TC combustion we used a custom-build quartz spoon, on which up to 16 cm^2 of filter material can be placed and combusted. Filter stacking must be omitted for ^{14}C(WINSOC) measurement. For this reason, filter loadings for S1 (pure WINSOC) of the Swiss_4S protocol must be >2 μg C cm^{-2}. ^{14}C(WINSOC) measurements were omitted in the current study, as only four of the 13 samples had a filter loading >2 μg C cm^{-2} with a mean loading of 1.8 μg C cm^{-2} (range: 0.9–5 μg C cm^{-2}).

2.4.4 Radiocarbon results

Radiocarbon measurements of TC show a dominant input from fossil carbon in winter months with an average F^{14}C of 0.85 ± 0.17 (Table 5). F^{14}C values close to non-fossil levels of radiocarbon were found for spring, summer, and autumn with an average F^{14}C of 0.95 ± 0.09 with the highest levels in spring and late summer. Large variations in ^{14}C(EC) were observed, ranging from 0.22 to 0.92 (mean: 0.66 ± 0.16). Both the highest and lowest value were observed in winter (23 Feb – 2 Mar 2017 and 23 – 31 Jan 2018), showing that the relative source composition of Arctic carbonaceous aerosol can vary widely within a season. The highest ^{14}C(EC) value had the second highest EC concentration (40 ng C m^{-3}) and an OC/EC ratio of 5.4, whereas the sample with the very low Fraction Modern carbon had an EC concentration of 16 ng C m^{-3} and OC/EC ratio of 9.6. Notably, the ^{14}C(WSOC) content of the high Fraction Modern carbon sample (1.077) was substantially higher than that of EC indicating different sources of WSOC and EC. Overall, ^{14}C(WSOC) values showed non-fossil levels of radiocarbon with maxima in spring and late summer and lower values in early summer and winter. The 31 May to 26 Jun sample had the lowest ^{14}C(WSOC) value (0.38), being even lower than the corresponding ^{14}C(EC) value (0.689), whereas the calculated value for F^{14}C(OC) (0.93) consisted overwhelmingly of carbon from non-fossil sources. Although this might look contradictory, an explanation can be derived from the concentration of the various fractions. The WSOC concentration was very low (4 ng C m^{-3}), indicating a higher uncertainty, whereas the concentration of

WINSOC + EC loss (WINSOC removal with Swiss_3S) was 93 ng C m^{-3}, of which pure WINSOC (S1) accounted for 71 ng C m^{-3}. Thus, WINSOC sources were largely non-fossil.

2.5 Conclusions

In the current study, we present an optimised separation procedure for radiocarbon measurements of TC, EC, and WSOC. Prior to thermal-optical OC/EC separation, a water extraction step was used to minimise charring and to provide eluates for ^{14}C(WSOC) measurement. Our method enables radiocarbon source apportionment of the EC and WSOC fraction in addition to TC, and, when sufficiently loaded filters are available, also the WINSOC fraction. Furthermore, the Fraction Modern of the OC can be calculated from these values. Prior to AMS ^{14}C analysis, combustion of TC, EC, and WINSOC are all performed with a Sunset OC/EC analyser, simplifying the measurement by using a single hyphenation device for multiple carbonaceous fractions. As demonstrated for the low-loaded Arctic filters, chemical wet oxidation is a simple and reliable method for measurement of the WSOC fraction, providing low procedural blanks.

We have developed a web tool for calculation of both amount and EC yield, named Sunset-calc, allowing an EC yield calculation after each run and providing the fraction of charring for each step in the Swiss_3S protocol. Sunset-calc enables rapid protocol optimisations for a low fraction of charring, while avoiding too large EC losses before the S4 step.

Our thermal desorption model approach for EC yield extrapolation provides a filter-specific non-linear correction based on the underlying physical properties of the OC/EC mixture and OC composition. The present method supersedes the currently used linear approach for EC yield extrapolation. Radiocarbon measurements using filters with deliberately lowered EC yields are no longer necessary. Our approach is independent of season and does not require additional filter material for EC yield extrapolation, which is crucial when only limited amounts of sample material are available.

Code availability

https://github.com/martin-rauber/compycalc

https://github.com/martin-rauber/sunset-calc

Author contribution

The work presented here was carried out in collaboration between all authors. S.S. conceived of the study and its design. M.R. performed the laboratory experiments, implemented the models, and led the preparation of the manuscript. G.S. created the models and provided guidance and supervision for the laboratory experiments, model implementation, and contributed to the preparation of the manuscript. K.E.Y. was responsible for collection of the aerosol filter samples and for determining their OC/EC/TC content. All authors contributed to the editing and proofreading of the manuscript.

2.6 References

Abbatt, J. P. D., Richard Leaitch, W., Aliabadi, A. A., Bertram, A. K., Blanchet, J. P., Boivin-Rioux, A., Bozem, H., Burkart, J., Chang, R. Y. W., Charette, J., Chaubey, J. P., Christensen, R. J., Cirisan, A., Collins, D. B., Croft, B., Dionne, J., Evans, G. J., Fletcher, C. G., Gali, M., Ghahremaninezhad, R., Girard, E., Gong, W., Gosselin, M., Gourdal, M., Hanna, S. J., Hayashida, H., Herber, A. B., Hesaraki, S., Hoor, P., Huang, L., Hussherr, R., Irish, V. E., Keita, S. A., Kodros, J. K., Köllner, F., Kolonjari, F., Kunkel, D., Ladino, L. A., Law, K., Levasseur, M., Libois, Q., Liggio, J., Lizotte, M., MacDonald, K. M., Mahmood, R., Martin, R. V., Mason, R. H., Miller, L. A., Moravek, A., Mortenson, E., Mungall, E. L., Murphy, J. G., Namazi, M., Norman, A. L., O'Neill, N. T., Pierce, J. R., Russell, L. M., Schneider, J., Schulz, H., Sharma, S., Si, M., Staebler, R. M., Steiner, N. S., Thomas, J. L., Von Salzen, K., Wentzell, J. J. B., Willis, M. D., Wentworth, G. R., Xu, J. W., and Yakobi-Hancock, J. D.: Overview paper: New insights into aerosol and climate in the Arctic, Atmos. Chem. Phys., 19, 2527–2560, https://doi.org/10.5194/acp-19-2527-2019, 2019.

Agrios, K., Salazar, G., Zhang, Y.-L., Uglietti, C., Battaglia, M., Luginbühl, M., Ciobanu, V. G., Vonwiller, M., and Szidat, S.: Online coupling of pure O_2 thermo-optical methods – ^{14}C AMS for source apportionment of carbonaceous aerosols, Nucl. instruments methods Phys. Res. Sect. B beam Interact. with Mater. atoms, 361, 288–293, https://doi.org/10.1016/j.nimb.2015.06.008, 2015.

Andersson, A., Sheesley, R. J., Kruså, M., Johansson, C., and Gustafsson, Ö.: ^{14}C-Based source assessment of soot aerosols in Stockholm and the Swedish EMEP-Aspvreten regional background site, Atmos. Environ., 45, 215–222, https://doi.org/10.1016/j.atmosenv.2010.09.015, 2011.

Barrett, T. E., Robinson, E. M., Usenko, S., and Sheesley, R. J.: Source Contributions to Wintertime Elemental and Organic Carbon in the Western Arctic Based on Radiocarbon and Tracer Apportionment, Environ. Sci. Technol., 49, 11631–11639, https://doi.org/10.1021/acs.est.5b03081, 2015.

Barrie, L. A.: Arctic air pollution: An overview of current knowledge, Atmos. Environ., 20, 643–663, https://doi.org/10.1016/0004-6981(86)90180-0, 1986.

Barrie, L. A., Hoff, R. M., and Daggupaty, S. M.: The influence of mid-latitudinal pollution sources on haze in the Canadian arctic, Atmos. Environ., 15, 1407–1419, https://doi.org/10.1016/0004-

6981(81)90347-4, 1981.

Bedjanian, Y., Nguyen, M. L., and Guilloteau, A.: Desorption of Polycyclic Aromatic Hydrocarbons from Soot Surface: Five- and Six-Ring (C_{22}, C_{24}) PAHs, J. Phys. Chem. A, 114, 3533–3539, https://doi.org/10.1021/jp912110b, 2010.

Bernardoni, V., Calzolai, G., Chiari, M., Fedi, M., Lucarelli, F., Nava, S., Piazzalunga, A., Riccobono, F., Taccetti, F., Valli, G., and Vecchi, R.: Radiocarbon analysis on organic and elemental carbon in aerosol samples and source apportionment at an urban site in Northern Italy, J. Aerosol Sci., 56, 88–99, https://doi.org/10.1016/j.jaerosci.2012.06.001, 2013.

Birch, M. E. and Cary, R. A.: Elemental Carbon-Based Method for Monitoring Occupational Exposures to Particulate Diesel Exhaust, Aerosol Sci. Technol., 25, 221–241, https://doi.org/10.1080/02786829608965393, 1996.

Bond, T. C., Doherty, S. J., Fahey, D. W., Forster, P. M., Berntsen, T., Deangelo, B. J., Flanner, M. G., Ghan, S., Kärcher, B., Koch, D., Kinne, S., Kondo, Y., Quinn, P. K., Sarofim, M. C., Schultz, M. G., Schulz, M., Venkataraman, C., Zhang, H., Zhang, S., Bellouin, N., Guttikunda, S. K., Hopke, P. K., Jacobson, M. Z., Kaiser, J. W., Klimont, Z., Lohmann, U., Schwarz, J. P., Shindell, D., Storelvmo, T., Warren, S. G., and Zender, C. S.: Bounding the role of black carbon in the climate system: A scientific assessment, J. Geophys. Res. Atmos., 118, 5380–5552, https://doi.org/10.1002/jgrd.50171, 2013.

Cadle, S. H., Groblicki, P. J., and Stroup, D. P.: Automated Carbon Analyzer For Particulate Samples, Anal. Chem., 52, 2201–2206, https://doi.org/10.1021/ac50063a047, 1980.

Cavalli, F., Viana, M., Yttri, K. E., Genberg, J., and Putaud, J. P.: Toward a standardised thermal-optical protocol for measuring atmospheric organic and elemental carbon: The EUSAAR protocol, Atmos. Meas. Tech., 3, 79–89, https://doi.org/10.5194/amt-3-79-2010, 2010.

Chang, W., Cheng, J., Allaire, J., Xie, Y., and McPherson, J.: Shiny: web application framework for R, R Packag. version, 1, 2017, 2017.

Chow, J. C., Watson, J. G., Pritchett, L. C., Pierson, W. R., Frazier, C. A., and Purcell, R. G.: The DRI thermal/optical reflectance carbon analysis system: description, evaluation and applications in U.S. Air quality studies, Atmos. Environ. Part A. Gen. Top., 27, 1185–1201, https://doi.org/10.1016/0960-1686(93)90245-T, 1993.

Chow, J. C., Watson, J. G., Chen, L. W. A., Arnott, W. P., Moosmüller, H., and Fung, K.: Equivalence of elemental carbon by thermal/optical reflectance and transmittance with different temperature protocols, Environ. Sci. Technol., 38, 4414–4422, https://doi.org/10.1021/es034936u, 2004.

Contini, D., Vecchi, R., and Viana, M.: Carbonaceous Aerosols in the Atmosphere, Atmosphere (Basel)., 9, 181, https://doi.org/10.3390/atmos9050181, 2018.

Daellenbach, K. R., Uzu, G., Jiang, J., Cassagnes, L.-E., Leni, Z., Vlachou, A., Stefenelli, G., Canonaco, F., Weber, S., Segers, A., Kuenen, J. J. P., Schaap, M., Favez, O., Albinet, A., Aksoyoglu, S., Dommen, J., Baltensperger, U., Geiser, M., El Haddad, I., Jaffrezo, J.-L., and Prévôt, A. S. H.: Sources of

particulate-matter air pollution and its oxidative potential in Europe, Nature, 587, 414–419, https://doi.org/10.1038/s41586-020-2902-8, 2020.

Dusek, U., Prokopiou, M., Gongriep, F., Hitzenberger, R., Meijer, H. A. J., and Röckmann, T.: Evaluation of a two-step thermal method for separating organic and elemental carbon for radiocarbon analysis, 1943–1955, https://doi.org/10.5194/amt-7-1943-2014, 2014.

Eller, P. M. and Cassinelli, M. E.: Niosh, Elemental Carbon (Diesel Particulate): Method 5040. NIOSH Manual of Analytical Methods, Natl. Inst. Occup. Saf. Heal. Cincinatti, OH, USA, 2003–2154, 1996.

Engelmann, R., Ansmann, A., Ohneiser, K., Griesche, H., Radenz, M., Hofer, J., Althausen, D., Dahlke, S., Maturilli, M., Veselovskii, I., Jimenez, C., Wiesen, R., Baars, H., Bühl, J., Gebauer, H., Haarig, M., Seifert, P., Wandinger, U., and Macke, A.: Wildfire smoke, Arctic haze, and aerosol effects on mixed-phase and cirrus clouds over the North Pole region during MOSAiC: an introduction, Atmos. Chem. Phys., 21, 13397–13423, https://doi.org/10.5194/acp-21-13397-2021, 2021.

Fahrni, S. M., Wacker, L., Synal, H. A., and Szidat, S.: Improving a gas ion source for ^{14}C AMS, Nucl. Instruments Methods Phys. Res. Sect. B Beam Interact. with Mater. Atoms, 294, 320–327, https://doi.org/10.1016/j.nimb.2012.03.037, 2013.

Forouzanfar, Afshin, A., Alexander, L. T., Anderson, H. R., Bhutta, Z. A., Biryukov, S., Brauer, M., Burnett, R., Cercy, K., Charlson, F. J., Cohen, A. J., Dandona, L., Estep, K., Ferrari, A. J., Frostad, J. J., Fullman, N., Gething, P. W., Godwin, W. W., Griswold, M., Hay, S. I., Kinfu, Y., Kyu, H. H., Larson, H. J., Liang, X., Lim, S. S., Liu, P. Y., Lopez, A. D., Lozano, R., Marczak, L., Mensah, G. A., Mokdad, A. H., Moradi-Lakeh, M., Naghavi, M., Neal, B., Reitsma, M. B., Roth, G. A., Salomon, J. A., Sur, P. J., Vos, T., Wagner, J. A., Wang, H., Zhao, Y., Zhou, M., Aasvang, G. M., Abajobir, A. A., Abate, K. H., Abbafati, C., Abbas, K. M., Abd-Allah, F., Abdulle, A. M., Abera, S. F., Abraham, B., Abu-Raddad, L. J., Abyu, G. Y., Adebiyi, A. O., Adedeji, I. A., Ademi, Z., Adou, A. K., Adsuar, J. C., Agardh, E. E., Agarwal, A., Agrawal, A., Kiadaliri, A. A., Ajala, O. N., Akinyemiju, T. F., Al-Aly, Z., Alam, K., Alam, N. K. M., Aldhahri, S. F., Aldridge, R. W., Alemu, Z. A., Ali, R., Alkerwi, A., Alla, F., Allebeck, P., Alsharif, U., Altirkawi, K. A., Martin, E. A., Alvis-Guzman, N., Amare, A. T., Amberbir, A., Amegah, A. K., Amini, H., Ammar, W., Amrock, S. M., Andersen, H. H., Anderson, B. O., Antonio, C. A. T., Anwari, P., Ärnlöv, J., Artaman, A., Asayesh, H., Asghar, R. J., Assadi, R., Atique, S., Avokpaho, E. F. G. A., Awasthi, A., Quintanilla, B. P. A., Azzopardi, P., et al.: Global, regional, and national comparative risk assessment of 79 behavioural, environmental and occupational, and metabolic risks or clusters of risks, 1990–2015: a systematic analysis for the Global Burden of Disease Study 2015, Lancet, 388, 1659–1724, https://doi.org/10.1016/S0140-6736(16)31679-8, 2016.

Gentner, D. R., Jathar, S. H., Gordon, T. D., Bahreini, R., Day, D. A., El Haddad, I., Hayes, P. L., Pieber, S. M., Platt, S. M., De Gouw, J., Goldstein, A. H., Harley, R. A., Jimenez, J. L., Prévôt, A. S. H., and Robinson, A. L.: Review of Urban Secondary Organic Aerosol Formation from Gasoline and

Diesel Motor Vehicle Emissions, Environ. Sci. Technol., 51, 1074–1093, https://doi.org/10.1021/acs.est.6b04509, 2017.

Ghosh, U., Talley, J. W., and Luthy, R. G.: Particle-Scale Investigation of PAH Desorption Kinetics and Thermodynamics from Sediment, Environ. Sci. Technol., 35, 3468–3475, https://doi.org/10.1021/es0105820, 2001.

Glatzel, S. and Well, R.: Evaluation of septum-capped vials for storage of gas samples during air transport, Environ. Monit. Assess., 136, 307–311, https://doi.org/10.1007/s10661-007-9686-2, 2008.

Gundel, L. A., Dod, R. L., Rosen, H., and Novakov, T.: the Relationship Between Optical Attenuation and Black Carbon, Sci. Total Environ., 36, 197–202, 1984.

Gustafsson, Ö., Bucheli, T. D., Kukulska, Z., Andersson, M., Largeau, C., Rouzaud, J. N., Reddy, C. M., and Eglinton, T. I.: Evaluation of a protocol for the quantification of black carbon in sediments, Global Biogeochem. Cycles, 15, 881–890, https://doi.org/10.1029/2000GB001380, 2001.

Hanke, U. M., Wacker, L., Haghipour, N., Schmidt, M. W. I., Eglinton, T. I., and McIntyre, C. P.: Comprehensive radiocarbon analysis of benzene polycarboxylic acids (BPCAs) derived from pyrogenic carbon in environmental samples, Radiocarbon, 59, 1103–1116, https://doi.org/10.1017/RDC.2017.44, 2017.

Heidam, N. Z., Christensen, J., Wåhlin, P., and Skov, H.: Arctic atmospheric contaminants in NE Greenland: Levels, variations, origins, transport, transformations and trends 1990-2001, Sci. Total Environ., 331, 5–28, https://doi.org/10.1016/j.scitotenv.2004.03.033, 2004.

Hung, H., Kallenborn, R., Breivik, K., Su, Y., Brorström-Lundén, E., Olafsdottir, K., Thorlacius, J. M., Leppänen, S., Bossi, R., Skov, H., Manø, S., Patton, G. W., Stern, G., Sverko, E., and Fellin, P.: Atmospheric monitoring of organic pollutants in the Arctic under the Arctic Monitoring and Assessment Programme (AMAP): 1993-2006, Sci. Total Environ., 408, 2854–2873, https://doi.org/10.1016/j.scitotenv.2009.10.044, 2010.

Huntzicker, J. J., Johnson, R. L., Shah, J. J., and Cary, R. A.: Analysis of Organic and Elemental Carbon in Ambient Aerosols by a Thermal-Optical Method, in: Particulate Carbon: Atmospheric Life Cycle, edited by: Wolff, G. T. and Klimisch, R. L., Springer US, Boston, MA, 79–88, https://doi.org/10.1007/978-1-4684-4154-3_6, 1982.

IPCC: Climate Change 2021: The Physical Science Basis. Contribution of Working Group I to the Sixth Assessment Report of the Intergovernmental Panel on Climate Change, Cambridge University Press, 2021.

Jenk, T. M., Szidat, S., Schwikowski, M., Gäggeler, H. W., Wacker, L., Synal, H.-A., and Saurer, M.: Microgram level radiocarbon (^{14}C) determination on carbonaceous particles in ice, Nucl. Instruments Methods Phys. Res. Sect. B Beam Interact. with Mater. Atoms, 259, 518–525, https://doi.org/10.1016/j.nimb.2007.01.196, 2007.

Jouan, C., Pelon, J., Girard, E., Ancellet, G., Blanchet, J. P., and Delanoë, J.: On the relationship between Arctic ice clouds and polluted air masses over the North Slope of Alaska in April 2008, Atmos.

Chem. Phys., 14, 1205–1224, https://doi.org/10.5194/acp-14-1205-2014, 2014.

Kanakidou, M., Seinfeld, J. H., Pandis, S. N., Barnes, I., Dentener, F. J., Facchini, M. C., Van Dingenen, R., Ervens, B., Nenes, A., Nielsen, C. J., Swietlicki, E., Putaud, J. P., Balkanski, Y., Fuzzi, S., Horth, J., Moortgat, G. K., Winterhalter, R., Myhre, C. E. L., Tsigaridis, K., Vignati, E., Stephanou, E. G., and Wilson, J.: Organic aerosol and global climate modelling: A review, Atmos. Chem. Phys., 5, 1053–1123, https://doi.org/10.5194/acp-5-1053-2005, 2005.

Keeling, C. D.: The concentration and isotopic abundances of atmospheric carbon dioxide in rural areas, Geochim. Cosmochim. Acta, 13, 322–334, https://doi.org/10.1016/0016-7037(58)90033-4, 1958.

Kim, K. H., Jahan, S. A., Kabir, E., and Brown, R. J. C.: A review of airborne polycyclic aromatic hydrocarbons (PAHs) and their human health effects, Environ. Int., 60, 71–80, https://doi.org/10.1016/j.envint.2013.07.019, 2013.

Kim, K. H., Kabir, E., and Kabir, S.: A review on the human health impact of airborne particulate matter, Environ. Int., 74, 136–143, https://doi.org/10.1016/j.envint.2014.10.005, 2015.

Kirillova, E. N., Andersson, A., Sheesley, R. J., Kruså, M., Praveen, P. S., Budhavant, K., Safai, P. D., Rao, P. S. P., and Gustafsson, Ö.: [13]C- and ^{14}C-based study of sources and atmospheric processing of water-soluble organic carbon (WSOC) in South Asian aerosols, J. Geophys. Res. Atmos., 118, 614–626, https://doi.org/10.1002/jgrd.50130, 2013.

Landrigan, P. J.: Air pollution and health, Lancet Public Heal., 2, e4–e5, https://doi.org/10.1016/S2468-2667(16)30023-8, 2017.

Lang, S. Q., Bernasconi, S. M., and Früh-Green, G. L.: Stable isotope analysis of organic carbon in small (µg C) samples and dissolved organic matter using a GasBench preparation device, Rapid Commun. Mass Spectrom., 26, 9–16, https://doi.org/10.1002/rcm.5287, 2012.

Lang, S. Q., Früh-Green, G. L., Bernasconi, S. M., and Wacker, L.: Isotopic (δ^{13}C, Δ^{14}C) analysis of organic acids in marine samples using wet chemical oxidation, Limnol. Oceanogr. Methods, 11, 161–175, https://doi.org/10.4319/lom.2013.11.161, 2013.

Lang, S. Q., McIntyre, C. P., Bernasconi, S. M., Früh-Green, G. L., Voss, B. M., Eglinton, T. I., and Wacker, L.: Rapid [14]C Analysis of Dissolved Organic Carbon in Non-Saline Waters, Radiocarbon, 58, 505–515, https://doi.org/10.1017/RDC.2016.17, 2016.

Lelieveld, J., Evans, J. S., Fnais, M., Giannadaki, D., and Pozzer, A.: The contribution of outdoor air pollution sources to premature mortality on a global scale, Nature, 525, 367–371, https://doi.org/10.1038/nature15371, 2015.

Mauderly, J. L. and Chow, J. C.: Health Effects of Organic Aerosols, 257–288 pp., https://doi.org/10.1080/08958370701866008, 2008.

McDow, S. R. and Huntzicker, J. J.: Vapor adsorption artifact in the sampling of organic aerosol: Face velocity effects, Atmos. Environ. Part A. Gen. Top., 24, 2563–2571, https://doi.org/10.1016/0960-1686(90)90134-9, 1990.

McNeill, V. F.: Atmospheric Aerosols: Clouds, Chemistry, and Climate, Annu. Rev. Chem. Biomol. Eng.,

8, https://doi.org/10.1146/annurev-chembioeng-060816-101538, 2017.

Menzel, D. W. and Vaccaro, R. F.: The measurement of dissolved organic and particulate carbon in seawater, Limnol. Oceanogr., 9, 138–142, https://doi.org/10.4319/lo.1964.9.1.0138, 1964.

Moschos, V., Gysel-Beer, M., Modini, R. L., Corbin, J. C., Massabò, D., Costa, C., Danelli, S. G., Vlachou, A., Daellenbach, K. R., Szidat, S., Prati, P., Prévôt, A. S. H., Baltensperger, U., and El Haddad, I.: Source-specific light absorption by carbonaceous components in the complex aerosol matrix from yearly filter-based measurements, Atmos. Chem. Phys., 21, 12809–12833, https://doi.org/10.5194/acp-21-12809-2021, 2021.

Moschos, V., Dzepina, K., Bhattu, D., Lamkaddam, H., Casotto, R., Daellenbach, K. R., Canonaco, F., Rai, P., Aas, W., Becagli, S., Calzolai, G., Eleftheriadis, K., Moffett, C. E., Schnelle-Kreis, J., Severi, M., Sharma, S., Skov, H., Vestenius, M., Zhang, W., Hakola, H., Hellén, H., Huang, L., Jaffrezo, J.-L., Massling, A., Nøjgaard, J. K., Petäjä, T., Popovicheva, O., Sheesley, R. J., Traversi, R., Yttri, K. E., Schmale, J., Prévôt, A. S. H., Baltensperger, U., and El Haddad, I.: Equal abundance of summertime natural and wintertime anthropogenic Arctic organic aerosols, Nat. Geosci., 15, 196–202, https://doi.org/10.1038/s41561-021-00891-1, 2022.

Novakov, T. and Corrigan, C. E.: Mikrochimica Acta Thermal Characterization of Biomass Smoke Particles, Mikrochim. Acta, 166, 157–166, 1995.

Peleg, M., Normand, M. D., and Corradini, M. G.: The Arrhenius Equation Revisited, Crit. Rev. Food Sci. Nutr., 52, 830–851, https://doi.org/10.1080/10408398.2012.667460, 2012.

Peterson, M. R. and Richards, M. H.: Thermal-Optical-Transmittance Analysis for Organic, Elemental, Carbonate, Total Carbon, and OCX2 in $PM_{2.5}$ by the EPA/NIOSH Method, Proceedings, Symposium on Air Quality Measurement Methods and Technology - 2002, Pittsburgh, PA, 83-81-83-19 pp., 2002.

Petzold, A., Ogren, J. A., Fiebig, M., Laj, P., Li, S.-M., Baltensperger, U., Holzer-Popp, T., Kinne, S., Pappalardo, G., Sugimoto, N., Wehrli, C., Wiedensohler, A., and Zhang, X.-Y.: Recommendations for reporting "black carbon" measurements, Atmos. Chem. Phys., 13, 8365–8379, https://doi.org/10.5194/acp-13-8365-2013, 2013.

Platt, S. M., Hov, Ø., Berg, T., Breivik, K., Eckhardt, S., Eleftheriadis, K., Evangeliou, N., Fiebig, M., Fisher, R., Hansen, G., Hansson, H.-C., Heintzenberg, J., Hermansen, O., Heslin-Rees, D., Holmén, K., Hudson, S., Kallenborn, R., Krejci, R., Krognes, T., Larssen, S., Lowry, D., Lund Myhre, C., Lunder, C., Nisbet, E., Nizzetto, P. B., Park, K.-T., Pedersen, C. A., Aspmo Pfaffhuber, K., Röckmann, T., Schmidbauer, N., Solberg, S., Stohl, A., Ström, J., Svendby, T., Tunved, P., Tørnkvist, K., van der Veen, C., Vratolis, S., Yoon, Y. J., Yttri, K. E., Zieger, P., Aas, W., and Tørseth, K.: Atmospheric composition in the European Arctic and 30 years of the Zeppelin Observatory, Ny-Ålesund, Atmos. Chem. Phys., 22, 3321–3369, https://doi.org/10.5194/acp-22-3321-2022, 2022.

Pope, C. A., Coleman, N., Pond, Z. A., and Burnett, R. T.: Fine particulate air pollution and human

mortality: 25+ years of cohort studies, Environ. Res., 183, 108924, https://doi.org/10.1016/j.envres.2019.108924, 2020.

Pöschl, U.: Aerosol particle analysis: Challenges and progress, Anal. Bioanal. Chem., 375, 30–32, https://doi.org/10.1007/s00216-002-1611-5, 2003.

Putaud, J. P., Van Dingenen, R., Alastuey, A., Bauer, H., Birmili, W., Cyrys, J., Flentje, H., Fuzzi, S., Gehrig, R., Hansson, H. C., Harrison, R. M., Herrmann, H., Hitzenberger, R., Hüglin, C., Jones, A. M., Kasper-Giebl, A., Kiss, G., Kousa, A., Kuhlbusch, T. A. J., Löschau, G., Maenhaut, W., Molnar, A., Moreno, T., Pekkanen, J., Perrino, C., Pitz, M., Puxbaum, H., Querol, X., Rodriguez, S., Salma, I., Schwarz, J., Smolik, J., Schneider, J., Spindler, G., ten Brink, H., Tursic, J., Viana, M., Wiedensohler, A., and Raes, F.: A European aerosol phenomenology - 3: Physical and chemical characteristics of particulate matter from 60 rural, urban, and kerbside sites across Europe, Atmos. Environ., 44, 1308–1320, https://doi.org/10.1016/j.atmosenv.2009.12.011, 2010.

Quinn, P. K., Miller, T. L., Bates, T. S., Ogren, J. A., Andrews, E., and Shaw, G. E.: A 3-year record of simultaneously measured aerosol chemical and optical properties at Barrow, Alaska, J. Geophys. Res. Atmos., 107, https://doi.org/10.1029/2001jd001248, 2002.

Quinn, P. K., Bates, T. S., Baum, E., Doubleday, N., Fiore, A. M., Flanner, M., Fridlind, A., Garrett, T. J., Koch, D., Menon, S., Shindell, D., Stohl, A., and Warren, S. G.: Short-lived pollutants in the Arctic: Their climate impact and possible mitigation strategies, Atmos. Chem. Phys., 8, 1723–1735, https://doi.org/10.5194/acp-8-1723-2008, 2008.

R Core Team: R: A Language and Environment for Statistical Computing. R Foundation for Statistical Computing, Vienna, Austria., https://www.r-project.org/, 2020.

Rauber, M.: sunset-calc, https://doi.org/10.5281/zenodo.4610145, March 2021.

Rauber, M. and Salazar, G.: martin-rauber/compycalc:, https://doi.org/10.5281/ZENODO.5958275, 2022.

Ruff, M., Wacker, L., Gäggeler, H. W., Suter, M., Synal, H.-A., and Szidat, S.: A Gas Ion Source for Radiocarbon Measurements at 200 kV, Radiocarbon, 49, 307–314, https://doi.org/10.1017/S0033822200042235, 2007.

Salazar, G., Zhang, Y. L., Agrios, K., and Szidat, S.: Development of a method for fast and automatic radiocarbon measurement of aerosol samples by online coupling of an elemental analyzer with a MICADAS AMS, Nucl. Instruments Methods Phys. Res. Sect. B Beam Interact. with Mater. Atoms, 361, 163–167, https://doi.org/10.1016/j.nimb.2015.03.051, 2015.

Schmale, J., Zieger, P., and Ekman, A. M. L.: Aerosols in current and future Arctic climate, Nat. Clim. Chang., 11, 95–105, https://doi.org/10.1038/s41558-020-00969-5, 2021.

Schmid, H., Laskus, L., Jürgen Abraham, H., Baltensperger, U., Lavanchy, V., Bizjak, M., Burba, P., Cachier, H., Crow, D., Chow, J., Gnauk, T., Even, A., Ten Brink, H. M., Giesen, K. P., Hitzenberger, R., Hueglin, C., Maenhaut, W., Pio, C., Carvalho, A., Putaud, J. P., Toom-Sauntry, D., and Puxbaum, H.: Results of the "carbon conference" international aerosol carbon round robin test stage I,

Atmos. Environ., 35, 2111–2121, https://doi.org/10.1016/S1352-2310(00)00493-3, 2001.

Schwaab, M. and Pinto, J. C.: Optimum reference temperature for reparameterization of the Arrhenius equation. Part 1: Problems involving one kinetic constant, Chem. Eng. Sci., 62, 2750–2764, https://doi.org/10.1016/j.ces.2007.02.020, 2007.

Sharp, J. H.: Total organic carbon in seawater - comparison of measurements using persulfate oxidation and high temperature combustion, Mar. Chem., 1, 211–229, https://doi.org/10.1016/0304-4203(73)90005-4, 1973.

Smichowski, P., Polla, G., and Gómez, D.: Metal fractionation of atmospheric aerosols via sequential chemical extraction: A review, Anal. Bioanal. Chem., 381, 302–316, https://doi.org/10.1007/s00216-004-2849-x, 2005.

Synal, H. A., Stocker, M., and Suter, M.: MICADAS: A new compact radiocarbon AMS system, Nucl. Instruments Methods Phys. Res. Sect. B Beam Interact. with Mater. Atoms, 259, 7–13, https://doi.org/10.1016/j.nimb.2007.01.138, 2007.

Szidat, S., Jenk, T. M., Gäggeler, H. W., Synal, H.-A., Fisseha, R., Baltensperger, U., Kalberer, M., Samburova, V., Wacker, L., Saurer, M., Schwikowski, M., and Hajdas, I.: Source Apportionment of Aerosols by [14]C Measurements in Different Carbonaceous Particle Fractions, Radiocarbon, 46, 475–484, https://doi.org/10.1017/S0033822200039783, 2004a.

Szidat, S., Jenk, T. M., Gäggeler, H. W., Synal, H.-A., Hajdas, I., Bonani, G., and Saurer, M.: THEODORE, a two-step heating system for the EC/OC determination of radiocarbon (^{14}C) in the environment, Nucl. Instruments Methods Phys. Res. Sect. B Beam Interact. with Mater. Atoms, 223–224, 829–836, https://doi.org/10.1016/j.nimb.2004.04.153, 2004b.

Szidat, S., Jenk, T. M., Synal, H.-A., Kalberer, M., Wacker, L., Hajdas, I., Kasper-Giebl, A., and Baltensperger, U.: Contributions of fossil fuel, biomass-burning, and biogenic emissions to carbonaceous aerosols in Zurich as traced by ^{14}C, J. Geophys. Res., 111, D07206, https://doi.org/10.1029/2005JD006590, 2006.

Szidat, S., Prévôt, A. S. H., Sandradewi, J., Alfarra, M. R., Synal, H. A., Wacker, L., and Baltensperger, U.: Dominant impact of residential wood burning on particulate matter in Alpine valleys during winter, Geophys. Res. Lett., 34, 1–6, https://doi.org/10.1029/2006GL028325, 2007.

Szidat, S., Ruff, M., Perron, N., Wacker, L., Synal, H. -a., Hallquist, M., Shannigrahi, a. S., Yttri, K. E., Dye, C., and Simpson, D.: Fossil and non-fossil sources of organic carbon (OC) and elemental carbon (EC) in Göteborg, Sweden, Atmos. Chem. Phys., 9, 1521–1535, https://doi.org/10.5194/acp-9-1521-2009, 2009.

Szidat, S., Salazar, G. A., Vogel, E., Battaglia, M., Wacker, L., Synal, H.-A., and Türler, A.: [14]C Analysis and Sample Preparation at the new Bern Laboratory for the Analysis of Radiocarbon with AMS (LARA), Radiocarbon, 56, 561–566, https://doi.org/10.2458/56.17457, 2014.

Tørseth, K., Aas, W., Breivik, K., Fjeraa, A. M., Fiebig, M., Hjellbrekke, A. G., Lund Myhre, C., Solberg, S., and Yttri, K. E.: Introduction to the European Monitoring and Evaluation Programme (EMEP)

and observed atmospheric composition change during 1972-2009, Atmos. Chem. Phys., 12, 5447–5481, https://doi.org/10.5194/acp-12-5447-2012, 2012.

Vlachou, A., Daellenbach, K. R., Bozzetti, C., Chazeau, B., Salazar, G. A., Szidat, S., Jaffrezo, J. L., Hueglin, C., Baltensperger, U., El Haddad, I., and Prévôt, A. S. H.: Advanced source apportionment of carbonaceous aerosols by coupling offline AMS and radiocarbon size-segregated measurements over a nearly 2-year period, Atmos. Chem. Phys., 18, 6187–6206, https://doi.org/10.5194/acp-18-6187-2018, 2018.

Wacker, L., Christl, M., and Synal, H. A.: Bats: A new tool for AMS data reduction, Nucl. Instruments Methods Phys. Res. Sect. B Beam Interact. with Mater. Atoms, 268, 976–979, https://doi.org/10.1016/j.nimb.2009.10.078, 2010.

Wacker, L., Fahrni, S. M., Hajdas, I., Molnar, M., Synal, H. A., Szidat, S., and Zhang, Y. L.: A versatile gas interface for routine radiocarbon analysis with a gas ion source, Nucl. Instruments Methods Phys. Res. Sect. B Beam Interact. with Mater. Atoms, 294, 315–319, https://doi.org/10.1016/j.nimb.2012.02.009, 2013.

Walker, B. D., Primeau, F. W., Beaupré, S. R., Guilderson, T. P., Druffel, E. R. M., and McCarthy, M. D.: Linked changes in marine dissolved organic carbon molecular size and radiocarbon age, Geophys. Res. Lett., 43, 10,385-10,393, https://doi.org/10.1002/2016GL070359, 2016.

Weber, R. J., Sullivan, A. P., Peltier, R. E., Russell, A., Yan, B., Zheng, M., de Grouw, J., Warneke, C., Brock, C., Holloway, J. S., Atlas, E. L., and Edgerton, E.: A study of secondary organic aerosol formation in the anthropogenic-influenced southeastern United States, J. Geophys. Res. Atmos., 112, 1–13, https://doi.org/10.1029/2007JD008408, 2007.

Wiedemeier, D. B., Lang, S. Q., Gierga, M., Abiven, S., Bernasconi, S. M., Früh-Green, G. L., Hajdas, I., Hanke, U. M., Hilf, M. D., McIntyre, C. P., Scheider, M. P. W., Smittenberg, R. H., Wacker, L., Wiesenberg, G. L. B., and Schmidt, M. W. I.: Characterization, Quantification and Compound-specific Isotopic Analysis of Pyrogenic Carbon Using Benzene Polycarboxylic Acids (BPCA), J. Vis. Exp., 111, https://doi.org/10.3791/53922, 2016.

Winiger, P., Andersson, A., Yttri, K. E., Tunved, P., and Gustafsson, Ö.: Isotope-Based Source Apportionment of EC Aerosol Particles during Winter High-Pollution Events at the Zeppelin Observatory, Svalbard, Environ. Sci. Technol., 49, 11959–11966, https://doi.org/10.1021/acs.est.5b02644, 2015.

Winiger, P., Andersson, A., Eckhardt, S., Stohl, A., and Gustafsson, Ö.: The sources of atmospheric black carbon at a European gateway to the Arctic, Nat. Commun., 7, 12776, https://doi.org/10.1038/ncomms12776, 2016.

Winiger, P., Andersson, A., Eckhardt, S., Stohl, A., Semiletov, I. P., Dudarev, O. V., Charkin, A., Shakhova, N., Klimont, Z., Heyes, C., and Gustafsson, Ö.: Siberian Arctic black carbon sources constrained by model and observation, Proc. Natl. Acad. Sci., 114, E1054–E1061, https://doi.org/10.1073/pnas.1613401114, 2017.

Yu, J. Z., Xu, J., and Yang, H.: Charring characteristics of atmospheric organic particulate matter in thermal analysis, Environ. Sci. Technol., 36, 754–761, https://doi.org/10.1021/es015540q, 2002.

Zencak, Z., Elmquist, M., and Gustafsson, Ö.: Quantification and radiocarbon source apportionment of black carbon in atmospheric aerosols using the CTO-375 method, Atmos. Environ., 41, 7895–7906, https://doi.org/10.1016/j.atmosenv.2007.06.006, 2007.

Zhang, Y., Liu, J., Salazar, G. A., Li, J., Zotter, P., Zhang, G., Shen, R., Schäfer, K., Schnelle-Kreis, J., Prévôt, A. S. H., and Szidat, S.: Micro-scale (µg) radiocarbon analysis of water-soluble organic carbon in aerosol samples, Atmos. Environ., 97, 1–5, https://doi.org/10.1016/j.atmosenv.2014.07.059, 2014a.

Zhang, Y. L., Liu, D., Shen, C. D., Ding, P., and Zhang, G.: Development of a preparation system for the radiocarbon analysis of organic carbon in carbonaceous aerosols in China, Nucl. Instruments Methods Phys. Res. Sect. B Beam Interact. with Mater. Atoms, 268, 2831–2834, https://doi.org/10.1016/j.nimb.2010.06.032, 2010.

Zhang, Y. L., Perron, N., Ciobanu, V. G., Zotter, P., Minguillón, M. C., Wacker, L., Prévôt, A. S. H., Baltensperger, U., and Szidat, S.: On the isolation of OC and EC and the optimal strategy of radiocarbon-based source apportionment of carbonaceous aerosols, Atmos. Chem. Phys., 12, 10841–10856, https://doi.org/10.5194/acp-12-10841-2012, 2012.

Zhang, Y. L., Li, J., Zhang, G., Zotter, P., Huang, R. J., Tang, J. H., Wacker, L., Prévôt, A. S. H., and Szidat, S.: Radiocarbon-based source apportionment of carbonaceous aerosols at a regional background site on Hainan Island, South China, Environ. Sci. Technol., 48, 2651–2659, https://doi.org/10.1021/es4050852, 2014b.

Zhang, Y. L., Huang, R. J., El Haddad, I., Ho, K. F., Cao, J. J., Han, Y., Zotter, P., Bozzetti, C., Daellenbach, K. R., Canonaco, F., Slowik, J. G., Salazar, G., Schwikowski, M., Schnelle-Kreis, J., Abbaszade, G., Zimmermann, R., Baltensperger, U., Prévôt, A. S. H., and Szidat, S.: Fossil vs. non-fossil sources of fine carbonaceous aerosols in four Chinese cities during the extreme winter haze episode of 2013, Atmos. Chem. Phys., 15, 1299–1312, https://doi.org/10.5194/acp-15-1299-2015, 2015.

Zhao, C. and Garrett, T. J.: Effects of Arctic haze on surface cloud radiative forcing, Geophys. Res. Lett., 42, https://doi.org/10.1002/2014GL062015, 2015.

Zotter, P., Ciobanu, V. G., Zhang, Y. L., El-Haddad, I., Macchia, M., Daellenbach, K. R., Salazar, G. A., Huang, R.-J., Wacker, L., Hueglin, C., Piazzalunga, A., Fermo, P., Schwikowski, M., Baltensperger, U., Szidat, S., and Prévôt, A. S. H.: Radiocarbon analysis of elemental and organic carbon in Switzerland during winter-smog episodes from 2008 to 2012 – Part 1: Source apportionment and spatial variability, Atmos. Chem. Phys., 14, 13551–13570, https://doi.org/10.5194/acp-14-13551-2014, 2014.

3   Investigation of relevant formation processes of particulate oxalate from compound-specific radiocarbon analysis

Martin Rauber[1,2], Gary Salazar[1,2], Chiara Uglietti[1,2,a], Deepika Bhattu[3], Vaios Moschos[4,b], Sachchida Tripathi[5], Imad El Haddad[4], André S. H. Prévôt[4], Sönke Szidat[1,2]

[1]Dept. of Chemistry, Biochemistry and Pharmaceutical Sciences, University of Bern, Bern, 3012, Switzerland
[2]Oeschger Centre for Climate Change Research, University of Bern, Bern, 3012, Switzerland
[3]Dept. of Civil and Infrastructure Engineering, Indian Institute of Technology Jodhpur, Jodhpur, 342037, India
[4]Laboratory of Atmospheric Chemistry, Paul Scherrer Institute, Villigen, 5232, Switzerland
[5]Dept. of Civil Engineering, Indian Institute of Technology Kanpur, Kanpur, 208016, India
[a]now at: Helsinn Group, Biasca, 6710, Switzerland
[b]now at: University of North Carolina System, Greensboro & Chapel Hill, North Carolina, USA

Correspondence to: Sönke Szidat (soenke.szidat@unibe.ch)

Abstract

Dicarboxylic acids (DCAs) have become of great interest for their abundance in atmospheric organic aerosols and their role as cloud condensation nuclei and therefore the Earth's climate. The sources and relevant formation processes of DCAs are not well understood. Previous studies indicate that DCAs may be formed as secondary organic aerosols (SOA) from both fossil-fuel and biogenic precursors including biomass burning. Oxalic acid is the most prevalent DCA at different sites around the world and understanding the sources and formation pathways of oxalic acid may help shedding the lights on the origins of DCA. Here, we report the results from a compound-specific radiocarbon analysis (CSRA) of oxalate from atmospheric aerosols sampled in several urban and rural sites. We performed CSRA of oxalate with a one-step chromatographic separation using ion chromatography (IC) followed by chemical wet oxidation and subsequent radiocarbon (^{14}C) measurement with accelerator mass spectrometry (AMS). Additional to oxalate, ^{14}C analysis was applied on the water-soluble organic carbon (WSOC) fraction, and for some sites to the total carbon (TC) and elemental carbon (EC) fractions. For the rural winter 2005 site in Råö, Sweden, a non-fossil fraction of 0.92 ± 0.10 was measured for oxalate and 0.77 ± 0.06 for WSOC. For Mexico City, in spring 2006, the non-fossil fraction was 0.63 ± 0.08 and 0.61 ± 0.10 for oxalate and WSOC, respectively. Daytime and night-time filters from January to March as well as daily filters from March to May sampled in 2018 were measured for India, Delhi. The samples were predominantly originating from non-fossil sources contributing to 0.60-0.84 and 0.59-0.86 of the total oxalate and WSOC, respectively. The SRM 1649a Urban Dust measured additionally to the atmospheric aerosol samples showed a nonfossil fraction of 0.66 ± 0.01 for oxalate and 0.62 ± 0.01 for WSOC. CSRA was not feasible on urban samples substantially affected by coal burning from 2018 in Kraków, Poland due to very low oxalate to TC ratios of 0.05 ± 0.04 %, far lower than what we observed in Delhi (0.4 ± 0.2 %), Mexico City (0.6 ± 0.2 %), and Råö (0.8 ± 0.5 %). Our results indicate that oxalic acid is predominately formed by non-fossil volatile organic compounds. Biomass burning as well as fossil-fuel sources are only minor contributors. Differences of the fraction nonfossil between oxalate and the bulk WSOC were most significant in rural samples. Furthermore, for Delhi we found evidence for a diurnal variation of oxalate and WSOC formation in winter and spring.

3.1 Introduction

Organic aerosols (OA) account for 20–50 % of the total aerosol mass in airborne particulate matter (PM) and up to 90 % of the submicron aerosol (Kanakidou et al., 2005; Putaud et al., 2010; Jimenez et al., 2009). OA have adverse effects to air quality and human health causing damage to the respiratory and cardiovascular systems (Kim et al., 2015; Lelieveld et al., 2015; Mauderly and Chow, 2008). Furthermore, OA have a significant relevance for the climate with opposite effects depending on the carbonaceous aerosol fraction. The decrease in surface albedo and increase in solar radiation absorption of elemental carbon (EC) causes a warming effect on the climate. In contrast, organic carbon (OC) has a cooling effect by reflecting the incident solar radiation (Boucher et al., 2013; Hansen and Nazarenko, 2004). Additional indirect effects include aerosol–cloud interactions of OA in the atmosphere. All these points highlight the importance of understanding the OA sources in the atmosphere (Kanakidou et al., 2005; Shrivastava et al., 2017).

OC emitted as primary organic aerosols (POA) or formed as a secondary organic aerosol (SOA) by photochemical reactions with oxidants such as ozone, hydroxyl radicals or nitrate radicals. Water–soluble organic carbon (WSOC) accounts for 30–80 % of the OA fraction with the majority originating from SOA and some from POA (Lim et al., 2010; Na et al., 2004; Jaffrezo et al., 2005). Photochemical processing of POA creates polar moieties (e.g., hydroxyl or carboxyl groups), which increases the OA water solubility (Kawamura et al., 2010b; Jimenez et al., 2009). A significant fraction of the water-soluble organic aerosol comprises of low-molecular-weight dicarboxylic acids (DCAs) such as oxalic acid. The low vapour pressure of C_2–C_4 DCAs favours their partitioning into the particle phase (Yang et al., 2008). Omnipresent in atmospheric aerosols, DCAs have been found at considerable concentrations at urban (Ho et al., 2010; Hsieh et al., 2008, 2007), rural (Cao et al., 2017; Limbeck et al., 2001), and remote Arctic (Narukawa et al., 2002; Kawamura et al., 2007), Antarctic (Kawamura et al., 1996), and marine (Kawamura and Sakaguchi, 1999; Fu et al., 2013) sites. The majority of DCAs are believed to be secondary, formed from both biogenic and fossil-fuel precursors.

A major source of DCAs and especially oxalic acid is from the oxidation of isoprene (2-methyl-1,3-butadiene, C_5H_8), the most emitted volatile organic compound originating from biogenic emissions. Overall, the total biogenic volatile organic compounds (BVOC) emissions were estimated to be 1000 Tg yr^{-1} (Guenther et al., 2012) and are a major source for SOA formation (Kroll et al., 2005, 2006; Kleindienst et al., 2007; Edney et al., 2005). Oxalic acid can form by dark ozonolysis of isoprene (Bikkina et al., 2021) or through the aqueous phase processing of isoprene oxidation products (Carlton et al., 2009, 2007; Herrmann et al., 2015; Lamkaddam et al., 2021) and have been observed in forested areas (Mochizuki et al., 2017, 2015; Chen et al., 2021). Several studies (Yu et al., 2005; Yao et al., 2002, 2004; Cheng et al., 2013) also reported a positive correlation between the oxalate and sulfate concentration, particularly in summer, which may indicate a similar in-cloud formation process of oxalate and sulfate. Currently, it is still unclear how important the contribution of biomass burning emissions to DCA concentrations are oxalate

(Deshmukh et al., 2018; Kundu et al., 2010; Deshmukh et al., 2019; Cheng et al., 2013). Some studies estimating high contributions of up to 30%, e.g., in Shanghai (Yang et al., 2014), and others suggesting little to no contributions, e.g., in Europe (van Pinxteren et al., 2014). Oxalate is also formed form fossil-fuel precursors (e.g., acetylene, ethylene) with very similar pathways to biogenic gaseous precursors (Warneck, 2003). Furthermore, DCAs are also released directly from fossil-fuel combustion engines without exhaust treatment (Kawamura and Kaplan, 1987; Bock et al., 2017). Nevertheless, the effect of photochemical aging of combustion emissions on oxalic acid formation remains poorly understood.

Radiocarbon (^{14}C) analysis allows for the unambiguous distinction of compounds originating from fossil fuels and modern biomass. OA from biogenic sources and biomass burning have a contemporary radiocarbon content whereas OA from fossil-fuel combustion are devoid of radiocarbon. Compound-specific radiocarbon analysis (CSRA) aims at the ^{14}C analysis of individual chemical substances (Haghipour et al., 2019; Eglinton and Eglinton, 2008). It requires a powerful chemical separation and the isolation of sufficient amounts of analyte, which limits CSRA to the most abundant compounds. Alternatively, several compounds may be pooled to fractions or compound classes. Radiocarbon analysis has been applied to alkanes and fatty acids (Matsumoto et al., 2001; Ren et al., 2020) as well as polycyclic aromatic hydrocarbons (Currie et al., 1997; Mandalakis et al., 2005; Sheesley et al., 2009). Although considerable effort has been made into the analysis of DCAs including oxalic acid, few performed radiocarbon analysis. As oxalic acid is among the most prevalent DCA, it is well suited for CSRA. Fahrni et al. (2010a) introduced a liquid chromatography method to separate oxalic acid from aerosol filters. After water extraction followed by a concentration step, Fahrni et al. (2010a) separated oxalic acid by ion chromatography (IC) and purified using high-performance liquid chromatography (HPLC). Then, the eluate was concentrated, dried in a vacuum, and oxidised with cupric oxide in an ampoule before radiocarbon measurement with an ampoule cracker system (Fahrni et al., 2010b; Ruff et al., 2007). The few measurements conducted by Fahrni et al. (2010a) on filters from a rural site in Ispra (Italy) and urban Gothenburg (Sweden) found predominately non-fossil contributions. More recently, Xu et al. (2021) reported a CSRA method for oxalic acid by dibutyl ester derivatisation followed by a preparative gas chromatographic (GC) separation and graphitisation for radiocarbon measurement. On very limited number of measurements, the authors found predominately a fossil and non-fossil contribution from urban and coastal background air masses, respectively.

Omnipresent in atmospheric aerosols, this work aims to identify sources of oxalate and apportion to their respective sources semi-quantitatively with a new method. PM filters from India, Mexico, and Sweden were analysed with a mean oxalate/WSOC ratio of 3.0 ± 2.3 %, 12.6 ± 2.8 %, and 1.7 ± 0.8 %, respectively. Additionally, urban dust reference material collected in Washington DC, USA was analysed. To evaluate the significance of the radiocarbon levels of oxalate, they were compared to ^{14}C from other fractions of the OA, such as WSOC, EC as well as total carbon (TC). We have developed a preparative IC method for the oxalate separation, which was coupled with chemical wet oxidation for CO_2 generation and radiocarbon measurement in an accelerator mass spectrometer (AMS).

3.2 Materials and methods

3.2.1 Filter sampling

Filters were sampled in Delhi, India (28.63 °N, 77.167 °E; ~220 m above msl) on the main building rooftop at the Indian Institute of Tropical Meteorology Delhi (Strähl, n.d.). Quartz fibre filters (QMA Whatman, Cytiva, Marlborough, MA, USA) were sampled daily for daytime and night-time filters from January to March (winter, spring) 2018 and daily (full day, 24 h) from end of March to May (summer) 2018 with a $PM_{2.5}$ high volume air sampler (Tisch Environmental, OH, USA). Sampling was performed with a flow of 1.13 m³ min⁻¹ on a total filter area of 428.7 cm² and a total volume of 737 m³, 874 m³, and 1627 m³ for day, night, and 24 h filters, respectively. From the total of 23 filters available for analysis, 12 were sampled for 12 h and 11 were sampled for a full day (24 h). 100 cm² of filter material was used for oxalate extraction, 4.5 cm² (3 × 1.5 cm²) for TC measurement in triplicates and four 22 mm circular punches (4 × 2.54 cm², total 10.2 cm²) were used for WSOC and partially for EC measurement from each filter. Sweden filters were collected (duration: 3–7 days) in February 2005 in in the rural area of Råö (57.4 °N, 11.92 °E, 10 m above msl) with a $PM_{2.5}$ size cut. Details about these filters can be found in Szidat et al. (2009). An area of 52–101 cm² from four filters was used for TC, WSOC, and oxalate analysis.
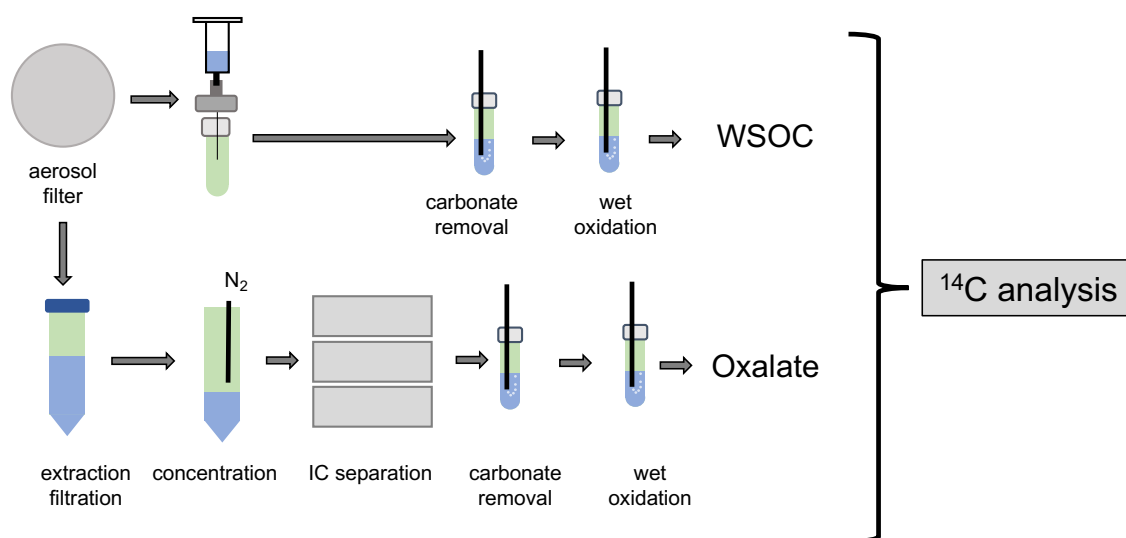
Figure 1: Overview chart of the analytical methods with the WSOC and oxalate fractions from the aerosol filter to the radiocarbon measurement.

Three Mexico filters utilised for this work were collected in March 2006 at the Instituto Mexicano del Petroleo, Mexico City (IMP, 19.49 °N, 99.15 °W, 2240 m above msl) with a $PM_{2.5}$ size cut. Further details can be found in Aiken et al. (2009). Poland filters from February to September 2018 were sampled for 24 h on the roof (~13 m above ground) of the Faculty of Physics and Applied Informatics building of the

Akademii Górniczo-Hutniczej in Kraków, Poland (50.07 °N, 19.91 °E, ~200 m above msl) (Casotto et al., 2022). Samples were collected for 24 h (midnight to midnight) with a flow of 0.5 m³ min⁻¹ with a high-volume air sampler (DHA-80, Digitel, Switzerland) and a PM₁ size cut on 155 mm (diameter) pre-combusted (450°C for 4 h) quartz filters (2500QAT-UP, Pallflex Products Corporation, USA). Always in pairs of two following days, 20 filters with an area of 14.1 cm² each was received for analysis. Additionally, to aerosol filters, the NIST standard reference material SRM 1649a Urban Dust was used (NIST, 2007).

3.2.2 Overview of the analytical methods

Most of the filter material was allocated for oxalate extraction and IC separation to yield sufficient oxalate for radiocarbon analysis. The remaining material was used for ¹⁴C-WSOC, ¹⁴C-EC, and ¹⁴C-TC analysis (i.e., the measurement of ¹⁴C in WSOC, EC and TC, respectively). CO₂ for radiocarbon measurement was generated by chemical wet oxidation for both oxalate and WSOC, and by total combustion in an OC/EC analyser for the analysis of both ¹⁴C-EC and ¹⁴C-TC. An overview of the procedure described in detail in the following paragraphs is shown in Fig. 1.

3.2.3 Filter extraction

Aerosol filter material was kept in a freezer (−20°C) for storage and thawed before use. Filter material cut into small strips (1 × 3 cm) using a scalpel was put in a 50 mL centrifuge tubes and filled with 10 or 20 mL ultrapure water to submerge all filter material. The tubes were vigorously shaken, then sonicated three times for 30 min. In between, the tubes were allowed to cool down to room temperature. The suspension was drawn with a syringe and filtrated through a 0.2 μm H-PTFE syringe filter (CHROMAFIL®, Macherey-Nagel, Germany) into a new 50 mL centrifuge tube. The extraction tube was rinsed (3 × 1 mL) and filtrated into the new tube to quantitatively transfer all extract. An aliquot was taken for IC to determine the amount of oxalate in the sample. The liquid was concentrated under a gentle stream of N₂ to < 1 mL and stored in a fridge at 4°C until transfer to an IC vial for separation. To prevent decomposition and avoid material loss, no block heater was used during extract concentration.

WSOC extraction set up consisted of 25 mm polycarbonate filter holders (Sartorius GmbH, Germany). Circular filter punches were restrained with silicone O-rings in the filter holders with inner diameters 4 mm smaller, leading to a 2 mm rim on the filters. The screw-type filter holder allowed for up to three stacked filters for each extraction. A baked out (500°C, 2 h) and rinsed glass syringe (10 mL) was attached on top and a needle (Sterican, B. Braun, Germany) was connected at the filter holder outlet. The glass syringe was filled with ultrapure water, the needle was inserted in a 12 mL EXETAINER® vial (12 mL, screw cap, item 938 W, Labco Ltd., Lampeter, UK) by piercing the vial caps' septum and 5.0 ± 0.2 mL of extract was collected. The extraction was conducted solely by gravity and excess air in the vial was released by partially unscrewing the vial cap before extraction. The water extracted filters were dried in a laminar flow cabinet and stored in a freezer (−20°C) until further use. Although WSOC was stripped off, WINSOC remained on the water-extracted filters. Thermal WINSOC removal is required for a physical separation of EC after

water extraction. Zhang et al. (2012) described an OC/EC separation procedure for a thermo-optical OC/EC analyser named Swiss_4S, which consists of three OC removal steps followed by EC combustion step. In this work, WINSOC removal was performed accordingly using the first three steps of the Swiss_4S protocol in a thermo-optical OC/EC analyser (Model 5L, Sunset Laboratories Inc., Tigard, OR, USA); see Rauber et al. (2022) for details. After completed OC/EC separation, the filters were kept in a freezer (-20°C) until radiocarbon measurement of EC.

12.5 ± 1.5 mg and 4.4 ± 1 mg of SRM 1649a Urban Dust for oxalate and WSOC, respectively, was balanced in 15 mL centrifuge tubes and extracted with 5.0 mL ultrapure water by vigorous shaking and sonication (3 × 30 min). After extraction, the samples were filtrated through a 0.2 μm H-PTFE syringe filter and further treated according to aerosol filter samples.

3.2.4 IC separation and collection of filters

Preparative oxalate separation was performed on a Dionex (Sunnyvale, CA, USA) IC20 equipped with a conductivity detector in a Dionex DS3 detection stabiliser, a self-regenerating suppressor (AERS 500, Dionex) running in external water mode, and a Dionex AS3500 autosampler with a switching valve (9010-092, Rheodyne, USA) containing a 500 μL sample loop. Eluent was generated by a Dionex EG40 eluent generator equipped with an EGC III KOH eluent generator cartridge. The IC system was controlled by a computer with Dionex Chromeleon 6.50 software. The separation was performed on an AS11-HC analytical column (4 × 250 mm) in combination with an AG11-HC guard column (4 × 50 mm) and an ATC-HC trap column (9 × 75 mm), all from Thermo Scientific (Sunnyvale, CA, USA). After 2 min with the initial eluent concentration of 5 mM KOH, a gradient from 5–40 mM KOH was applied for 18 minutes. The eluent flow rate was kept constant at 1 mL min⁻¹. A 21G × 4 3/4-inch needle was added at the line outlet after the suppressor and conductivity detector. Peaks were collected manually in cleaned and tared EXETAINER® vials by piercing the needle through the vials' septum. The vial cap was partially unscrewed before sampling for excess air to leave and to prevent damage to the suppressor membranes by excessive backpressure. Depending on the sample volume and concentration, one or two injections were made. The samples were concentrated to < 1 mL or < 0.5 mL of liquid for single or double injections, respectively. After collection, the vials were weighed, and an aliquot of the collected liquid was drawn from the vial to test for purity and identity. 150 μL of liquid was drawn using a Hamilton syringe and distributed over three IC vials (50 μL each) and 50 μL ultrapure water, oxalate standard, or sulfate standard was added, respectively.

Oxalate concentrations were measured by IC, using the aliquot reinjected after sampling for the Mexico and Sweden filters. For India filters, a 1 cm circular punch (0.785 cm²) was extracted with 2 mL of ultrapure water, filtrated using a 0.2 μm syringe filter and 300 μL injected into the IC as sufficient filter material was available for a separate analysis. For Poland filters, IC analysis after filter extraction showed insufficient oxalate concentrations for radiocarbon measurement for the filter area available, therefore radiocarbon analysis was omitted.

3.2.5 IC separation and collection of standard material

Different amounts of OxII (SRM 4990 C, Oxalic Acid II, $F^{14}C = 1.3407$) and fossil oxalic acid ($F^{14}C = 0.0082$) were used for constant and cross contamination assessment in the IC. Standard solutions containing oxalic acid were prepared and 300 µL injected, each standard corresponding to an amount of oxalic acid between 5 and 50 µg C. Five OxII (modern) and five fossil standards were used. The samples were collected and oxidised corresponding to the aerosol filter samples. Additional to single injection and collection of oxalic acid, also triple injections were made. Here, the same amount (300 µL) of standard was injected, although only containing a third of the amount of oxalate. Three injection and collection runs were made for each concentration with five modern and five fossil standards. Additionally, a single injection and collection run was performed with oxalic acid standards made in a 1000 ppm sulfate solution, yielding to 300 µg sulfate per injection. Multiple blank runs were conducted between isotopically different standards.

3.2.6 Chemical wet oxidation

Oxalate and WSOC samples were acidified and flushed to remove dissolved inorganic carbon and oxidised to CO_2 by chemical wet oxidation for radiocarbon measurement (Lang et al., 2012; Wiedemeier et al., 2016). For this, oxalate samples were topped up to 5 mL with ultrapure water with a baked-out glass beaker in a laminar flow cabinet. All vials were closed finger-tight and further liquid and gas handling was performed through the septum. WSOC sample vials did not need a top up as the volume is defined during WSOC extraction. The samples were acidified with 0.5 mL 8.5 % H_3PO_4 freshly prepared from 85 % H_3PO_4 (Suprapur® grade, Merck KGaA, Germany) and ultrapure water. After a 10 min reaction time, high-purity (99.999 %) helium was purged (50 mL min^{-1}) through the sample at room temperature for 3 min to remove all inorganic carbonaceous impurities. 0.25 mL oxidiser solution added to each sample was freshly prepared before each wet oxidation (10 % potassium persulfate (ACS grade, Sigma-Aldrich, USA) dissolved in 5 % H_3PO_4). Carbonaceous contaminants in the oxidiser were removed by pre-oxidizing the freshly prepared solution at 90°C for 30 min and helium purging (50 mL min^{-1}, 3 min) before use. Oxidiser solution and acid were added using a 1 mL Hamilton (Reno, NV, USA) glass syringe. Oxidation was performed in the heating block of a carbonate handling system (CHS, Ionplus AG, Switzerland) overnight at 75°C. Gas flushing for contaminant removal and CO_2 sampling was provided by a PAL HTC-xt (CTC Analytics AG, Switzerland) autosampler. The autosampler holder was equipped with a custom-made needle with a gas inlet and outlet hole for flushing and gas sampling (Molnár et al., 2013). To strip all the gas out of the solution, the custom needle was submerged in the sample solution for purging. Liquid exiting the vial was retained in a custom water container (25 mL) and the gas was dried using a P_2O_5 (Sicapent®, Merck KGaA, Germany) trap. The evolved CO_2 gas was sent to the gas interface system (GIS) for radiocarbon measurement (see below).

3.2.7 Radiocarbon measurement

Oxalate and WSOC samples were oxidised by chemical wet oxidation as described above and the sampled CO_2 was fed to the gas interface system (GIS). TC and EC filters were combusted at 870°C in pure O_2 in a Sunset OC/EC analyser coupled to a non-dispersive infrared (NDIR) for amount determination, which output was also connected to the GIS. On the GIS, the evolved CO_2 gas was trapped on X13-zeolite before thermal release and mixing with helium for radiocarbon measurement. All radiocarbon measurements were performed at LARA, the Laboratory for the Analysis of Radiocarbon with AMS (i.e., accelerator mass spectrometry) at the University of Bern on a MIni radioCArbon DAting System (MICADAS) (Synal et al., 2007; Szidat et al., 2014; Fahrni et al., 2013). Each AMS measurement day included multiple OxII radiocarbon standard (SRM 4990 C) and fossil sodium acetate (Szidat et al., 2014) samples for correction. Liquid standard solutions were prepared for chemical wet oxidation, solid grains were used in the OC/EC analyser. Corrections for background, blank, mass-fractionation, standard normalisation, and uncertainty data correction was performed with BATS software version 3.6 (Wacker et al., 2010). We applied a cross-contamination of 0.5 % due to the zeolite trap CO_2 adsorption memory effect and a constant contamination of 0.9 ± 0.2 μg C with $F^{14}C=0.20 \pm 0.08$ on wet oxidation samples. Samples subjected to total combustion in an OC/EC analyser were corrected for a cross-contamination of 0.2 % and a constant contamination correction of 0.40 ± 0.20 μg with $F^{14}C=0.80 \pm 0.36$ was applied (Agrios et al., 2015). To account for EC loss and charring during OC/EC separation, $F^{14}C$-EC values were further corrected with an R (R Core Team, 2020) script based on a thermal desorption model (Rauber and Salazar, 2020; Rauber et al., 2022).

The nonfossil fraction (fNF) was determined from the $F^{14}C$ results for the individual campaigns. For Sweden and Mexico, the factors from the original papers were estimated with a simpler approach. Here, more appropriate values deduced from a tree growth model have been used. These values supersede the original factors, however, both values differ from each other only within the given uncertainties. A summary of the reference values used for the calculation of fNF is shown in Table S3.

3.3 Results

3.3.1 Methodology

Contamination precautions

Carbonaceous contaminations were mitigated by diligent cleaning protocols. Polypropylene centrifuge tubes were cleaned by submerging the tubes in ultrapure water for two weeks and exchanging the water three times. The tubes were dried at 50°C before storage and use. Glassware was cleaned in 1 M H_3PO_4 (ACS grade, Merck KGaA, Germany) and baked out at 500°C for 5 h. The glass syringe for WSOC water extraction was only rinsed with ultrapure water and baked out at 500°C for 2 h. EXETAINER® vials used for chemical wet oxidation were leak tested overnight at 75°C and ~3 bar overpressure of N_2 after cleaning.

Vials not retaining gas were discarded. Aerosol filter handling and water extraction for WSOC was performed in a laminar flow cabinet. The filter holders and silicone O-rings for WSOC extraction were rinsed with ultrapure water and sonicated three times for 20 minutes with water exchange in between for cleaning and dried in a laminar flow cabinet. The IC was switched on and rinsed with 5 mM KOH at flow of 1 mL min^{-1} for at least 24 h before samples were injected and collected for radiocarbon analysis. Additionally, multiple blank (i.e., without injection) and matrix blank (i.e., injection of ultrapure water) samples were run before sample collection to flush all the lines.

Oxalate extraction and measurement

Oxalate extraction procedures for IC analysis for preparative and analytical use have been described before e.g., by Fahrni et al. (2010a) and Hsieh et al. (2008, 2007). Here, the procedure was only marginally modified. Concentration under a gentle stream of N_2 was performed without the aid of a heating block to avoid material loss and prevent decomposition at the expense of a slightly higher gas use. Recovery experiments using IC for analysis and different amounts of oxalic acid (7–21 µg C) in 5 mL of ultrapure water gave 98.5 ± 5.8 % recovered material after concentration. No difference was observed for the recovery of smaller compared to larger amounts. Although up to four times the volume of ultrapure water was used for filter extraction, the concentration step is considered efficient and retains oxalic acid quantitatively. The preparative separation caused column overloading and the recorded conductivity signal was not of analytical use. Oxalate eluates just after sulfate and for preparative separation, there was no baseline separation, as the oxalate was present in the tail of the sulfate peak. Generally, the amount of sulfate was at least an order of magnitude higher than the amount of oxalate, which is in accordance with previous work e.g., from Hsieh et al. (2008). An aliquot of the sample was injected after collection for purity and identity. Sulfate was present in most samples but not treated as a contaminant due to its non-carbonaceous nature. In the work of Fahrni et al. (2010a), a secondary separation step was required to remove sulfate before oxidation with cupric oxide in a quartz tube to prevent the formation of SO_2. In our work, sulfate remained in the aqueous solution even after oxidation and did not affect the ^{14}C measurement. The method presented here requires only one concentration step after filter extraction and chemical wet oxidation eliminates the water removal step and thermal oxidation. Fewer concentration steps simplify the procedure and reduce potential sources of contamination and increases sample throughput. Furthermore, omitting HPLC separation used by Fahrni et al. (2010a) further makes the method methodologically less elaborate. DCA separation is also feasible with preparative GC (Xu et al., 2021), however, this method requires derivatisation of the target compounds. The added carbon must be corrected by isotopic mass balance. This correction step adds an additional uncertainty. In our approach the fraction modern of oxalic acid is measured directly without derivatisation. The usage of the IC is furthermore advantageous to the preparative GC, as the isolation of sufficient amounts of oxalate is achieved already in one chromatographic run, whereas the preparative GC requires repeated (i.e., typically 50) injections.

Procedural blank

Radiocarbon analysis is highly sensitive to carbonaceous contaminants; however, the amount of carbon contamination is often too small to be determined directly (Ziolkowski and Druffel, 2009; Mollenhauer and Rethemeyer, 2009). Frequently, the amount of carbon contamination is constrained by analysing decreasing amounts of standards with modern and fossil $F^{14}C$ values and applying a model of constant contamination or a drift model (Salazar et al., 2015; Hanke et al., 2017). The chemical wet oxidation procedural blank was assessed by adding different amounts of OxII (SRM 4990 C) or fossil sodium acetate (Szidat et al., 2014) solutions (~1000 ppm) to vials containing 5 mL of ultrapure water followed by wet oxidation and radiocarbon measurement. IC separation could contribute additional contamination e.g., from handling, devices, and column bleed. Three drift models with different objectives were made to assess the contamination of the wet oxidation combined with IC (Salazar et al., 2015). Different amounts of OxII (SRM 4990 C) and fossil oxalic acid ($F^{14}C = 0.0082$) were injected and collected by IC. In a single injection, all oxalic acid for a standard sample was injected and collected all at once. For the triple injection, a third of the desired final sample concentration was injected and collected but repeated three times. Additionally, a single injection was made containing sulfate to verify that the inorganic contaminant does not cause unintended effects. As summarised in Table 1, IC separation affects the procedural blank negligibly. The chemical wet oxidation contributed to a constant contamination of $0.90 \pm 0.20\,\mu g\,C$ with $F^{14}C = 0.20 \pm 0.08$. The amount and fraction modern of the contamination with an additional IC separation with or without added sulfate yields to values that are identical within uncertainties. The amount of contaminant with three injections and collections of oxalic acid yields only to a small increase of increase of contamination. Overall, the contribution of the procedural blank has only little influence on the result. The median amount of oxalate per sample this study was $21\,\mu g\,C$ (n = 34, mean = $25 \pm 18\,\mu g\,C$). As an example, for a $21\,\mu g\,C$ sample the effectively measured $F^{14}C$ value with the contamination would be 0.97 ± 0.02 and 0.01 ± 0.01 for a modern ($F^{14}C = 1$) and fossil ($F^{14}C = 0$) sample, respectively.

Table 1: Procedural blank of wet oxidation only and IC separation with wet oxidation. The results for the wet oxidation only were obtained with OxII and fossil sodium acetate, IC results by injecting and collecting OxII and fossil oxalic acid. The number of samples corresponds to the total modern and fossil samples.

	Wet ox. only	Single inj.	Single + sulfate	Triple inj.
Contamination ($\mu g\,C$)	0.90 ± 0.20	0.92 ± 0.20	0.80 ± 0.20	1.18 ± 0.20
Contamination ($F^{14}C$)	0.20 ± 0.08	0.25 ± 0.08	0.21 ± 0.08	0.26 ± 0.08
Number of samples	30	20	10	10

[14]C Field blanks were not investigated in this work; therefore, no field blank corrections were made. Field blank filter analysis from others show that there may be a small contribution of oxalate. In an intercomparison of oxalic acid measurement in Arctic aerosols by gas chromatography and IC, Kawamura et al. (2010a) reported that concentrations in field blank filters were less than 10 % of aerosol filter samples. In another study on marine Arctic aerosols, the amounts on the field blanks contributed to less than 5 % of the actual samples (Kawamura et al., 2012). Bikkina et al. (2020) analysed oxalate in the Bay of Bengal and reported that the oxalate concentration in procedural field blank filters less than 3 % of the minimum observed for the samples.

The several steps required (i.e., extraction, volume reduction, IC separation) for oxalic acid extraction and the followed chemical wet oxidation may add contaminations. Nevertheless, the chemical wet oxidation contributed to a constant contamination of $0.90 \pm 0.20\,\mu g$ C with $F^{14}C = 0.20 \pm 0.08$, while the IC separation added only negligible amounts of contamination (see Table 1). Online coupling of a Sunset OC/EC analyser is the main procedure for the analysis of other aerosol fractions (e.g., TC, EC, WINSOC). Agrios et al. (2015) constrained the contamination of the AMS coupled with the Sunset OC/EC analyser at $0.4 \pm 0.2\,\mu g$ C with $F^{14}C = 0.80 \pm 0.36$. The Sunset-AMS measurement is semiautomatic; each sample must be loaded manually into the Sunset combustion chamber. Providing sufficient filter loading, TC measurements directly with aerosol filter punches as well as separated aerosol fractions are also feasible by an Elemental analyser coupled to an AMS (Zhang et al., 2014, 2017). For an elemental analyser coupled to an AMS, Salazar et al. (2015) reported a constant contamination of $1.4 \pm 0.2\,\mu g$ C with $F^{14}C = 0.7 \pm 0.7$, substantially higher than the AMS-Sunset coupling but with a comparable Fraction Modern. The chemical wet oxidation procedural blank is best compared to analyses utilising the same instrumentation and similar type of analyte. Solid carbonate analysis for gas dating of foraminifera is performed with the CHS coupled with the GIS and AMS, and Gottschalk et al. (2018) reported a constant contamination of $0.68 \pm 0.10\,\mu g$ C with $F^{14}C = 0.30 \pm 0.04$. There, the foraminifera compromising mostly of inorganic $CaCO_3$ are leached with 200 μL HCl (0.01 M), flushed with helium before the foraminifera are dissolved with 0.5 mL 85 % H_3PO_4 at 65°C overnight. Instead of the 12 mL EXETAINER® vials used for the chemical wet oxidation, smaller 4.5 mL vials with the same screw caps are used for foraminifera samples. Compared to the chemical wet oxidation, the volume of the liquid is much smaller and therefore also the acid exposed surface. The hot and strongly acidic environment also dissolves any inorganic contaminants; however, organic contaminants should remain mostly unchanged. With the chemical wet oxidation, the hot acidic and oxidative environment will oxidise also organic contaminants. The chemical wet oxidation procedure is preceded with a necessary acidification step to remove all inorganic contaminants, but this may be another source for the introduction of organic contaminants. Furthermore, the slightly larger contamination for the chemical wet oxidation compared to solid carbonate may be explained by the more complex procedure with inorganic carbon removal and the fact that the contamination of surfaces and chemicals from organic compounds tend to be larger and more persistent than contamination from inorganic carbonates.

Hanke et al. (2017) performed radiocarbon analysis by chemical wet oxidation of benzene polycarboxylic acids from pyrogenic samples with a chemical pretreatment followed by liquid chromatography purification step. Despite the chemical pretreatment and the liquid chromatography purification step using organic solvents, Hanke et al. (2017) reported that the chemical wet oxidation accounts for 81 % of the total contamination. This is in accordance with this work, where the bulk of the contamination stems from the chemical wet oxidation and the IC separation added only a small contamination.

3.3.2 Source apportionment results

The most comprehensive oxalate measurement dataset was made with urban filters from Delhi, India, providing both diurnal and daily filters, although at different seasons. From January to March 2018 (winter and spring) diurnal filters were sampled, for April and May 2018 (summer) daily filters. From the total 23 filters available, on 20 filters separation and radiocarbon measurement of oxalic acid was successfully applied, separation failed on the remaining three filters. Additionally, WSOC, EC, and TC were measured on all filters. Mean oxalate concentrations for the daytime filters were 131 ± 120 ng C m^{-3} (n = 6, range: 40–313), 142 ± 94 ng C m^{-3} (n = 6, range: 48–279) for the night-time filters, and 79 ± 67 ng C m^{-3} (n = 11, range: 9–216) for the daily filters. Mean WSOC concentrations for the daytime filters were 7.0 ± 2.9 µg C m^{-3} (range: 3.1–10.5), 7.5 ± 3.9 µg C m^{-3} (range: 3.6–14.8) for the night-time filters, and 4.7 ± 2.9 µg C m^{-3} (range: 2.1–11.0) for the daily filters. Mean EC loadings were 4.1 ± 1.4 µg C m^{-3} and 6.6 ± 2.8 µg C m^{-3} for the daytime and night-time filters, and 3.2 ± 2.8 µg C m^{-3} for the daily filters. The oxalate content in WSOC (C/C ratio) was similar for daytime, night-time, and daily filters with mean ratios of 1.75 %, 1.90 %, and 1.56 % with mean over all measured filters of 1.70 % (range: 0.36–3.28). The oxalate content in TC was 0.47 %, 0.45 %, and 0.41 % for day, night, and daily filters with an overall mean of 0.44 % (range: 0.11–0.91). The EC/TC ratio for daytime and night-time filters was 0.18 ± 0.04 (range: 0.11–0.23) and 0.23 ± 0.02 (range: 0.21–26), respectively, and 0.17 ± 0.04 (range: 0.11–0.26) for the summer 24 h filters. The mean nonfossil fractions for oxalate was 0.71 ± 0.06 (range: 0.60–0.84), 0.73 ± 0.06 (range: 0.63–0.85) for WSOC, 0.58 ± 0.06 (range: 0.46–0.70) for TC, and 0.41 ± 0.07 (range 0.24–0.55) for EC.

The three Mexico City 24 h samples from March 2006 revealed a mean filter loading for of 52.7 ± 5.5 µg C m^{-3} for TC, 7.2 ± 2.1 µg C m^{-3} for EC, and 2.9 ± 0.2 µg C m^{-3} for WSOC with an EC/TC ratio of 0.09 ± 0.02. The nonfossil fractions of TC, OC (calculated) and EC were 0.39 ± 0.12, 0.43 ± 0.13 and 0.09 ± 0.05, respectively. The oxalate content in TC and WSOC was 0.6 ± 0.2 % and 12.6 ± 2.8 %, respectively. The mean fraction nonfossil was 0.61 ± 0.10 for WSOC and with 0.64 ± 0.08 slightly higher ($p = 0.046$, n = 3) for oxalate. The filters from February 2005 sampled for multiple days (3, 4, 7, 7) at the rural Råö site close to Gothenburg, Sweden were analysed for TC, WSOC, and oxalate. The mean fraction nonfossil was 0.67 ± 0.08 for TC, 0.77 ± 0.06 for WSOC, and 0.92 ± 0.10 for oxalate. The oxalate content in TC was 0.8 ± 0.5% and in WSOC 3.0 ± 2.3 %. AMS measurements of the TC, EC, WSOC, and WINSOC fractions were performed with the Kraków filters (Casotto et al., 2022). Filters from two following days were pooled for oxalate analysis, however, due to very low oxalate concentrations,

radiocarbon measurement was not possible. The oxalate concentration in TC (WSOC) was very low with < 0.02 % (0.02 ± 0.01 %) in winter and 0.08 ± 0.02 % (0.13 ± 0.02 %) in summer. The mean WSOC/TC ratio was 0.64 ± 0.06 both in winter and in summer. The oxalate concentration for winter and summer was 7.2 ± 2.2 ng m^{-3} and 13.6 ± 5.4 ng m^{-3}, respectively. EC/TC ratio were 0.09 ± 0.03 (n = 10) in winter and 0.12 ± 0.06 (n = 8) in summer. The nonfossil fraction for TC, WSOC, and WINSOC was 0.46 ± 0.05, 0.56 ± 0.2, and 0.39 ± 0.05 for winter filters and 0.69 ± 0.08, 0.76 ± 0.09, and 0.61 ± 0.09 for summer filters, respectively. NIST SRM 1649a urban dust standard was water extracted in quadruplicates and the WSOC and oxalate fractions measured with AMS. The nonfossil fraction for WSOC was 0.62 ± 0.02 and 0.66 ± 0.00 for oxalate. The mean fraction nonfossil for oxalate and the corresponding WSOC (n = 31) in this study over all sites (without NIST SRM 1649a standard) did not differ significantly ($p > 0.05$) with 0.71 ± 0.08 and 0.70 ± 0.07, respectively. A measurement summary with monthly means for Delhi is shown in Table 2, the summary of all radiocarbon measurements is shown in Table S1 and Table S2.

Table 2: Nonfossil fraction and F^{14}C values for oxalate, WSOC, TC, and EC with uncertainties (1σ). For the filters from Delhi, India monthly means are shown.

Site	Sampling date	Oxalate F^{14}C	WSOC F^{14}C	TC F^{14}C	EC F^{14}C
NIST SRM 1649a	1976-1977	0.89 ± 0.01	0.83 ± 0.01	0.51 ± 0.00	-
Råö	11 Feb 2005 – 14 Feb 2005	0.81 ± 0.06	0.72 ± 0.01	0.63 ± 0.02	-
Råö	14 Feb 2005 – 18 Feb 2005	0.84 ± 0.03	0.72 ± 0.01	0.60 ± 0.01	-
Råö	18 Feb 2005 – 25 Feb 2005	1.00 ± 0.02	0.81 ± 0.01	0.67 ± 0.01	-
Råö	25 Feb 2005 – 04 Mar 2005	1.01 ± 0.03	0.83 ± 0.01	0.78 ± 0.01	-
Mexico City	21 Mar 2006 – 22 Mar 2006	0.77 ± 0.01	0.76 ± 0.01	0.56 ± 0.01	0.13 ± 0.06
Mexico City	22 Mar 2006 – 23 Mar 2006	0.72 ± 0.01	0.70 ± 0.01	0.42 ± 0.01	0.08 ± 0.06
Mexico City	29 Mar 2006 – 30 Mar 2006	0.59 ± 0.01	0.55 ± 0.01	0.29 ± 0.01	0.22 ± 0.04
Delhi*	10 Jan 2018 – 22 Jan 2018	0.83 ± 0.02	0.83 ± 0.01	0.70 ± 0.01	0.49 ± 0.04
Delhi*	03 Feb 2018 – 28 Feb 2018	0.74 ± 0.02	0.78 ± 0.02	0.62 ± 0.01	0.38 ± 0.05
Delhi*	12 Mar 2018 – 30 Mar 2018	0.74 ± 0.02	0.76 ± 0.01	0.62 ± 0.01	0.45 ± 0.04
Delhi*	05 Apr 2018 – 29 Apr 2018	0.70 ± 0.01	0.72 ± 0.01	0.59 ± 0.02	0.48 ± 0.04
Delhi*	05 May 2018 – 29 May 2018	0.75 ± 0.01	0.77 ± 0.01	0.55 ± 0.04	0.46 ± 0.04
Site	Sampling date	Oxalate fNF	WSOC fNF	TC fNF	EC fNF
NIST SRM 1649a	1976-1977	0.66 ± 0.48	0.62 ± 0.44	0.38 ± 0.00	-
Råö	11 Feb 2005 – 14 Feb 2005	0.74 ± 0.06	0.66 ± 0.01	0.56 ± 0.02	-
Råö	14 Feb 2005 – 18 Feb 2005	0.76 ± 0.03	0.66 ± 0.01	0.54 ± 0.01	-
Råö	18 Feb 2005 – 25 Feb 2005	0.91 ± 0.01	0.73 ± 0.01	0.60 ± 0.01	-
Råö	25 Feb 2005 – 04 Mar 2005	0.91 ± 0.03	0.76 ± 0.01	0.71 ± 0.01	-
Mexico City	21 Mar 2006 – 22 Mar 2006	0.70 ± 0.01	0.69 ± 0.01	0.51 ± 0.01	0.11 ± 0.05
Mexico City	22 Mar 2006 – 23 Mar 2006	0.66 ± 0.01	0.64 ± 0.01	0.38 ± 0.01	0.07 ± 0.05
Mexico City	29 Mar 2006 – 30 Mar 2006	0.54 ± 0.01	0.50 ± 0.01	0.27 ± 0.01	0.19 ± 0.04
Delhi*	10 Jan 2018 – 22 Jan 2018	0.79 ± 0.02	0.79 ± 0.01	0.66 ± 0.01	0.45 ± 0.04
Delhi*	03 Feb 2018 – 28 Feb 2018	0.70 ± 0.02	0.74 ± 0.02	0.59 ± 0.01	0.36 ± 0.04
Delhi*	12 Mar 2018 – 30 Mar 2018	0.71 ± 0.02	0.73 ± 0.01	0.59 ± 0.01	0.42 ± 0.04
Delhi*	05 Apr 2018 – 29 Apr 2018	0.67 ± 0.01	0.69 ± 0.01	0.55 ± 0.02	0.44 ± 0.04
Delhi*	05 May 2018 – 29 May 2018	0.72 ± 0.01	0.73 ± 0.01	0.52 ± 0.04	0.43 ± 0.04

*Monthly mean

3.4 Discussion

3.4.1 Significance of ^{14}C analysis of oxalate

Delhi is a densely populated and highly polluted city in India, and a comprehensive understanding of its sources is of high importance. Indication for divergent sources of bulk WSOC and oxalate may lead to a better understanding. A significant ($p = 0.012$) temporal variability was observed in the diurnal oxalate and WSOC measurements with higher nonfossil fractions at night for both fractions.
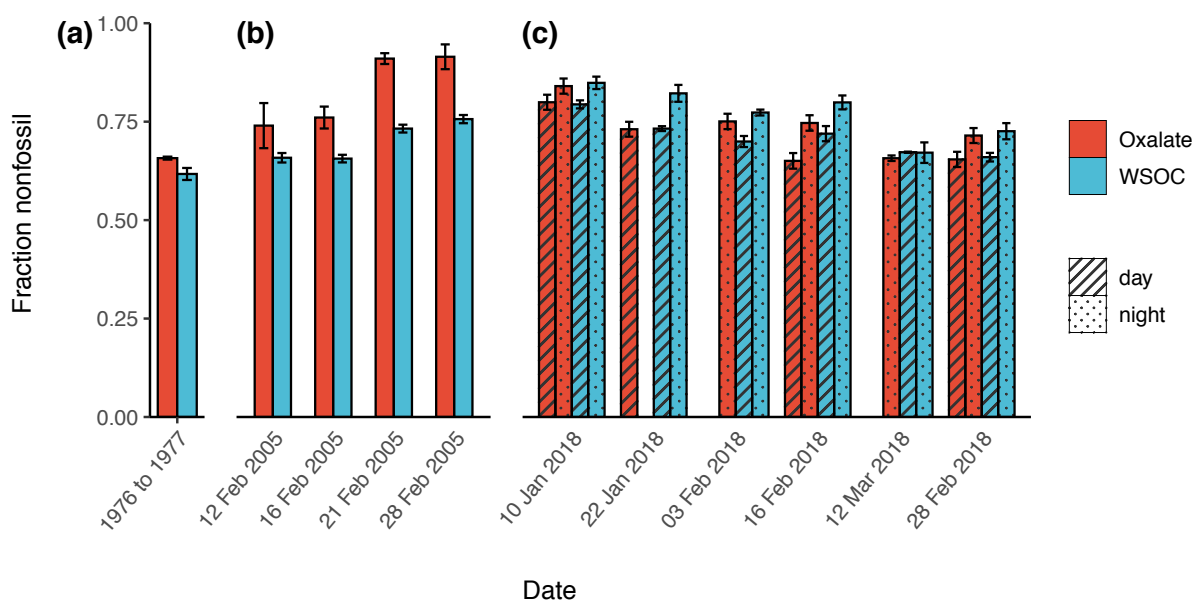

Figure 2: Fraction nonfossil of oxalate and WSOC. a) NIST SRM urban dust reference sampled for ~1 year in 1976 and 1977 the Washington DC area. b) Rural Råö, Sweden in February 2005 sampled for 3–7 days. c) Diurnal filters from Delhi, India. Please note the missing night-time oxalate measurement for the 22nd of January and missing daytime oxalate measurements for the 28th of February and 2nd of March.

The nonfossil fraction of oxalate and WSOC was 0.74 ± 0.07 (range: 0.66–0.84) and 0.77 ± 0.07 (range: 0.67–0.85) for night-time filters (n = 5), respectively. For daytime (n = 4), the difference of the nonfossil fraction of oxalate and WSOC was not significant ($p > 0.05$), with 0.71 ± 0.07 (range: 0.65–0.80) for oxalate and 0.71 ± 0.05 (range: 0.66–0.79) for WSOC. When the night-time and daytime filters form January, February, and March are compared together (n = 9), then there is a significant ($p = 0.002$) difference between oxalate and WSOC, with 0.73 ± 0.07 (range: 0.65–0.84) for oxalate and 0.76 ± 0.06 (range: 0.68–0.86) for WSOC. For the daily (24 h) filters from summer (n = 11), the nonfossil fraction was 0.70 ± 0.05 (range: 0.60–0.78) for oxalate and 0.69 ± 0.07 (range: 0.59–0.80) for WSOC, meaning that the difference is not significant ($p > 0.05$). Overall, there significant difference between oxalate and the bulk WSOC for night-time filters from January, February, and March. The difference remains significant when both the night-time and the daytime filters are considered together, however, there is no significant difference solely

for the daytime filters (see Fig. 2c). This indicates that there is a diurnal variation of oxalate and WSOC formation in winter and spring. During the summer months (April, Mai) the nonfossil fractions of oxalate did not differ from WSOC (see Fig. S1b). This implies that the formation processes for oxalate during the summer months are different from the winter months, and that the formations of oxalate in summer is comparable to the formation of the bulk of WSOC compounds.

For TC, the nonfossil fraction in the diurnal filters was 0.59 ± 0.05 (range: 0.54–0.69) and 0.61 ± 0.07 (range: 0.49–0.70) for the day and night filters, thus did not differ significantly in the selected filters from January to March. The daily summer filters had a nonfossil fraction of 0.55 ± 0.05 (range: 0.46–0.64). For EC, the nonfossil fraction in the diurnal filters did not differ significantly from each other ($p > 0.05$) with 0.39 ± 0.07 (range: 0.30–0.51) and 0.39 ± 0.10 (range: 0.24–0.55) for the day and night filters.

Mexico City and its surrounding Metropolitan Area is in a tropical location (19 °N) and at high altitude (2240 m above sea level). With over 20 million people, it is the largest megacity in North America. The high altitude results in elevated UV fluxes and intense photochemistry as well as reduced ventilation as the basin is surrounded by mountains on three sides (Aiken et al., 2009). These prerequisites may favour highly divergent formation processes for WSOC and oxalate, however, three measurements from March 2006 show the contrary. The mean fraction nonfossil was 0.61 ± 0.10 and 0.63 ± 0.08 ($p > 0.05$, n = 3) for WSOC and oxalate, respectively. Despite comparably low nonfossil fractions of TC, OC (calculated) and EC (0.38 ± 0.12, 0.42 ± 0.14, and 0.12 ± 0.06, respectively), oxalate and WSOC were predominately formed from biogenic sources with little input from fossil sources. The very low nonfossil fraction for EC indicates that only a minor part of the EC originates form biomass combustion, and the overwhelming majority of EC was generated by fossil-fuel combustion processes. Nevertheless, the whole campaign included a high biomass-burning period (March 21/22 and March 22/23) followed by a low biomass-burning period (March 29/30). The values of the individual filters indicate that the change from a high biomass-burning period to a low biomass-burning period are visible in both the oxalate and WSOC fraction to a similar degree. The nonfossil fraction for the March 21/22 and March 22/23 are 0.70 ± 0.01 and 0.66 ± 0.01 for oxalate, and 0.69 ± 0.01 and 0.64 ± 0.01 for WSOC. On the other hand, the nonfossil fraction for the low biomass-burning period in March 29/30 was 0.54 ± 0.01 and 0.50 ± 0.01 for oxalate and WSOC (see Fig. S1a). The values for the two fractions in the high biomass-burning period are equivalent; the difference in the low biomass-burning period is too little for a single measurement to indicate divergent formation processes of WSOC and oxalate. Nevertheless, the change of the biomass-burning intensity is still visible, even though it seems obvious that biogenic SOA was the dominant source of nonfossil oxalate in Mexico City.

The filters from February 2005 sampled at the rural Råö site close to Gothenburg, Sweden show a significant ($p = 0.010$) difference between the WSOC and oxalate with a nonfossil fraction of 0.70 ± 0.05 and 0.83 ± 0.09, respectively (see Fig. 2b). All Råö filters were sampled for multiple days (3, 4, 7, 7). Evidently, biogenic SOA was the dominant source of nonfossil oxalate at the rural site. Furthermore, the

samples show a higher nonfossil fraction for oxalate, contrary to the night-time Delhi filters where a higher nonfossil fraction for WSOC was observed.

SRM 1649a Urban Dust standard was sampled 1976 to 1977 (sampling time: ~1 year) in Washington, DC (USA) with a 100 µm size cut (sieved). Due to the large size cut of this material, the results obtained may not be directly comparable to the aerosol filters from ambient PM sampling. Nevertheless, this reference material has been extensively investigated (Waterman et al., 2000; Larsen et al., 2006; Szidat et al., 2004b, a). A significant ($p < 0.01$, n = 4) difference between WSOC and oxalate was found with a mean $F^{14}C$ value of 0.83 ± 0.02 and 0.89 ± 0.01, respectively (see Fig. 2a). Previous measurements showed a substantial nonfossil influence on OC ($f_M = 0.70 ± 0.05$), a half-modern TC value ($f_M = 0.522 ± 0.018$), and EC ($f_M = 0.066 ± 0.020$) of overwhelmingly fossil origin (Szidat et al., 2004b). Levoglucosan contributes < 1 ‰ to the TC mass for SRM 1649a, thus the biomass burning contribution is low. The high nonfossil fraction obtained for both WSOC and oxalate indicates formation from biogenic SOA. These results contrast the situation in Mexico City, which were dominated by biomass burning episodes. However, it corresponds to rural Råö, where the nonfossil contribution is likely biogenic SOA.

Filters from Kraków, Poland were analysed as a site for its high prevalence of fossil-fuel combustion sources. Poland produces most of its electric energy from coal and lignite with major coal fire plants in the Upper Silesian region, where significant coal resources are present and coal power stations are located nearby. The closest power station is only 13 km southwest from the sampling site in Kraków, another one is located around 110 km east and a cluster of six power stations are located 35–120 km west-northwest from Kraków. Filters were received in pairs of two following days. The individual filters were measured for TC, EC, WSOC, and WINSOC. Filters from two following days were pooled for oxalate analysis. EC/TC ratio were 0.09 ± 0.03 (n = 10) in winter and 0.12 ± 0.06 (n = 8) in summer. The oxalate concentration in TC (WSOC) was very low with < 0.02 % (0.02 ± 0.01 %) in winter and 0.08 ± 0.02 % (0.13 ± 0.02 %) in summer, with a WSOC/TC ratio of 0.64 ± 0.06 for both winter and summer. To put this into perspective, the mean oxalate/WSOC ratios were more than an order of magnitude lower compared to the other sites. With the available filter material, radiocarbon analysis of oxalate was not possible. Even with seasonally (winter/summer) pooled filters, the gained amount would be more than an order of magnitude smaller than the ~3 µg C required for an analysis. Radiocarbon measurement was performed for TC, WSOC, and WINSOC on all filters for winter (n = 10) and summer (n = 8). EC was also measured, however, due to low loadings, fewer measurements were possible. Measurements show an overwhelming fossil contribution, but no credible values can be reported. The fraction nonfossil for TC, WSOC, and WINSOC was 0.46 ± 0.05, 0.56 ± 0.2, and 0.39 ± 0.05 for winter filters and 0.69 ± 0.08, 0.76 ± 0.09, and 0.61 ± 0.09 for summer filters, respectively. As expected, the fraction nonfossil was lower in winter than in summer in all fractions due to numerous fossil combustion sources. Although the fraction nonfossil for WSOC differs substantially by season, the WSOC/TC ratio was rather similar. Very little oxalate was formed with even lower concentrations in winter, thus the oxalate/WSOC ratio was also lower in winter than in summer. Casotto et al. (2022) reported the sources of OA for winter, spring, and summer in Kraków for the same

sampling campaign. In winter, winter oxygenated organic aerosols (WOOA) make up the majority of OA, with 34.4 ± 4.3 % for fossil WOOA and 38.0 ± 4.8 % for nonfossil WOOA, while primary biogenic organic aerosols (PBOA), biomass burning organic aerosols (BBOA), and coal combustion organic aerosol (CCOA) only make up the smaller fraction of OA with 5.5 ± 2.7 %, 2.9 ± 2.4 %, 11.5 ± 9.9 %. The largest fraction for summer OA are summer oxygenated organic aerosols (SOOA) with 42.9 ± 6.2 %, while PBOA, BBOA, and CCOA make up 34.7 ± 14.3 %, 5.2 ± 3.1 %, and −4.3 ± 14.8 %.

Already low compared to the other sites, the oxalate concentration Kraków was roughly a factor of two lower in winter than summer. This indicates that the oxalate is mostly formed from PBOA. Despite their large fractions of the total OA in winter and summer, respectively, WOOA and SOOA are less relevant sources for oxalate formation. The fraction of CCOA in OA is higher in winter than summer, however, the fraction of CCOA in OA is small. The higher fraction of CCOA occurs in winter, while the concentration of oxalate is higher in summer. Thus, COOA are not a relevant contributor to the formation of oxalate.

3.4.2 Implications

The most pronounced differences of the nonfossil fraction of oxalate to WSOC were suspected in urban high pollution sites, however, the results from this study indicate the contrary. The most pronounced differences were found for Råö with a mean fraction nonfossil of 0.70 ± 0.05 and 0.83 ± 0.09 for WSOC and oxalate, respectively. Szidat et al. (2009) previously reported radiocarbon measurements (EC, WINSOC, and calculated WSOC) from this campaign as well as results from urban Gothenburg, Sweden, located approximately 35 km north of the Råö site. Additional to radiocarbon measurements, also levoglucosan was measured both at the urban and rural site. The mean levoglucosan concentration in winter for Gothenburg was 62 ± 30 ng m^{-3} while the mean concentration for Råö was lower at 35 ± 20 ng m^{-3}. Compared to other European sites, the levoglucosan values reported by Szidat et al. (2009) are generally lower than in Gothenburg (Szidat et al., 2006; Jedynska et al., 2015; Yttri et al., 2009). Therefore, the biomass burning contribution in Gothenburg is relatively low and even lower for Råö. These measurements are evidence for the low influence on oxalate formation from biomass burning. Previously, Fahrni et al. (2010a) reported a substantial nonfossil contribution in oxalate for this campaign in urban Gothenburg, with a mean fraction nonfossil of 0.83 ± 0.09 for five pooled filters sampled from 11 February to 4 March 2005. This Gothenburg oxalate measurement is in excellent agreement with the calculated mean fraction nonfossil of 0.83 ± 0.09 for Råö, collected for the same period from this study. The high fraction nonfossil has also been seen in the oxalate measurements by Fahrni et al. (2010a) for rural Ispra, Italy on filters from September 2008. There, a fraction nonfossil of 0.75 ± 0.08 was reported, indicating again to an oxalate formation mainly from nonfossil precursors. Fahrni et al. (2010a) did not report any WSOC measurements for Gothenburg or Ispra, thus we can only hypothesise whether the reported oxalate measurement would differ substantially from WSOC.

Diurnal variability of oxalate and WSOC was observed for the dry season (winter) Delhi filters with significant differences for the night-time filters but not significant differences for the daytime filters. The

temporal variation in the fraction nonfossil could be due to a shift in major soot sources from firewood/biomass burning for cooking and heating during daytime to traffic from heavy vehicles (fossil) at night. The mixing rate of the boundary layers and precipitation could add additional variability in the diurnal nonfossil EC fraction. Tobler et al. (2020) performed chemical characterisation and source apportionment of $PM_{2.5}$ aerosols using positive matrix factorisation of OA at a site very close (~6 km) to the sampling station for this study and for the same year (2018). Tobler et al. (2020) revealed that the biggest contributors to the total OA in decreasing relevance were oxygenated OA, OA from solid fuel burning, and hydrocarbon-like OA (fossil-fuel sources). In this study, the nonfossil fraction of EC was 0.39 ± 0.07, 0.39 ± 0.10, and 0.44 ± 0.06 for daytime, night-time, and daily filters, respectively, and substantially higher than for Mexico City (0.12 ± 0.06) or Kraków (0.15 ± 0.07). This strongly indicates that biomass burning is a major contributor to PM for Delhi. There is indication for a diurnal variability of EC similar to equivalent Black Carbon (eBC) as seen by Tobler et al. (2020) with $4.1 \pm 1.4 \, \mu g \, C \, m^{-3}$ and $6.6 \pm 2.8 \, \mu g \, C \, m^{-3}$ for the daytime and night-time filters, however, it was not significant ($p > 0.05$). Most likely, this diurnal variability is strongest December and January, but not January to March.

For the Mexico City filters, there was no significant difference between oxalate and WSOC neither for the high biomass-burning period (March 21/22 and March 22/23) nor for the low biomass-burning period (March 29/30). This is another indication that biomass burning has only a small effect on oxalate formation. Further, for the low biomass-burning period the lowest nonfossil contribution (0.54 ± 0.01) from the total of 31 oxalate measurements was recorded, however, there is no evidence of divergent sources for WSOC compared to oxalate.

Recently, Xu et al. (2021) reported substantial spatial variations for oxalate in Heshan, China with a nonfossil contribution of 0.24 and 0.72 for urban and coastal air masses. Like Fahrni et al. (2010a) for Gothenburg, also Xu et al. (2021) did not report any WSOC results which raises the question on whether the reported oxalate measurement would differ from WSOC for these selected measurements. Furthermore, the oxalate in the urban air masses show an exceptionally low nonfossil contribution. Most likely, the WSOC from this sample would also show a very low nonfossil contribution. In fact, the lowest fraction nonfossil in this study was measured for 29–30 March 2006 for Mexico City during a low biomass burning period with a value of 0.54 ± 0.01, and the highest was measured for the sample from 25 February to 4 March 2005 in Råö with a fraction nonfossil of 0.91 ± 0.03. The corresponding WSOC measurements were 0.50 ± 0.01 and 0.76 ± 0.01 for Råö and Mexico City, respectively.

A significant difference between WSOC and oxalate was observed for SRM 1649a Urban Dust with a higher nonfossil fraction for oxalate. As the different size cut of this material may not be comparable to aerosol filters, the low levoglucosan content (< 1 ‰ of TC) underlines that biomass burning contribution is low. Although there is substantial evidence (Jaffrezo et al., 1998; Deshmukh et al., 2018; Kundu et al., 2010; Deshmukh et al., 2019; Falkovich et al., 2005) that oxalate may be formed by biomass burning events, this study provides an opposite trend for multiple sites. For Råö, Mexico City, and for SRM 1649a Urban Dust

(Washington DC, USA) biomass burning may only be a small contributor to the formation of oxalate, similar to the conditions found by van Pinxteren et al. (2014) for continental Europe.

Radiocarbon source apportionment with oxalate can reveal new insights in the DCA formation processes in the atmosphere and the origins of their precursors. The limited number of measurements performed in this work should be extended in conjunction with WSOC measurement to more sites, in particular to the investigation of diurnal variation of urban sites affected by biomass burning similar to Delhi in the dry season. Furthermore, it might be of interest to measure marine aerosols, as such filters were not measured in this work and Xu et al. (2021) only analysed coastal background.

Chemical wet oxidation coupled with radiocarbon analysis further allows for the extension to other DCAs and compound-class-specific measurements. Oxalate measurements as well as a potential extension to other DCAs (e.g., succinic, malic, and malonic acid) bears high opportunity costs as the low concentration requires pooling or large quantities of filter material, therefore, a simple method with low processing blanks is necessary. The method presented here is far simpler than previous approaches based on two chromatographic separations or gas chromatography (Fahrni et al., 2010a; Xu et al., 2021) while requiring lower amounts of sample owing to the low processing blank.

3.5   Conclusion

We developed a CSRA method for radiocarbon measurement of oxalate from ambient aerosols. Oxalate was separated by IC and oxidised by chemical wet oxidation to CO_2 before radiocarbon measurement. Low procedural blanks were achieved, and the method was applied on a selection of filters. To benchmark the CSRA method, radiocarbon measurements of oxalate were supplemented with ^{14}C analysis of WSOC and partially also of TC, EC, and WINSOC. The high nonfossil fraction of oxalate shows that this compound may be predominately formed from both biogenic SOA and biomass burning. Especially the rural site of Råö, where the nonfossil fraction of oxalate was substantially higher than the WSOC fraction, revealed the dominate contribution of biogenic SOA to nonfossil oxalate. Biomass burning played only a minor role in the formation of oxalate for all sites investigated, except for Delhi. Here, we observed a significant difference for oxalate and WSOC in night-time filters, whereas no difference occurred during daytime in the dry season at night. A high fossil contribution was observed in all fractions from Kraków; however, oxalate concentrations were insufficient for a radiocarbon measurement. We therefore conclude that primary or secondary organic aerosols from coal combustion are not a relevant contributor for oxalate formation.

Author contribution

The work presented here was carried out in collaboration between all authors. S.S. conceived of the study and its design. M.R. performed the laboratory experiments and led the preparation of the manuscript. G.S. provided support for the radiocarbon measurements and contributed to the preparation of the manuscript. All authors contributed to the editing and proofreading of the manuscript.

Competing interests

The authors declare that they have no conflict of interest.

3.6 References

Agrios, K., Salazar, G., Zhang, Y.-L., Uglietti, C., Battaglia, M., Luginbühl, M., Ciobanu, V. G., Vonwiller, M., and Szidat, S.: Online coupling of pure O_2 thermo-optical methods – ^{14}C AMS for source apportionment of carbonaceous aerosols, Nucl. instruments methods Phys. Res. Sect. B beam Interact. with Mater. atoms, 361, 288–293, https://doi.org/10.1016/j.nimb.2015.06.008, 2015.

Aiken, A. C., Salcedo, D., Cubison, M. J., Huffman, J. A., DeCarlo, P. F., Ulbrich, I. M., Docherty, K. S., Sueper, D., Kimmel, J. R., Worsnop, D. R., Trimborn, A., Northway, M., Stone, E. A., Schauer, J. J., Volkamer, R. M., Fortner, E., De Foy, B., Wang, J., Laskin, A., Shutthanandan, V., Zheng, J., Zhang, R., Gaffney, J., Marley, N. A., Paredes-Miranda, G., Arnott, W. P., Molina, L. T., Sosa, G., and Jimenez, J. L.: Mexico City aerosol analysis during MILAGRO using high resolution aerosol mass spectrometry at the urban supersite (T0) - Part 1: Fine particle composition and organic source apportionment, Atmos. Chem. Phys., 9, 6633–6653, https://doi.org/10.5194/acp-9-6633-2009, 2009.

Bikkina, S., Kawamura, K., Sarin, M., and Tachibana, E.: ^{13}C Probing of Ambient Photo-Fenton Reactions Involving Iron and Oxalic Acid: Implications for Oceanic Biogeochemistry, ACS Earth Sp. Chem., 4, 964–976, https://doi.org/10.1021/acsearthspacechem.0c00063, 2020.

Bikkina, S., Kawamura, K., Sakamoto, Y., and Hirokawa, J.: Low molecular weight dicarboxylic acids, oxocarboxylic acids and α-dicarbonyls as ozonolysis products of isoprene: Implication for the gaseous-phase formation of secondary organic aerosols, Sci. Total Environ., 769, 144472, https://doi.org/10.1016/j.scitotenv.2020.144472, 2021.

Bock, N., Baum, M. M., Anderson, M. B., Pesta, A., and Northrop, W. F.: Dicarboxylic Acid Emissions from Aftertreatment Equipped Diesel Engines, Environ. Sci. Technol., 51, 13036–13043, https://doi.org/10.1021/acs.est.7b03868, 2017.

Boucher, O., Randall, D., Artaxo, P., Bretherton, C., Feingold, G., Forster, P., Kerminen, V.-M., Kondo,

Y., Liao, H., Lohmann, U., Rasch, P., Satheesh, S. K., Sherwood, S., Stevens, B., and Zhang, X.-Y.: Clouds and Aerosols, Cambridge University Press, Cambridge, United Kingdom and New York, NY, USA., 2013.

Cao, F., Zhang, S. C., Kawamura, K., Liu, X., Yang, C., Xu, Z., Fan, M., Zhang, W., Bao, M., Chang, Y., Song, W., Liu, S., Lee, X., Li, J., Zhang, G., and Zhang, Y. L.: Chemical characteristics of dicarboxylic acids and related organic compounds in $PM_{2.5}$ during biomass-burning and non-biomass-burning seasons at a rural site of Northeast China, Environ. Pollut., 231, 654–662, https://doi.org/10.1016/j.envpol.2017.08.045, 2017.

Carlton, A. G., Turpin, B. J., Altieri, K. E., Seitzinger, S., Reff, A., Lim, H.-J., and Ervens, B.: Atmospheric oxalic acid and SOA production from glyoxal: Results of aqueous photooxidation experiments, Atmos. Environ., 41, 7588–7602, https://doi.org/10.1016/j.atmosenv.2007.05.035, 2007.

Carlton, A. G., Wiedinmyer, C., and Kroll, J. H.: A review of Secondary Organic Aerosol (SOA) formation from isoprene, Atmos. Chem. Phys., 9, 4987–5005, https://doi.org/10.5194/acp-9-4987-2009, 2009.

Casotto, R., Skiba, A., Rauber, M., and Strähl, J.: Organic aerosol sources in Krakow, Poland, before implementation of a solid fuel residential heating ban (in preparation), 2022.

Chen, Y., Guo, H., Nah, T., Tanner, D. J., Sullivan, A. P., Takeuchi, M., Gao, Z., Vasilakos, P., Russell, A. G., Baumann, K., Huey, L. G., Weber, R. J., and Ng, N. L.: Low-Molecular-Weight Carboxylic Acids in the Southeastern U.S.: Formation, Partitioning, and Implications for Organic Aerosol Aging, Environ. Sci. Technol., 55, 6688–6699, https://doi.org/10.1021/acs.est.1c01413, 2021.

Cheng, Y., Engling, G., He, K.-B., Duan, F.-K., Ma, Y.-L., Du, Z.-Y., Liu, J.-M., Zheng, M., and Weber, R. J.: Biomass burning contribution to Beijing aerosol, Atmos. Chem. Phys., 13, 7765–7781, https://doi.org/10.5194/acp-13-7765-2013, 2013.

Currie, L. A., Eglinton, T. I., Benner, B. A., and Pearson, A.: Radiocarbon "dating" of individual chemical compounds in atmospheric aerosol: First results comparing direct isotopic and multivariate statistical apportionment of specific polycyclic aromatic hydrocarbons, Nucl. Instruments Methods Phys. Res. Sect. B Beam Interact. with Mater. Atoms, 123, 475–486, https://doi.org/10.1016/S0168-583X(96)00783-5, 1997.

Deshmukh, D. K., Mozammel Haque, M., Kawamura, K., and Kim, Y.: Dicarboxylic acids, oxocarboxylic acids and α-dicarbonyls in fine aerosols over central Alaska: Implications for sources and atmospheric processes, Atmos. Res., 202, 128–139, https://doi.org/10.1016/j.atmosres.2017.11.003, 2018.

Deshmukh, D. K., Kawamura, K., Gupta, T., Haque, M. M., Zhang, Y.-L., Singh, D. K., and Tsai, Y. I.: High Loadings of Water-Soluble Oxalic Acid and Related Compounds in $PM_{2.5}$ Aerosols in Eastern Central India: Influence of Biomass Burning and Photochemical Processing, Aerosol Air Qual. Res., 9, 2625–2644, https://doi.org/10.4209/aaqr.2019.10.0543, 2019.

Edney, E. O., Kleindienst, T. E., Jaoui, M., Lewandowski, M., Offenberg, J. H., Wang, W., and Claeys, M.:

Formation of 2-methyl tetrols and 2-methylglyceric acid in secondary organic aerosol from laboratory irradiated isoprene/NO_X/SO_2/air mixtures and their detection in ambient $PM_{2.5}$ samples collected in the eastern United States, Atmos. Environ., 39, 5281–5289, https://doi.org/10.1016/j.atmosenv.2005.05.031, 2005.

Eglinton, T. I. and Eglinton, G.: Molecular proxies for paleoclimatology, Earth Planet. Sci. Lett., 275, 1–16, https://doi.org/10.1016/j.epsl.2008.07.012, 2008.

Fahrni, S. M., Ruff, M., Wacker, L., Perron, N., Gäggeler, H. W., and Szidat, S.: A Preparative 2D-Chromatography Method for Compound-Specific Radiocarbon Analysis of Dicarboxylic Acids in Aerosols, Radiocarbon, 52, 752–760, https://doi.org/10.1017/S0033822200045768, 2010a.

Fahrni, S. M., Gäggeler, H. W., Hajdas, I., Ruff, M., Szidat, S., and Wacker, L.: Direct measurements of small ^{14}C samples after oxidation in quartz tubes, Nucl. Instruments Methods Phys. Res. Sect. B Beam Interact. with Mater. Atoms, 268, 787–789, https://doi.org/10.1016/j.nimb.2009.10.031, 2010b.

Fahrni, S. M., Wacker, L., Synal, H. A., and Szidat, S.: Improving a gas ion source for ^{14}C AMS, Nucl. Instruments Methods Phys. Res. Sect. B Beam Interact. with Mater. Atoms, 294, 320–327, https://doi.org/10.1016/j.nimb.2012.03.037, 2013.

Falkovich, A. H., Graber, E. R., Schkolnik, G., Rudich, Y., Maenhaut, W., and Artaxo, P.: Low molecular weight organic acids in aerosol particles from Rondônia, Brazil, during the biomass-burning, transition and wet periods, Atmos. Chem. Phys., 5, 781–797, https://doi.org/10.5194/acp-5-781-2005, 2005.

Fu, P., Kawamura, K., Usukura, K., and Miura, K.: Dicarboxylic acids, ketocarboxylic acids and glyoxal in the marine aerosols collected during a round-the-world cruise, Mar. Chem., 148, 22–32, https://doi.org/10.1016/j.marchem.2012.11.002, 2013.

Gottschalk, J., Szidat, S., Michel, E., Mazaud, A., Salazar, G., Battaglia, M., Lippold, J., and Jaccard, S. L.: Radiocarbon Measurements of Small-Size Foraminiferal Samples with the Mini Carbon Dating System (MICADAS) at the University of Bern: Implications for Paleoclimate Reconstructions, Radiocarbon, 60, 469–491, https://doi.org/10.1017/RDC.2018.3, 2018.

Guenther, A. B., Jiang, X., Heald, C. L., Sakulyanontvittaya, T., Duhl, T., Emmons, L. K., and Wang, X.: The Model of Emissions of Gases and Aerosols from Nature version 2.1 (MEGAN2.1): an extended and updated framework for modeling biogenic emissions, Geosci. Model Dev., 5, 1471–1492, https://doi.org/10.5194/gmd-5-1471-2012, 2012.

Haghipour, N., Ausin, B., Usman, M. O., Ishikawa, N., Wacker, L., Welte, C., Ueda, K., and Eglinton, T. I.: Compound-Specific Radiocarbon Analysis by Elemental Analyzer–Accelerator Mass Spectrometry: Precision and Limitations, Anal. Chem., 91, 2042–2049, https://doi.org/10.1021/acs.analchem.8b04491, 2019.

Hanke, U. M., Wacker, L., Haghipour, N., Schmidt, M. W. I., Eglinton, T. I., and McIntyre, C. P.: Comprehensive radiocarbon analysis of benzene polycarboxylic acids (BPCAs) derived from

pyrogenic carbon in environmental samples, Radiocarbon, 59, 1103–1116, https://doi.org/10.1017/RDC.2017.44, 2017.

Hansen, J. and Nazarenko, L.: Soot climate forcing via snow and ice albedos, Proc. Natl. Acad. Sci., 101, 423–428, https://doi.org/10.1073/pnas.2237157100, 2004.

Herrmann, H., Schaefer, T., Tilgner, A., Styler, S. A., Weller, C., Teich, M., and Otto, T.: Tropospheric Aqueous-Phase Chemistry: Kinetics, Mechanisms, and Its Coupling to a Changing Gas Phase, Chem. Rev., 115, 4259–4334, https://doi.org/10.1021/cr500447k, 2015.

Ho, K. F., Lee, S. C., Ho, S. S. H., Kawamura, K., Tachibana, E., Cheng, Y., and Zhu, T.: Dicarboxylic acids, ketocarboxylic acids, α-dicarbonyls, fatty acids, and benzoic acid in urban aerosols collected during the 2006 Campaign of Air Quality Research in Beijing (CAREBeijing-2006), J. Geophys. Res. Atmos., 115, 1–14, https://doi.org/10.1029/2009JD013304, 2010.

Hsieh, L.-Y., Chen, C.-L., Wan, M.-W., Tsai, C.-H., and Tsai, Y. I.: Speciation and temporal characterization of dicarboxylic acids in PM$_{2.5}$ during a PM episode and a period of non-episodic pollution, Atmos. Environ., 42, 6836–6850, https://doi.org/10.1016/j.atmosenv.2008.05.021, 2008.

Hsieh, L., Kuo, S., Chen, C., and Tsai, Y. I.: Origin of low-molecular-weight dicarboxylic acids and their concentration and size distribution variation in suburban aerosol, Atmos. Environ., 41, 6648–6661, https://doi.org/10.1016/j.atmosenv.2007.04.014, 2007.

Jaffrezo, J.-L., Davidson, C. I., Kuhns, H. D., Bergin, M. H., Hillamo, R., Maenhaut, W., Kahl, J. W., and Harris, J. M.: Biomass burning signatures in the atmosphere of central Greenland, J. Geophys. Res. Atmos., 103, 31067–31078, https://doi.org/10.1029/98JD02241, 1998.

Jaffrezo, J. L., Aymoz, G., Delaval, C., and Cozic, J.: Seasonal variations of the water soluble organic carbon mass fraction of aerosol in two valleys of the French Alps, Atmos. Chem. Phys., 5, 2809–2821, https://doi.org/10.5194/acp-5-2809-2005, 2005.

Jedynska, A., Hoek, G., Wang, M., Eeftens, M., Cyrys, J., Beelen, R., Cirach, M., De Nazelle, A., Keuken, M., Visschedijk, A., Nystad, W., Akhlaghi, H. M., Meliefste, K., Nieuwenhuijsen, M., de Hoogh, K., Brunekreef, B., and Kooter, I. M.: Spatial variations of levoglucosan in four European study areas, Sci. Total Environ., 505, 1072–1081, https://doi.org/10.1016/j.scitotenv.2014.10.091, 2015.

Jimenez, J. L., Canagaratna, M. R., Donahue, N. M., Prevot, A. S. H., Zhang, Q., Kroll, J. H., DeCarlo, P. F., Allan, J. D., Coe, H., Ng, N. L., Aiken, A. C., Docherty, K. S., Ulbrich, I. M., Grieshop, A. P., Robinson, A. L., Duplissy, J., Smith, J. D., Wilson, K. R., Lanz, V. A., Hueglin, C., Sun, Y. L., Tian, J., Laaksonen, A., Raatikainen, T., Rautiainen, J., Vaattovaara, P., Ehn, M., Kulmala, M., Tomlinson, J. M., Collins, D. R., Cubison, M. J., Dunlea, J., Huffman, J. A., Onasch, T. B., Alfarra, M. R., Williams, P. I., Bower, K., Kondo, Y., Schneider, J., Drewnick, F., Borrmann, S., Weimer, S., Demerjian, K., Salcedo, D., Cottrell, L., Griffin, R., Takami, A., Miyoshi, T., Hatakeyama, S., Shimono, A., Sun, J. Y., Zhang, Y. M., Dzepina, K., Kimmel, J. R., Sueper, D., Jayne, J. T., Herndon, S. C., Trimborn, A. M., Williams, L. R., Wood, E. C., Middlebrook, A. M., Kolb, C. E., Baltensperger, U., and Worsnop, D. R.: Evolution of Organic Aerosols in the Atmosphere, Sci. ,

326, 1525–1529, https://doi.org/10.1126/science.1180353, 2009.

Kanakidou, M., Seinfeld, J. H., Pandis, S. N., Barnes, I., Dentener, F. J., Facchini, M. C., Van Dingenen, R., Ervens, B., Nenes, A., Nielsen, C. J., Swietlicki, E., Putaud, J. P., Balkanski, Y., Fuzzi, S., Horth, J., Moortgat, G. K., Winterhalter, R., Myhre, C. E. L., Tsigaridis, K., Vignati, E., Stephanou, E. G., and Wilson, J.: Organic aerosol and global climate modelling: A review, Atmos. Chem. Phys., 5, 1053–1123, https://doi.org/10.5194/acp-5-1053-2005, 2005.

Kawamura, K. and Kaplan, I. R.: Motor exhaust emissions as a primary source for dicarboxylic acids in Los Angeles ambient air, Environ. Sci. Technol., 21, 105–110, https://doi.org/10.1021/es00155a014, 1987.

Kawamura, K. and Sakaguchi, F.: Molecular distributions of water soluble dicarboxylic acids in marine aerosols over the Pacific Ocean including tropics, J. Geophys. Res. Atmos., 104, 3501–3509, https://doi.org/10.1029/1998JD100041, 1999.

Kawamura, K., Seméré, R., Imai, Y., Fujii, Y., and Hayashi, M.: Water soluble dicarboxylic acids and related compounds in Antarctic aerosols, J. Geophys. Res. Atmos., 101, 18721–18728, https://doi.org/10.1029/96jd01541, 1996.

Kawamura, K., Narukawa, M., Li, S. M., and Barrie, L. A.: Size distributions of dicarboxylic acids and inorganic ions in atmospheric aerosols collected during polar sunrise in the Canadian high Arctic, J. Geophys. Res. Atmos., 112, https://doi.org/10.1029/2006JD008244, 2007.

Kawamura, K., Barrie, L. A., and Toom-Sauntry, D.: Intercomparison of the measurements of oxalic acid in aerosols by gas chromatography and ion chromatography, Atmos. Environ., 44, 5316–5319, https://doi.org/10.1016/j.atmosenv.2010.08.051, 2010a.

Kawamura, K., Kasukabe, H., and Barrie, L. A.: Secondary formation of water-soluble organic acids and α-dicarbonyls and their contributions to total carbon and water-soluble organic carbon: Photochemical aging of organic aerosols in the Arctic spring, J. Geophys. Res. Atmos., 115, https://doi.org/10.1029/2010JD014299, 2010b.

Kawamura, K., Ono, K., Tachibana, E., Charriére, B., and Sempéré, R.: Distributions of low molecular weight dicarboxylic acids, ketoacids and α-dicarbonyls in the marine aerosols collected over the Arctic Ocean during late summer, 9, 4725–4737, https://doi.org/10.5194/bg-9-4725-2012, 2012.

Kim, K. H., Kabir, E., and Kabir, S.: A review on the human health impact of airborne particulate matter, Environ. Int., 74, 136–143, https://doi.org/10.1016/j.envint.2014.10.005, 2015.

Kleindienst, T. E., Lewandowski, M., Offenberg, J. H., Jaoui, M., and Edney, E. O.: Ozone-isoprene reaction: Re-examination of the formation of secondary organic aerosol, Geophys. Res. Lett., 34, L01805, https://doi.org/10.1029/2006GL027485, 2007.

Kroll, J. H., Ng, N. L., Murphy, S. M., Flagan, R. C., and Seinfeld, J. H.: Secondary organic aerosol formation from isoprene photooxidation under high-NO_x conditions, Geophys. Res. Lett., 32, 1–4, https://doi.org/10.1029/2005GL023637, 2005.

Kroll, J. H., Ng, N. L., Murphy, S. M., Flagan, R. C., and Seinfeld, J. H.: Secondary Organic Aerosol

Formation from Isoprene Photooxidation, Environ. Sci. Technol., 40, 1869–1877, https://doi.org/10.1021/es0524301, 2006.

Kundu, S., Kawamura, K., Andreae, T. W., Hoffer, A., and Andreae, M. O.: Molecular distributions of dicarboxylic acids, ketocarboxylic acids and α-dicarbonyls in biomass burning aerosols: implications for photochemical production and degradation in smoke layers, Atmos. Chem. Phys., 10, 2209–2225, https://doi.org/10.5194/acp-10-2209-2010, 2010.

Lamkaddam, H., Dommen, J., Ranjithkumar, A., Gordon, H., Wehrle, G., Krechmer, J., Majluf, F., Salionov, D., Schmale, J., Bjelić, S., Carslaw, K. S., El Haddad, I., and Baltensperger, U.: Large contribution to secondary organic aerosol from isoprene cloud chemistry, Sci. Adv., 7, https://doi.org/10.1126/sciadv.abe2952, 2021.

Lang, S. Q., Bernasconi, S. M., and Früh-Green, G. L.: Stable isotope analysis of organic carbon in small (µg C) samples and dissolved organic matter using a GasBench preparation device, Rapid Commun. Mass Spectrom., 26, 9–16, https://doi.org/10.1002/rcm.5287, 2012.

Larsen, R., Schantz, M., and Wise, S.: Determination of levoglucosan in particulate matter reference materials, Aerosol Sci. Technol., 40, 781–787, https://doi.org/10.1080/02786820600596909, 2006.

Lelieveld, J., Evans, J. S., Fnais, M., Giannadaki, D., and Pozzer, A.: The contribution of outdoor air pollution sources to premature mortality on a global scale, Nature, 525, 367–371, https://doi.org/10.1038/nature15371, 2015.

Lim, Y. B., Tan, Y., Perri, M. J., Seitzinger, S. P., and Turpin, B. J.: Aqueous chemistry and its role in secondary organic aerosol (SOA) formation, Atmos. Chem. Phys., 10, 10521–10539, https://doi.org/10.5194/acp-10-10521-2010, 2010.

Limbeck, A., Puxbaum, H., Otter, L., and Scholes, M. C.: Semivolatile behavior of dicarboxylic acids and other polar organic species at a rural background site (Nylsvley, RSA), Atmos. Environ., 35, 1853–1862, https://doi.org/10.1016/S1352-2310(00)00497-0, 2001.

Mandalakis, M., Gustafsson, Ö., Alsberg, T., Egebäck, A. L., Reddy, C. M., Xu, L., Klanova, J., Holoubek, I., and Stephanou, E. G.: Contribution of biomass burning to atmospheric polycyclic aromatic hydrocarbons at three european background sites, Environ. Sci. Technol., 39, 2976–2982, https://doi.org/10.1021/es048184v, 2005.

Matsumoto, K., Kawamura, K., Uchida, M., Shibata, Y., and Yoneda, M.: Compound specific radiocarbon and $\delta^{13}C$ measurements of fatty acids in a continental aerosol sample, Geophys. Res. Lett., 28, 4587–4590, https://doi.org/10.1029/2001GL013599, 2001.

Mauderly, J. L. and Chow, J. C.: Health Effects of Organic Aerosols, 257–288 pp., https://doi.org/10.1080/08958370701866008, 2008.

Mochizuki, T., Miyazaki, Y., Ono, K., Wada, R., Takahashi, Y., Saigusa, N., Kawamura, K., and Tani, A.: Emissions of biogenic volatile organic compounds and subsequent formation of secondary organic aerosols in a *Larix kaempferi* forest, Atmos. Chem. Phys., 15, 12029–12041,

https://doi.org/10.5194/acp-15-12029-2015, 2015.

Mochizuki, T., Kawamura, K., Miyazaki, Y., Wada, R., Takahashi, Y., Saigusa, N., and Tani, A.: Secondary formation of oxalic acid and related organic species from biogenic sources in a larch forest at the northern slope of Mt. Fuji, Atmos. Environ., 166, 255–262, https://doi.org/10.1016/j.atmosenv.2017.07.028, 2017.

Mollenhauer, G. and Rethemeyer, J.: Compound-specific radiocarbon analysis – Analytical challenges and applications, IOP Conf. Ser. Earth Environ. Sci., 5, 012006, https://doi.org/10.1088/1755-1307/5/1/012006, 2009.

Molnár, M., Hajdas, I., Janovics, R., Rinyu, L., Synal, H.-A., Veres, M., and Wacker, L.: C-14 analysis of groundwater down to the millilitre level, Nucl. Instruments Methods Phys. Res. Sect. B Beam Interact. with Mater. Atoms, 294, 573–576, https://doi.org/10.1016/j.nimb.2012.03.038, 2013.

Na, K., Sawant, A. A., Song, C., and Cocker, D. R.: Primary and secondary carbonaceous species in the atmosphere of Western Riverside County, California, Atmos. Environ., 38, 1345–1355, https://doi.org/10.1016/j.atmosenv.2003.11.023, 2004.

Narukawa, M., Kawamura, K., Li, S. M., and Bottenheim, J. W.: Dicarboxylic acids in the Arctic aerosols and snowpacks collected during ALERT 2000, Atmos. Environ., 36, 2491–2499, https://doi.org/10.1016/S1352-2310(02)00126-7, 2002.

NIST: Standard Reference Material (SRM) 1649a, Urban Dust. National Institute of Standards and Technology, Gaithersburg, MD 20899., https://cellgenix.com/products/gmp-scgm/, 2007.

van Pinxteren, D., Neusüß, C., and Herrmann, H.: On the abundance and source contributions of dicarboxylic acids in size-resolved aerosol particles at continental sites in central Europe, Atmos. Chem. Phys., 14, 3913–3928, https://doi.org/10.5194/acp-14-3913-2014, 2014.

Putaud, J. P., Van Dingenen, R., Alastuey, A., Bauer, H., Birmili, W., Cyrys, J., Flentje, H., Fuzzi, S., Gehrig, R., Hansson, H. C., Harrison, R. M., Herrmann, H., Hitzenberger, R., Hüglin, C., Jones, A. M., Kasper-Giebl, A., Kiss, G., Kousa, A., Kuhlbusch, T. A. J., Löschau, G., Maenhaut, W., Molnar, A., Moreno, T., Pekkanen, J., Perrino, C., Pitz, M., Puxbaum, H., Querol, X., Rodriguez, S., Salma, I., Schwarz, J., Smolik, J., Schneider, J., Spindler, G., ten Brink, H., Tursic, J., Viana, M., Wiedensohler, A., and Raes, F.: A European aerosol phenomenology - 3: Physical and chemical characteristics of particulate matter from 60 rural, urban, and kerbside sites across Europe, Atmos. Environ., 44, 1308–1320, https://doi.org/10.1016/j.atmosenv.2009.12.011, 2010.

R Core Team: R: A Language and Environment for Statistical Computing. R Foundation for Statistical Computing, Vienna, Austria., https://www.r-project.org/, 2020.

Rauber, M. and Salazar, G.: COMPYCALC: a tool for EC yield extrapolation and charring correction, https://doi.org/https://doi.org/10.5281/zenodo.5958275, 12 December 2020.

Rauber, M., Salazar, G., Yttri, K. E., and Szidat, S.: An Optimised OC/EC Fraction Separation Method for Radiocarbon Source Apportionment Applied to Low-Loaded Arctic Aerosol Filters (submitted to Atmos. Meas. Tech.), 2022.

Ren, L., Ren, L., Wang, Y., Wang, Y., Kawamura, K., Bikkina, S., Haghipour, N., Haghipour, N., Wacker, L., Pavuluri, C. M., Zhang, Z., Yue, S., Yue, S., Sun, Y., Wang, Z., Zhang, Y., Feng, X., Liu, C. Q., Eglinton, T. I., and Fu, P.: Source forensics of n-alkanes and n-fatty acids in urban aerosols using compound specific radiocarbon/stable carbon isotopic composition, Environ. Res. Lett., 15, https://doi.org/10.1088/1748-9326/ab8333, 2020.

Ruff, M., Wacker, L., Gäggeler, H. W., Suter, M., Synal, H.-A., and Szidat, S.: A Gas Ion Source for Radiocarbon Measurements at 200 kV, Radiocarbon, 49, 307–314, https://doi.org/10.1017/S0033822200042235, 2007.

Salazar, G., Zhang, Y. L., Agrios, K., and Szidat, S.: Development of a method for fast and automatic radiocarbon measurement of aerosol samples by online coupling of an elemental analyzer with a MICADAS AMS, Nucl. Instruments Methods Phys. Res. Sect. B Beam Interact. with Mater. Atoms, 361, 163–167, https://doi.org/10.1016/j.nimb.2015.03.051, 2015.

Sheesley, R. J., Kruså, M., Krecl, P., Johansson, C., and Gustafsson, Ö.: Source apportionment of elevated wintertime PAHs by compound-specific radiocarbon analysis, Atmos. Chem. Phys., 9, 3347–3356, https://doi.org/10.5194/acp-9-3347-2009, 2009.

Shrivastava, M., Cappa, C. D., Fan, J., Goldstein, A. H., Guenther, A. B., Jimenez, J. L., Kuang, C., Laskin, A., Martin, S. T., Ng, N. L., Petaja, T., Pierce, J. R., Rasch, P. J., Roldin, P., Seinfeld, J. H., Shilling, J., Smith, J. N., Thornton, J. A., Volkamer, R., Wang, J., Worsnop, D. R., Zaveri, R. A., Zelenyuk, A., and Zhang, Q.: Recent advances in understanding secondary organic aerosol: Implications for global climate forcing, Rev. Geophys., 55, 509–559, https://doi.org/10.1002/2016RG000540, 2017.

Strähl, J.: India filters (in preparation), n.d.

Synal, H. A., Stocker, M., and Suter, M.: MICADAS: A new compact radiocarbon AMS system, Nucl. Instruments Methods Phys. Res. Sect. B Beam Interact. with Mater. Atoms, 259, 7–13, https://doi.org/10.1016/j.nimb.2007.01.138, 2007.

Szidat, S., Jenk, T. M., Gäggeler, H. W., Synal, H.-A., Fisseha, R., Baltensperger, U., Kalberer, M., Samburova, V., Wacker, L., Saurer, M., Schwikowski, M., and Hajdas, I.: Source Apportionment of Aerosols by [14]C Measurements in Different Carbonaceous Particle Fractions, Radiocarbon, 46, 475–484, https://doi.org/10.1017/S0033822200039783, 2004a.

Szidat, S., Jenk, T. M., Gäggeler, H. W., Synal, H.-A., Hajdas, I., Bonani, G., and Saurer, M.: THEODORE, a two-step heating system for the EC/OC determination of radiocarbon (^{14}C) in the environment, Nucl. Instruments Methods Phys. Res. Sect. B Beam Interact. with Mater. Atoms, 223–224, 829–836, https://doi.org/10.1016/j.nimb.2004.04.153, 2004b.

Szidat, S., Jenk, T. M., Synal, H.-A., Kalberer, M., Wacker, L., Hajdas, I., Kasper-Giebl, A., and Baltensperger, U.: Contributions of fossil fuel, biomass-burning, and biogenic emissions to carbonaceous aerosols in Zurich as traced by ^{14}C, J. Geophys. Res., 111, D07206, https://doi.org/10.1029/2005JD006590, 2006.

Szidat, S., Ruff, M., Perron, N., Wacker, L., Synal, H., Hallquist, M., Shannigrahi, S., Yttri, K. E., Dye, C., and Simpson, D.: Fossil and non-fossil sources of organic carbon (OC) and elemental carbon (EC) in Göteborg, Sweden, Atmos. Chem. Phys., 9, 1521–1535, https://doi.org/10.5194/acp-9-1521-2009, 2009.

Szidat, S., Salazar, G. A., Vogel, E., Battaglia, M., Wacker, L., Synal, H.-A., and Türler, A.: [14]C Analysis and Sample Preparation at the new Bern Laboratory for the Analysis of Radiocarbon with AMS (LARA), Radiocarbon, 56, 561–566, https://doi.org/10.2458/56.17457, 2014.

Tobler, A., Bhattu, D., Canonaco, F., Lalchandani, V., Shukla, A., Thamban, N. M., Mishra, S., Srivastava, A. K., Bisht, D. S., Tiwari, S., Singh, S., Močnik, G., Baltensperger, U., Tripathi, S. N., Slowik, J. G., and Prévôt, A. S. H.: Chemical characterization of $PM_{2.5}$ and source apportionment of organic aerosol in New Delhi, India, Sci. Total Environ., 745, 140924, https://doi.org/10.1016/j.scitotenv.2020.140924, 2020.

Wacker, L., Christl, M., and Synal, H. A.: Bats: A new tool for AMS data reduction, Nucl. Instruments Methods Phys. Res. Sect. B Beam Interact. with Mater. Atoms, 268, 976–979, https://doi.org/10.1016/j.nimb.2009.10.078, 2010.

Warneck, P.: In-cloud chemistry opens pathway to the formation of oxalic acid in the marine atmosphere, Atmos. Environ., 37, 2423–2427, https://doi.org/10.1016/S1352-2310(03)00136-5, 2003.

Waterman, D., Horsfield, B., Leistner, F., Hall, K., and Smith, S.: Quantification of polycyclic aromatic hydrocarbons in the NIST Standard Reference Material (SRM1649A) urban dust using thermal desorption GC/MS, Anal. Chem., 72, 3563–3567, https://doi.org/10.1021/ac991372x, 2000.

Wiedemeier, D. B., Lang, S. Q., Gierga, M., Abiven, S., Bernasconi, S. M., Früh-Green, G. L., Hajdas, I., Hanke, U. M., Hilf, M. D., McIntyre, C. P., Scheider, M. P. W., Smittenberg, R. H., Wacker, L., Wiesenberg, G. L. B., and Schmidt, M. W. I.: Characterization, Quantification and Compound-specific Isotopic Analysis of Pyrogenic Carbon Using Benzene Polycarboxylic Acids (BPCA), J. Vis. Exp., 111, https://doi.org/10.3791/53922, 2016.

Xu, B., Cheng, Z., Gustafsson, Ö., Kawamura, K., Jin, B., Zhu, S., Tang, T., Zhang, B., Li, J., and Zhang, G.: Compound-Specific Radiocarbon Analysis of Low Molecular Weight Dicarboxylic Acids in Ambient Aerosols Using Preparative Gas Chromatography: Method Development, Environ. Sci. Technol. Lett., 8, 135–141, https://doi.org/10.1021/acs.estlett.0c00887, 2021.

Yang, F., Gu, Z., Feng, J., Liu, X., and Yao, X.: Biogenic and anthropogenic sources of oxalate in $PM_{2.5}$ in a mega city, Shanghai, Atmos. Res., 138, 356–363, https://doi.org/10.1016/j.atmosres.2013.12.006, 2014.

Yang, L., Ray, M. B., and Yu, L. E.: Photooxidation of dicarboxylic acids—Part II: Kinetics, intermediates and field observations, Atmos. Environ., 42, 868–880, https://doi.org/10.1016/j.atmosenv.2007.10.030, 2008.

Yao, X., Chan, C. K., Fang, M., Cadle, S., Chan, T., Mulawa, P., He, K., and Ye, B.: The water-soluble ionic composition of $PM_{2.5}$ in Shanghai and Beijing, China, Atmos. Environ., 36, 4223–4234,

https://doi.org/10.1016/S1352-2310(02)00342-4, 2002.

Yao, X., Fang, M., Chan, C. K., Ho, K. F., and Lee, S. C.: Characterization of dicarboxylic acids in $PM_{2.5}$ in Hong Kong, Atmos. Environ., 38, 963–970, https://doi.org/10.1016/j.atmosenv.2003.10.048, 2004.

Yttri, K. E., Dye, C., Braathen, O.-A., Simpson, D., and Steinnes, E.: Carbonaceous aerosols in Norwegian urban areas, Atmos. Chem. Phys., 9, 2007–2020, https://doi.org/10.5194/acp-9-2007-2009, 2009.

Yu, J. Z., Huang, X.-F., Xu, J., and Hu, M.: When Aerosol Sulfate Goes Up, So Does Oxalate: Implication for the Formation Mechanisms of Oxalate, Environ. Sci. Technol., 39, 128–133, https://doi.org/10.1021/es049559f, 2005.

Zhang, Y., Liu, J., Salazar, G. A., Li, J., Zotter, P., Zhang, G., Shen, R., Schäfer, K., Schnelle-Kreis, J., Prévôt, A. S. H., and Szidat, S.: Micro-scale (µg) radiocarbon analysis of water-soluble organic carbon in aerosol samples, Atmos. Environ., 97, 1–5, https://doi.org/10.1016/j.atmosenv.2014.07.059, 2014.

Zhang, Y., Ren, H., Sun, Y., Cao, F., Chang, Y., Liu, S., Lee, X., Agrios, K., Kawamura, K., Liu, D., Ren, L., Du, W., Wang, Z., Prévôt, A. S. H., Szidat, S., and Fu, P.: High Contribution of Nonfossil Sources to Submicrometer Organic Aerosols in Beijing, China, Environ. Sci. Technol., 51, 7842–7852, https://doi.org/10.1021/acs.est.7b01517, 2017.

Zhang, Y. L., Perron, N., Ciobanu, V. G., Zotter, P., Minguillón, M. C., Wacker, L., Prévôt, A. S. H., Baltensperger, U., and Szidat, S.: On the isolation of OC and EC and the optimal strategy of radiocarbon-based source apportionment of carbonaceous aerosols, Atmos. Chem. Phys., 12, 10841–10856, https://doi.org/10.5194/acp-12-10841-2012, 2012.

Ziolkowski, L. A. and Druffel, E. R. M.: Quantification of extraneous carbon during compound specific radiocarbon analysis of black carbon, Anal. Chem., 81, 10156–10161, https://doi.org/10.1021/ac901922s, 2009.

4 Organic aerosols at Trollhaugen Observatory (Antarctica) in summer are dominated by marine sources

M. Rauber[1,2], G. Salazar[1,2], V. Moschos[3], I. El Haddad[3], A. S. H. Prévôt[3], D. Thomsen[4], M. Glasius[4], S. M. Platt[5], A. Bäcklund[5], M. Fiebig[5], W. Aas[5], K. E. Yttri[5], S. Szidat[1,2]

[1]Dept. of Chemistry, Biochemistry and Pharmaceutical Sciences, University of Bern, Bern, 3012, Switzerland
[2]Oeschger Centre for Climate Change Research, University of Bern, Bern, 3012, Switzerland
[3]Laboratory of Atmospheric Chemistry, Paul Scherrer Institute, Villigen, 5232, Switzerland
[4]Department of Chemistry, Aarhus University, Aarhus C, 8000, Denmark
[5]Department Atmospheric and Climate Research, NILU – Norwegian Institute for Air Research, Kjeller, 2007, Norway

Correspondence to: Sönke Szidat (soenke.szidat@unibe.ch)

Manuscript in preparation

Abstract

Antarctica has few terrestrial biogenic and anthropogenic sources of particulate organic carbon (OC), and it is well isolated from continental pollution of particulate matter (PM) from long-range transport. Upwellings in the Southern Ocean convey aged refractory dissolved organic carbon (DOC) to the surface, which is pre-aged, i.e., depleted regarding levels of radiocarbon (^{14}C) compared to contemporary sources. Sea spray from breaking waves brings ^{14}C-depleted DOC as primary marine aerosol (PMA) into the atmosphere from unknown sources. We analysed PM_{10} quartz fibre filters sampled at the Trollhaugen Observatory from 2016–2018 located between the Antarctic coastal zone and inland ice plateau. Radiocarbon (^{14}C) analysis was carried out on fractions of the carbonaceous PM. Based on these measurements, our analysis suggests that ^{14}C-depleted PMA sources dominate in all measured carbonaceous fractions in austral summer. Both secondary marine aerosols and biomass burning are only minor sources. For water-insoluble organic carbon (WINSOC) a mean Δ^{14}C value of $-260 \pm 83‰$ was measured, for water-soluble organic carbon (WSOC) $-365 \pm 184‰$, and for total carbon (TC) $-390 \pm 191‰$.

4.1 Introduction

Antarctica is the most isolated of all landmasses and believed to be hardly affected by pollution from other continents. Although Antarctica presents one of the lowest concentrations of aerosols on Earth, it is important to characterise their sources to identify the actual contribution of current pollution of this pristine environment and to determine a benchmark for the quantification of a possible future change. Carbonaceous aerosols are a major fraction of PM, and its composition consists of light-absorbing black carbon (BC, also referred to as elemental carbon, EC) and non-absorbing organic carbon (OC)[1]. The light and heat absorbing properties of EC is detrimental to ice sheets due to the albedo effect, which explicitly affects the clean cryosphere such as the one of Antarctica[2,3]. Different characteristics of Antarctic aerosols have been studied including their chemical composition, size distribution and sources[4–7]. The sulphate and sea salt fractions increase in concentration at sites closer to the Southern Ocean coast[8–10]. Previous studies have shown that EC concentrations decrease from the coasts towards the interior of the continent[11–16]. Biomass burning and wildfires in South America, Africa, and Australia have been suggested as main contributors to EC based on the investigation of chemical tracers and air-mass back-trajectories[12,13,17,18]. Although to smaller extend than in the Arctic, secondary organic aerosols (SOA) are a relevant source of organic aerosols (OA) in Antarctica with spikes driven by phytoplankton blooms[19–21]. Furthermore, recent works have documented the significance of the oceans as a source of both primary and secondary OA[22–24]. First, Spracklen et al.[23] hypothesized that south of 40°S, oceans must contribute significant amounts of OA so that their chemical transport models match ambient measurements. Second, Beaupré et al.[24] showed that a substantial fraction of freshly produced primary marine aerosol (PMA) consists of refractory dissolved OC (DOC). Dissolved organic carbon (DOC) is a major carbon reservoir of organic carbon on earth. In the Southern Ocean, DOC reaches a mean age of 5600 years[25] and is therefore much older than the global ocean currents mixing period of 400–2200 years[26], implying that a fraction of DOC is very resistant to degradation (i.e., refractory) and survives multiple ocean mixing cycles. Due its resistance to degradation, this DOC is frequently also called refractory DOC (rDOC). This DOC is therefore depleted regarding its ^{14}C signature compared to contemporary sources and is frequently also referred to as pre-aged. The removal processes of DOC are not fully understood. Photochemical degradation, bacterial degradation as well as adsorption to particles have been proposed as a potential removal process[25].

Biogenic material generally reflects ^{14}C levels corresponding to atmospheric CO_2 at the time of growth. Known as the 'bomb spike', above-ground nuclear tests primarily in the 1950s and 1960s resulted in an increase of radiocarbon in the atmosphere[27]. Mostly due to exchange atmospheric $^{14}CO_2$ levels have since approached pre bomb spike levels again with $\Delta^{14}C$ values ~0‰. Therefore, OC from fresh biogenic emission will exhibit $\Delta^{14}C$ values corresponding atmospheric CO_2 at the time of growth of the terrestrial plant material (i.e., $\Delta^{14}C$ = ~0‰ for present-day emissions). OC and EC from biomass burning represents the average ^{14}C level of the tree rings weighted by their individual masses resulting in ranges of $\Delta^{14}C$ of 103 to 28‰, regardless of whether the emissions were caused naturally or by anthropogenic activities[28]. In contrast, fossil fuel emissions are completely devoid of radiocarbon ($\Delta^{14}C$ = −1000‰)[29]. Intrusions and

mixing with the overlying water supplies DOC to the surface layers. $\Delta^{14}C$ DOC values in ranges of -420 to $-470‰$ were found in the surface water of the Southern Ocean[30,31]. Out of these upwellings into surface waters, ^{14}C-depleted DOC may contribute to a substantial PMA generation.

Here, we present radiocarbon measurements of PM_{10} quartz fibre filters (QFF) for three consecutive summers collected at the Norwegian Trollhaugen Observatory located at a transition zone between the coast and the Antarctic Plateau. Three fractions of the carbonaceous aerosol were used for radiocarbon analysis: total carbon (TC), water-soluble organic carbon (WSOC), and water-insoluble organic carbon (WINSOC) to quantify or estimate an upper limit for the contributions of fossil sources, pre-aged DOC and biogenic emissions / biomass burning. To our knowledge, no multiyear ambient aerosol radiocarbon analysis from Antarctic filters have been published so far. Additionally, the filters were analysed by ion chromatography (IC) for organic and inorganic ions as well as by Aerosol Mass Spectrometry (AMS), and high-resolution mass spectrometry for the organic composition.

4.2 Results and Discussion

4.2.1 Insights into aerosol sources from radiocarbon analyses
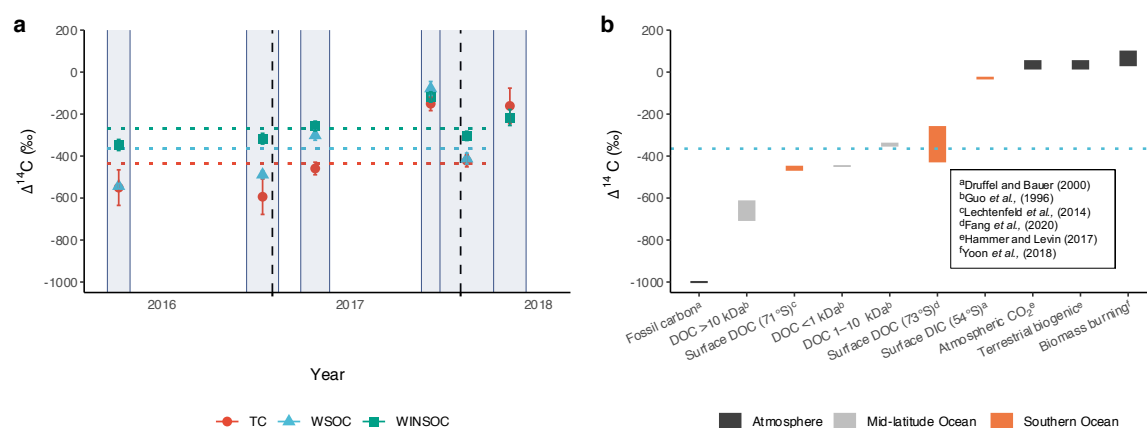

Figure 1. (a) Measured $\Delta^{14}C$ (‰) for the carbonaceous aerosol fractions TC, WSOC, and WINSOC. Note that the ^{14}C measurement of WSOC for May 2018 failed. The dotted horizontal lines represent the mean value for each fraction (excluding the samples of May 2018). The shaded area shows the sampling intervals. (b) $\Delta^{14}C$ (‰) ranges for different sources from fossil carbon ($\Delta^{14}C = -1000‰$) to several DOC fractions and dissolved inorganic carbon (DIC) in the ocean compared to contemporary carbon sources in the atmosphere (i.e., atmospheric CO_2, terrestrial biogenic emissions, biomass burning). Surface DOC measurements from the Southern Ocean represent a depth range of 0–100 m. Deep water DOC from the Mid-latitude Ocean was defined as >250 m.

Radiocarbon measurements of PM_{10} summer filters reveal a substantial depletion in ^{14}C compared to the ambient terrestrial biosphere (Fig. 1a). The mean $\Delta^{14}C$ value for WSOC was $-365 \pm 184‰$. A similar clear depletion was found for the WINSOC fraction. The mean $\Delta^{14}C$ value for WINSOC was $-269 \pm 90‰$ and therefore less depleted than the WSOC fraction. The most substantial depletion was recorded in the TC

fraction with a mean $\Delta^{14}C$ value of $-435 \pm 173‰$. The course of the results for the summer 2017/2018 indicates that the lowest $\Delta^{14}C$ value are reached in summer, while both the preceding spring/early summer and the succeeding later summer/autumn show higher levels. This implies seasonality as the driver of this effect. Since TC is more depleted than both WSOC and WINSOC, the $\Delta^{14}C$ value of the EC fraction must be even substantially lower. Thermal-optical OC-EC analysis revealed EC/TC ratios of 0.17 ± 0.07. Aethalometer based measurements have previously documented clear seasonal patterns of BC in Antarctica with a maximum in austral spring. The spring maximum in October–November was observed in coastal and continental stations[12,13,16]. Measurements from the coastal Halley station[12] showed summer values in the range of 0.5–5.0 ng m^{-3}, and Hara et al.[32] reported median values of 3.1 ng m^{-3} for the maximum period of August–November at Syowa Station. This seems also to be relevant at Trollhaugen. Unfortunately, ^{14}C of EC could not be measured as the loadings were too low. A semi-quantitative estimation of the $\Delta^{14}C$ value of EC by the isotopic mass balance approach yielded a level of slightly below $-1000‰$.

The interpretation of these measurement results requires the consideration of the special conditions at the sampling site, which are widely different from ^{14}C source apportionment studies that have been performed in densely population regions such as Central Europe, North America or East Asia that are close to the emission sources or even for remote areas in the Northern Hemisphere like alpine or arctic sites that are frequently affected by long-range transport of pollution[33–37]. For example, organic aerosol from Svalbard and other Arctic sites may be dominated by emissions from North America and Northern Eurasia, and still be influenced from local sources[21,38]. In contrast, the Trollhaugen station is even further away from any continental site outside Antarctica then the investigated Arctic sites and the next large settlement (pop. >1 million) is Cape Town, South Africa, located over 4000 km away. Moreover, the aerosol sampling system (Figure S2) largely excluded emissions of EC from local sources (i.e., from fossil-fuel driven vehicles and stationary power sources of the station) as well as from long-range transport by differentiation of Antarctic baseline aerosol (ABA) using an on-line nephelometer and weather monitoring system. The nephelometer flagged potential local fossil-fuel pollution by the single scattering albedo and weather monitoring ensured that neither local EC contamination from the sector of the station nor any low wind speeds occurred[20]. Therefore, the collected airmasses originating from the free troposphere and lower stratosphere region are regarded as ABA. Consequently, we interpret the sources of the organic aerosols at Trollhaugen for summer based on the ^{14}C measurements as follows:

- Despite the isolation of ABA with the nephelometer and weather monitoring system, some EC was detected on the filters. The EC loadings were extremely low (i.e., 2.7 ± 1.5 ng C m^{-3}). Due to its estimated $\Delta^{14}C$ value of $\sim-1000‰$, EC is regarded as completely fossil, e.g., originating from remaining local emissions from the station or long-range transport from ships in the Southern Ocean.

- OC concentrations from fossil-fuel combustion related to diesel engines (OC_{ff}) were estimated from EC concentrations based on $(OC/EC)_{tr,pri}$, i.e., the primary emission ratio from traffic of 0.58[39]. This is explicitly relevant for local emissions that are produced directly on site at conditions

that do not allow any aging or SOA formation. OC_{ff} contributes on average 12% to total OC. As these emissions are predominantly water insoluble, we focus on the source apportionment of WSOC to reduce the risk of unrecognised anthropogenic emissions. Daellenbach et al.[40] determined that the AMS-PMF factor for hydrocarbon-like OA (HOA), which is assigned to primary emissions from traffic, contains only 11% of water-soluble components. Consequently, 4% of WSOC may be traced back to primary fossil-fuel emissions ($WSOC_{ff}$).

• WSOC contributions from biomass-burning ($WSOC_{bb}$) from continental areas of the Southern hemisphere were apportioned from levoglucosan measurement, which were as low as 10 pg m^{-3} on average. Based on an emission ratio of $WSOC_{bb}$ to levoglucosan of 7.5 biomass burning seems to be negligible. Due to its limited stability in the atmosphere[41], however, levoglucosan may have been decomposed during transport. To compensate for this and to determine an upper OC_{bb} limit, we assumed a loss of 90%, which yielded an upper limit of 4% for the $WSOC_{bb}$ portion of WSOC.

The average remaining WSOC fraction (i.e., without $WSOC_{ff}$ and $WSOC_{bb}$) still comprises 92% of total WSOC and shows a $\Delta^{14}C$ value of −356 ‰, which hardly differs from the average measured value of −365 ‰ for total WSOC. The source(s) of this dominant part of WSOC is *per se* unknown. In principle, primary and secondary terrestrial biogenic OC, primary and secondary marine OC, or yet unconsidered fossil OC emissions are possible. Figure 1b presents the $\Delta^{14}C$ signatures of these sources. Terrestrial biogenic and fossil-fuel sources are completely modern and devoid of ^{14}C so that a contribution of the one requires a counterbalancing contribution of the other (e.g., a mixture of 64% terrestrial biogenic OC and 36% fossil OC seems to be the straightforward solution). Although such combinations of sources typically occur at sites close to the emissions[33–37], they cannot be applied here, as two unlikely options need to be postulated at the same time.

Different marine sources therefore provide a better explanation regarding the ^{14}C depletion measured at Trollhaugen, as many of them appear to be pre-aged (see Fig. 1b) so that only one single source – or a set of similar sources – are required[42].

The thermohaline circulation is part of the large-scale ocean circulation combining the world's oceans. Upwellings in the Southern Ocean and in the North Pacific bring old water containing ^{14}C–depleted DOC to the surface. This pre-aged carbon is used as feedstock by marine biota and moves through the food chain. This Antarctic reservoir effect is visible in marine organisms. In terms of the radiocarbon age, Antarctic marine organisms appear older than they really are, e.g., in seals and penguins this effect makes them appear several centuries older[43].

As shown by Beaupré et al.[24], freshly produced PMA consists of pre-aged ^{14}C–depleted DOC. Assuming that PMA is produced in Antarctic waters and contribute to a large extend to the total aerosol; in consequence the observed $\Delta^{14}C$ DOC values in aerosols should resemble the values observed in deep waters brought to the surface by upwellings. Druffel and Bauer[29] analysed DOC in the Pacific closer to

Antarctica (54°S, 176°W) and found surface (3 m depth) $\Delta^{14}C$ DOC values of −366‰. More recently, Bercovici et al.[44] found $\Delta^{14}C$ values of −428‰ for DOC at 5 m in the South Indian Ocean (56°S, 85°E). Measurements from the Southern Ocean performed by Fang et al.[45] reported surface layer (0–25 m) $\Delta^{14}C$ DOC values of −257‰ to −430‰ collected at two sites in the western Amundsen Sea (~73°S, ~115°W), and Druffel et al.[46] reported similar values of $\Delta^{14}C$ −421‰ (20 m depth) in the same region (69°S, 103°W). On a site (71°S, 8°W) close to the Antarctic coast and less than 500 km from Trollhaugen, Lechtenfeld et al.[31] reported $\Delta^{14}C$ DOC values of −458 ± 12‰ (20 m depth) in surface waters. These findings support the notion that depleted PMA are a major contribution to ABA. Fig. 1b illustrates the depleted DOC from the deep seas as well as Southern Ocean surface waters compared to fossil and contemporary carbon sources.

Previous work on DOC in mid-latitude oceans revealed depletions for different size fractions. Using ultrafiltration for size separation, Guo et al.[47] reported $\Delta^{14}C$ values of −336‰ and −355‰ for 1–10 kDa, −443‰ and −452‰ for DOC of <1 kDa, and −611‰ and −709‰ for >10 kDa at a sampling depth of 250 m and 2600 m, respectively. Most abundant was the <1 kDa fraction with 71–72% (C fraction of the total DOC) followed by the 1–10 kDa (24–25%) and >10 kDa (5–3%) fraction. The depletion recorded for the most abundant <1 kDa DOC fraction matches the range of the mean ^{14}C depletion of WSOC measured on the aerosol filters from Trollhaugen. Similarly, Zigah et al.[48] analysed DOC in the Pacific (22°45'N, 158°00'E) between the surface and 3500 m of depth and separated the high molecular weight DOC (>1 kDa) from the low molecular weight DOC (< 1 kDa), which again was separated in hydrophobic and hydrophilic by solid phase extraction, with hydrophobic defined as the DOC retained on the solid phase. For >1 kDa DOC, $\Delta^{14}C$ values of −24‰ to −294‰ were measured, and −270‰ to −795‰ for <1 kDa DOC. For the total DOC fraction, $\Delta^{14}C$ values in deep waters (250–4500 m) ranged from −320‰ to −564‰. The values differ from the DOC depletions recorded in the Atlantic by Guo et al.[47], however, the size and the fraction constitution were different as well. The strongest depletion occurs in the first 1000 m, afterwards, $\Delta^{14}C$ DOC values do not diverge much with increasing depth.

In conclusion, the comparison of our ^{14}C measurements from the carbonaceous aerosols at Trollhaugen station in Antarctica with the investigation of ^{14}C levels of marine DOC suggests that WSOC at Trollhaugen is dominated (by up to 92%) by PMA that originate from <1 kDa fraction of DOC from the Southern Ocean. This conclusion is corroborated by further analytical investigation in the following.

4.2.2 Further information from complementary methods

Offline aerosol mass spectrometry (AMS) revealed predominately CH and CHS fragments such as CH_3, CHS, CH_2S, CH_2SO, and CH_2SO_2 additional to oxygenated fragments such as CO and CO_2 originating from carboxylic acids (Fig. 2). The mean H:C ratio was 1.8 ± 0.2, suggesting a low contribution from unsaturated hydrocarbons. The measured O:C ratio of 0.4 ± 0.1 is substantially higher than fresh emissions (~0.1), thus suggesting a low contribution of local emissions and additional evidence for ABA sources. Fragments CH_3, CHS, CH_2S, CH_3S, CH_2SO_2, and CH_4SO_3 are typical marker fragments for marine

secondary organic aerosol (MSOA) emissions and were present with a substantial intensity. Sulphur containing fragments are indicative of MSOA emissions, which are produced from dimethyl sulphide (DMS) oxidation[49].
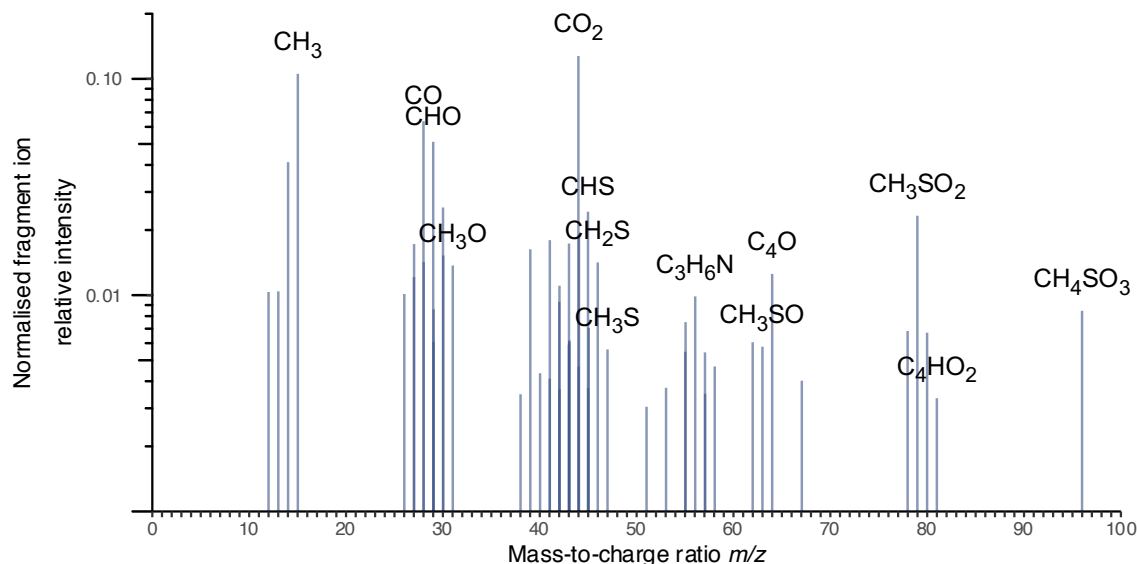

Figure 2. Seasonally averaged mass spectra recorded with an aerosol mass spectrometer (AMS) shows the presence of oxygenated and sulphur containing compounds, the latter indicative for a marine influence.

Methanesulphonic acid (MSA) concentrations were 7.0 ± 2.4 ng m^{-3} with two additional datapoints excluded from the mean, one below detection limit and one exceedingly high at 41.7 ng m^{-3}. As shown by Legrand et al.[50], MSA is known to show a seasonal pattern at the coastal Dumont d'Urville (DDU), Neumayer (NM), and the central Antarctic Concordia (DC) site with a maximum in austral summer and minimum in winter, however, with local maximal peaks in October and March for the Concordia. The MSA to non-sea-salt sulphate (R_{MSA}) ratio[50] to separate marine biogenic emissions from other sulphate sources was 0.06 ± 0.03 with the highest value of 0.10 recorded in March–Mai 2018. As reported by Legrand et al.[50], MSA concentrations for DC, NM, and DDU were 5.2 ± 2.0, 154 ± 77, and 60 ± 23 ng m^{-3} and the R_{MSA} ratios 0.05 ± 0.02, 0.41 ± 0.13, and 0.21 ± 0.05. Therefore, the values recorded at Trollhaugen more closely resemble central Antarctica than the coastal area, despite the relative proximity of Trollhaugen (~235 km) to the coast. Back of the envelope calculations with MSA/TC (ng C m^{-3}/ng C m^{-3}) gave a ratio of $7 \pm 5\%$ and MSA to water-soluble organic matter (WSOM) gave a ratio of $20 \pm 10\%$, strongly suggesting that only the minority of aerosol is of secondary marine origin.

Quantitative analysis revealed the presence of various organic acids and organosulphates (OS). Five out of six samples were analysed, one sample was unfortunately lost during work-up. The presence of adipic acid can come from atmospheric oxidation of cyclic olefins[51], while phthalic acid has been suggested to result

from incomplete combustion of fossil fuels, burning of plastic waste, and from oxidation of aromatic hydrocarbons[52–54]. Adipic acid was present in three out of five samples (Table S5) and phthalic acid was present in two samples. Adipic acid and phthalic acid are formed as SOA and their precursors originate from incomplete combustion of fossil fuels and aromatic hydrocarbons, respectively[55,56]. This indicates that anthropogenic influences from long range transport may contribute to aerosols collected on the QFF despite a shutter system to sample only ABA. Fossil fuel emissions may originate from long range transport, vessels in the Southern Oceans or emissions from neighbouring research stations. Although ^{14}C–depleted DOC is the dominant source, fossil fuel derived aerosols may still contribute additionally; the lowest Δ^{14}C–values were measured on the March 2016 and December 2016 where both adipic acid and phthalic acid was present. Azelaic acid has been suggested to form from fatty acids from the surface ocean microlayer[57] and was present in all samples. Additionally, an OS with MW 254 (m/z 253 [M-H]$^-$) was present in all samples. Claeys et al.[57] found MW 254 in atmospheric aerosols sampled from December 2006–March 2007 at Amsterdam Island (37.48°S, 77.34°E) in the southern Indian Ocean. The proposed formation pathway by Claeys et al.[57] starts from algae or bacterial fatty acid residues containing a double bond at the ω9 position and oxidation to (sulphoxy)nonanoic acid with hydroxy–aldehyde and hydroxy-acid intermediates. The presence of OS 254 emphasizes the marine origin of the austral summer aerosols. Furthermore, the presence of MSA previously measured by IC was confirmed in all samples. There was limited evidence for the presence of OS originating from isoprene and monoterpene in several samples. The low molecular weight OS compounds acetone sulphate (OS154, $C_3H_6O_5S$) and acetic acid sulphate (OS156, $C_2H_4O_6S$), which can be formed from isoprene oxidation products[58–61], were detected in the March 2016 and December 2016 samples, and December 2016 sample, respectively. OS 168 was tentatively detected in the three samples from 11/17, 01/18 and 04/18. This compound is as an isoprene degradation product originating form methacrolein and 2-methylglyceric acid[58,61]. OS 216, which is formed by isoprene epoxydiol (IEPOX) uptake of acidic sulphate aerosol[62], was present with a low response for January 2018 and tentatively detected in the sample for December 2016. OS 228 can be formed by photooxidation from isoprene[63] and was only present in the January 2018 sample. There was no detection of other organosulphates originating from isoprene, nor of organosulphates such as OS 250 originating from the monoterpenes, α- and β-pinene.

Our results describe for the first time the contribution of ^{14}C–depleted marine DOC to atmospheric aerosols in Antarctica by the means of the univocal measurement of ^{14}C signature by Accelerator Mass Spectrometry. AMS measurements indicate that the MSOA contribution to Trollhaugen is relatively small. Our measurements agree with the idea that aged DOC is injected into the atmosphere as PMA from breaking waves, where it makes up the largest part of the carbonaceous aerosol fraction in ABA. Evidence for contemporary biogenic sources is visible on multiple filters, however, their contribution to the total carbonaceous aerosol is rather small.

4.3 Methods

4.3.1 Site and sample collection

Sampling was performed at the Trollhaugen Observatory (72°00'42"S, 02°32'06"E, 1553 m.a.s.l.) adjacent to the Norwegian Troll station (Figure S1). Troll is located on ice-free bedrock at in the Nunatak area of Jutulsessen glacier, around 235 km from the coast in Dronning Maud Land, Antarctica. Antarctic baseline aerosol (ABA) was differentiated from non-ABA by input from in-situ on-line nephelometer (TSI 3563) measurements, as defined by Fiebig et al.[20]. No sampling took place at wind speeds > 10 m s^{-1} to prevent harsh weather conditions destroying the inserted filters. ABA and non-ABA aerosol were collected using two separate high-volume samplers (Digitel DHA-80 with PM$_{10}$ inlet), with double quartz fibre filters (Pallflex 2500)[64]. All QFF were prebaked (850°C; 3 h) to remove organic impurities (see Supplementary Text S Site).

4.3.2 Radiocarbon analysis

QFF were water extracted for ^{14}C-WSOC analysis using a polycarbonate filter holder with a glass syringe mounted at the top. 5.0 ± 0.2 mL ultrapure water (18.2 MΩ·cm) was fed by gravity through the water extraction setup (see Supplementary Text S Water Extraction). The eluate was collected in 12 mL Exetainer (Labco, Lampeter, UK) vials and stored at 4°C until analysis. The extracted QFF for WINSOC analysis were dried, wrapped in aluminium foil and kept in air-tight polyethylene bags at -20°C until further use. Filter handling and water extraction were made in a laminar flow cabinet. All glassware was cleaned in H$_3$PO$_4$ (1 M, ACS grade) and prebaked (500°C; 5 h), plastics were rinsed and sonicated with ultrapure water.

Chemical wet oxidation for radiocarbon analysis has been described before[65,66]. Briefly, WSOC eluate was acidified (0.5 mL 8.5% H$_3$PO$_4$) and flushed (50 mL min^{-1}) with high-purity (99.999%) helium at room temperature for 3 min to remove inorganic carbonaceous impurities. Oxidiser was freshly prepared (10% ACS grade K$_2$S$_2$O$_8$ in 5% (m/m) H$_3$PO$_4$) and pre-oxidized at 90°C for 30 min, then flushed with helium (50 mL min^{-1}, 3 min) to remove all carbonaceous contaminants. 0.25 mL oxidiser was added to each sample and oxidised overnight at 75°C on a hot plate (Ionplus, Switzerland). The evolved CO$_2$ was sampled (50 mL min^{-1}, 3 min) using a custom-made double gas needle and a PAL autosampler (CTC Analytics, Switzerland), dried, and ^{14}C measured on a MICADAS accelerator mass spectrometer[67–69] equipped with a gas interface system (GIS) for measuring CO$_2$[70,71]. Water extracted QFF were combusted using the Swiss_4S protocol[72] in a Sunset OC-EC analyser (Sunset laboratories, USA). The first fraction (pure WINSOC) was trapped with GIS and measured on-line for radiocarbon[73]. Additionally, ^{14}C-TC was measured accordingly by complete combustion (760°C, pure O$_2$). Radiocarbon values are reported as Δ^{14}C according to Stuiver and Polach[74].

4.3.3 Aerosol mass spectrometry

The offline aerosol mass spectrometry (AMS) technique was introduced in Daellenbach et al.[40]. The sample extraction, AMS measurements and data analysis follow the protocol presented in Moschos et al.[21].Briefly, punches from the QFF samples were extracted in 8 mL ultrapure water (18.2 MΩ·cm). Typical QFF water-extracted organic concentrations were 2–3 μg C·mL^{-1}. The liquid extracts were inserted into an ultrasonic bath for 20 min at 30°C. The ultrasonicated samples were then filtered through a 0.45 μm nylon membrane syringe (Infochroma, Switzerland) and transferred to a 50 mL centrifuge tube. Out of the resulting solutions, aerosols were generated in synthetic air (N_2 + O_2 20 ± 2% v/v, Carbagas, Switzerland) via a customised Apex Q nebuliser (Elemental Scientific, NE, USA) operating at 60°C. The resulting droplets were dried by passing through a Nafion dryer, and then injected and analysed using a long-time-of-flight AMS (L-ToF-AMS). Each sample was recorded for 8 min, with a collection time for each spectrum of ~40 s. Water-blanks (nebulised ultrapure water without filter extract) were measured for 12 min before and after each sample measurement. The technique was performed on 36 extracts of front and back ABA and non-ABA filters. For data analysis, we used Squirrel v1.59B (SeQUential Igor data RetRiEvaL) for m/z calibration and baseline subtraction, and Pika v1.19B (Peak Integration by Key Analysis, D. Sueper) for high-resolution (HR) analysis in the Igor Pro software package 6.37. The HR peak fitting was performed in the m/z range 12–133 and in total 584 organic fragment ions were fitted. After the peak fitting (fragments consisting of C, O, H, N and/or S), the isotope ions and inorganic fragments were removed, and the average water-blank signal was subtracted from the average signal of the following sample. The resulting data matrix was the bulk water-soluble organic aerosol (OA) fraction mass spectra (normalized fragment ion intensity) time series. The AMS-based OA:OC mass ratios (which can be used together with WSOC to calculate the ambient WSOA mass concentrations), as well as the atomic O:C and H:C ratios, were calculated using the Analytical Procedure for Elemental Separation (APES light) Ver. 1.05 within Igor.

4.3.4 Other Methods

For high-resolution mass spectrometry, QFF were extracted in 50:50 (vol/vol%) acetonitrile and methanol using a cooled ultrasonic bath for 30 minutes. The extracts were filtered through a Qmax PTFE hydrophobic syringe filter (0.22 μm pore size, 26 mm) and dried under a nitrogen flow to almost complete dryness. The extracts were difficult to evaporate, and a yellow oily residue was left. The dried extracts were reconstituted in 200 μL 10% acetonitrile in ultrapure water (<0.05 μS cm^{-1}, Millipore) and transferred to a vial for immediate analysis. The analysis was performed on an ultra-high performance liquid chromatograph (UHPLC, Dionex UltiMate 3000, Thermo Fisher) coupled to an electrospray ionization inlet of a quadrupole time of flight mass spectrometer (QToF-MS, Compact, Bruker). The UHPLC method is described elsewhere[75]. The QToF-MS was operated using the following settings: Nebulizer pressure at 3.5 bar, dry gas flow at 8.0 L min^{-1}, dry gas temperature at 210°C, capillary voltage of 3.5 kV, end plate offset of −500 V. Trace constituents were identified based on their retention times and fragmentation patterns.

Total carbon (TC), elemental carbon (EC), and organic carbon (OC) were quantified using the Sunset OC-EC analyser[76], using transmission for charring correction, and operated according to the EUSAAR-2 temperature program[77]. For the lowest loaded filter samples, 2–3 filter punches (1.5 cm^2) were stacked to obtain EC levels > LOD.

Ion chromatography was used for the analysis of organic and inorganic ions. Briefly, QFF were soaked in 10 mL ultrapure water (18.2 MΩ·cm) before ultrasonic agitation (30 min). Analysis was performed on a Dionex Integrieon ion chromatograph with a conductivity detector. Cation separation was carried out by a CS16 column (3 mm × 250 mm) using methane sulphonic acid (34 mM) at a flow rate of 0.5 ml min^{-1} as an eluent, anions were separated by an AS9-SC column (4 mm × 250 mm) and eluted using carbonate (K_2CO_3, 2.0 mM; HCO_3^-, 0.75 mM) at a flow rate of 2 ml min^{-1}.

Author Contributions

The work presented here was carried out in collaboration between all authors. K.E.Y. and S.S. contributed to the conception and design of the analysis. M.R., V.M., and D.T. performed the lab work and sample analysis. M.R. provided the first version of the manuscript and all authors contributed to the further writing of it.

Competing interests

The authors declare no competing interests.

4.4   References

1.   Contini, D., Vecchi, R. & Viana, M. Carbonaceous Aerosols in the Atmosphere. *Atmosphere* **9**, 181 (2018).

2.   Flanner, M. G. *et al.* Springtime warming and reduced snow cover from carbonaceous particles. *Atmospheric Chemistry and Physics* **9**, 2481–2497 (2009).

3.   Hansen, J. & Nazarenko, L. Soot climate forcing via snow and ice albedos. *Proceedings of the National Academy of Sciences* **101**, 423–428 (2004).

4.   Legrand, M. *et al.* Year-round record of bulk and size-segregated aerosol composition in central Antarctica (Concordia site) - Part 2: Biogenic sulfur (sulfate and methanesulfonate) aerosol. *Atmospheric Chemistry and Physics* **17**, 14055–14073 (2017).

5.   Legrand, M. *et al.* Year-round records of bulk and size-segregated aerosol composition in central Antarctica (Concordia site) - Part 1: Fractionation of sea-salt particles. *Atmospheric Chemistry and Physics* **17**, 14039–14054 (2017).

6.   Hong, S. *et al.* Seasonality of aerosol chemical composition at King Sejong Station (Antarctic Peninsula) in 2013. *Atmospheric Environment* **223**, 117185 (2020).

7.   Teinilä, K., Kerminen, V. M. & Hillamo, R. A study of size-segregated aerosol chemistry in the Antarctic atmosphere. *Journal of Geophysical Research Atmospheres* **105**, 3893–3904 (2000).

8.   Teinilä, K., Frey, A., Hillamo, R., Tülp, H. C. & Weller, R. A study of the sea-salt chemistry using size-segregated aerosol measurements at coastal Antarctic station Neumayer. *Atmospheric Environment* **96**, 11–19 (2014).

9.   Weller, R. & Lampert, A. Optical properties and sulfate scattering efficiency of boundary layer aerosol at coastal Neumayer Station, Antarctica. *Journal of Geophysical Research Atmospheres* **113**, 1–9 (2008).

10.   Wagenbach, D. *et al.* Sea-salt aerosol in coastal Antarctic regions. *Journal of Geophysical Research: Atmospheres* **103**, 10961–10974 (1998).

11.   Hansen, A. D. A., Bodhaine, B. A., Dutton, E. G. & Schnell, R. C. Aerosol black carbon measurements at the South Pole: Initial results, 1986-1987. *Geophysical Research Letters* **15**, 1193–1196 (1988).

12.   Wolff, E. W. & Cachier, H. Concentrations and seasonal cycle of black carbon in aerosol at a coastal Antarctic station. *Journal of Geophysical Research: Atmospheres* **103**, 11033–11041 (1998).

13.   Weller, R., Minikin, A., Petzold, A., Wagenbach, D. & König-Langlo, G. Characterization of long-term and seasonal variations of black carbon (BC) concentrations at Neumayer, Antarctica. *Atmospheric Chemistry and Physics* **13**, 1579–1590 (2013).

14.   Pereira, E. B., Evangelista, H., Pereira, K. C. D., Cavalcanti, I. F. A. & Setzer, A. W. Apportionment of black carbon in the South Shetland Islands, Antarctic Peninsula. *Journal of Geophysical Research* **111**, D03303 (2006).

15.   Hansen, A. D. A., Lowenthal, D. H., Chow, J. C. & Watson, J. G. Black carbon aerosol at McMurdo Station, Antarctica. *Journal of the Air and Waste Management Association* **51**, 593–600 (2001).

16.   Bodhaine, B. A. Aerosol absorption measurements at Barrow, Mauna Loa and the south pole. *Journal of Geophysical Research* **100**, 8967 (1995).

17.   Fiebig, M., Lunder, C. R. & Stohl, A. Tracing biomass burning aerosol from South America to Troll Research Station, Antarctica. *Geophysical Research Letters* **36**, 1–5 (2009).

18.   Hu, Q.-H., Xie, Z.-Q., Wang, X.-M., Kang, H. & Zhang, P. Levoglucosan indicates high levels of biomass burning aerosols over oceans from the Arctic to Antarctic. *Scientific Reports* **3**, 3119 (2013).

19.   Hu, Q.-H. *et al.* Secondary organic aerosols over oceans via oxidation of isoprene and monoterpenes from Arctic to Antarctic. *Scientific Reports* **3**, 2280 (2013).

20.   Fiebig, M. *et al.* Annual cycle of Antarctic baseline aerosol: Controlled by photooxidation-limited aerosol formation. *Atmospheric Chemistry and Physics* **14**, 3083–3093 (2014).

21.   Moschos, V. *et al.* Equal abundance of summertime natural and wintertime anthropogenic Arctic organic aerosols. *Nat Geosci* **15**, 196–202 (2022).

22. O'Dowd, C. D. *et al.* Biogenically driven organic contribution to marine aerosol. *Nature* **431**, 676–680 (2004).

23. Spracklen, D. v., Arnold, S. R., Sciare, J., Carslaw, K. S. & Pio, C. Globally significant oceanic source of organic carbon aerosol. *Geophysical Research Letters* **35**, (2008).

24. Beaupré, S. R. *et al.* Oceanic efflux of ancient marine dissolved organic carbon in primary marine aerosol. *Science Advances* **5**, (2019).

25. Baltar, F. *et al.* What Is Refractory Organic Matter in the Ocean? *Front Mar Sci* **8**, 1–7 (2021).

26. Key, R. M. *et al.* A global ocean carbon climatology: Results from Global Data Analysis Project (GLODAP). *Global Biogeochemical Cycles* **18**, 1–23 (2004).

27. Hua, Q., Barbetti, M. & Rakowski, A. Z. Atmospheric Radiocarbon for the Period 1950–2010. *Radiocarbon* **55**, 2059–2072 (2013).

28. Yoon, S., Fairley, D., Barrett, T. E. & Sheesley, R. J. Biomass and fossil fuel combustion contributions to elemental carbon across the San Francisco Bay Area. *Atmospheric Environment* **195**, 229–242 (2018).

29. Druffel, E. R. M. & Bauer, J. E. Radiocarbon distributions in Southern Ocean dissolved and particulate organic matter. *Geophysical Research Letters* **27**, 1495–1498 (2000).

30. Bercovici, S. K., McNichol, A. P., Xu, L. & Hansell, D. A. Radiocarbon Content of Dissolved Organic Carbon in the South Indian Ocean. *Geophysical Research Letters* **45**, 872–879 (2018).

31. Lechtenfeld, O. J. *et al.* Molecular transformation and degradation of refractory dissolved organic matter in the Atlantic and Southern Ocean. *Geochimica et Cosmochimica Acta* **126**, 321–337 (2014).

32. Hara, K. *et al.* Seasonal features and origins of carbonaceous aerosols at Syowa Station, coastal Antarctica. *Atmospheric Chemistry and Physics* **19**, 7817–7837 (2019).

33. Winiger, P. *et al.* Source apportionment of circum-Arctic atmospheric black carbon from isotopes and modeling. *Science Advances* **5**, (2019).

34. Budhavant, K. *et al.* Radiocarbon-based source apportionment of elemental carbon aerosols at two South Asian receptor observatories over a full annual cycle. *Environmental Research Letters* **10**, 064004 (2015).

35. Mousavi, A. *et al.* Source apportionment of black carbon (BC) from fossil fuel and biomass burning in metropolitan Milan, Italy. *Atmospheric Environment* **203**, 252–261 (2019).

36. Vlachou, A. *et al.* Advanced source apportionment of carbonaceous aerosols by coupling offline AMS and radiocarbon size-segregated measurements over a nearly 2-year period. *Atmospheric Chemistry and Physics* **18**, 6187–6206 (2018).

37. Zotter, P. *et al.* Diurnal cycle of fossil and nonfossil carbon using radiocarbon analyses during CalNex. *Journal of Geophysical Research: Atmospheres* **119**, 6818–6835 (2014).

38. Rauber, M., Salazar, G., Yttri, K. E. & Szidat, S. An Optimised Fraction Separation Method for Radiocarbon Source Apportionment Applied on Low-Loaded Arctic Aerosol Filters (in preparation). (2022).

39. Gelencsér, A. *et al.* Source apportionment of PM$_{2.5}$ organic aerosol over Europe: Primary/secondary, natural/anthropogenic, and fossil/biogenic origin. *Journal of Geophysical Research Atmospheres* **112**, (2007).

40. Daellenbach, K. R. *et al.* Characterization and source apportionment of organic aerosol using offline aerosol mass spectrometry. *Atmospheric Measurement Techniques* **9**, 23–39 (2016).

41. Hennigan, C. J., Sullivan, A. P., Collett, J. L. & Robinson, A. L. Levoglucosan stability in biomass burning particles exposed to hydroxyl radicals. *Geophysical Research Letters* **37**, (2010).

42. Ceburnis, D. *et al.* Quantification of the carbonaceous matter origin in submicron marine aerosol by δ^{13}C and ^{14}C isotope analysis. *Atmospheric Chemistry and Physics* **11**, 8593–8606 (2011).

43. Omoto, K., Oliver, R. L., James, P. R. & Jago, J. B. The problem and significance of radiocarbon geochronology in Antarctica. in *Antarctic earth science* 450–452 (Australian Academy of Science Canberra, 1983).

44. Bercovici, S. K., McNichol, A. P., Xu, L. & Hansell, D. A. Radiocarbon Content of Dissolved Organic Carbon in the South Indian Ocean. *Geophysical Research Letters* **45**, 872–879 (2018).

45. Fang, L. *et al.* Removal of Refractory Dissolved Organic Carbon in the Amundsen Sea, Antarctica. *Scientific Reports* **10**, 1–8 (2020).

46. Druffel, E. R. M. *et al.* Dissolved Organic Radiocarbon in the Eastern Pacific and Southern Oceans. *Geophysical Research Letters* **48**, (2021).

47. Guo, L., Santschi, P. H., Cifuentes, L. A., Trumbore, S. E. & Southon, J. Cycling of high-molecular-weight dissolved organic matter in the Middle Atlantic Bight as revealed by carbon isotopic (^{13}C and ^{14}C) signatures. *Limnology and Oceanography* **41**, 1242–1252 (1996).

48. Zigah, P. K. *et al.* Allochthonous sources and dynamic cycling of ocean dissolved organic carbon revealed by carbon isotopes. *Geophysical Research Letters* **44**, 2407–2415 (2017).

49. Bullock, H. A., Luo, H. & Whitman, W. B. Evolution of dimethylsulfoniopropionate metabolism in marine phytoplankton and bacteria. *Frontiers in Microbiology* **8**, 1–17 (2017).

50. Legrand, M. *et al.* Year-round record of bulk and size-segregated aerosol composition in central Antarctica (Concordia site) - Part 2: Biogenic sulfur (sulfate and methanesulfonate) aerosol. *Atmospheric Chemistry and Physics* **17**, 14055–14073 (2017).

51. Hatakeyama, Shiro. *et al.* Ozone-cyclohexene reaction in air: quantitative analysis of particulate products and the reaction mechanism. *Environmental Science & Technology* **19**, 935–942 (1985).

52. Kawamura, Kimitaka. & Kaplan, I. R. Motor exhaust emissions as a primary source for dicarboxylic acids in Los Angeles ambient air. *Environmental Science & Technology* **21**, 105–110 (1987).

53. Fraser, M. P., Yue, Z. W. & Buzcu, B. Source apportionment of fine particulate matter in Houston, TX, using organic molecular markers. *Atmospheric Environment* **37**, 2117–2123 (2003).

54. Glasius, M. *et al.* Chemical characteristics and sources of organosulfates, organosulfonates, and carboxylic acids in aerosols in urban Xi'an, Northwest China. *Science of The Total Environment* 151187 (2021).

55. Kawamura, K. & Ikushima, K. Seasonal changes in the distribution of dicarboxylic acids in the urban atmosphere. *Environmental Science & Technology* **27**, 2227–2235 (1993).

56. Nguyen, Q. T. *et al.* Understanding the anthropogenic influence on formation of biogenic secondary organic aerosols in Denmark via analysis of organosulfates and related oxidation products. *Atmospheric Chemistry and Physics* **14**, 8961–8981 (2014).

57. Claeys, M. *et al.* Chemical characterisation of marine aerosol at Amsterdam Island during the austral summer of 2006–2007. *Journal of Aerosol Science* **41**, 13–22 (2010).

58. Surratt, J. D. *et al.* Evidence for Organosulfates in Secondary Organic Aerosol. *Environmental Science & Technology* **41**, 517–527 (2007).

59. Olson, C. N. *et al.* Hydroxycarboxylic Acid-Derived Organosulfates: Synthesis, Stability, and Quantification in Ambient Aerosol. *Environmental Science & Technology* **45**, 6468–6474 (2011).

60. Shalamzari, M. S. *et al.* Mass spectrometric characterization of organosulfates related to secondary organic aerosol from isoprene. *Rapid Communications in Mass Spectrometry* **27**, 784–794 (2013).

61. Schindelka, J., Iinuma, Y., Hoffmann, D. & Herrmann, H. Sulfate radical-initiated formation of isoprene-derived organosulfates in atmospheric aerosols. *Faraday Discussions* **165**, 237 (2013).

62. Surratt, J. D. *et al.* Reactive intermediates revealed in secondary organic aerosol formation from isoprene. *Proceedings of the National Academy of Sciences* **107**, 6640–6645 (2010).

63. Nozière, B., Ekström, S., Alsberg, T. & Holmström, S. Radical-initiated formation of organosulfates and surfactants in atmospheric aerosols. *Geophysical Research Letters* **37**, (2010).

64. McDow, S. R. & Huntzicker, J. J. Vapor adsorption artifact in the sampling of organic aerosol: Face velocity effects. *Atmospheric Environment Part A, General Topics* **24**, 2563–2571 (1990).

65. Lang, S. Q., Bernasconi, S. M. & Früh-Green, G. L. Stable isotope analysis of organic carbon in small (μg C) samples and dissolved organic matter using a GasBench preparation device. *Rapid Communications in Mass Spectrometry* **26**, 9–16 (2012).

66. Wiedemeier, D. B. *et al.* Characterization, Quantification and Compound-specific Isotopic Analysis of Pyrogenic Carbon Using Benzene Polycarboxylic Acids (BPCA). *Journal of Visualized Experiments* **111**, (2016).

67. Synal, H. A., Stocker, M. & Suter, M. MICADAS: A new compact radiocarbon AMS system. *Nuclear Instruments and Methods in Physics Research, Section B: Beam Interactions with Materials and Atoms* **259**, 7–13 (2007).

68. Szidat, S. *et al.* ^{14}C Analysis and Sample Preparation at the new Bern Laboratory for the Analysis of Radiocarbon with AMS (LARA). *Radiocarbon* **56**, 561–566 (2014).

69. Fahrni, S. M., Wacker, L., Synal, H. A. & Szidat, S. Improving a gas ion source for ^{14}C AMS. *Nuclear Instruments and Methods in Physics Research, Section B: Beam Interactions with Materials and Atoms* **294**, 320–327 (2013).

70. Ruff, M. *et al.* A Gas Ion Source for Radiocarbon Measurements at 200 kV. *Radiocarbon* **49**, 307–314 (2007).

71. Wacker, L. *et al.* A versatile gas interface for routine radiocarbon analysis with a gas ion source. *Nuclear Instruments and Methods in Physics Research, Section B: Beam Interactions with Materials and Atoms* **294**, 315–319 (2013).

72. Zhang, Y. L. *et al.* On the isolation of OC and EC and the optimal strategy of radiocarbon-based source apportionment of carbonaceous aerosols. *Atmospheric Chemistry and Physics* **12**, 10841–10856 (2012).

73. Agrios, K. *et al.* Online coupling of pure O_2 thermo-optical methods – ^{14}C AMS for source apportionment of carbonaceous aerosols. *Nuclear instruments and methods in physics research section B: beam interactions with materials and atoms* **361**, 288–293 (2015).

74. Stuiver, M. & Polach, H. A. Discussion Reporting of ^{14}C data. *Radiocarbon* **19**, 355–363 (1977).

75. Kristensen, K., Bilde, M., Aalto, P. P., Petäjä, T. & Glasius, M. Denuder/filter sampling of organic acids and organosulfates at urban and boreal forest sites: Gas/particle distribution and possible sampling artifacts. *Atmospheric Environment* **130**, 36–53 (2016).

76. Birch, M. E. & Cary, R. A. Elemental Carbon-Based Method for Monitoring Occupational Exposures to Particulate Diesel Exhaust. *Aerosol Science and Technology* **25**, 221–241 (1996).

77. Cavalli, F., Viana, M., Yttri, K. E., Genberg, J. & Putaud, J. P. Toward a standardised thermal-optical protocol for measuring atmospheric organic and elemental carbon: The EUSAAR protocol. *Atmospheric Measurement Techniques* **3**, 79–89 (2010).

5 Conclusions and Outlook

The optimised OC/EC separation procedure coupled with WSOC measurement by chemical wet oxidation provides a new framework on how to perform radiocarbon measurement on atmospheric aerosol fractions. This work builds up on previous developments of Zhang et al.[1] for charring minimisation and the chemical wet oxidation technique from Lang et al.[2], here applied on the WSOC fraction of atmospheric aerosols. We showed that direct ^{14}C-WSOC measurements are feasible without the need for prior volume reduction e.g., by lyophilisation. This simplifies the workflow and increases sample throughput. Furthermore, the chemical wet oxidation is a simple and reliable method with low procedural blanks and a constant contamination below 1 µg C. Low procedural blanks are desirable in any case, however, particularly in this work as the method was applied on low loaded Arctic filters from Svalbard.

With COMPYCALC, we developed a novel thermal desorption model for EC extrapolation. This non-linear correction approach is based on the underlying physical properties of the OC/EC compound mixture and thus specific for each filter. Site specific or even season specific EC correction slopes[1,3] have been replaced by this non-linear correction. Beyond the improved correction, this approach has several other benefits. With the classical approach, different WINSOC removal runs with higher temperatures to deliberately lower EC yield must be made from a single filter followed by radiocarbon analysis. The F^{14}C result as a function of the EC yield is then used to calculate the slope for F^{14}C(EC) correction. Best practice is to repeat this process for a few filters and use an average slope for correction. It is evident that this procedure is laborious and requires much more valuable sample material. Furthermore, radiocarbon measurements are cost intensive. Therefore, a high number of measurements that only serve to correct the remaining samples may reduce the number of samples that are feasible for a campaign with the means intended for radiocarbon measurements. Alternatively, the slopes could be estimated from other sites when insufficient filter material is available for slope determination. This approach is obviously not desirable and will lead to additional and uncertainties that are hard to estimate, as it is evident that the sources in different environments are not comparable, e.g., a European city versus an Indian city or the Arctic. Additionally, the COMPYCALC application will reduce the workload as well as the amount of filter material and radiocarbon measurements solely required for slope correction. COMPYCALC was applied on the Svalbard filters for their low loading and large portion of pyrolysable species. The model has since then also been applied on EC from filters sampled in rural and urban Thailand[4]. In an ongoing study, COMPYCALC is also applied on EC from melted and filtrated glacier ice core samples. So far, COMPYCALC is an R script available from the GitHub repository and the script is run on a scientist's personal computer e.g., with the R Studio integrated development environment (IDE). Thus, COMPYCALC requires at least a version of R. A selection of packages for calculation are automatically downloaded and installed. The necessity for a web-based user interface e.g., based on R Shiny is not given as the tool is used only once after a measurement campaign. The additional complexity of the Shiny application and seldom usage of the script does not justify such a step, especially considering that there is little to be gained in terms of speed and user

friendliness. Furthermore, any R Shiny application as well as R server needs to be maintained occasionally and debugging an R Shiny application is more demanding than debugging a regular R script. Alternatively, R Studio Cloud may be used in the future, which allows to load the latest version from GitHub and run COMPYCALC in a cloud session inside a web browser without the need for R on the personal computer. A limited number of project hours and computing time is available for free on R Studio Cloud.

The thermal desorption model was optimised with data from previous measurements campaigns shown in Zotter et al.[3]. These measurements were from various sites in Switzerland. As shown with the challenging Svalbard filters, we were able to demonstrate that the model works even with filters form demanding sampling sites. In the future, the uncertainty estimation may be improved to reduce the dependence on assumptions, e.g., with the implementation of a Monte Carlo method into the calculation. The novelty of thermal desorption model relies on the extrapolation of EC to 100% yield. However, the calculation of the charring has not been changed and relies on the calculation and assumptions made in previous work[3]. Although charring should ideally not occur at all, it is not completely avoidable. There might be a possibility to extend the idea of the thermal desorption model also on the pyrolysis of OC and implement this in the charring correction. Any further development should also optimise the current code for speed as there is certainly room for improvement. Overall, the calculation for each sample requires a couple of seconds, thus speed optimisation is not a top priority for improving COMPYCALC but should be considered when new features are implemented.

In addition to COMPYCALC, we developed Sunset-calc, an R Shiny application for the analysis of raw data from the Sunset OC/EC analyser. The web application with a simple drag and drop interface replaces previous Excel spreadsheets and provides EC yield calculation and the fraction of charring for each step in the Swiss_3S protocol. Therefore, Sunset-calc enables rapid protocol optimisations for a low fraction of charring, while avoiding too large EC losses. Additionally, Sunset-calc can split raw data files with multiple Sunset runs, can calculate the amount of carbon in each step for the individual protocols, and provides EC-yield-corrected amount calculations with the OC/EC yield app within the Sunset-calc web tool. Sunset-calc was built modularly, thus allowing relatively simple expansion for new protocols, e.g., a protocol dedicated for the analysis of soil sediments. Expandability and a simple core structure are fundamental for future development of the application. Sunset-calc also serves as an example on how other laboratory data analysis tasks could be handled through a R Shiny application.

The chemical wet oxidation was optimised with low procedural blanks with stringent cleaning protocols. Automatisation was achieved with the PAL autosampler, thus radiocarbon measurements were performed supervised but with little interventions. The custom-made long gas sampling needle with easily exchangeable parts allowed preventive maintenance and made the chemical wet oxidation setup more resilient. The drawback of this system was that the gas sampling needle is briefly an open system when entering a sampling vial as the space between the needle helium outlet and needle inlet is empty (i.e., not

filled with any material). Therefore, some sample material is lost, and amount determinations cannot be made accurately.

Future developments of the wet oxidation procedure should therefore focus on creating a filled sampling needle and adding an in-line NDIR for accurate amount determinations. For creating a filled gas sampling needle, preferably a non-carbonaceous material should be used as a filler. Although not a carbon-free compound, trials with epoxy resin filler ("glue", i.e., Araldite®) were made. Initial trials showed that these gas sampling needles are feasible, however, the long-term stability in the hot, acidic, and oxidative environment are questionable. Adding an in-line NDIR would be highly desirable for the CHS system. The amount of WSOC could be precisely determined and would allow for a chemical mass balance calculation of the omitted fractions (e.g., WINSOC when not directly measured, the S2 and S3 mixed fractions in the Swiss_4S protocol). Also, the WSOC extraction with the filter holder system could be compared to other WSOC extraction methods (e.g., sonication and vortexing). Furthermore, the chemical wet oxidation could be extended to support larger vials if volumes above the current 5 mL of sample liquid is desired. Beside new vials with gastight caps, this would require a modified vial holder and cover and adjusted autosampler initialisation file. The constant and cross contamination would have to be determined again. Additionally, the sampling and flushing time would have to be extended.

CSRA of oxalate provided new indications on its formation in the atmosphere. Previous CSRA attempts on oxalate from atmospheric aerosols focused on method development and have only measured a very limited number of aerosol samples. In this work, IC separation of oxalate was combined with chemical wet oxidation previously used for WSOC. Furthermore, oxalate analysis was benchmarked with WSOC, thus providing the information on whether oxalate as a subfraction of WSOC is different from the bulk WSOC. Significant differences of oxalate to WSOC were found for rural Råö (Sweden), where the nonfossil fraction of oxalate was substantially higher than measured for WSOC. This indicates dominant contribution of biogenic SOA to the nonfossil oxalate fraction. Biomass burning has been suggested as a major contributor to the formation of oxalate oxalate[5–9], however, except for Delhi (India), our work indicates that biomass burning plays only a minor role in oxalate formation for the filters analysed. With aerosol filters from Kraków (Poland) also a site heavily influenced from coal combustion was investigated. The high fossil-fuel contribution predominantly from coal was observed in all measured fractions (TC, EC, WSOC, WINSOC). The oxalate to TC ratio as well as oxalate to WSOC ratio for the Kraków filters were much lower than in all other sites, therefore the oxalate concentrations were insufficient for a ^{14}C analysis. Although no nonfossil fraction has been measured, this indicates that primary or secondary organic aerosols from coal combustion are not a relevant contributor for oxalate formation. Overall, oxalate is predominantly formed from biogenic sources. More measurements from different rural sites should be performed to confirm these indications. More results from cloud chamber experiments may provide further evidence. Interesting would also be the addition of marine aerosol to determine whether the oxalate/WSOC differences are comparable to rural sites. Furthermore, future CSRA measurements of oxalate should always be coupled with radiocarbon measurements of the other fractions, especially WSOC to correctly evaluate any differences.

We are very likely the firsts to perform direct radiocarbon analysis of multiple carbonaceous aerosol fractions (TC, WSOC, and WINSOC) from Antarctic aerosols. Here, the results of the summer filters from the sampling campaign performed at the Norwegian Troll station in February 2016 to September 2018 were discussed. The sampling site is located neither at the coast nor on the inland ice plateau but roughly 200 km from the coast on dry bedrock. Very low filter loadings made the radiocarbon analysis challenging; however, TC, WSOC, and WINSOC were successfully measured on the 13 Antarctic background air filters received. Due to the low loadings, EC analysis was not attempted. All austral summer measurements revealed substantially depleted ^{14}C values otherwise only observed at heavily polluted urban sites in Winter. Local fossil-fuel pollution sources are an unlikely contributor to Antarctic background air with such an extent. Our radiocarbon measurements indicate that ^{14}C-depleted PMA sources originating in the Southern Ocean surrounding Antarctica dominate in all measured carbonaceous fractions in austral summer, and secondary marine aerosols and biomass burning are only minor contributors. PMA is likely formed by sea spray in the Southern Ocean from upwellings containing ^{14}C depleted rDOC[10,11]. Although not measured, this means that the EC fraction must be even more depleted than the measured TC, WSOC, and WINSOC fractions. Granted that this is very difficult, future ^{14}C measurements should at least attempt to measure the EC fraction as well, and if not feasible for individual samplings at least try for seasonally pooled samples. Several limitations need to be overcome. Low filter loading makes the filter blank contribution larger, and the Sunset OC/EC analyser can only hold a certain area (~10 cm²) of filter material depending on the analyser spoon. Furthermore, the contribution of charred WINSOC to the EC fraction should not be underestimated. Nevertheless, especially due to the low number of measurements, more ^{14}C analysis should be performed on the filters collected since September 2018. Also, to confirm the ^{14}C-depleted PMA hypothesis, aerosol filters from other Antarctic sites would be desirable. Samples from coastal sites may even show different signatures than from sites more inland. Shipborne aerosol samples from the Southern Ocean could also be included at a later stage.

Although austral winter filters were also measured, the results of these measurements were not included in this thesis as more measurements and data analysis is needed.

Beyond the ongoing work on the topics mentioned above, there are several opportunities for the Laboratory for the Analysis of Radiocarbon (LARA) to develop further in the future. Currently, most of the AMS measurements performed at LARA are its own research or research of collaborators using the device. Only less than a third of the measurement time is allocated for service (i.e., conducting AMS measurements on behalf of others) to clients within the University of Bern and other research institutes. Providing sufficient demand, the lab could focus to a larger part on AMS service for both solid and gas measurements with the currently available hyphenation techniques. This would require further process optimisations to reduce costs, improve efficiency, and reduce lead times. The impact on research could be minimised with a higher sample throughput per measurement day, i.e., only by extending the researchers presence during a measurement day or by working in shifts with no MICADAS downtime at night.

Most likely, with the currently available tools and techniques at LARA the research focus will likely shift towards on ^{14}C measurements instead of method development. Nevertheless, the lab may continue to conduct method development research including the implementation or improvement of hyphenation techniques for AMS. As shown in various cases in the introduction, stable carbon isotope (^{13}C) measurements can be used complementary to radiocarbon analysis and has been used in conjunction with ^{14}C analysis of carbonaceous aerosols as well[12]. So far, ^{13}C measurements are not performed at LARA and must be conducted elsewhere if desired. Therefore, it would be advantageous to couple an isotope-ratio mass spectrometry device to the AMS setup e.g., with a split injection where fraction of the sample is analysed for ^{13}C and the other is used for ^{14}C analysis in the MICADAS. This would allow measuring both isotopes at high precision with the choice of different hyphenation techniques such as elemental analyser, chemical wet oxidation, and Sunset OC/EC analyser.

1.1 References

1. Zhang, Y. L. *et al.* On the isolation of OC and EC and the optimal strategy of radiocarbon-based source apportionment of carbonaceous aerosols. *Atmospheric Chemistry and Physics* **12**, 10841–10856 (2012).

2. Lang, S. Q. *et al.* Rapid [14]C Analysis of Dissolved Organic Carbon in Non-Saline Waters. *Radiocarbon* **58**, 505–515 (2016).

3. Zotter, P. *et al.* Radiocarbon analysis of elemental and organic carbon in Switzerland during winter-smog episodes from 2008 to 2012 – Part 1: Source apportionment and spatial variability. *Atmospheric Chemistry and Physics* **14**, 13551–13570 (2014).

4. Song, W. *et al.* Is biomass burning always a dominant contributor of fine aerosols in northern Thailand? (submitted to Environmental International). (2022).

5. Jaffrezo, J.-L. *et al.* Biomass burning signatures in the atmosphere of central Greenland. *Journal of Geophysical Research: Atmospheres* **103**, 31067–31078 (1998).

6. Deshmukh, D. K., Mozammel Haque, Md., Kawamura, K. & Kim, Y. Dicarboxylic acids, oxocarboxylic acids and α-dicarbonyls in fine aerosols over central Alaska: Implications for sources and atmospheric processes. *Atmospheric Research* **202**, 128–139 (2018).

7. Kundu, S., Kawamura, K., Andreae, T. W., Hoffer, A. & Andreae, M. O. Molecular distributions of dicarboxylic acids, ketocarboxylic acids and α-dicarbonyls in biomass burning aerosols: implications for photochemical production and degradation in smoke layers. *Atmospheric Chemistry and Physics* **10**, 2209–2225 (2010).

8. Deshmukh, D. K. *et al.* High Loadings of Water-Soluble Oxalic Acid and Related Compounds in PM$_{2.5}$ Aerosols in Eastern Central India: Influence of Biomass Burning and Photochemical Processing. *Aerosol and Air Quality Research* **9**, 2625–2644 (2019).

9.   Falkovich, A. H. *et al.* Low molecular weight organic acids in aerosol particles from Rondônia, Brazil, during the biomass-burning, transition and wet periods. *Atmospheric Chemistry and Physics* **5**, 781–797 (2005).

10.   Bercovici, S. K., McNichol, A. P., Xu, L. & Hansell, D. A. Radiocarbon Content of Dissolved Organic Carbon in the South Indian Ocean. *Geophysical Research Letters* **45**, 872–879 (2018).

11.   Lechtenfeld, O. J. *et al.* Molecular transformation and degradation of refractory dissolved organic matter in the Atlantic and Southern Ocean. *Geochimica et Cosmochimica Acta* **126**, 321–337 (2014).

12.   Winiger, P. *et al.* Source apportionment of circum-Arctic atmospheric black carbon from isotopes and modeling. *Science Advances* **5**, eaau8052 (2019).

6 Appendices

6.1 Supplementary material for Chapter 2

Text S1: COMPYCALC correction workflow

In this section, the COMPYCALC correction workflow is explained. A colour code is applied on the input value Table S1 and output Table (Table S2) to highlight corresponding values. The $F^{14}C$ values from the TC and EC radiocarbon measurements (Table S1) were used to calculate F_{OC} using Eq. S1. F_{EC} is corresponding to the EC value from the radiocarbon measurement. The output from the COMPYCALC run is shown in Table S2. The output includes the input EC value (F_{EC}), the EC value correct to 100% yield ($F_{EC(corr)}$), and the EC value correct to 100% yield with 0% charring ($F_{EC(final)}$). Note that in the COMPYCALC output file the terms F14C_EC, F14C_EC100, and F14C_EC100_0_charr are used for F_{EC}, $F_{EC(corr)}$, and $F_{EC(final)}$, respectively. The workflow for $F^{14}C(EC)$ correction using COMPYCALC is summarised below in Fig. S1:

Figure S1: The workflow for corrections with COMPYCALC. The input $F^{14}C$ values F_{EC} and F_{OC} are added as csv files to the COMPYCALC folder, the COMPYCALC script run, and with the resulting $F_{EC(final)}$ the $F_{OC(final)}$ value calculated.

Input values

Table S1: COMPYCALC input values. Columns used for input are marked in colour; the F_{EC} refers to the $F^{14}C(EC)$ value obtained from the radiocarbon measurement, F_{OC} was calculated using Eq. S1 from the $F^{14}C(TC)$, $F^{14}C(EC)$, and EC/TC ratio. TC and EC loadings are from measurements at the University of Bern. Filters that were pooled for ^{14}C analysis are marked with an asterisk.

Start date	End date	TC $F^{14}C$	TC $\mu g\ C\ cm^{-2}$	F_{EC} $F^{14}C$	EC $\mu g\ C\ cm^{-2}$	EC/TC ratio	F_{OC} $F^{14}C$
23 Feb 2017	02 Mar 2017	0.770	9.5	0.881	1.47	0.15	0.749
05 May 2017	15 May 2017	1.068	7.1	0.597	1.21	0.17	1.165
31 May 2017	26 Jun 2017	0.852	2.6	0.642	0.82	0.32	0.951
*08 Sep 2017	28 Sep 2017	0.959	4.1	0.689	0.47	0.11	0.993
28 Sep 2017	06 Oct 2017	1.036	22.3	0.544	2.41	0.11	1.095
*06 Oct 2017	24 Oct 2017	0.825	3.4	0.748	0.44	0.13	0.837
*05 Dec 2017	21 Dec 2017	0.509	3.3	0.563	0.82	0.25	0.492
23 Jan 2018	31 Jan 2018	0.573	6.1	0.184	1.03	0.17	0.652
21 Mar 2018	29 Mar 2018	0.951	5.0	0.570	0.71	0.14	1.014
06 Apr 2018	16 Apr 2018	0.957	6.0	0.527	0.84	0.14	1.027
*12 Jul 2018	30 Jul 2018	0.786	2.8	0.677	0.34	0.12	0.802
*30 Jul 2018	15 Aug 2018	0.997	9.5	0.767	0.55	0.06	1.011
23 Nov 2018	03 Dec 2018	0.727	3.9	0.554	0.56	0.14	0.756

*Pooled filters

$$F_{OC} = \frac{F_{TC} - F_{EC} * \frac{EC}{TC}}{1 - \frac{EC}{TC}} \tag{S1}$$

Text S2: COMPYCALC Output

In the main folder with the compycalc.R script, a summary pdf file and a summary csv are generated by COMPYCALC. In the csv file (see Table S2), the first COMPYCALC output column is called filter_name_short and defined by the last letter of the folder name, in which the Sunset raw data files for each filter are placed. Self-descriptive are the following five columns: EC_yield, charring_S1, charring_S2, charring_S3, and charring_total are the mean EC yields obtained by OC removal, the charring for each step in the Swiss_4S protocol, and the toal charring (sum of charring S1-S3), respectively. F14C_EC is the initial uncorrected EC value (F_{EC}), F14C_EC100 corresponds to the $F^{14}C$ value for EC extrapolated to 100% EC yield ($F_{EC(corr)}$), F14C_EC100_0_charr to the $F^{14}C$ value for EC extrapolated to 100% EC yield with 0% charring ($F_{EC(final)}$). The corresponding columns with a _u-suffix estimate the uncertainty by error propagation. The corrected OC value ($F_{OC(final)}$) was calculated with Eq. S1 and the F14C_EC100_0_charr value. As shown in Fig. S2, the summary pdf gives a visual overview of the $F^{14}C$ results, the EC yield, and the charring for each step.

Table S2: Summary output of COMPYCALC with the filter sampling start and end date added in the first and second column. Filters that were pooled for ^{14}C analysis are marked with an asterisk.

Start date	End date	COMPYCALC output					
23 Feb 2017	02 Mar 2017	filter_name_short	EC_yield	charring_S1	charring_S2	charring_S3	charring_total
05 May 2017	15 May 2017	A	0.720	0.015	-0.001	0.013	0.027
31 May 2017	26 Jun 2017	B	0.865	0.029	0.001	0.024	0.054
*08 Sep 2017	28 Sep 2017	C	0.854	0.039	0.000	0.089	0.129
28 Sep 2017	06 Oct 2017	D	0.892	0.049	0.012	0.045	0.106
*06 Oct 2017	24 Oct 2017	E	0.803	0.068	-0.005	0.030	0.093
*05 Dec 2017	21 Dec 2017	F	0.854	0.021	0.011	0.022	0.055
23 Jan 2018	31 Jan 2018	G	0.930	0.016	0.006	0.022	0.045
21 Mar 2018	29 Mar 2018	H	0.921	0.012	0.003	0.014	0.030
06 Apr 2018	16 Apr 2018	I	0.919	0.020	0.002	0.017	0.039
*12 Jul 2018	30 Jul 2018	J	0.859	0.025	0.004	0.035	0.064
*30 Jul 2018	15 Aug 2018	K	0.941	0.028	0.014	0.021	0.062
23 Nov 2018	03 Dec 2018	L	0.951	0.037	0.024	0.054	0.115
Start date	End date	M	0.818	0.010	0.002	0.014	0.026

*Pooled filters

Table S2 continued:

COMPYCALC output						
F_{EC}		$F_{EC(corr).}$			$F_{EC(final)}$	
F14C_EC	F14C_EC_u	F14C_EC100	F14C_EC100_u	linear_slope	F14C_EC100_0_charr	F14C_EC100_0_charr_u
0.881	0.043	0.925	0.044	0.157	0.918	0.078
0.597	0.027	0.714	0.038	0.867	0.648	0.060
0.642	0.047	0.756	0.051	0.787	0.689	0.091
0.689	0.044	0.782	0.048	0.863	0.726	0.106
0.544	0.021	0.694	0.036	0.760	0.605	0.054
0.748	0.047	0.841	0.049	0.632	0.800	0.087
0.563	0.039	0.653	0.052	1.301	0.614	0.079
0.184	0.030	0.267	0.123	1.058	0.222	0.136
0.570	0.040	0.665	0.052	1.185	0.614	0.086
0.527	0.035	0.654	0.049	0.903	0.583	0.081
0.677	0.052	0.754	0.056	1.301	0.716	0.097
0.767	0.042	0.826	0.045	1.206	0.786	0.084
0.554	0.051	0.696	0.059	0.782	0.632	0.096
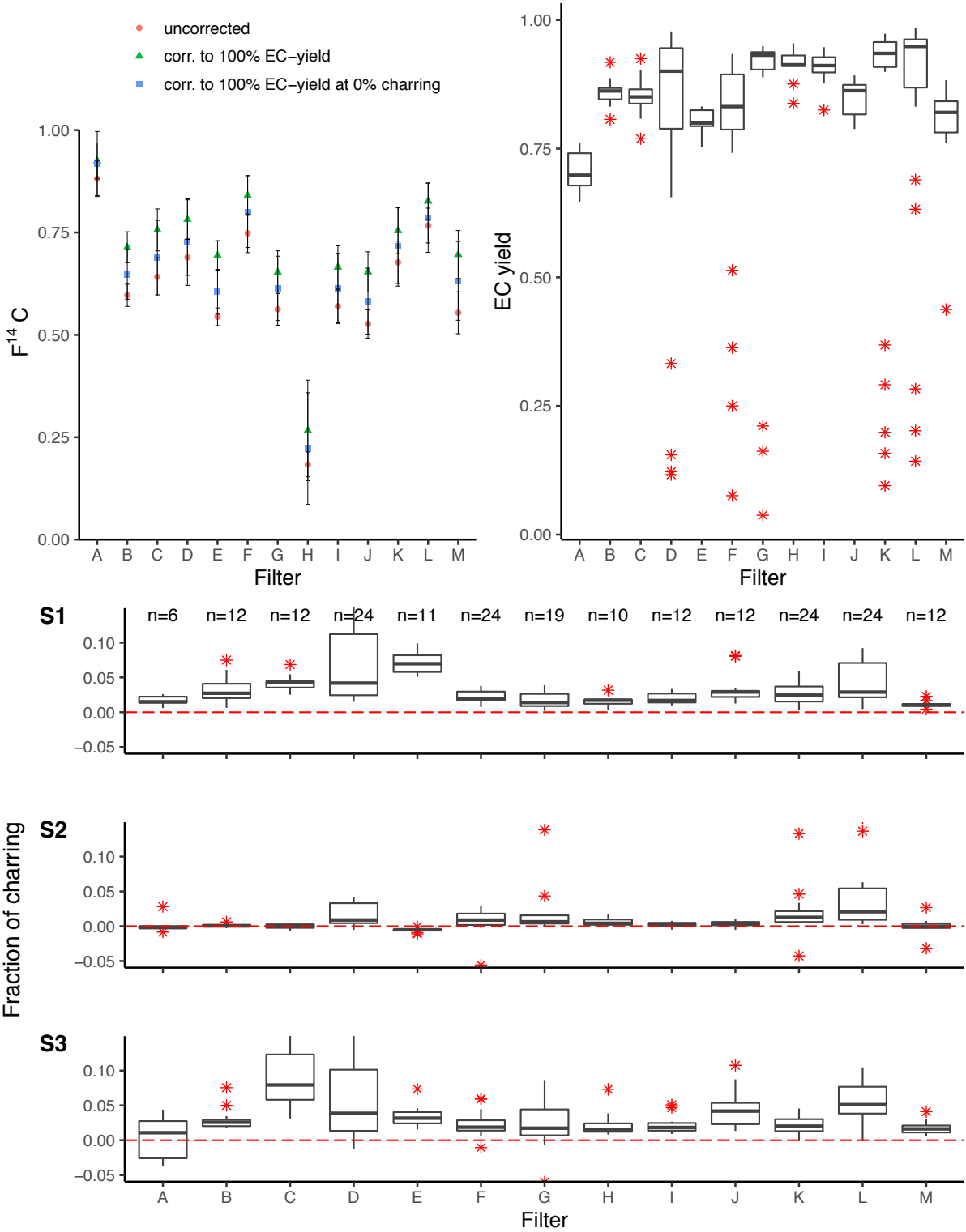
Figure S2: Summary pdf generated by COMPYCALC. The filter names correspond to the filter sampling start and end dates outlined in Table S2.

172

Text S3: COMPYCALC file and folder structure

The COMPYCALC (COMprehensive Yield CALCulation) script (compycalc.R) consists of three subscripts in the zsrc folder (see Fig. S3) for data input and output (yields_calc_io.R), EC yield and charring (yields_calc_ext.R), as well as an extrapolation of the $F^{14}C(EC)$ values to 100% EC yield (corr_100_EC.R). Additionally, the folder contains a generic 4th step file corresponding to the S4 step in the Swiss_4S protocol (cooldown_data.csv). For each sample, the OC/EC analyser raw data files containing the laser transmission signal for each OC removal run need to be in a designated subfolder. When multiple Sunset WINSOC removal runs have been recorded to a single (txt) file, they must be split to individual files, e.g., using the 'file splitter' tool from Sunset-calc (see Chapter 3.10). Additionally, the script requires two input files in the csv format in the main folder (i.e., where the compycalc.R script is located). The first file contains two columns: the first column with the uncorrected $F^{14}C(EC)$ and the second column with the measurement uncertainties. The second csv file contains a single column with the $F^{14}C(OC)$ data. The data input and output script (yields_calc_io.R) loads the OC/EC analyser raw data (txt) files for each sample folder and initiates the calculation with the EC yield and charring script (yields_calc_ext.R). The results written in each sample folder is then read by the main script and forwarded to the second calculation script for the correction to 100% EC yield (corr_100_EC.R). Finally, the $F^{14}C(EC)$ value extrapolated to 100% EC yield corrects for charring in the main script (compycalc.R). After all calculations, a summary data file (csv format) with overall EC yield, the fraction of charring for each OC removal step (S1, S2, S3), the total fraction of charring as well as the raw $F^{14}C(EC)$ (F14C_EC), F14C(EC) extrapolated to 100% EC yield (F14C_EC100), and $F^{14}C(EC)$ extrapolated to 100% EC yield and corrected for charring (F14C_EC100_0_charr) is generated as an output. Additionally, a summary pdf is generated with plots for all $F^{14}C$ results, EC yields, and the fraction of charring for each step (S1, S2, S3). Figure S4 provides an overview scheme of COMPYCALC.

```
compycalc/
├── compycalc.R
├── Filter-A
│   ├── Filter-A-WINSOC-removal-1.txt
│   ├── Filter-A-WINSOC-removal-2.txt
│   ├── Filter-A-WINSOC-removal-3.txt
│   ├── Filter-A-WINSOC-removal-4.txt
│   ├── Filter-A-WINSOC-removal-5.txt
│   └── Filter-A-WINSOC-removal-6.txt
├── Filter-B
│   ├── Filter-B-WINSOC-removal-1.txt
│   ├── Filter-B-WINSOC-removal-2.txt
│   ├── Filter-B-WINSOC-removal-3.txt
│   └── Filter-B-WINSOC-removal-4.txt
└── zsrc/
    ├── yields_calc_io.R
    ├── yields_calc_ext.R
    ├── corr_100_EC.R
    └── cooldown_data.csv
```

Figure S3: Example of the COMPYCALC folder structure with two filters (A, B). 6 individual WINSOC removal run text files are in the folder for filter A and 4 text files for filter B as an example. The COMPYCALC folder must not contain any other file(s), including hidden files.

How does COMPYCALC work?
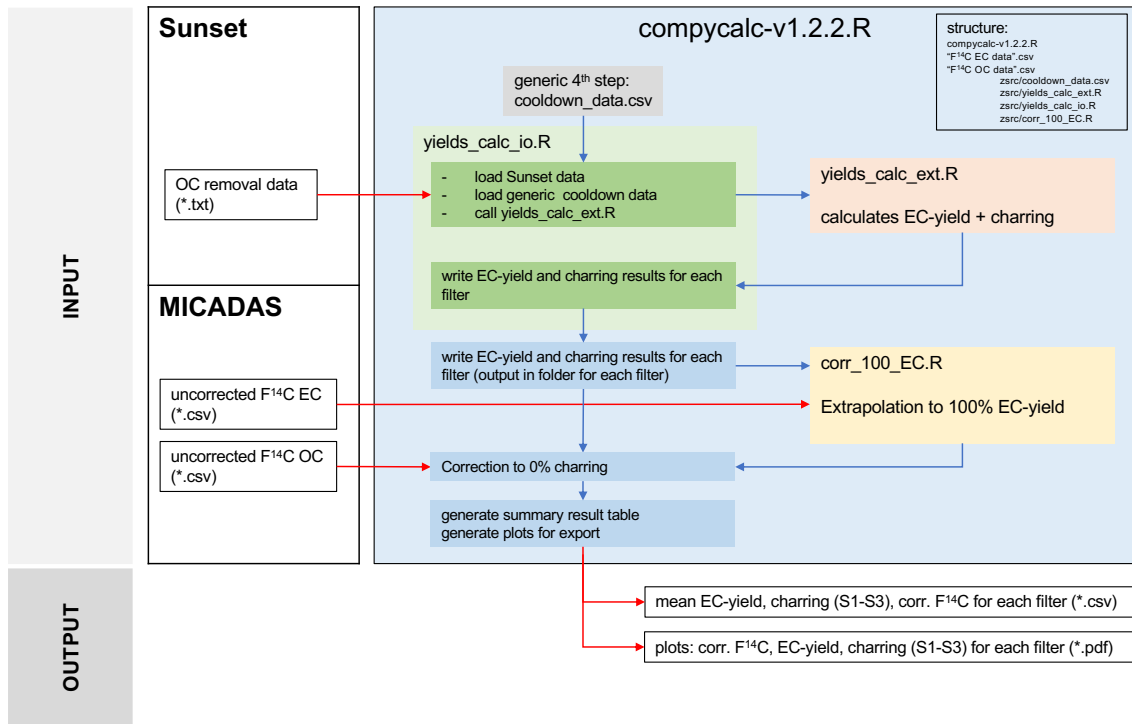
Figure S4: Scheme on how COMPYCALC loads raw data from the Sunset OC/EC analyser and from radiocarbon measurement (e.g., MICADAS AMS) data and performs the EC yield and charring calculation and extrapolation.

Text S4: Additional result tables and figures

Table S4 summarises the filter loadings for each fraction measured at the University of Bern. The circular water-extracted filters were cut in quarters before they were subjected to individual WINSOC removal. Although all filters after WINSOC removal were used for radiocarbon EC measurement, some filters were outliers and not used for EC yield and charring calculation. Table S5 summarises the total number of filters cuts used for WINSOC removal, the number of filters used for calculation, and the outliers. Table S6 and S7 summarise the EC yield and charring for S1, S2, and S3 values before and after filtering (i.e., outliers removed for EC yield and charring calculation). Figure S5 shows the $F^{14}C$ values of EC before and after EC yield and charring corrections were applied.

Table S4: Filter loadings measured in Bern using the Swiss_4S protocol. EC uncorrected denotes the total measured EC including charred OC. The EC corrected value corrects for the losses during WINSOC removal. WINSOC corrected denotes the calculated WINSOC amount without EC loss during WINSOC removal and charring. WSOC was calculated as WSOC = TC − EC_{corr} − $WINSOC_{corr}$. Filters that were pooled for ^{14}C analysis are marked with an asterisk.

Start date	End date	EC uncorr.	EC corr.	WINSOC + EC loss	WINSOC corr.	WSOC	OC
		ng C m^{-3}	ng C m^{-3}	ng C m^{-3}	ng C m^{-3}	ng C m^{-3}	ng C m^{-3}
23 Feb 2017	02 Mar 2017	27	39	70	58	92	150
05 May 2017	15 May 2017	20	23	31	28	70	98
31 May 2017	26 Jun 2017	17	20	93	90	4	93
*08 Sep 2017	28 Sep 2017	8	8	16	12	19	31
28 Sep 2017	06 Oct 2017	53	67	164	151	283	435
*06 Oct 2017	24 Oct 2017	8	5	12	11	19	30
*05 Dec 2017	21 Dec 2017	18	9	18	12	15	27
23 Jan 2018	31 Jan 2018	23	25	54	51	59	110
21 Mar 2018	29 Mar 2018	15	16	38	36	57	93
06 Apr 2018	16 Apr 2018	14	16	37	35	54	89
*12 Jul 2018	30 Jul 2018	6	4	13	13	9	23
*30 Jul 2018	15 Aug 2018	11	8	28	26	70	97
23 Nov 2018	03 Dec 2018	9	12	32	29	26	55

*Pooled filters

Table S5: Total number of filters for each sampling period used for WINSOC removal, the number of filters used by COMPYCALC for calculation after filtering, and the number of outlier filters removed for calculation (total filters – filters used for calculation). Filters that were pooled for ^{14}C analysis are marked with an asterisk.

Start date	End date	Total filters	Filters used for calculation	Outliers
23 Feb 2017	02 Mar 2017	6	4	2
05 May 2017	15 May 2017	12	6	6
31 May 2017	26 Jun 2017	12	9	3
*08 Sep 2017	28 Sep 2017	24	20	4
28 Sep 2017	06 Oct 2017	11	8	3
*06 Oct 2017	24 Oct 2017	24	17	7
*05 Dec 2017	21 Dec 2017	19	14	5
23 Jan 2018	31 Jan 2018	10	6	4
21 Mar 2018	29 Mar 2018	12	10	2
06 Apr 2018	16 Apr 2018	12	10	2
*12 Jul 2018	30 Jul 2018	24	18	6
*30 Jul 2018	15 Aug 2018	24	18	6
23 Nov 2018	03 Dec 2018	12	7	5

*Pooled filters

Table S6: EC yield and charring for S1, S2, S3, and the total charring before filtering, i.e., including outliers Filters that were pooled for ^{14}C analysis are marked with an asterisk.

Start date	End date	EC yield	charring S1	charring S2	charring S3	charring total
23 Feb 2017	02 Mar 2017	0.705	0.017	0.002	-0.013	0.006
05 May 2017	15 May 2017	0.860	0.033	0.001	0.020	0.054
31 May 2017	26 Jun 2017	0.852	0.042	0.000	0.114	0.156
*08 Sep 2017	28 Sep 2017	0.774	0.148	0.055	0.817	1.020
28 Sep 2017	06 Oct 2017	0.803	0.072	-0.006	0.034	0.100
*06 Oct 2017	24 Oct 2017	0.757	0.028	0.008	0.094	0.130
*05 Dec 2017	21 Dec 2017	0.803	0.094	0.112	1.323	1.529
23 Jan 2018	31 Jan 2018	0.911	0.016	0.006	0.023	0.045
21 Mar 2018	29 Mar 2018	0.908	0.020	0.002	0.023	0.045
06 Apr 2018	16 Apr 2018	0.849	0.034	0.003	0.046	0.083
*12 Jul 2018	30 Jul 2018	0.792	0.140	0.039	0.151	0.329
*30 Jul 2018	15 Aug 2018	0.829	0.172	0.074	0.334	0.580
23 Nov 2018	03 Dec 2018	0.788	0.011	0.000	0.018	0.029

*Pooled filters

Table S7: EC yield and charring for S1, S2, S3, and the total charring after filtering, i.e., without outliers as defined in COMPYCALC. Filters that were pooled for ^{14}C analysis are marked with an asterisk.

Start date	End date	EC yield	charring S1	charring S2	charring S3	charring total
23 Feb 2017	02 Mar 2017	0.720	0.015	-0.001	0.013	0.027
05 May 2017	15 May 2017	0.865	0.029	0.001	0.024	0.054
31 May 2017	26 Jun 2017	0.854	0.039	0.000	0.089	0.129
*08 Sep 2017	28 Sep 2017	0.892	0.049	0.012	0.045	0.106
28 Sep 2017	06 Oct 2017	0.803	0.068	-0.005	0.030	0.093
*06 Oct 2017	24 Oct 2017	0.854	0.021	0.011	0.022	0.055
*05 Dec 2017	21 Dec 2017	0.930	0.016	0.006	0.022	0.045
23 Jan 2018	31 Jan 2018	0.921	0.012	0.003	0.014	0.030
21 Mar 2018	29 Mar 2018	0.919	0.020	0.002	0.017	0.039
06 Apr 2018	16 Apr 2018	0.859	0.025	0.004	0.035	0.064
*12 Jul 2018	30 Jul 2018	0.941	0.028	0.014	0.021	0.062
*30 Jul 2018	15 Aug 2018	0.951	0.037	0.024	0.054	0.115
23 Nov 2018	03 Dec 2018	0.818	0.010	0.002	0.014	0.026
*Pooled filters						
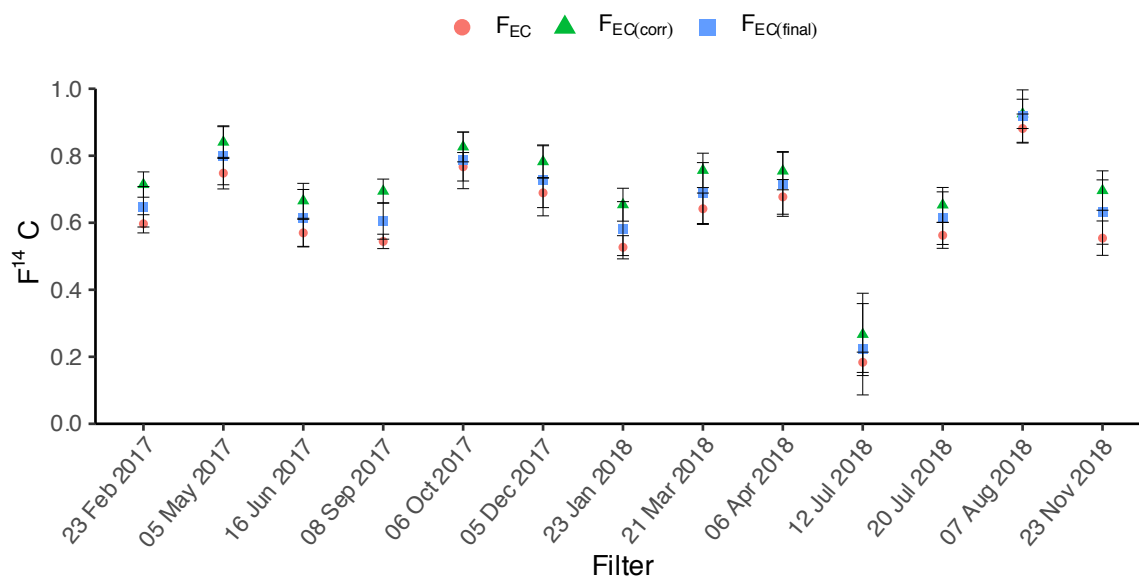
Figure S5: F^{14}C(EC) values for the EC yield and charring correction. Starting from the initial EC value (F$_{EC}$), COMPYCALC computes the yield extrapolated EC value (F$_{EC(corr)}$) and with the charring correction, the final corrected EC value is calculated (F$_{EC(final)}$).
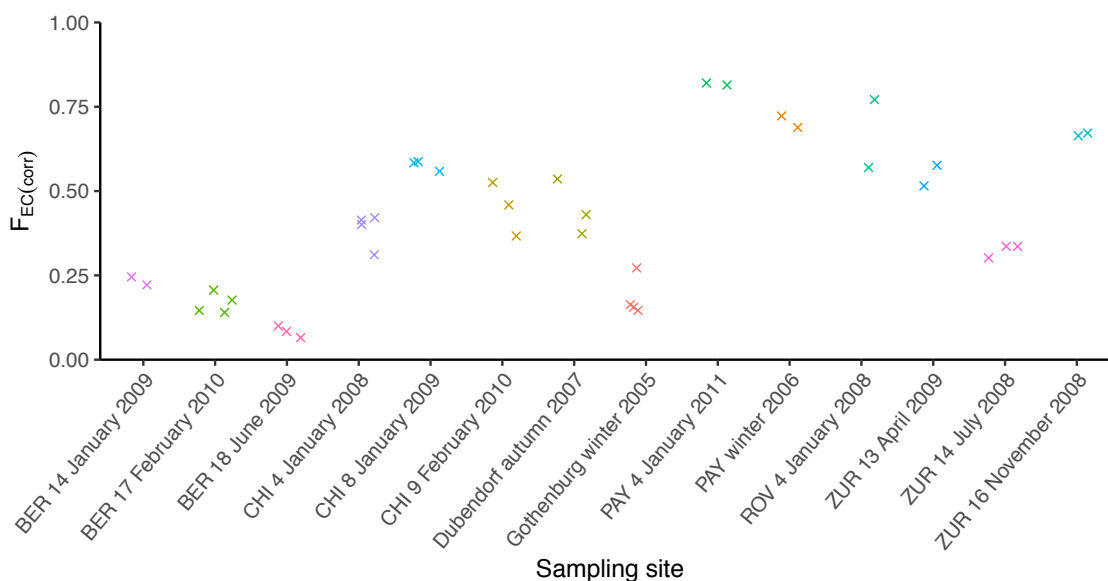
Figure S6: Extrapolation and correction jitter plot of the data from Zotter et al. (2014) with the Arrhenius approach. Figure S2 of Zotter et al. (2014) shows the Fraction Modern of EC as a function of the EC yield from multiple sites. Here the thermal desorption model corrected Fraction Modern for each site is shown. In an optimal case, the $F_{EC(corr)}$ should be independent of the EC yield and lead to the same $F_{EC(corr)}$ value. We estimate an uncertainty of 0.1. The abbreviation BER refers to the sampling station in Bern, Switzerland, CHI to Chiasso, Switzerland, PAY to Payerne, Switzerland, ROV to Roveredo, Switzerland, and ZUR to Zurich, Switzerland. Sampling site details can be found in Zotter et al. (2014) Table 1.
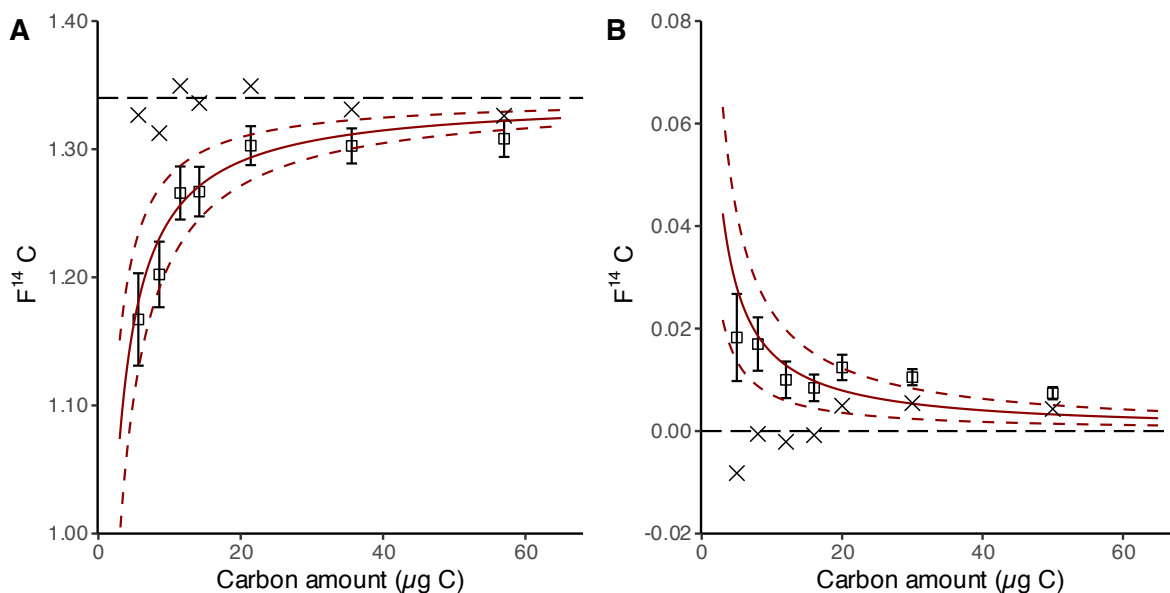
Figure S7: Constant contamination of the chemical wet oxidation (procedural blank). Measured radiocarbon data plotted as $F^{14}C$ with measurement uncertainty versus sample size (μg C) for modern OxII standard (A) and fossil NaAc standard (B). The solid dark red lines with the 1σ uncertainty ranges (dashed) are the drift model curves, the crosses the drift corrected $F^{14}C$ values.

Text S5: Constant contamination chemical wet oxidation

OxII (SRM 4990 C) and fossil NaAc (Szidat et al., 2014) standards were used to prepare ~1000 ppm stock solutions in ultrapure water. An aliquot of the standard stock solutions equivalent to 3.5–57.0 µg C and 5.0–50.0 µg C for OxII and NaAc, respectively were added to an Exetainer vial (12 mL) containing ultrapure water (5.0 ± 0.2 mL). Inorganic carbonaceous impurities were removed by purging with helium. The chemical wet oxidation was performed as described in Chapter 2.4. The constant contamination of 0.9 ± 0.2 µg C with $F^{14}C = 0.20 \pm 0.08$ was determined by a drift model (Salazar et al., 2015; Hanke et al., 2017) and shown in Fig. S7. Constrains 0 to 1 for the Fraction Modern (R_S) and of 0.1–6 µg C for the mass of the contaminant (m_k) were made, then the drift correction minimised for both m_k and R_S within the given constrains.

References

Hanke, U. M., Wacker, L., Haghipour, N., Schmidt, M. W. I., Eglinton, T. I., and McIntyre, C. P.: Comprehensive radiocarbon analysis of benzene polycarboxylic acids (BPCAs) derived from pyrogenic carbon in environmental samples, Radiocarbon, 59, 1103–1116, https://doi.org/10.1017/RDC.2017.44, 2017.

Salazar, G., Zhang, Y. L., Agrios, K., and Szidat, S.: Development of a method for fast and automatic radiocarbon measurement of aerosol samples by online coupling of an elemental analyzer with a MICADAS AMS, Nucl. Instruments Methods Phys. Res. Sect. B Beam Interact. with Mater. Atoms, 361, 163–167, https://doi.org/10.1016/j.nimb.2015.03.051, 2015.

Szidat, S., Salazar, G. A., Vogel, E., Battaglia, M., Wacker, L., Synal, H.-A., and Türler, A.: 14C Analysis and Sample Preparation at the new Bern Laboratory for the Analysis of Radiocarbon with AMS (LARA), Radiocarbon, 56, 561–566, https://doi.org/10.2458/56.17457, 2014.

Zotter, P., Ciobanu, V. G., Zhang, Y. L., El-Haddad, I., Macchia, M., Daellenbach, K. R., Salazar, G. A., Huang, R.-J., Wacker, L., Hueglin, C., Piazzalunga, A., Fermo, P., Schwikowski, M., Baltensperger, U., Szidat, S., and Prévôt, A. S. H.: Radiocarbon analysis of elemental and organic carbon in Switzerland during winter-smog episodes from 2008 to 2012 – Part 1: Source apportionment and spatial variability, Atmos. Chem. Phys., 14, 13551–13570, https://doi.org/10.5194/acp-14-13551-2014, 2014.

6.2 Supplementary material for Chapter 3

Table S1: Summary of radiocarbon measurements for NIST SRM 1649a standard, and all aerosol filter measurements from the site Råö (Sweden), Mexico City (Mexico), and Delhi (India). The Råö (Sweden) measurements from Szidat et al. (2009) are also included.

Site	Start date	End date	Oxalate F^{14}C	Oxalate fNF	WSOC F^{14}C	WSOC fNF	TC F^{14}C	TC fNF	EC uncorr. F^{14}C	EC corr. F^{14}C	EC fNF
NIST SRM 1649a	1976	1977	0.90 ± 0.01	0.66 ± 0.01	0.83 ± 0.01	0.61 ± 0.01					
NIST SRM 1649a	1976	1977	0.89 ± 0.01	0.66 ± 0.01	0.81 ± 0.01	0.60 ± 0.01					
NIST SRM 1649a	1976	1977	0.88 ± 0.01	0.65 ± 0.01	0.85 ± 0.01	0.63 ± 0.01					
NIST SRM 1649a	1976	1977	0.89 ± 0.01	0.66 ± 0.01	0.85 ± 0.01	0.63 ± 0.01					
Råö, Sweden	11 Feb 2005	14 Feb 2005	0.81 ± 0.06	0.74 ± 0.06	0.72 ± 0.01	0.66 ± 0.01	0.63 ± 0.02	0.56 ± 0.02			
Råö, Sweden	14 Feb 2005	18 Feb 2005	0.84 ± 0.03	0.76 ± 0.03	0.72 ± 0.01	0.66 ± 0.01	0.60 ± 0.01	0.54 ± 0.01			
Råö, Sweden	18 Feb 2005	25 Feb 2005	1.00 ± 0.02	0.91 ± 0.01	0.81 ± 0.01	0.73 ± 0.01	0.67 ± 0.01	0.60 ± 0.01			
Råö, Sweden	25 Feb 2005	04 Mar 2005	1.01 ± 0.03	0.91 ± 0.03	0.83 ± 0.01	0.76 ± 0.01	0.78 ± 0.01	0.71 ± 0.01			
Raö, Sweden*	14 Feb 2005	18 Feb 2005			0.75 ± 0.05	0.68 ± 0.05			0.42 ± 0.06		0.37 ± 0.05
Raö, Sweden*	18 Feb 2005	25 Feb 2005			0.87 ± 0.04	0.79 ± 0.04			0.35 ± 0.03		0.31 ± 0.03
Mexico City, Mexico	21 Mar 2006	22 Mar 2006	0.77 ± 0.01	0.70 ± 0.01	0.76 ± 0.01	0.69 ± 0.01	0.56 ± 0.01	0.51 ± 0.01	0.04 ± 0.01	0.13 ± 0.06	0.11 ± 0.05
Mexico City, Mexico	22 Mar 2006	23 Mar 2006	0.72 ± 0.01	0.66 ± 0.01	0.70 ± 0.01	0.64 ± 0.01	0.42 ± 0.01	0.38 ± 0.01	0.05 ± 0.00	0.08 ± 0.06	0.07 ± 0.05
Mexico City, Mexico	29 Mar 2006	30 Mar 2006	0.59 ± 0.01	0.54 ± 0.01	0.55 ± 0.01	0.50 ± 0.01	0.29 ± 0.01	0.27 ± 0.01	0.16 ± 0.00	0.22 ± 0.04	0.19 ± 0.04
Delhi, India	10 Jan 2018	10 Jan 2018	0.84 ± 0.02	0.80 ± 0.02	0.83 ± 0.01	0.79 ± 0.01	0.73 ± 0.01	0.69 ± 0.01	0.46 ± 0.02	0.55 ± 0.04	0.51 ± 0.03
Delhi, India	10 Jan 2018	10 Jan 2018	0.88 ± 0.02	0.84 ± 0.02	0.89 ± 0.02	0.85 ± 0.02	0.74 ± 0.01	0.70 ± 0.01	0.54 ± 0.02	0.59 ± 0.04	0.55 ± 0.03
Delhi, India	22 Jan 2018	22 Jan 2018	0.77 ± 0.02	0.73 ± 0.02	0.77 ± 0.01	0.73 ± 0.01	0.62 ± 0.01	0.59 ± 0.01	0.26 ± 0.02	0.33 ± 0.05	0.30 ± 0.05
Delhi, India	22 Jan 2018	22 Jan 2018			0.86 ± 0.02	0.82 ± 0.02	0.68 ± 0.01	0.64 ± 0.01	0.37 ± 0.02	0.43 ± 0.04	0.40 ± 0.04
Delhi, India	03 Feb 2018	03 Feb 2018			0.73 ± 0.01	0.70 ± 0.01	0.57 ± 0.01	0.54 ± 0.01	0.34 ± 0.02	0.43 ± 0.04	0.40 ± 0.04
Delhi, India	03 Feb 2018	03 Feb 2018	0.79 ± 0.02	0.75 ± 0.02	0.81 ± 0.01	0.77 ± 0.01	0.65 ± 0.01	0.61 ± 0.01	0.37 ± 0.02	0.45 ± 0.04	0.42 ± 0.04
Delhi, India	16 Feb 2018	16 Feb 2018	0.68 ± 0.02	0.65 ± 0.02	0.75 ± 0.02	0.72 ± 0.02	0.65 ± 0.00	0.61 ± 0.00	0.35 ± 0.02	0.43 ± 0.04	0.40 ± 0.04

Delhi, India	16 Feb 2018	16 Feb 2018	0.78 ± 0.02	0.75 ± 0.02	0.84 ± 0.02	0.80 ± 0.02	0.67 ± 0.01	0.64 ± 0.01	0.34 ± 0.02	0.40 ± 0.04	0.37 ± 0.04
Delhi, India	12 Mar 2018	12 Mar 2018	0.69 ± 0.02	0.65 ± 0.02	0.69 ± 0.01	0.66 ± 0.01	0.61 ± 0.02	0.57 ± 0.02	0.35 ± 0.02	0.44 ± 0.05	0.41 ± 0.04
Delhi, India	12 Mar 2018	12 Mar 2018	0.75 ± 0.02	0.71 ± 0.02	0.76 ± 0.02	0.73 ± 0.02	0.59 ± 0.01	0.56 ± 0.01	0.30 ± 0.02	0.38 ± 0.04	0.36 ± 0.04
Delhi, India	30 Mar 2018	31 Mar 2018	0.80 ± 0.02	0.76 ± 0.02	0.83 ± 0.01	0.79 ± 0.01	0.67 ± 0.00	0.64 ± 0.00	0.46 ± 0.02	0.52 ± 0.04	0.49 ± 0.03
Delhi, India	05 Apr 2018	06 Apr 2018	0.72 ± 0.01	0.68 ± 0.01	0.74 ± 0.01	0.70 ± 0.01	0.60 ± 0.01	0.57 ± 0.01	0.44 ± 0.02	0.52 ± 0.04	0.48 ± 0.03
Delhi, India	11 Apr 2018	12 Apr 2018	0.63 ± 0.01	0.60 ± 0.01	0.66 ± 0.01	0.63 ± 0.01	0.56 ± 0.01	0.53 ± 0.01	0.29 ± 0.02	0.38 ± 0.05	0.35 ± 0.04
Delhi, India	17 Apr 2018	18 Apr 2018	0.68 ± 0.01	0.65 ± 0.01	0.68 ± 0.01	0.65 ± 0.01	0.51 ± 0.01	0.49 ± 0.01	0.43 ± 0.02	0.52 ± 0.04	0.48 ± 0.04
Delhi, India	23 Apr 2018	24 Apr 2018	0.72 ± 0.01	0.69 ± 0.01	0.77 ± 0.01	0.74 ± 0.01	0.62 ± 0.02	0.59 ± 0.02	0.38 ± 0.02	0.50 ± 0.04	0.47 ± 0.03
Delhi, India	29 Apr 2018	30 Apr 2018	0.77 ± 0.01	0.73 ± 0.01	0.78 ± 0.02	0.74 ± 0.02	0.63 ± 0.04	0.60 ± 0.04	0.40 ± 0.02	0.48 ± 0.04	0.44 ± 0.04
Delhi, India	05 May 2018	06 May 2018	0.74 ± 0.01	0.71 ± 0.01	0.78 ± 0.00	0.75 ± 0.00	0.56 ± 0.04	0.53 ± 0.04	0.46 ± 0.02	0.57 ± 0.04	0.53 ± 0.04
Delhi, India	11 May 2018	12 May 2018	0.81 ± 0.01	0.78 ± 0.01	0.85 ± 0.00	0.81 ± 0.00	0.62 ± 0.04	0.59 ± 0.04	0.39 ± 0.02	0.47 ± 0.04	0.44 ± 0.04
Delhi, India	17 May 2018	18 May 2018	0.72 ± 0.01	0.69 ± 0.01	0.73 ± 0.01	0.70 ± 0.01	0.49 ± 0.05	0.46 ± 0.05	0.34 ± 0.02	0.46 ± 0.04	0.43 ± 0.04
Delhi, India	23 May 2018	24 May 2018	0.74 ± 0.01	0.70 ± 0.01	0.75 ± 0.00	0.72 ± 0.00	0.54 ± 0.00	0.52 ± 0.00	0.32 ± 0.02	0.41 ± 0.04	0.38 ± 0.04
Delhi, India	29 May 2018	30 May 2018	0.75 ± 0.01	0.72 ± 0.01	0.72 ± 0.01	0.68 ± 0.01	0.54 ± 0.06	0.51 ± 0.06	0.31 ± 0.02	0.39 ± 0.04	0.36 ± 0.04
Delhi, India	28 Feb 2018	28 Feb 2018			0.70 ± 0.00	0.67 ± 0.00	0.58 ± 0.01	0.55 ± 0.01	0.30 ± 0.02	0.36 ± 0.05	0.34 ± 0.04
Delhi, India	28 Feb 2018	28 Feb 2018	0.69 ± 0.01	0.66 ± 0.01	0.70 ± 0.03	0.67 ± 0.03	0.51 ± 0.01	0.49 ± 0.01	0.23 ± 0.02	0.26 ± 0.06	0.24 ± 0.05

* Values from Szidat et al. (2009)

Table S2: Summary of radiocarbon measurements for Kraków (Poland) filters.

Site	Start date	End date	WSOC F^{14}C	WSOC fNF	TC F^{14}C	TC fNF	EC uncorr. F^{14}C	EC corr. F^{14}C	EC fNF	WINSOC F^{14}C	WINSOC fNF
Kraków, Poland	01 Feb 2018	02 Feb 2018	0.72 ± 0.01	0.68 ± 0.01	0.48 ± 0.02	0.46 ± 0.02	0.18 ± 0.01	0.23 ± 0.05	0.21 ± 0.05	0.47 ± 0.01	0.44 ± 0.01
Kraków, Poland	02 Feb 2018	03 Feb 2018	0.63 ± 0.01	0.60 ± 0.01	0.42 ± 0.02	0.40 ± 0.02	0.14 ± 0.03	0.17 ± 0.07	0.16 ± 0.07	0.36 ± 0.01	0.34 ± 0.01
Kraków, Poland	10 Feb 2018	11 Feb 2018			0.46 ± 0.02	0.43 ± 0.02	0.17 ± 0.03	0.22 ± 0.07	0.20 ± 0.06	0.36 ± 0.01	0.34 ± 0.01
Kraków, Poland	11 Feb 2018	12 Feb 2018	0.59 ± 0.01	0.56 ± 0.01	0.45 ± 0.02	0.42 ± 0.02	0.13 ± 0.03	0.16 ± 0.08	0.15 ± 0.08	0.37 ± 0.01	0.35 ± 0.01
Kraków, Poland	25 Feb 2018	26 Feb 2018	0.61 ± 0.01	0.58 ± 0.01						0.41 ± 0.01	0.39 ± 0.01
Kraków, Poland	26 Feb 2018	27 Feb 2018	0.61 ± 0.01	0.58 ± 0.01	0.47 ± 0.02	0.45 ± 0.02	0.12 ± 0.04	0.15 ± 0.10	0.14 ± 0.09	0.39 ± 0.01	0.37 ± 0.01
Kraków, Poland	02 Mar 2018	03 Mar 2018	0.68 ± 0.01	0.65 ± 0.01						0.51 ± 0.01	0.48 ± 0.01
Kraków, Poland	03 Mar 2018	04 Mar 2018	0.67 ± 0.01	0.64 ± 0.01	0.57 ± 0.02	0.54 ± 0.02	0.25 ± 0.02	0.29 ± 0.06	0.27 ± 0.05	0.46 ± 0.01	0.44 ± 0.01
Kraków, Poland	09 Mar 2018	10 Mar 2018	0.63 ± 0.01	0.60 ± 0.01	0.41 ± 0.02	0.39 ± 0.02	0.19 ± 0.01	0.24 ± 0.05	0.22 ± 0.05	0.36 ± 0.01	0.34 ± 0.01
Kraków, Poland	10 Mar 2018	11 Mar 2018	0.64 ± 0.01	0.61 ± 0.01	0.41 ± 0.02	0.39 ± 0.02	0.18 ± 0.01	0.21 ± 0.06	0.20 ± 0.05	0.36 ± 0.01	0.34 ± 0.01
Kraków, Poland	12 May 2018	13 May 2018	0.72 ± 0.01	0.69 ± 0.01	0.67 ± 0.02	0.64 ± 0.02	0.09 ± 0.07	0.10 ± 0.14	0.09 ± 0.13	0.70 ± 0.03	0.67 ± 0.03
Kraków, Poland	13 May 2018	14 May 2018	0.71 ± 0.01	0.68 ± 0.01						0.68 ± 0.04	0.65 ± 0.03
Kraków, Poland	21 Jun 2018	22 Jun 2018	0.71 ± 0.01	0.68 ± 0.01						0.45 ± 0.05	0.43 ± 0.05
Kraków, Poland	22 Jun 2018	23 Jun 2018	0.62 ± 0.01	0.60 ± 0.01						0.68 ± 0.04	0.64 ± 0.04
Kraków, Poland	23 Jul 2018	24 Jul 2018	0.86 ± 0.01	0.82 ± 0.01						0.72 ± 0.03	0.69 ± 0.03
Kraków, Poland	24 Jul 2018	25 Jul 2018	0.91 ± 0.01	0.87 ± 0.01						0.55 ± 0.03	0.53 ± 0.03
Kraków, Poland	24 Aug 2018	25 Aug 2018	0.83 ± 0.01	0.79 ± 0.01	0.75 ± 0.02	0.71 ± 0.02	0.06 ± 0.03	0.08 ± 0.09	0.07 ± 0.09	0.72 ± 0.03	0.69 ± 0.03
Kraków, Poland	25 Aug 2018	26 Aug 2018	0.81 ± 0.01	0.77 ± 0.01						0.70 ± 0.04	0.66 ± 0.03
Kraków, Poland	17 Sep 2018	18 Sep 2018	0.76 ± 0.01	0.72 ± 0.01	0.59 ± 0.02	0.56 ± 0.02	0.04 ± 0.03	0.05 ± 0.09	0.04 ± 0.08	0.64 ± 0.03	0.61 ± 0.03
Kraków, Poland	18 Sep 2018	19 Sep 2018	0.81 ± 0.01	0.77 ± 0.01	0.59 ± 0.02	0.56 ± 0.02	0.08 ± 0.02	0.11 ± 0.07	0.10 ± 0.06	0.55 ± 0.02	0.52 ± 0.02

Table S3: Reference values for biogenic, biomass burning (bb) material as well as the reference values for total carbon (TC), organic carbon (OC), water-soluble organic carbon (WSOC), water-insoluble organic carbon (WINSOC), oxalate, and elemental carbon (EC) fractions.

Campaign	Year of sampling	Ref (biogenic) $F^{14}C$	Ref (bb) $F^{14}C$	Ref (TC) $F^{14}C$	Ref (OC, WSOC, WINSOC, oxalate) $F^{14}C$	Ref (EC) $F^{14}C$
Råö, Sweden; winter	2005	1.061 ± 0.015	1.141 ± 0.050	1.109 ± 0.031	1.101 ± 0.026	1.141 ± 0.050
Mexico City, Mexico; spring	2006	1.060 ± 0.015	1.135 ± 0.050	1.105 ± 0.031	1.097 ± 0.026	1.135 ± 0.050
Delhi, India; winter/spring	2018	1.017 ± 0.015	1.080 ± 0.050	1.055 ± 0.031	1.049 ± 0.026	1.080 ± 0.050
Kraków, Poland; winter/summer	2018	1.017 ± 0.015	1.080 ± 0.050	1.055 ± 0.031	1.049 ± 0.026	1.080 ± 0.050
SRM 1649a full year	1976.5	1.346 ± 0.015	1.355 ± 0.050	1.352 ± 0.031	1.351 ± 0.026	1.355 ± 0.050

Table S4: Summary of the oxalate concentration and amount of oxalate used for each radiocarbon analysis. A mean oxalate amount of 25 ± 18 µg C (median = 21) was used. A total of 34 oxalate samples were analysed. Additionally, the oxalate to TC and oxalate to WSOC ratio is shown.

Site	Start date	End date	Oxalate* µg C	Oxalate** ng m⁻³	Oxalate/TC %	Oxalate/WSOC %
NIST SRM 1649a	1976	1977	20			
NIST SRM 1649a	1976	1977	21			
NIST SRM 1649a	1976	1977	19			
NIST SRM 1649a	1976	1977	24			
Raö, Sweden	11 Feb 2005	14 Feb 2005	2	6	0.6	1.8
Raö, Sweden	14 Feb 2005	18 Feb 2005	5	13	0.8	2.1
Raö, Sweden	18 Feb 2005	25 Feb 2005	15	24	1.5	6.5
Raö, Sweden	25 Feb 2005	04 Mar 2005	5	4	0.4	1.6
Mexico City, Mexico	21 Mar 2006	22 Mar 2006	59	1528	0.9	15.8
Mexico City, Mexico	22 Mar 2006	23 Mar 2006	45	1198	0.6	10.7
Mexico City, Mexico	29 Mar 2006	30 Mar 2006	38	921	0.4	11.3
Delhi, India	10 Jan 2018	10 Jan 2018	54	1174	0.9	3.2
Delhi, India	10 Jan 2018	10 Jan 2018	59	1046	0.6	3.3
Delhi, India	22 Jan 2018	22 Jan 2018	44	952	0.6	2.4
Delhi, India	22 Jan 2018	22 Jan 2018	49	900	0.5	1.6
Delhi, India	03 Feb 2018	03 Feb 2018	10	209	0.2	1.2
Delhi, India	03 Feb 2018	03 Feb 2018	19	338	0.4	1.4
Delhi, India	16 Feb 2018	16 Feb 2018	7	149	0.2	0.5
Delhi, India	16 Feb 2018	16 Feb 2018	10	179	0.2	0.8
Delhi, India	12 Mar 2018	12 Mar 2018	9	199	0.5	2.3
Delhi, India	12 Mar 2018	12 Mar 2018	22	408	0.5	2.3
Delhi, India	30 Mar 2018	31 Mar 2018	37	808	0.3	0.9
Delhi, India	05 Apr 2018	06 Apr 2018	24	454	0.5	2.1
Delhi, India	11 Apr 2018	12 Apr 2018	4	35	0.5	2.0
Delhi, India	17 Apr 2018	18 Apr 2018	10	103	0.4	1.5
Delhi, India	23 Apr 2018	24 Apr 2018	15	147	0.1	0.4
Delhi, India	29 Apr 2018	30 Apr 2018	23	225	0.3	1.0
Delhi, India	05 May 2018	06 May 2018	21	211	0.3	0.9
Delhi, India	11 May 2018	12 May 2018	71	709	0.6	1.5
Delhi, India	17 May 2018	18 May 2018	22	215	0.4	1.6
Delhi, India	23 May 2018	24 May 2018	21	208	0.8	2.5
Delhi, India	29 May 2018	30 May 2018	13	132	0.4	1.9
Delhi, India	28 Feb 2018	28 Feb 2018	26	271	0.4	2.6
Delhi, India	28 Feb 2018	28 Feb 2018	32	313	0.3	1.3

Kraków, Poland	01 Feb 2018	02 Feb 2018			
Kraków, Poland	02 Feb 2018	03 Feb 2018	6	0.01	0.03
Kraków, Poland	10 Feb 2018	11 Feb 2018			
Kraków, Poland	11 Feb 2018	12 Feb 2018	6	0.01	0.02
Kraków, Poland	25 Feb 2018	26 Feb 2018			
Kraków, Poland	26 Feb 2018	27 Feb 2018	6	0.02	0.03
Kraków, Poland	02 Mar 2018	03 Mar 2018			
Kraków, Poland	03 Mar 2018	04 Mar 2018	11	0.02	0.03
Kraków, Poland	09 Mar 2018	10 Mar 2018			
Kraków, Poland	10 Mar 2018	11 Mar 2018	7	0.01	0.01
Kraków, Poland	12 May 2018	13 May 2018			
Kraków, Poland	13 May 2018	14 May 2018	13	0.07	0.09
Kraków, Poland	21 Jun 2018	22 Jun 2018			
Kraków, Poland	22 Jun 2018	23 Jun 2018	6	0.07	0.11
Kraków, Poland	23 Jul 2018	24 Jul 2018			
Kraków, Poland	24 Jul 2018	25 Jul 2018	18	0.10	0.14
Kraków, Poland	24 Aug 2018	25 Aug 2018			
Kraków, Poland	25 Aug 2018	26 Aug 2018	16	0.09	0.14
Kraków, Poland	17 Sep 2018	18 Sep 2018			
Kraków, Poland	18 Sep 2018	19 Sep 2018	15	0.07	0.12

*Amount for AMS measurement

**two subsequent filters pooled for Kraków
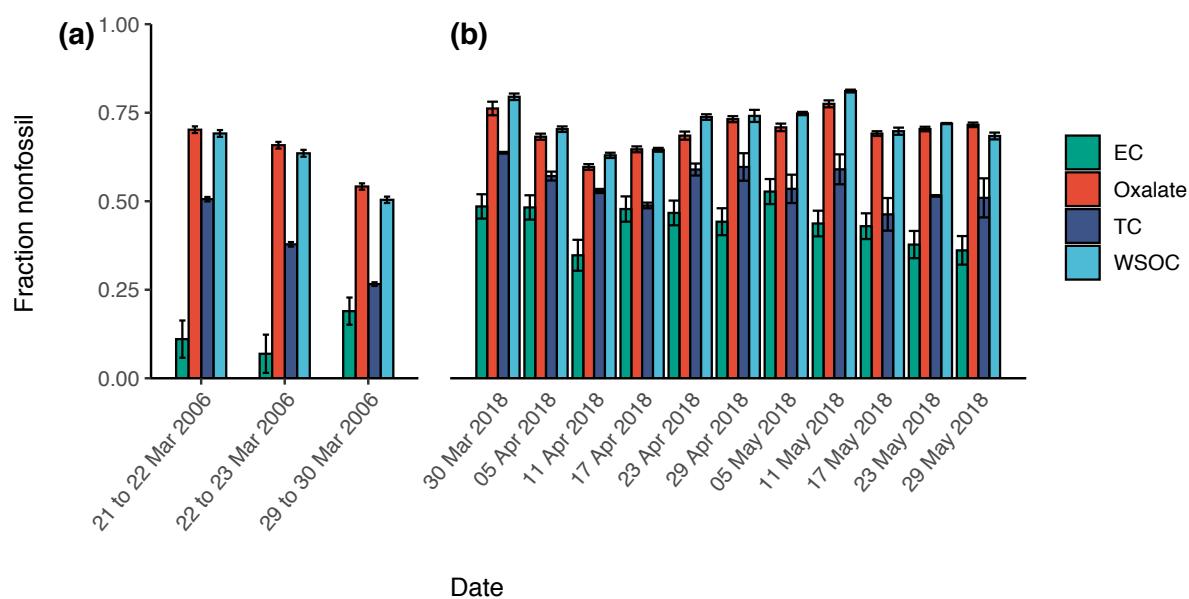
Figure S1: Fraction nonfossil of EC, oxalate, TC and WSOC. a) Mexico City, Mexico. b) Daily filter from Delhi, India.
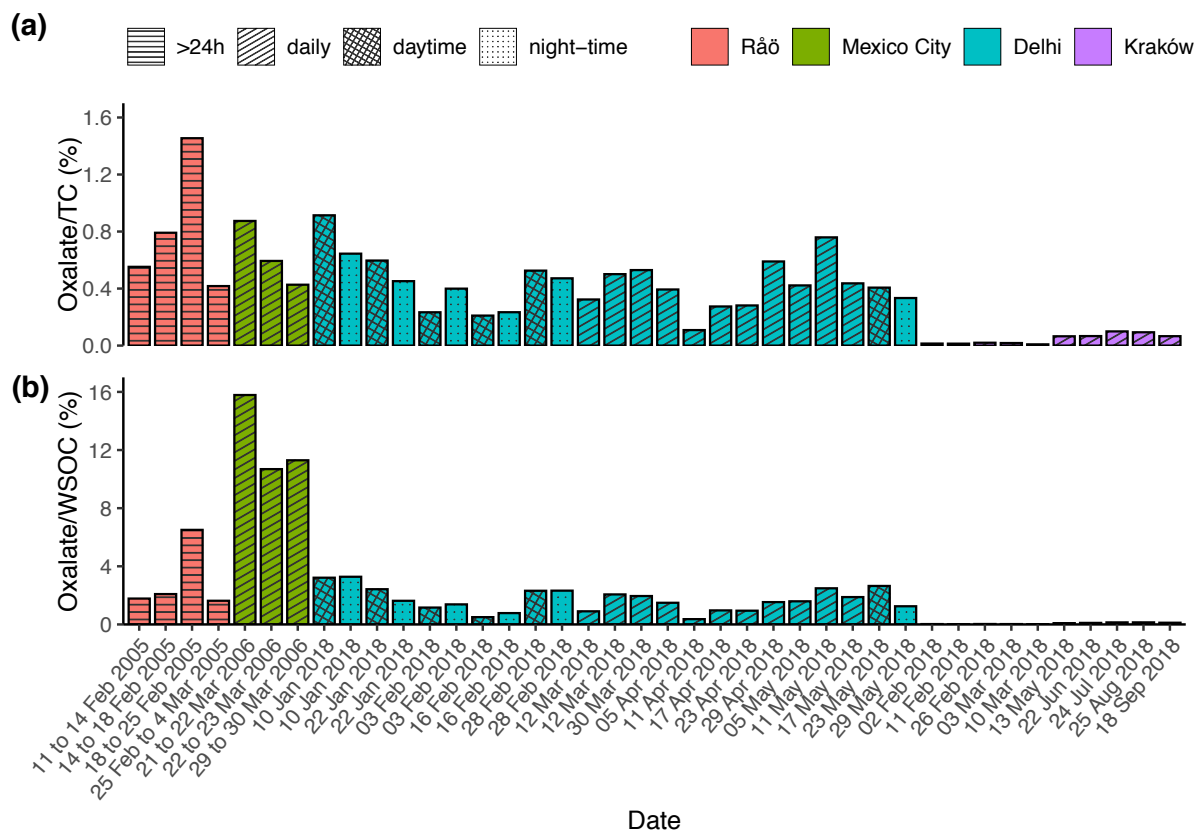
Figure S2: Oxalate/TC ratio (a) and oxalate/WSOC ratio (b) for each site.
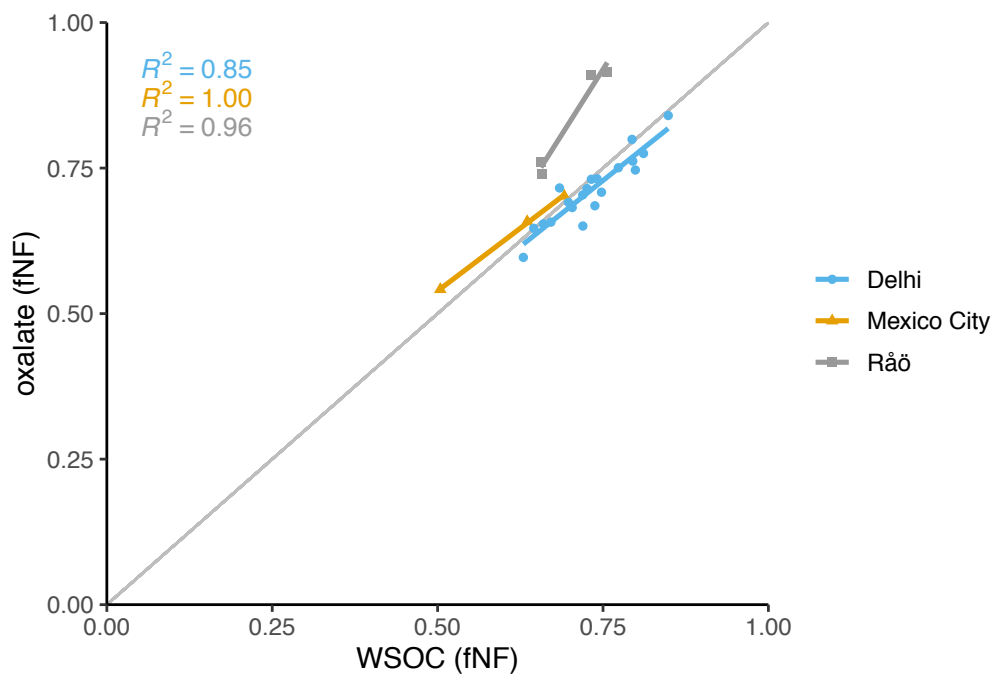
Figure S3: The non-fossil fraction of oxalate vs. WSOC for each site.
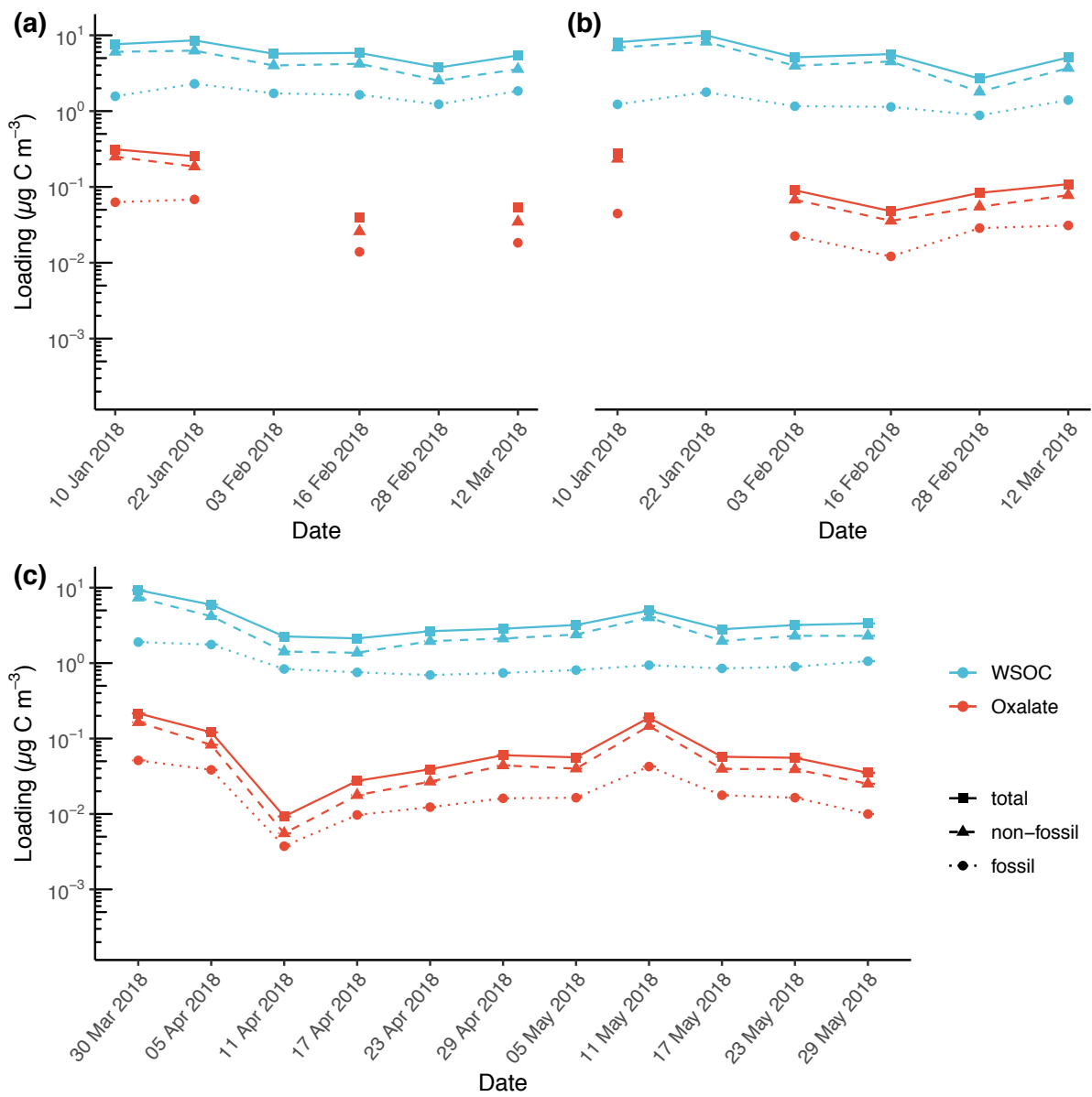
Figure S4: Total, non-fossil, and fossil loading (log scale) of WSOC and oxalate a) for day b) night, and c) 24 h in Delhi.
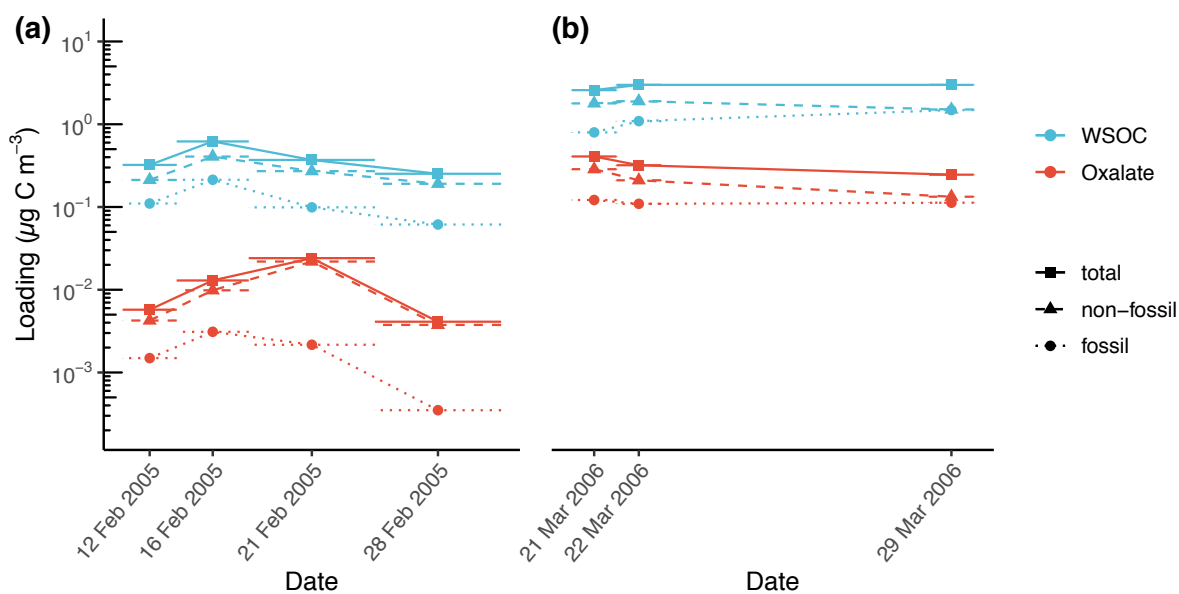
Figure S5: Total, non-fossil, and fossil loading (log scale) of WSOC and oxalate for a) Råö and b) Mexico City with sampling duration on x-axis.

References

Szidat, S., Ruff, M., Perron, N., Wacker, L., Synal, H., Hallquist, M., Shannigrahi, S., Yttri, K. E., Dye, C., and Simpson, D.: Fossil and non-fossil sources of organic carbon (OC) and elemental carbon (EC) in Göteborg, Sweden, Atmos. Chem. Phys., 9, 1521–1535, https://doi.org/10.5194/acp-9-1521-2009, 2009.

6.3 Supplementary material for Chapter 4

Text S1 Site

The Norwegian Troll station is a year-round manned station with a blue ice airfield ~7 km North of the station. The station is located on a nunatak (i.e., rock ground) at 1275 m.a.s.l and the Trollhaugen Observatory (72°00'42"S, 02°32'06"E, 1553 m.a.s.l.) for sampling approximately 2 km east of the station[1]. Input from in-situ on-line nephelometer (TSI 3563) was used to differentiate Antarctic baseline aerosol (ABA) from non–ABA. As defined by Fiebig et al.[2], any value smaller than the threshold of 4 weeks running 5th percentile × 2.5 of the aerosols scattering coefficient (σsp) measured at 550 nm was considered ABA, whereas values above this was defined as non–ABA. Harsh weather conditions destroy inserted filters; thus, sampling was omitted at wind speeds > 10 m s^{-1}, ABA and non–ABA aerosols were collected using two separate high-volume samplers (Digitel DHA-80) with a PM_{10} inlet. To account for positive sampling artefacts caused by semi volatile organic compounds (SVOC), sampling was performed with double quartz fibre filters (Pallflex 2500)[3].

A schematic drawing of the sampling set up is shown in Figure S1. The nephelometer and high-volume samplers' inlets were placed 5.5 metres above the ground.

All quartz fibre filters were preheated (850°C; 3 h) to remove organic impurities and were picked from the same batch number to minimize differences in the adsorptive capacity, which otherwise could bias the positive artefact estimate[4]. Double quartz fibre filters mounted in filter holders were inserted into custom-made stainless-steel containers, then wrapped in bubble wrap and placed in double polyethylene zip-lock bags for storage (−20°C), transport and to prevent contamination. Back and forth to Antarctica, the parcels were placed in an air-tight bag. Filter holders and stainless-steel containers were washed with soap and soaked in water (24 h), then rinsed using pentane, acetone, methanol, and ultrapure water (Milli-Q) in the order described, and finally dried in a furnace (100°C) to reduce the possibility of contamination.

Text S2 Water Extraction

The extraction setup for WSOC consists of a 10 mL glass syringe (Eterna Matic, Sanitex, Switzerland) a 25 mm polycarbonate syringe filter holder (Sartorius, Germany), and a 21G × 4 3⁄4 inch needle (Sterican, B. Braun, Germany) at the filter holder outlet. Three circular aerosol filters punches (diameter: 20 mm) were stacked with the loaded side facing upwards and separated by 0.5 mm silicone spacers at the top and bottom. For sample collection, the needle was pierced through the 12 mL Exetainer vial septum (Labco, Lampeter, UK) and excess air was released by opening the vial septum's cap half a twist. Front and backup filters were water extracted separately for front and backup filter WSOC and WINSOC measurement.

Text S3 Radiocarbon Data Processing

Data corrections for mass-fractionation, background, blank, standard normalisation, and uncertainty were performed with the BATS software version 3.6[5]. OxII (SRM 4990 C) and fossil NaAc[6] standards were included in each batch of samples analysed. We applied a constant contamination correction of 0.40 ± 0.20 µg with $F^{14}C = 0.80 \pm 0.36$ and a general cross contamination factor of $0.5 \pm 0.4\%$[7] for TC and WINSOC. For samples subjected to chemical wet oxidation (WSOC), we applied a cross-contamination of 0.5% and a constant contamination of 0.9 ± 0.2 µg C with $F^{14}C = 0.20 \pm 0.08$. The processed $F^{14}C$ values were converted from $F^{14}C$ to $\Delta^{14}C$ (‰) using Equation S1:

$$\Delta^{14}C = \left(F^{14}C\ e^{\left(\frac{1950 - t_0}{8267}\right)} - 1 \right) \cdot 1000‰ \qquad \text{Equation S1}$$
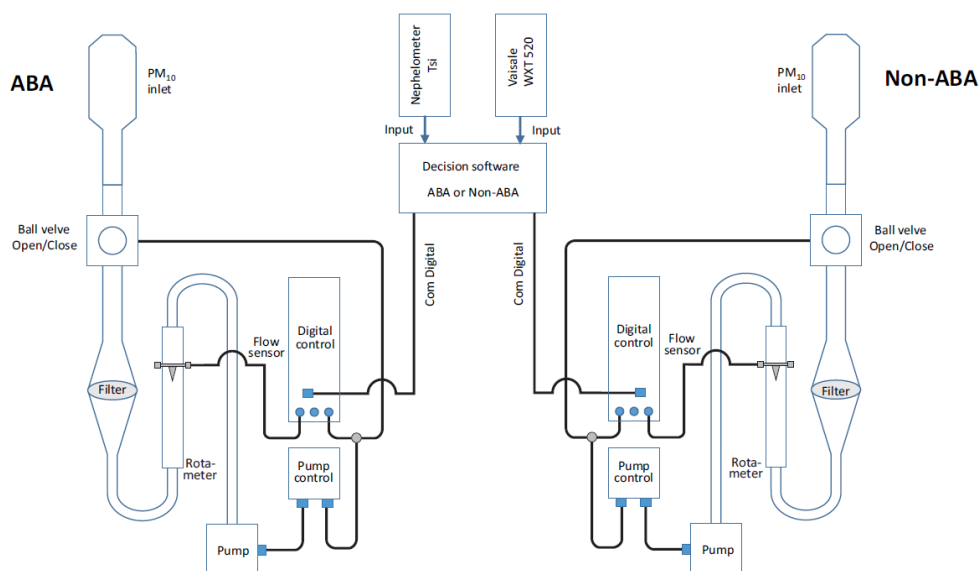
Figure S1: Schematic drawing of ABA and Non–ABA sampling set up operated from February 2016 to November 2018 at the Trollhaugen Observatory.
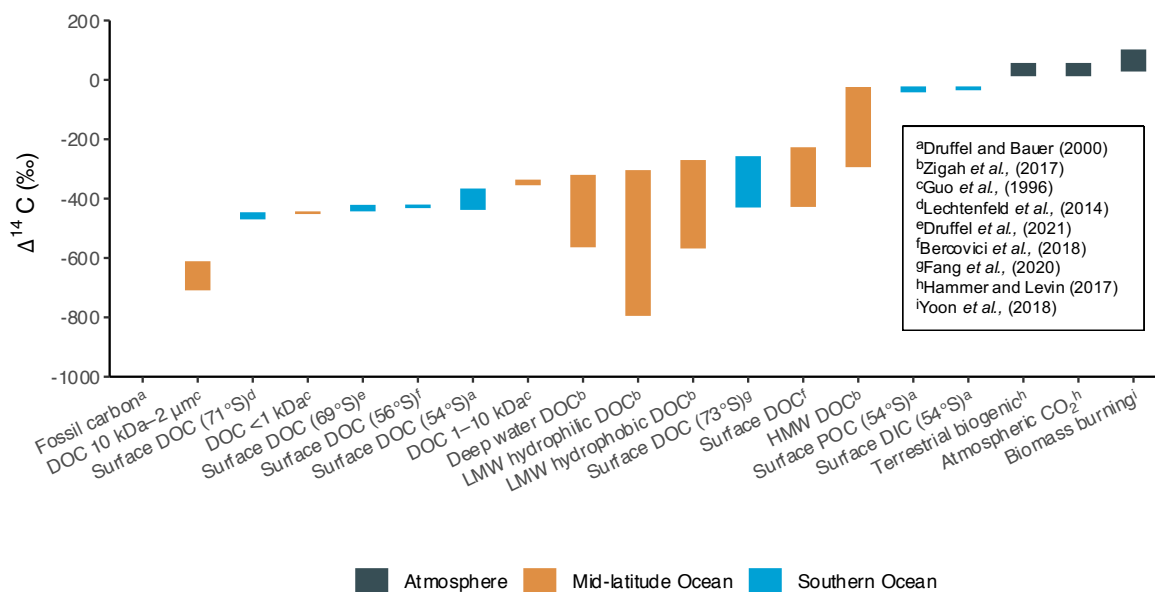
Figure S2: $\Delta^{14}C$ ranges of DOC compared to other sources.

Table S1: $\Delta^{14}C$ (‰) values of the TC, WSOC, and WINSOC fraction.

Start date (MM/YY)	End date (MM/YY)	TC $\Delta^{14}C$ (‰)	WSOC $\Delta^{14}C$ (‰)	WINSOC $\Delta^{14}C$ (‰)
02/16	03/16	-550	-543	-347
11/16	01/17	-594	-489	-317
02/17	04/17	-459	-301	-257
10/17	11/17	-151	-78	-118
11/17	03/18	-423	-412	-304
03/18	05/18	-161		-216

Table S2: Concentrations of the individual fractions. The WSOC and WINSOC concentrations were indirectly determined, and some calculations were not possible due to device malfunction.

Start date (MM/YY)	End date (MM/YY)	EC ng C m^{-3}	OC ng C m^{-3}	TC ng C m^{-3}	WSOC ng C m^{-3}	WINSOC ng C m^{-3}
02/16	03/16	2	19	21	9	15
11/16	01/17	3	11	14		
02/17	04/17	2	10	12	3	7
10/17	11/17	5	23	28		
11/17	03/18	3	12	15	5	9
03/18	05/18	1	6	7	5	3

Table S3: Concentrations of cations; ss/nss refers to sea salt and non-sea salt, respectively.

Start date (MM/YY)	End date (MM/YY)	Na^+ ng m^{-3}	K^+ ng m^{-3}	NH_4^+ ng m^{-3}	ssK^+ ng m^{-3}	$nssK^+$ ng m^{-3}
02/16	03/16	10.5	2.3	31.4	0.4	1.9
11/16	01/17	9.7	1.2	27.6	0.3	0.9
02/17	04/17	19.6	1.3	9.8	0.7	0.6
10/17	11/17	18.9	1.9	14.7	0.7	1.2
11/17	03/18	7.9	1.9	29.6	0.3	1.6
03/18	05/18	11.4	0.5	7.1	0.4	0.1

Table S4: Concentrations of divalent ions; ss/nss refers to sea salt and non-sea salt, respectively.

Start date (MM/YY)	End date (MM/YY)	Mg_2^+ ng m^{-3}	Ca_2^+ ng m^{-3}	SO_4^{2-} ng m^{-3}	$ssSO_4^{2-}$ ng m^{-3}	$nssSO_4^{2-}$ ng m^{-3}	$ssCa_2^+$ ng m^{-3}	$nssCa_2^+$ ng m^{-3}
02/16	03/16	2.4	5.1	212	2.7	210	0.4	4.7
11/16	01/17	1.7	1.0	154	2.4	152	0.4	0.6
02/17	04/17	2.7	1.3	113	4.9	108	0.7	0.6
10/17	11/17	2.3	0.0	114	4.8	109		
11/17	03/18	1.6	1.2	198	2.0	196	0.3	0.9
03/18	05/18	1.5	0.6	79	2.9	77	0.4	0.2

Table S5: Quantitative MS measurements with response for individual fragments. MW 254 is an organosulphate (OS) with a molecular mass of 254 (m/z 253 [M-H]$^-$).

Start date (MM/YY)	End date (MM/YY)	Adipic acid	Azelaic acid	Phthalic acid	Sulphate	MSA	MW 254
02/16	03/16	+	+	+*	+	+	+
11/16	01/17	(+)	+	−	+	+	+
02/17	04/17	sp	sp	sp	sp	sp	sp
10/17	11/17	(+)	+	0	+	+	+
11/17	03/18	0	L	0	+	+	+
03/18	05/18	0	L	0	+	+	+

Start date (MM/YY)	End date (MM/YY)	OS							
		154	156	168	212	216	228	240	250
02/16	03/16	-	0	0	0	0	0	0	0
11/16	01/17	-	-	0	0	-	0	0	0
02/17	04/17	sp	sp	sp	sp	sp	sp	sp	sp
10/17	11/17	0	0	+*	0	0	0	0	0
11/17	03/18	0	0	+*	0	L	+	0	0
03/18	05/18	0	0	+*	0	0	0	0	0

+	Present with nice peak and high response
L	Present with nice peak and low response
(+)	Present with co-elution
(-)	Present in EIC with low intensity, but not in mass spectra for chosen peak
*	Could be a fragment
0	NA
sp	sample spilled

Isoprene/anthropogenic

Isoprene

Monoterpene

References

1.   Hansen, G. *et al.* Atmospheric monitoring at the Norwegian Antarctic station Troll: measurement programme and first results. *Polar Research* **28**, 353–363 (2009).

2.   Fiebig, M. *et al.* Annual cycle of Antarctic baseline aerosol: Controlled by photooxidation-limited aerosol formation. *Atmospheric Chemistry and Physics* **14**, 3083–3093 (2014).

3.   McDow, S. R. & Huntzicker, J. J. Vapor adsorption artifact in the sampling of organic aerosol: Face velocity effects. *Atmospheric Environment Part A, General Topics* **24**, 2563–2571 (1990).

4.   Kirchstetter, T. W., Corrigan, C. E. & Novakov, T. Laboratory and field investigation of the adsorption of gaseous organic compounds onto quartz filters. *Atmospheric Environment* **35**, 1663–1671 (2001).

5.   Wacker, L., Christl, M. & Synal, H. A. Bats: A new tool for AMS data reduction. *Nuclear Instruments and Methods in Physics Research, Section B: Beam Interactions with Materials and Atoms* **268**, 976–979 (2010).

6.   Szidat, S. *et al.* ^{14}C Analysis and Sample Preparation at the new Bern Laboratory for the Analysis of Radiocarbon with AMS (LARA). *Radiocarbon* **56**, 561–566 (2014).

7.   Agrios, K. *et al.* Online coupling of pure O_2 thermo-optical methods – ^{14}C AMS for source apportionment of carbonaceous aerosols. *Nuclear instruments and methods in physics research section B: beam interactions with materials and atoms* **361**, 288–293 (2015).

6.4 Software tools

COMPYCALC (COMPrehensive Yield CALCulation) is an R script to extrapolate the EC losses from the thermal desorption to 100% EC yield using a thermal-desorption model. Furthermore, charring is corrected for in another step to obtain the EC-yield and charring corrected ^{14}C-EC value. The script written in the programming language R is discussed in detail in Chapter 2. COMPYCALC is free and opensource (MIT license) and available as a public repository on GitHub (github.com/martin-rauber/compycalc) and archived in Zenodo (doi.org/10.5281/zenodo.5958275).

Micadas-manual was created as a solution for printed and frequently outdated manuals or checklists on how to operate the Mini Carbon Dating System (MICADAS) at LARA, the Laboratory for the Analysis of Radiocarbon with AMS at the University of Bern. Checklists are a helpful tool to operate complex systems and devices in an efficient and safe manner. Micadas-manual is a web-based checklist build with the ionic framework (github.com/ionic-team/ionic-framework) made to work with both desktop computers and mobile devices. It is kept very simple on purpose for people with little prior programming skills to modify and extend the checklist in the future. Jan Strähl has been a major contributor both in creating of the micadas-manual as well as implementation and testing. Micadas-manual is free and opensource (MIT license) and available as a public repository on GitHub (github.com/martin-rauber/micadas-manual) and is available online (martin-rauber.com/micadas-manual/micadas-manual). As shown in Figure 1, updates to the micadas-manual web server are performed manually by the developers.
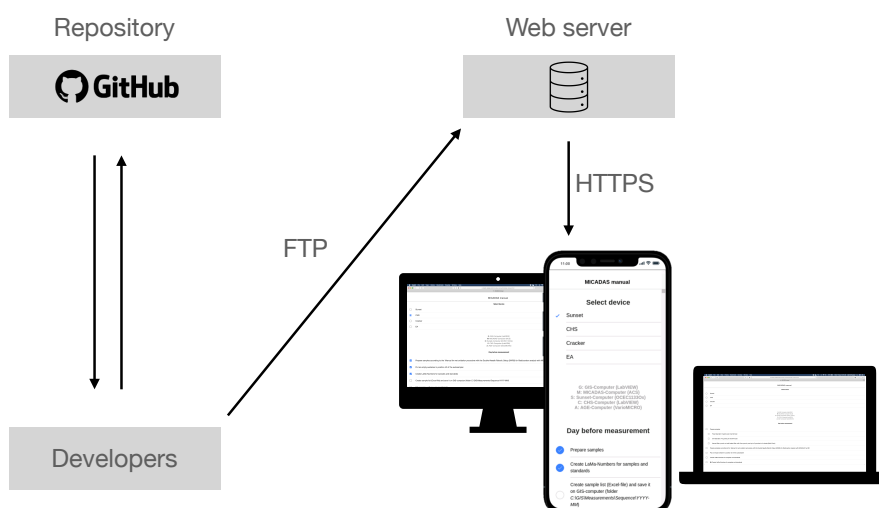
Figure 1: micadas-manual is stored in a GitHub repository. Changes are uploaded by the developers to a web server using the File Transfer Protocol (FTP). The checklist is available on the web for the MICADAS user on any web-enabled device and a simple access for mobile devices is provided with a QR-code in the LARA MICADAS lab.

Sunset-calc is a web application made with R and R Shiny. It allows for the amount determination of individual steps in custom OC/EC analyser protocols, EC yield calculation, and OC/EC yield calculation and carbon amount calculation with amount correction. The application is discussed in Chapter 2. The application runs on a University of Bern R server and is available to the public (14c.unibe.ch/sunsetcalc). Sunset-calc is free and opensource (MIT license) and available as a public repository on GitHub (github.com/martin-rauber/sunset-calc) and archived in Zenodo (doi.org/10.5281/zenodo.6148364).

6.5 List of publications

Rauber, M.; Salazar, G.; Yttri, K. E.; Szidat, S., An Optimised OC/EC Fraction Separation Method for Radiocarbon Source Apportionment Applied to Low-Loaded Arctic Aerosol Filters, Submitted to: *Atmospheric Measurement Techniques*

Song, W.; Zhang, Y-L.; Zhang, Y.; Cao, F.; **Rauber, M.;** Szidat, S.; Kawichai, S.; Prapamontol, T., Is biomass burning always a dominant contributor of fine aerosols in northern Thailand?, Submitted to: *Environment International*

Casotto R.; Skiba, A.; **Rauber, M.;** Strähl, J.; Tobler, A.; Bhattu, D.; Lamkaddam, H.; I. Manousakas, M. I.; Salazar, G.; Cui, T.; Canonaco, F.; Samek, L.; Ryś, A.; El Haddad, I.; Kasper-Giebl, A.; Baltensperger, U.; Necki, J.; Szidat, S.; Styszko, K.; Slowik, J. G.; Daellenbach, K. R., Prévôt, A. S. H., Organic aerosol sources in Krakow, Poland, before implementation of a solid fuel residential heating ban, Submitted to: *Science of The Total Environment*

Guillemot, T., Salazar, G., **Rauber, M.**, Kunz, D., Szidat, S., Wieland, E., Carbon-14 release and speciation during corrosion of irradiated steel under radioactive waste disposal conditions, *Science of The Total Environment*, 817, 152596, 2022

Mousavi A., Sowlat M. H., Lovett C., **Rauber M.**, Szidat S., Boffi R., Borgini A., De Marco C., Ruprecht A. A., Sioutas C., Source apportionment of black carbon (BC) from fossil fuel and biomass burning in metropolitan Milan, Italy, *Atmospheric Environment*, 203, 252–261, 2019

6.6 List of reports

Guillemot, T., Kunz, D., Salazar, G., **Rauber, M.**, Szidat, S., Wieland, E., 2021. Long-term monitoring of dissolved and gaseous ^{14}C-bearing carbon compounds during anoxic alkaline corrosion of irradiated steel. Nagra Working Report NAB 21-26. Nagra, Wettingen, Switzerland.

Guillemot, T., Cvetković, B. Z., Kunz, D., Salazar, G., **Rauber, M.**, Szidat, S., Wieland, E., 2021. Development of Analytical Methods for the Detection of ^{14}C-bearing Carbon Compounds at Ultra-low Concentrations. Nagra Working Report NAB 21-03. Nagra, Wettingen, Switzerland.

6.7 List of presentations

2022

M. Rauber, G. Salazar, V. Moschos, A. S. H. Prévôt, S. Szidat

Compound-specific radiocarbon analysis (CSRA) of oxalate in aerosols: first results from multiple sites

11th International Aerosol Conference (IAC 2022), Athens, Greece

04–09.09.2022

Abstract accepted for a Poster presentation

M. Rauber, J. Strähl, G. Salazar, S. Szidat

Sunset-calc: An R Shiny Application for Processing Thermo-Optical Analysis Data from Atmospheric Aerosol Measurements

Bern Data Science Day 2022, Bern, Switzerland

06.05.2022

Poster presentation

2021

M. Rauber, G. Salazar, K. E. Yttri, V. Moschos, I. El Haddad, A. Prévôt, D. Thomsen, M. Glasius, S. Szidat

Marine Contribution to Antarctic Carbonaceous Aerosol

European Aerosol Conference (EAC 2021) Ireland – virtually

30.08.–03.09.2021

Oral presentation

M. Rauber, G. Salazar, K. E. Yttri, S. Szidat

Optimised Aerosol Fraction Separation in Arctic Aerosol for Radiocarbon Measurement

3rd International Radiocarbon in the Environment Conference, Gliwice, Poland – virtually

05.–09.07.2021

Oral presentation

2019

M. Rauber, G. Salazar, K. E. Yttri, S. Szidat

^{14}C on aerosol filters from Antarctica and Svalbard

Laboratory for Environmental Chemistry Seminar, Paul Scherrer Institute, Villigen, Switzerland

13.12.2019

Oral presentation

M. Rauber, C. Uglietti, G. Salazar, S. Szidat

Chromatographic Separation and Wet Oxidation of Oxalic Acid from Aerosols for Radiocarbon Source Apportionment

18th International Swiss Climate Summer School, Monte Verità, Switzerland

08.–13.11.2019

Poster presentation

M. Rauber, C. Uglietti, G. Salazar, S. Szidat

Chromatographic Separation and Wet Oxidation of Oxalic Acid from Aerosols for Radiocarbon Source Apportionment

12th International Conference on Carbonaceous Particles in the Atmosphere (ICCPA 2019), Vienna, Austria

03.–06.04.2019

Oral presentation

6.8 Teaching activity

Spring semester 2019	Praktikum Allgemeine Chemie für Studierende der Biologie und Minor Biochemie/Chemie
April 2019	Supervision of Manuel Bruppacher, a high-school student from Gymnasium Lerbermatt. Manuel joined for two weeks in the lab and conducted radiocarbon measurements with aerosol filters from India.
Spring semester 2020	Praktikum Allgemeine Chemie für Studierende der Biologie und Minor Biochemie/Chemie
January 2020 – January 2021	Supervision of Alessandra Riva. Alessandra investigated in her Master Thesis Black Carbon in sediments
February 2020 – March 2021	Supervision of Wenhuai Song, a PhD exchange student from the Nanjing University of Information Science & Technology
Spring semester 2021	Praktikum Allgemeine Chemie für Studierende der Erdwissenschaften

6.9   Acknowledgements

hikes around Bern. My gratitude extends also to other radiochemistry people, which infrequently visited in Bern.

Furthermore, my gratitude goes to my colleagues at LARA. First, I would like to thank Edith Vogel, who was always up for nice chat and was a permanent member of the group. Gary Salazar, for all the measurements performed together and the time you took for all my technical and scientific questions. My gratitude also goes to Chiara Uglietti, who introduced me to the IC system in Bern and performed some preliminary chemical wet oxidation experiments, which where a great starting point for me. Here, I would like to thank Matthias Vonwiller as well, who introduced me to the water extraction and the Sunset device. Additionally, although technically taking part during my masters, I would like to thank Erich Malach for completing his bachelor thesis in the group and the opportunity I had to introduce him to several techniques in the lab.

Many thanks go all the people which I had the honour to share an office with. Many thanks go to Tabea Arnold who warmly welcomed me when I first started in Bern. I also had many interesting discussions with Christophe Espic. Beyond the office, I had the honour to join Christophe on an overnight sampling at Jungfraujoch – a memorable experience, it was just a pity that I had to take the small bottle of French red wine I brought with me back to Bern – unopened!

It was a joy to have Selina Etzensperger as a Master student in our group. I had the opportunity to introduce Selina to several tools and devices in the lab and her open and communicative nature made Selina a pleasure to work with. Over the years, we did not only had people leaving, but there were also several additions. Matthias Bantle was a Master student working on Jungfraujoch atmospheric air samples. While sitting opposite each other, we had many fruitful and sometimes quite funny discussions about a wide range of topics – work and far beyond that. With Franziska Lechleitner and Sarah Rowan, the Szidat group grew larger, and I had the pleasure to share my knowledge regarding the chemical wet oxidation with Franziska and Sarah, now also applied beyond aerosols. Despite coming from Scotland, thanks to Sarah the Szidat group has finally someone that is able to speak proper English!

Thomas Laemmel and Dylan Geissbühler will continue and expand the work from Christophe – work on atmospheric gases will remain in the hands of French speakers! I had great discussions with Dylan, admired his creativity and I am confident he will continue to build useful Raspberry based gadgets. I have asked Thomas for advice on many things, shared ideas, had very interesting discussions, and got highly useful input from him. I highly admire his enthusiasm for his work and his caring nature for each and everyone in the group.

Jan Strähl joined the Szidat group to work on a joint project with the Paul Scherer Institute on aerosol filters from India, thus applied and improved on many tools and techniques I set up in the first place. It was always a delight to work with Jan and I highly appreciated his precise and considered way of working in the lab and finding the right solutions.

Eine eigene Seite möchte ich meiner Familie widmen, welcher Ich sehr viel zu verdanken habe. Besonders möchte ich mich bei meiner Mutter Susanna, meinem Vater Hansueli und meiner Schwester Patricia bedanken, welche mich in all den Jahren immer unterstützt haben, meine Ziele zu erreichen.

6.10 Erklärung

gemäss Art. 18 PromR Phil.-nat. 2019

Name/Vorname: Rauber Martin

Matrikelnummer: 11-268-919

Studiengang: Chemistry and Molecular Sciences

        Bachelor ☐   Master ☐   Dissertation ☒

Titel der Arbeit: Radiocarbon source apportionment of carbonaceous aerosols using water-soluble organic carbon and oxalate fractions

Leiter der Arbeit: Prof. Dr. Sönke Szidat

Ich erkläre hiermit, dass ich diese Arbeit selbständig verfasst und keine anderen als die angegebenen Quellen benutzt habe. Alle Stellen, die wörtlich oder sinngemäss aus Quellen entnommen wurden, habe ich als solche gekennzeichnet. Mir ist bekannt, dass andernfalls der Senat gemäss Artikel 36 Absatz 1 Buchstabe r des Gesetzes über die Universität vom 5. September 1996 und Artikel 69 des Universitätsstatuts vom 7. Juni 2011 zum Entzug des Doktortitels berechtigt ist.

Für die Zwecke der Begutachtung und der Überprüfung der Einhaltung der Selbständigkeitserklärung bzw. der Reglemente betreffend Plagiate erteile ich der Universität Bern das Recht, die dazu erforderlichen Personendaten zu bearbeiten und Nutzungshandlungen vorzunehmen, insbesondere die Doktorarbeit zu vervielfältigen und dauerhaft in einer Datenbank zu speichern sowie diese zur Überprüfung von Arbeiten Dritter zu verwenden oder hierzu zur Verfügung zu stellen.

Ort/Datum   Unterschrift

6.11 Curriculum Vitae

Family Name:	Rauber
First Name:	Martin
Web:	martin-rauber.com

Education

09/2018 – 08/2022	**PhD of Science in Chemistry and Molecular Sciences** – University of Bern, DCBP, Bern, Switzerland
	Thesis: Radiocarbon source apportionment of carbonaceous aerosols using water-soluble organic carbon and oxalate fractions
08/2017 – 08/2018	**MSc in Chemistry and Molecular Sciences** – University of Bern, DCBP, Bern, Switzerland
	Thesis: Compound-specific Radiocarbon Analysis of Aerosols
02/2015 – 02/2017	**MSc in Molecular Technologies** – University of Applied Sciences and Arts Northwestern Switzerland FHNW, Basel, Switzerland
	Thesis: Development of implantable pH–sensitive Polymers for Pest Control
09/2011 – 09/2014	**BSc in Molecular Life Sciences** – University of Applied Sciences and Arts Northwestern Switzerland FHNW, Basel, Switzerland
	Thesis: Effect of Size, Shape and Crystallinity of Tripod Shaped SPIO Nanoparticles on Relaxivity
08/2009 – 06/2010	**Professional baccalaureate**, Technical College – GIB Thun, Switzerland
08/2006 – 07/2009	**Apprenticeship Laboratory Technician** – University of Bern, DCBP, Bern, Switzerland

Professional Experience

08/2017 – 09/2018	**Assistant** (*Hilfsassistent*), University of Bern, DCBP, Bern, Switzerland
04/2017 – 08/2017	**Research assistant**, University of Applied Sciences and Arts Northwestern Switzerland FHNW, Basel, Switzerland
	Synthesis, processing, purification, and analysis of organic products from medicinal chemistry
10/2016 – 01/2017	**Traveling**: Australia, New Zealand, Fiji, Hong Kong
02/2016 – 10/2016	**Master Thesis** – Applied Chemistry and Translational Biomaterials (ACTB) Group of Anton Blencowe, University of South Australia, Adelaide, Australia
01/2015 – 02/2015	**Research assistant**, University of Applied Sciences and Arts Northwestern Switzerland FHNW, Basel, Switzerland
10/2014 – 12/2014	**Internship** – iC42, University of Colorado Denver, Denver, United States
	Generation of tacrolimus metabolites with human liver microsomes, HPLC–MS analysis
04/2014 – 07/2014	**Bachelor Thesis** – Shastri lab, Albert Ludwig University of Freiburg, Freiburg im Breisgau, Germany
04/2011 – 08/2011	**Construction worker** – temporary employment
11/2010 – 04/2011	**Military Service**, Swiss Army; duty completed